Transport stationnaire dans des fluides quantiques de basse dimensionnalité

Juliette Huynh

Institut de Physique de Nice (INPHYNI)

UMR CNRS 7010, Nice, France

Présentée en vue de l'obtention du grade de docteur en physique d'Université Côte d'Azur

Dirigée par : Frédéric Hébert / Pierre-Élie Larré

Soutenue le : 18 novembre 2024

Devant le jury, composé de :

Mathias Albert : Professeur
INPHYNI, Université Côte d'Azur

Romain Dubessy : Professeur
PIIM, Université d'Aix-Marseille

Christophe Josserand : Directeur de recherche CNRS
LadHyx, École Polytechnique

Aleksandra Petković : Maîtresse de conférences
LPT, Université Paul Sabatier

Peter Schlagheck : Professeur
Université de Liège

Patrizia Vignolo : Professeure
INPHYNI, Université Côte d'Azur

Transport stationnaire dans des fluides quantiques de basse dimensionnalité

Stationary transport in low-dimensional quantum fluids

Jury:

– *Président*
Patrizia Vignolo, Professeure, INPHYNI, Université Côte d'Azur, Nice

– *Rapporteurs*
Aleksandra Petković, Maîtresse de conférences, LPT, Université Paul Sabatier, Toulouse
Peter Schlagheck, Professeur, Université de Liège

– *Examinateurs*
Romain Dubessy, Professeur, PIIM, Université d'Aix-Marseille
Christophe Josserand, Directeur de recherche CNRS
LadHyx, Ecole Polytechnique, Palaiseau

– *Directeur de thèse*
Frédéric Hébert, Professeur, INPHYNI, Université Côte d'Azur, Nice

– *Co-directeur de thèse*
Pierre-Élie Larré, Chargé de recherche CNRS, INPHYNI, Nice

– *Invité*
Mathias Albert, Professeur, INPHYNI, Université Côte d'Azur, Nice

Résumé

Transport stationnaire dans des fluides quantiques de basse dimensionalité : Du mouvement superfluide à la résistance ondulatoire

Les fluides quantiques, tels que les condensats de Bose-Einstein ou les superfluides de lumière – deux systèmes d'intérêt dans ce manuscrit – offrent des plateformes fascinantes pour explorer des phénomènes physiques fondamentaux sous des conditions extrêmes. L'un des aspects cruciaux de ces systèmes est leur comportement face à des perturbations, pouvant entraîner des transitions entre différents régimes de transport pour des vitesses critiques bien définies. L'objet de notre étude est donc d'examiner un fluide quantique s'écoulant à une vitesse donnée et rencontrant un obstacle aux paramètres arbitraires. Nous avons développé des modèles intégrant le potentiel non-linéaire d'interaction, permettant de traiter divers systèmes tels que les atomes froids ou les fluides de lumière, et d'aller au delà des résultats bien connus dans la communauté. Nous avons commencé par explorer les systèmes unidimensionnels, cherchant à établir une carte complète des régimes de transport stationnaires possibles. Notre attention s'est d'abord portée sur le régime superfluide, avec une étude analytique et numérique approfondie de la vitesse critique de superfluidité, montrant une dépendance non-triviale des paramètres du problème. Ce travail a ensuite été étendu aux superfluides de lumière en incluant un traitement systématique des pertes, montrant qu'elles ne modifient pas fondamentalement nos résultats tant qu'elles restent linéaires et homogènes. S'ensuit l'étude d'un autre régime de transport stationnaire à une dimension, à des vitesses supersoniques. Grâce à des méthodes similaires, nous avons mis en lumière une autre vitesse critique, la séparatrice supersonique, et l'avons étudiée analytiquement et numériquement en fonction des paramètres du problème. Cette étude a révélé l'existence d'états ayant une dynamique similaire à celle du régime superfluide, mais à des vitesses supersoniques. Enfin, nous avons exploré la superfluidité dans des systèmes bidimensionnels. Afin d'aller au delà des résultats préexistants, nous avons développé un modèle tenant compte de la compressibilité du fluide, la non-linéarité du système, et la pénétrabilité de l'obstacle. L'analyse conjointe de notre modèle et des simulations a mis en évidence deux mécanismes distincts pour briser la superfluidité, dépendant de l'amplitude de l'obstacle. Nous avons ensuite réalisé diverses simulations numériques afin d'avoir une vision plus concrète de ces phénomènes, et avons entamé une étude préliminaire sur l'éjection des vortex dans le fluide quantique. En accord qualitatif avec des résultats expérimentaux récents obtenus pour d'autres types d'obstacles, notre modèle simplifié constitue un pas en avant dans l'étude de la superfluidité, avec des implications potentielles pour d'autres plateformes expérimentales, au-delà des atomes froids.

Mots clés : Superfluidité, Fluides quantiques, Transport quantique, Vortex

Abstract

Stationary transport in low dimensional quantum fluids: From superfluid motion to wave resistance

Quantum fluids, such as Bose-Einstein condensates and superfluids of light – two systems of interest in this manuscript – offer fascinating platforms for exploring fundamental physical phenomena under extreme conditions. A crucial aspect of these systems is their behavior when encountering perturbations, which can lead to transitions between different transport regimes at well-defined critical velocities. The objective of our study is to examine a quantum fluid flowing at a given velocity past an obstacle with arbitrary parameters. We developed models that incorporate various nonlinear interaction potential, enabling us to address various systems such as cold atoms and quantum fluids of light, and to extend beyond the well-established results in the field. We began by exploring one-dimensional systems, aiming to establish a comprehensive map of the possible stationary transport regimes. Our initial focus was on the superfluid regime, for which we conducted an in-depth analytical and numerical study of the critical velocity for superfluidity, revealing a nontrivial dependence on the system's parameters. This work was then extended to superfluids of light, with a systematic treatment of losses, showing that they do not fundamentally alter our previous results as long as they remain linear and homogeneous. This was followed by the study of another stationary transport regime in one dimension, specifically at supersonic velocities. Using similar methods, we highlighted another critical velocity, the supersonic separatrix, and studied it analytically and numerically as well. This study revealed the existence of states with dynamics similar to those of the superfluid regime, but at supersonic velocities. Finally, we explored superfluidity in two-dimensional systems. To go beyond previous results, we developed a model that accounts for the compressibility of the fluid, the nonlinearity of the system, and the penetrability of the obstacle. The combined analysis of our model and simulations revealed two distinct mechanisms for the breakdown of superfluidity, depending on the amplitude of the obstacle. We then conducted several numerical simulations to gain a more concrete understanding of these phenomena, and initiated a preliminary study on vortex ejection in the quantum fluid. In qualitative agreement with recent experimental results obtained for other types of obstacles, our simplified model marks a step forward in the study of superfluidity, with potential implications for other experimental platforms beyond cold atoms.

Keywords: Superfluidity, Quantum fluids, Quantum transport, Vortex

Acknowledgements

Ces dernières années, bien qu'intenses, furent aussi incroyablement riches en travail, en découvertes et en émotions. Elles m'auront permis — je l'espère — de me rapprocher de l'idée que je me fais d'une chercheuse accomplie. Cependant, cette thèse n'aurait jamais vu le jour sans l'accompagnement, l'expertise, et le soutien de nombreuses personnes, que je tiens à remercier ici.

Tout d'abord, je souhaite exprimer ma profonde gratitude envers mes encadrants "officiels", Fred et Pierre-Élie. Votre disponibilité, vos conseils avisés, et votre soutien constant ont été essentiels tout au long de mon parcours, et vous avez toujours été présents dans les moments décisifs. Merci pour toutes les discussions — qu'elles soient scientifiques ou autres — qui m'ont enrichie tant sur le plan intellectuel que personnel. Je ne peux évidemment pas oublier Mathias, mon directeur "non-officiel", sans qui mon parcours à Nice depuis toutes ces années aurait été bien triste. Ton incroyable pédagogie a rendu la physique non seulement accessible, mais aussi passionnante. Que ce soit au labo, sur un terrain, ou aux Distilleries Idéales, nos échanges m'ont permis d'aborder ma thèse de manière sereine et efficace.

Je tiens également à remercier tous les enseignants et chercheurs de Nice qui ont croisé mon chemin depuis mes années de licence jusqu'à aujourd'hui. Vos cours, vos conseils, et vos discussions m'ont beaucoup apporté. Mention spéciale à Claire et Céline, mais aussi à Fabrice. Je ne pourrais pas ne pas mentionner l'École de Physique des Houches, qui m'a accueillie maintes fois sur son site incroyable. J'espère que je pourrai prendre des actions chez vous un jour.

Je souhaite aussi adresser un grand merci aux collègues rencontrés en chemin, que ce soient les thésards de Sophia : Gianni, Apoorva, Loïc, Les Pierre, Martial, Stephan; et ceux du nouveau labo : Léo, Clément, Klint, Lucas, Charlotte, JM et bien d'autres. Vous avez rendu les longues journées au labo bien plus agréables et enrichissantes. Je pense aussi à tous les collègues rencontrés en conférences, en particulier Tangui, Myrann et Manon, pour leurs échanges stimulants.

Mon parcours atypique, marqué par le handball, a également joué un rôle clé dans mon orientation vers la physique. Merci à toutes les personnes rencontrées en chemin, qui m'ont permis d'arriver à Nice au bon moment et au bon endroit. Une pensée particulière à Éric Baradat, sans qui je n'aurais probablement pas poursuivi mes études jusqu'à ce niveau.

En dehors du cadre professionnel, je suis plus que tout reconnaissante à tous mes amis, qu'ils soient de la physique ou d'ailleurs, pour leur soutien sans faille depuis mon arrivée à Nice. Un immense merci à Ana, Anaïs, Ines, Antho, Adnan, Kévin, Sarah, David, Hazel, Benji, Axel, et pardon à tous ceux que j'ai probablement oubliés. Vous avez toujours été là pour m'apporter du fun au quotidien, et sans vous toutes ces années auraient été bien fades. Vous êtes épiques !

Finalement, rien de tout cela n'aurait été possible sans le soutien indéfectible de mes proches : mes parents, mes grands-parents et ma soeur (et Matou), qui ont toujours été présents quoi qu'il advienne, et qui m'ont toujours encouragée quels que soient les choix que je fasse, qu'ils soient avisés ou non.

Enfin bref, vous l'aurez compris, merci à tous !

Contents

Introduction

> *"When Kapitza and the great theoretical physicist Landau, followed by physicists such as Fritz London, Lars Onsager, Richard Feynman and other greats, came on board, there was a tremendous surge of excitement, which lasted for many years and helped bring the subject to its present state of understanding"*
>
> R. Donnelly [1]

The story of superfluidity is a testament to the unexpected and often astonishing discoveries that have emerged from the realm of fundamental physics. Its history is intertwined with the development of quantum mechanics and the exploration of matter at extremely low temperatures. The phenomenon of superfluidity, characterized by its complete absence of viscosity and other remarkable behaviors, was first observed in the early 20th century, challenging classical physics and opening the door to the investigation of new quantum phenomena. Here are the main points of the long and tortuous history of superfluidity, leading to the theory as we know it today. For a more detailed account of the historical part, we invite the reader to refer to Refs. [1–5].

The early stages of superfluidity

Onnes & the premises of superfluidity

The roots of superfluidity can be traced back to the early 20th century when the race to liquefy gases was at its peak. It was on July 10th 1908 that Kamerlingh Onnes' group in Leiden achieved a groundbreaking feat by successfully liquefying helium for the first time with cryostats. Though the concept was unknown at the time, the foundations for the study of superfluidity were laid.

A few years later, Onnes' team observed the superfluid transition in liquid helium on August 2nd 1911, supposedly the very same day they observed superconductivity in mercury. They indeed noticed a peculiar property when cooling helium down to extremely low temperatures: The ability to flow without dissipation, a hallmark of superfluidity [6, 7]. For a long time, liquid helium stood as the sole example of a simple bosonic quantum liquid displaying a superfluid behavior until the creation of the first gaseous condensates in 1995 in the groups of E. Cornell and C. Wieman in Boulder [8], and the group of W. Ketterle at MIT [9].

Even though Onnes' primary focus was in practice on liquid helium, it is not what he is most renowned for. It is indeed for his serendipitous discovery of superconductivity in 1911 that he was awarded the Nobel Prize in 1913 *"for his investigations on the properties of matter at low temperatures which led, inter alia, to the production of liquid helium"* [10].

A shared discovery in 1937

It is no wonder that the next important step also took place both in Leiden and with liquid helium as after Onnes' discovery, his laboratory possessed a monopoly on liquid helium for

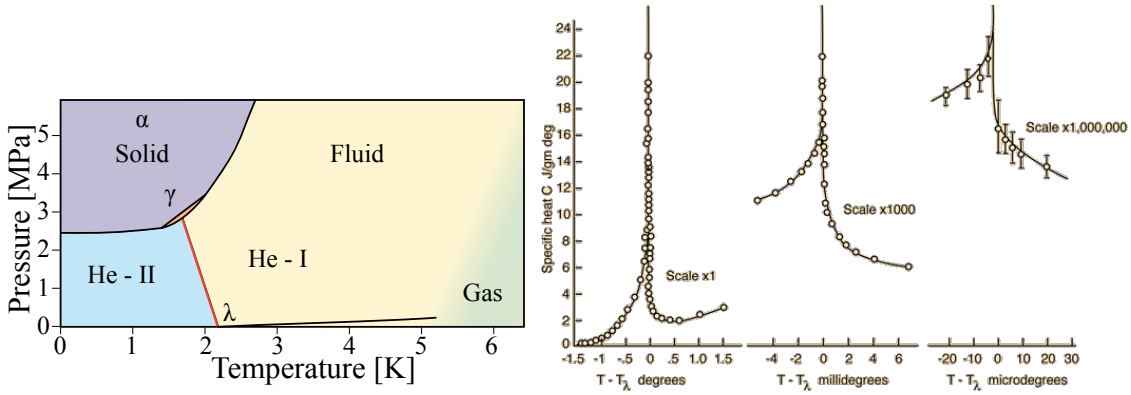

Figure 1: Left: Phase diagram of ^{4}He as a function of the pressure and the temperature. The liquid shows a phase transition to a superfluid phase (He II) at the $\lambda-$point ($T_\lambda = 2.17$ K and $P = 1$ atm), but also all along the $\lambda-$line (in red). Right: Specific heat data C of ^{4}He as a function of the temperature $T - T_\lambda$. C shows a discontinuity as the temperature drops past the $\lambda-$point, heralding the transition from normal He I to superfluid He II. Figure from Ref. [12].

a while. Over the next 30 years, researchers worked on the interesting phase transitions of liquid helium, but the situation remained still until Keesom and his daughter discovered in 1930 that helium-4 (also written ^{4}He) had two different liquid states called "He I" and "He II", respectively above and below $T_\lambda = 2.17$ K for a pressure of about 1 atm [11]. This point, called the $\lambda-$point, determines the so-called $\lambda-$transition, from which normal fluid helium (He I) goes to superfluid He II (see the left panel of Fig. 1). Interestingly, this point is called like this because the graph of the specific heat capacity as a function of temperature (for a given pressure) resembles the Greek letter lambda λ at the transition (see the right panel of Fig. 1).

In the wake of 1938, a first explanation for the nature of ^{4}He below the $\lambda-$point was given in two seminal papers [13, 14], in which the goal was to show that a small viscosity could be responsible for the large apparent thermal conductivity. This intuition was proved right, and the authors showed experimentally that liquid helium could flow through small channels with apparently zero viscosity. In other words, the fluid flows without any resistance. As explained by Kapitza, *"by analogy with superconductors, [...] the helium below the $\lambda-$point enters a special state which might be called superfluid"*. For the first time, the concept of superfluidity was mentioned [3], and the nature of He II was then recognized as a manifestation of it.

But who between the Russian or the Canadians gets to have the primacy of the discovery, as both papers were published side by side in Nature in January 1938, respectively on page 74 and 75? That question was up to debate for a while as P. Kapitza received the Nobel Prize in 1978 for superfluidity-related works, more precisely *"for his basic inventions and discoveries in the area of low-temperature physics"*. However, credit where credit is due, and it is nowadays commonly admitted that superfluidity was independently discovered in December 1937 by P. Kapitza in Moscow [13], and J. F. Allen and A. D. Misener in Cambridge [14].

This new domain of physics really became a hot topic of the moment, attracting the interest of many renowned researchers. This was the case for example of Landau, at that time a promising young researcher at the Physical Technical Institute in Kharkov, who was engaged to work with Kapitza in Moscow on that new mysterious phenomenon occurring close to absolute zero temperature. Ultimately, he became one of the pioneers of the domain, and laid the groundwork of the theory of superfluidity that later led to his obtention of the Nobel Prize in 1962 *"for his pioneering theories for condensed matter, especially liquid helium"*.

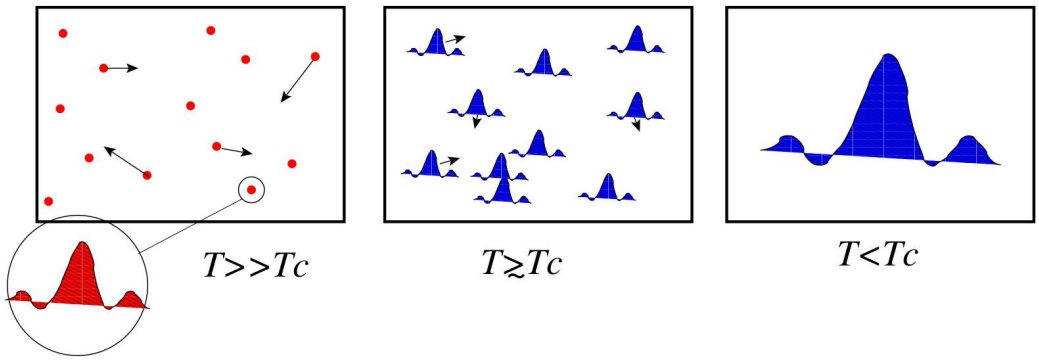

Figure 2: Left: An atomic gas at high temperature, the atoms behave as independent particles. Center: As the temperature decreases, the de Broglie wavelength λ_{th} increases and the classical vision starts to fail. Right: λ_{th} is of the order of the interatomic distance when the temperature decreases even further. If the particles are bosons, all the wave packets overlap, and the atoms form a giant matter wavefunction, the BEC.

The advent of various theories: From liquid helium to cold atoms

Bose-Einstein condensation (BEC)

The explanation of the wave-particle duality is one of the most important results of quantum mechanics: It states that any quantum entity can exhibit both a wave and a particle behavior depending on the experimental circumstances. As a consequence, to each atom with a given velocity (or momentum) is associated a wave with a given wavelength. The existence of a perfectly localized particle is precluded by Heisenberg's uncertainty principle $\Delta x \Delta p \geq \hbar/2$: It is not possible to simultaneously know the position x and velocity $v = p/m$ of a given particle. Instead, a particle is described using a wave packet, and its size is quantified by the de Broglie wavelength $\lambda_{\mathrm{th}} \propto \hbar/\sqrt{k_{\mathrm{B}}T}$ at finite temperature T. At typical room temperature, this wavelength is usually negligible compared to the average interatomic distance, and a quantum view of the system is not necessary because the spatial extension of each wave packet is really small: The atoms behave as independent classical particles. In low-temperature quantum fluids however, the atoms slow down and their de Broglie wavelength λ_{th} is of the order of the average interatomic distance. The overlapping between each wave packets results in the inability to distinguish individual particles, as they all occupy the same quantum state with minimal energy if they are bosons. This gives rise to a macroscopic coherent system known as the condensate[1] (see Fig. 2).

According to the Penrose-Onsager criterion [15], true BEC exists when the one-body density matrix (OBDM) tends to a constant – the condensed fraction n_0 – for a large separation between two arbitrary points in space:

$$\lim_{|\boldsymbol{r}-\boldsymbol{r'}|\to\infty} \rho(\boldsymbol{r},\boldsymbol{r'}) = \lim_{|\boldsymbol{r}-\boldsymbol{r'}|\to\infty} \langle \hat{\Phi}^\dagger(\boldsymbol{r})\hat{\Phi}(\boldsymbol{r'})\rangle = n_0, \tag{1}$$

with $\hat{\Phi}^\dagger(\boldsymbol{r})$ ($\hat{\Phi}(\boldsymbol{r})$) the field operator creating (annihilating) a particle at point $\boldsymbol{r}$. Physically, this mathematical definition means that BEC is present whenever a finite fraction of the particles occupies the state of lowest energy. This is called off-diagonal long-range order (ODLRO) as it involves the nondiagonal components of the one-body density matrix [15–17].

Different behaviors can be expected for the OBDM depending on the temperature and the dimensionality of the system. We invite the reader to refer to [18] for a detailed calculation of the OBDM in various dimensions. In D = 3, the most important parameter is the temperature of the system: If $T > T_c$, the distribution exponentially decays to zero over a distance close

[1] This phenomenon is exclusive to bosonic particles, as Pauli's exclusion principle prohibits it for fermions.

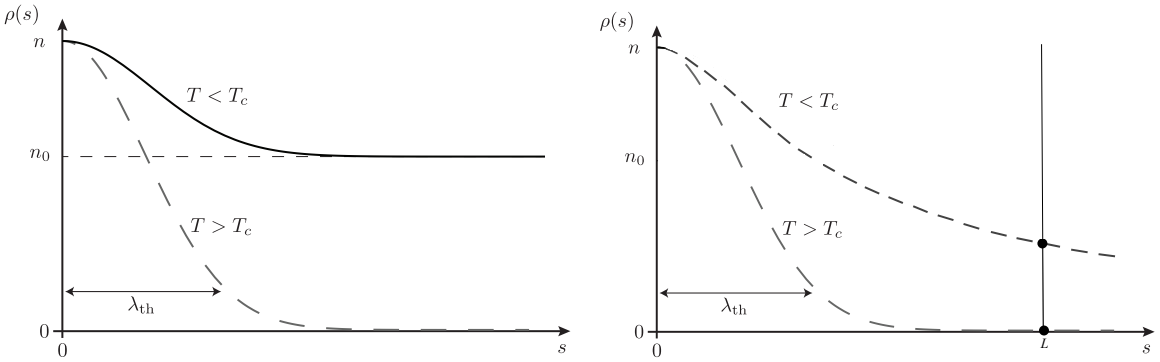

Figure 3: Left: Sketch of the one-body density matrix $\rho(s)$ for a 3D weakly interacting Bose gas below (solid line) or above the critical temperature T_c (dashed line). The convergence of the OBDM to a finite value for $T < T_c$ indicates the presence of a BEC. Right: Idem, but for a 2D system. The upper dashed line corresponds to the powerlaw algebraic decay obtained at $T < T_c$. Even though the OBDM does not converge for $s \to +\infty$, is is still finite when reaching the boundary L of the system: We talk of quasicondensate.

to the de Broglie wavelength. There is no long-range order, and true BEC is not possible. On the contrary, if $T < T_c$, the one-body density matrix is also decaying over the same distance but does not vanish [19], such that $\lim_{s\to\infty} \rho(s) = n_0$. The system is a true BEC as there is ODLRO. A representation of the one-body density matrix for D = 3 is provided in the left part of Fig. 3, as a function of the modulus $s = |\boldsymbol{r} - \boldsymbol{r'}|$ of the separation between two arbitrary points in space.

Things become more complicated in D = 1 and D = 2: Strictly speaking, true BEC is not supposed to occur in dimensions lower than D = 3 because long-range order (LRO) does not exist at finite temperatures [20, 21], as the phase fluctuations are too important. Yet, one can generally define a coherence length, on which the phase fluctuations are small enough, and below which the system exhibits coherence. When the typical size L of the system is smaller than this length – which is usually the case in most experiments – the system is locally similar to a true BEC: We then talk of quasicondensate [22]. In that case, the system can be divided into different blocks of size the coherence length, each being considered as a true condensate. The only difference is that the phases of different blocks are not correlated with each other.

In D = 2, the density matrix does not converge to a finite value but instead shows the presence of an algebraic powerlaw decay [23] (top dashed line in the right part of Fig. 3) much slower than for $T > T_c$ (the exponent depends on the temperature of the system). Particles far away from each other will still be correlated over the size L of the system, indicating the possibility of phase transition at sufficiently low temperature: This is called quasi-long-range order (QLRO). Note that phase fluctuations are negligible in 2D. There are only thermal fluctuations in the system, so the OBDM will converge to a finite value at $T = 0$: True BEC is possible.

In 1D, the situation is even more dire because in addition to thermal fluctuations, the OBDM also presents phase fluctuations at $T = 0$, which lead to a powerlaw decay. One finds that the thermal fluctuations can be neglected in the limit of small temperature such that $k_{\rm B}T \ll \sqrt{\mu k_{\rm B} T_d}$, with μ the chemical potential and T_d the temperature of quantum degeneracy. In the end, at finite temperature the OBDM usually exhibits an exponential decay, making it impossible for BEC to occur. When $k_{\rm B}T \ll \sqrt{\mu k_{\rm B} T_d}$, this transforms into an algebraic powerlaw decay, resulting into a quasicondensate over the size L of the system. At $T = 0$ however, the presence of phase fluctuations prevents the OBDM from converging to a finite value, and true BEC is not possible. The OBDM and the possibility of quasicondensation in 1D will be further discussed in Sec. 1.1.2.

To sum up, Bose-Einstein condensation is a phenomenon that, albeit supposed to be

restricted to 3D bosonic systems, can actually occur in any dimension and at low temperatures if the typical size L of the experiment is small enough that the phase coherence is maintained over the whole system. The particles then all occupy a single ground state, which population is so large that is gives rise to a coherent macroscopic system.

A link between BEC and superfluidity? The superfluidity of liquid helium below $T_\lambda = 2.17$ K has long been, since its discovery in 1938, one of the major research topics in low-temperature physics. Indeed Fritz London developed, shortly after its discovery, an innovative theory suggesting that the superfluidity of ^{4}He actually resulted from the Bose-Einstein condensation of said atoms, as they are bosons at very low temperature. This theory was notably supported by the fact that the $\lambda-$transition and condensation temperatures of liquid helium are very close, namely $T_\lambda = 2.17$ K and $T_C = 3.13$ K respectively (note that T_λ comes from an experimental measurement, whereas T_C is a theoretical prediction). This proximity then suggests a fundamental correlation between the two phenomena. However, according to Landau, the involvement of quantum statistics seemed unjustified, and the link proposed by London unfounded. Why would superfluidity be associated with Bose-Einstein condensation, which is applicable solely to bosons? This skepticism arose particularly because superfluidity resembles superconductivity, a phenomenon observed for fermions. It was not until the late 1950s with the development of the BCS theory [24] that it became clear that electrons actually form Cooper pairs, i.e. bosons which can undergo Bose-Einstein condensation, thus leading to superconductivity. London's intuition was proved right, which Landau never admitted [5].

The two-fluid model

Several explanations were developed simultaneously to explain superfluidity in liquid helium, notably by London and Tisza [25–27], who presented a hydrodynamic description of superfluid helium based on a two-fluid model. This entailed an interaction-less mixture of a condensate and a normal liquid, each having its own velocity field and density. The sum of both the condensed and the normal densities (respectively n_s and n_n) must be constant and equal to the total density of the fluid: $n = n_s + n_n$. The condensed part is the one exhibiting superfluidity, flowing without friction and not carrying entropy. Its proportion increases as the temperature decreases, going from $n_s(T = T_\lambda)/n = 0$ to $n_s(T = 0)/n = 1$. Conversely, the normal fraction carries all the entropy and behaves like an ordinary fluid, viscous, composed of "classical" particles subjected to thermal excitations [5]. Both parts satisfy the hydrodynamic equations (4) to (8) provided in Ref. [28], and are at the origin of two sound velocities in He II [29].

This model was then more rigorously developed by Landau [28, 30], but with different interpretations for its components. He considered the superfluid as the ground state of the quantum fluid (regardless of its statistics), and the normal part as a gas of elementary excitations. This led to a rather peculiar spectrum of excitations for liquid helium, as shown in Fig. 4. He then arrived at the conclusion that *"every weakly excited state can be considered as an aggregate of single 'elementary excitations'"*, which are divided in two categories: At small momenta, the excitations are phonons propagating at the speed of sound in the fluid, with linear dispersion relation $\varepsilon = cp$. A minimum appears at larger momenta, giving rise to another type of excitations called *rotons*, with dispersion relation $\varepsilon = \Delta + \frac{(p-p_*)^2}{2\mu}$, μ being the effective mass, Δ the minimum energy of rotons, and p_* the impulsion at the minimum.

One equation to rule them all

A theoretical description of liquid helium remained quite complex and superfluidity in such systems not entirely understood, mainly because of the significant interactions between the particles, which complicates the physics as further proved by the appearance of a roton part

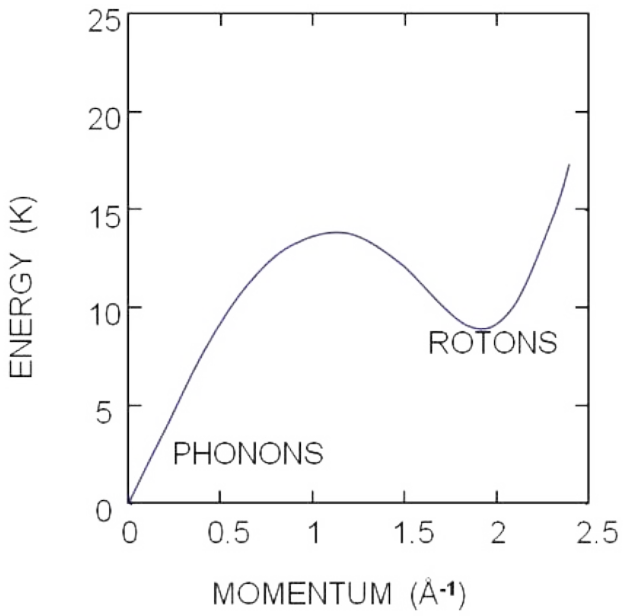

Figure 4: Spectrum of excitations of liquid helium, as proposed by Landau. It has a low energy branch that corresponds to phonons, as well as a higher energy branch associated to rotons. Δ is the energy of the roton minimum.

in the dispersion relation of liquid helium (see Fig. 4). Only 10% of the atoms enter the condensed fraction, which is not enough to experimentally observe Bose-Einstein condensation. Important progress was then made in the understanding of more diluted quantum fluids such as BECs, which are described by simpler interactions, making a theoretical description more accessible. Initially, these weakly interacting systems had few experimental representations and were mostly theoretical, but the advent of ultracold gases in the 1990s opened the way to a vast domain of physics that remains very active today.

One of the main characteristics of a generic quantum fluid is interactions between particles. While overlooking them makes it easier to derive analytical solutions for the dynamics, they are necessary for superfluidity to occur. In a typical ultracold quantum gas, the average interparticle distance is much larger than the range of the interatomic potential. This means that these particles are generally far apart from each other because the system is dilute, and only binary collisions between the particles need to be considered. The detailed form of the potential is however not relevant, and this two-body interaction potential can be replaced by a contact potential [31], which simplifies the mathematical treatment:

$$V(|\boldsymbol{r}_i - \boldsymbol{r}_j|) = g\delta(\boldsymbol{r}_i - \boldsymbol{r}_j), \tag{2}$$

where $g = 4\pi\hbar^2 a_s/m$. In such dilute systems at low temperatures, s-wave scattering is predominant, and the scattering length a_s is the only parameter needed to characterize the strength of the interactions. Its value can be computed using the Born approximation within the framework of scattering theory [19, 31]. Experimentally, the scattering length a_s can be tuned via Feshbach resonances [32], making it possible to change its sign, and work with either repulsive ($a_s > 0$) or attractive ($a_s < 0$) interactions.

For a fully condensed system, all N particles are in the same state $\phi(\boldsymbol{r})$: It is thus possible to build a many-body wavefunction, which can be expressed as the product of N fundamental single-particle wavefunctions (Hartree-Fock approximation) [19]

$$\Phi(\boldsymbol{r}_1, \boldsymbol{r}_2, ..., \boldsymbol{r}_N, t) = \phi(\boldsymbol{r}_1, t) \times \phi(\boldsymbol{r}_2, t) \times ... \times \phi(\boldsymbol{r}_N, t). \tag{3}$$

Each single-particle wavefunction will be subjected to the Hamiltonian

$$H = \sum_{i=1}^{N} \left(\frac{\boldsymbol{p}_i^2}{2m} + U(\boldsymbol{r}_i) \right) + \frac{1}{2} \sum_{i \neq j}^{N} V(|\boldsymbol{r}_i - \boldsymbol{r}_j|), \tag{4}$$

with $U(\boldsymbol{r}_i)$ an external potential acting on the particle i[2], and $V(|\boldsymbol{r}_i - \boldsymbol{r}_j|)$ the interaction potential previously defined in Eq. (2).

In order to find the expression of ϕ, we use a variational approach on the total energy $E[\phi] = \langle \phi | H | \phi \rangle$. This energy functional is given by

$$E[\phi] = N \int d\boldsymbol{r}\, \phi^*(\boldsymbol{r}) \left(-\frac{\hbar^2}{2m} \nabla^2 + U(\boldsymbol{r}) \right) \phi(\boldsymbol{r}) + \frac{gN(N-1)}{2} \int d\boldsymbol{r}\, |\phi(\boldsymbol{r})|^4. \tag{5}$$

Note that as the number of particles N is really large, then $N(N-1) \sim N^2$. A solution for the wavefunction can be found by minimizing this energy functional with a constraint on the normalization of the wavefunction: $\int d\boldsymbol{r}\, |\phi(\boldsymbol{r})|^2 = 1$. Using a Lagrange multiplier μ, one has to compute $\delta \left(E[\phi] - \mu N \int d\boldsymbol{r}\, |\phi(\boldsymbol{r})|^2 \right) = 0$. This leads to

$$\left(-\frac{\hbar^2}{2m} \nabla^2 + U(\boldsymbol{r}) + g|\psi(\boldsymbol{r})|^2 \right) \psi(\boldsymbol{r}) = \mu \psi(\boldsymbol{r}), \tag{6}$$

where we introduced $\psi(\boldsymbol{r}) = \sqrt{N}\phi(\boldsymbol{r})$, with $\int d\boldsymbol{r}\, |\psi(\boldsymbol{r})|^2 = N$ this time. $|\psi(\boldsymbol{r})|^2$ can then be interpreted as the density at point $\boldsymbol{r}$: $|\psi(\boldsymbol{r})|^2 = n(\boldsymbol{r})$. The Lagrange multiplier μ corresponds here to the chemical potential, such that $\mu = \partial_N E$. This equation is the time-independent Gross-Pitaevskii equation [19, 33, 34], which describes the ground state of a quantum system composed of identical interacting bosons.

On the other hand, obtaining the time-dependent Gross-Pitaevskii equation is harder, and involves using the action principle (see Ref. [31] for the full derivation). We simply consider here that it is possible to substitute $i\hbar\partial_t$ by μ by analogy with the Schrödinger equation. We thus obtain

$$i\hbar \partial_t \psi(\boldsymbol{r}, t) = \left(-\frac{\hbar^2}{2m} \nabla^2 + U(\boldsymbol{r}, t) + g|\psi(\boldsymbol{r}, t)|^2 \right) \psi(\boldsymbol{r}, t). \tag{7}$$

The terms on the right-hand side of Eq. (7) are respectively the kinetic energy with the Laplacian, $U(\boldsymbol{r}, t)$ represents an external trap or an obstacle within the fluid, and $g|\psi(\boldsymbol{r}, t)|^2$ is the nonlinear interactions between the atoms. This equation is nonlinear as stated by the $g|\psi(\boldsymbol{r}, t)|^2 \psi(\boldsymbol{r}, t)$ term, and, as a result, does not agree with the superposition principle as a linear combination of two solutions of Eq. (7) is not a solution.

Equation (7) holds a significant importance as it provides a rigorous theoretical framework for studying bosonic systems with weak interactions. More precisely, it is a nonlinear Schrödinger equation that describes the time evolution of a wavefunction associated with a gas of interacting bosons. It accounts for interactions between particles in the gas and is often used to study phenomena such as Bose-Einstein condensation, collective excitations, and solitons. This approach allows for a precise description of superfluidity and, thus, will be the most important equation in this manuscript.

Bogoliubov and the model in weak interactions

Deriving exact analytical solutions to the Gross-Pitaevskii equation (7) remains challenging because of its nonlinearity. However, it is possible to investigate certain limiting behaviors to gain insights into the fundamental properties of weakly interacting quantum fluids, particularly by examining how the fluid responds to small perturbations.

[2]This potential can for example be an external trap in which the system is confined, or an impurity within the fluid. We consider the latter in this manuscript.

In 1947, Bogoliubov showed that BEC can occur in the case of a Bose gas in weak interactions [35], laying the groundwork for the future observation of BEC in alkaline gases in 1995 [8, 9]. His initial goal was to study the elementary excitations in weakly interacting Bose systems, and understand the nature of these excitations and how they influence the properties of BECs and superfluidity. We provide here a classical version of his canonical transformations (the Bogoliubov transformations [35]), leading to a peculiar energy spectrum.

In this approach, we consider a Bose gas in the presence of a localized obstacle that induces a small perturbation. We define the chemical potential μ_∞ from its value far away from the obstacle: It is the characteristic energy of the system. The weakly perturbed solution is such that

$$\psi(\boldsymbol{r},t) = [\psi(\boldsymbol{r}) + \delta\phi(\boldsymbol{r},t)]\, e^{-i\mu_\infty t/\hbar}, \tag{8}$$

with $U(\boldsymbol{r},t) = U(\boldsymbol{r})$. After linearizing Eq. (7) around the stationary solution, one obtains the following coupled system

$$i\hbar\partial_t \begin{pmatrix} \delta\phi \\ \delta\phi^* \end{pmatrix} = \mathcal{L} \begin{pmatrix} \delta\phi \\ \delta\phi^* \end{pmatrix} \tag{9}$$

with operator $\mathcal{L}$ defined as

$$\mathcal{L} = \begin{pmatrix} -\frac{\hbar^2}{2m}\nabla^2 + U + 2g|\psi|^2 - \mu_\infty & g\psi^2 \\ -g{\psi^*}^2 & \frac{\hbar^2}{2m}\nabla^2 - U - 2g|\psi|^2 + \mu_\infty \end{pmatrix}. \tag{10}$$

By diagonalizing the operator $\mathcal{L}$, one can access the spectrum of the elementary excitations with its eigenvalues ω, and the modes with the eigenvectors (u, v) of the system

$$\mathcal{L} \begin{pmatrix} u(\boldsymbol{r}) \\ v(\boldsymbol{r}) \end{pmatrix} = \hbar\omega \begin{pmatrix} u(\boldsymbol{r}) \\ v(\boldsymbol{r}) \end{pmatrix}. \tag{11}$$

This system yields the Bogoliubov-de Gennes equations. Once they are solved, one obtains the wavefunction of the weakly perturbed system as a linear combination of the eigenmodes

$$\psi(\boldsymbol{r},t) = \left[\psi(\boldsymbol{r}) + u(\boldsymbol{r})e^{-i\omega t} + v^*(\boldsymbol{r})e^{i\omega t}\right] e^{-i\mu_\infty t/\hbar}. \tag{12}$$

$u(\boldsymbol{r})$ and $v(\boldsymbol{r})$ are crucial quantities as they characterize quasiparticle modes created by the perturbation of the quantum fluid. In the end, the wavefunction is a linear combination of $u(\boldsymbol{r})$ and $v(\boldsymbol{r})$, describing the elementary excitations of the weakly interacting Bose gas. Because of the interactions, not all particles remain condensed and some are excited out of the condensate, reducing the density of the system: This is the quantum depletion [35, 36].

A simple case: The homogeneous gas The easiest treatable case is that of the Bose gas when $U(\boldsymbol{r}) = 0$. In the homogeneous case, the density is spatially uniform throughout the system, such that $n_0 = |\psi|^2$. The spectrum of the elementary excitations of the system is given by the Bogoliubov dispersion relation $E(k) = E_B(k)$, obtained after diagonalizing the operator $\mathcal{L}$:

$$E_B(k) = \sqrt{\frac{\hbar^2k^2}{2m}\left[\frac{\hbar^2k^2}{2m} + 2gn_0\right]}. \tag{13}$$

In the right-hand side of Eq. (13), the first term $\hbar^2k^2/2m$ corresponds to the kinetic energy of a free particle, and the shift $2gn_0$ is due to the interactions between particles, with $gn_0 = \mu_0$ being the chemical potential of the weakly interacting gas.

Two really different limits arise depending on the value of k, and then on the wavelength of the excitation $\lambda \sim 1/k$. This allows us to introduce a characteristic length-scale of the problem, the healing length ξ_0 of the homogeneous and stationary quantum fluid. It is mathematically defined as being the separation between the two different limits reachable

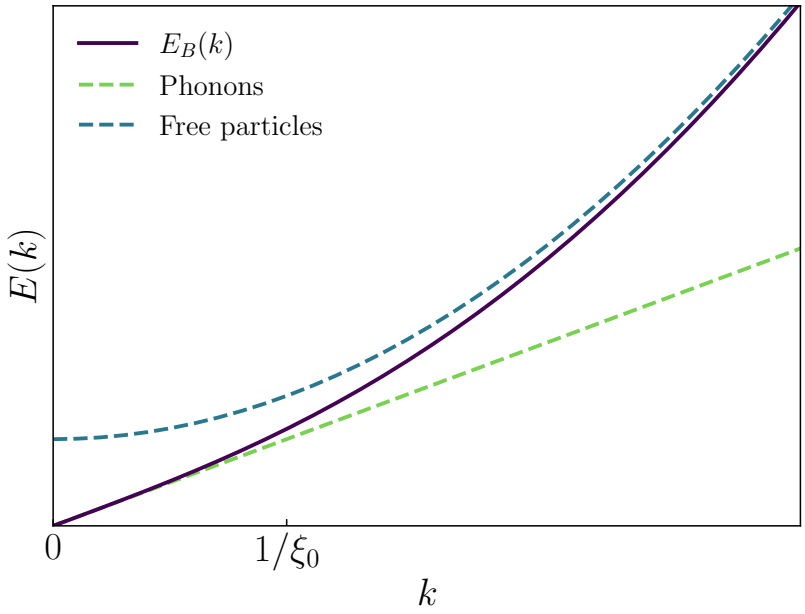

Figure 5: Bogoliubov excitation spectrum for a weakly interacting Bose gas at zero temperature. The dashed lines represent the asymptotic limits of low energy (green) and high energy (blue), leading respectively to a phononic or a free particles behavior. The transition between these two different regimes takes place for excitation wavelengths close to the healing length ξ_0.

in $E_B(k)$, and is obtained through $\hbar^2k^2/2m = 2gn_0$, which is equivalent to $k = 2/\xi_\infty$, with $\xi_0 = \hbar/\sqrt{mgn_0}$. The two different limits in the Bogoliubov dispersion can be seen in Fig. 5, and are as follow

- $k \ll 1/\xi_0$ (long-wavelength perturbation): $E(k) = \hbar k\sqrt{gn_0/m}$. The dispersion relation is linear in $p = \hbar k$. This is characteristic of phonons of velocity $c_0 = \sqrt{gn_0/m}$, c_0 being the speed of sound. It is interesting to note that the speed of sound is linked to the chemical potential through $\mu_0 = mc_0^2$.
- $k \gg 1/\xi_0$ (small-wavelength perturbation): $E(k) = \hbar^2k^2/2m + gn_0$. This is the dispersion relation of free particles, with the kinetic energy $\hbar^2k^2/2m = p^2/2m$ being shifted by the term $gn_0 = \mu_0$ stemming from the interactions between particles.

The healing length ξ_0 then corresponds to the separation between phononic and free particle behavior. This dispersion relation is an important result of the theory of superfluidity, and has been experimentally validated in many experiments with atomic BECs [37–40], quantum fluids of light with exciton-polaritons [41], in hot atomic vapors [42, 43] or nonlocal nonlinear liquids [44].

Concerning the amplitude of the quasiparticle modes $u(\boldsymbol{r})$ and $v(\boldsymbol{r})$, we search for them as plane waves $u_k e^{i\boldsymbol{k}\cdot\boldsymbol{r}}$ and $v_k e^{i\boldsymbol{k}\cdot\boldsymbol{r}}$, with the normalization condition $u_k^2 - v_k^2 = 1$, leading to

$$u_k^2 = \frac{1}{2}\left(\frac{\frac{\hbar^2k^2}{2m} + gn_0}{E_B(k)} + 1\right) \approx \frac{1}{2}\left(\frac{E_B(k)}{\frac{\hbar^2k^2}{2m}} + 1\right), \tag{14a}$$

$$v_k^2 = \frac{1}{2}\left(\frac{\frac{\hbar^2k^2}{2m} + gn_0}{E_B(k)} - 1\right) \approx \frac{1}{2}\left(\frac{E_B(k)}{\frac{\hbar^2k^2}{2m}} - 1\right). \tag{14b}$$

In the low energy limit, one finds $u_k^2 \approx v_k^2 \approx \frac{\sqrt{mgn_0}}{\hbar k}$. The excitation is a superposition of plane waves with wavevectors $\boldsymbol{k}$ and $-\boldsymbol{k}$ with the same coefficients. The dispersion relation is linear: It is a sound wave. On the other hand, in the high energy limit, $u_k^2 \approx 1$ and $v_k^2 \approx 0$: The quasiparticle is a free particle, and with a quadratic dispersion.

The critical velocity for superfluidity

Driven by the need to explain the unusual behaviors previously witnessed in liquid helium, Landau formulated a criterion to see whether a system is superfluid or not, based on the fact that energy dissipation is only possible through the emission of elementary excitations for a superfluid (in other words either phonons or rotons for liquid helium). The conceptual model relies on energetic considerations and examines the stability of the superfluid flow, aiming to predict the critical velocity at which the transition to superfluidity occurs.

Originally proposed by Landau in 1941, this criterion defines the mere existence of a critical velocity for superfluidity, which is a fundamental aspect of the theory of superfluidity. Below this speed, the fluid experiences no resistance in the presence of small external perturbations (e.g. the rugosity of the capillary walls in the original experiments [13, 14], or an impurity in the fluid). More precisely, in the superfluid regime, the fluid does not lose any kinetic energy by emitting long-wavelength excitations as long as its velocity relative to the impurity is less than a certain critical velocity. This characteristic of quantum fluids results from a collective response of the system that is absent in the case of a non-interacting gas. The critical velocity is related to the spectrum of elementary excitations of the system through Landau's criterion [30]

$$v_c = \min_p \left[\frac{E(p)}{p} \right], \tag{15}$$

and is calculated over all possible values of momentum, with $E(p)$ the dispersion relation of the elementary excitations in a generic fluid at rest. If $v_\infty < v_c$, there will be no spontaneous formation of elementary excitation, indicating that the considered system is superfluid. Following this criterion, the critical velocity for superfluidity is given by the roton minimum observed in Fig. 4 for liquid helium.

When looking at the Bogoliubov excitation spectrum in Fig. 5, one can see that the Landau criterion is applicable to the weakly interacting Bose gas at zero temperature[3]. Note that the presence of an obstacle $U(\boldsymbol{r}) \neq 0$ will induce small variations in the density, which is not constant anymore. We consider here n_∞ the unperturbed density at infinity, allowing us to define the chemical potential μ_∞. In that case, the derivation of the Bogoliubov dispersion relation is more complex because the density varies spatially. However, when the typical energy of the potential $U(\boldsymbol{r})$ is much smaller than that of the interactions $\mu_\infty = gn_\infty$, the two limits of $E_B(k)$ obtained for $k \ll 1/\xi_\infty$ and $k \gg 1/\xi_\infty$ are still valid, leading to either a phononic or a free particle behavior. The system possesses a nonzero critical velocity for superfluidity given by the sound velocity $c_\infty = \sqrt{gn_\infty/m}$, and dissipation results from the emission of phonons (a density wave through the fluid) beyond $v_c = c_\infty$. Below it, no elementary excitations are emitted in the fluid. However, the critical velocity decreases as the interactions between particles decrease, and will disappear in the limit of an ideal gas of free particles, in which case $E(p) = p^2/2m$, leading to $v_c = 0$. Interactions between particles is then a requirement to observe superfluidity.

To sum up, the behavior of a weakly interacting Bose gas varies depending on its velocity, describing two distinct regimes: The subsonic regime, devoid of any disturbances, in which the fluid exhibits a superfluid behavior; And the supersonic regime, in which superfluidity is destroyed due to the emission of excitations. The velocity at which this transition occurs is given by the Landau criterion, and is the sound velocity in the system.

Yet, in the majority of experiments involving obstacles bigger than small impurities, the critical velocity for superfluidity appears to be lower than the one predicted by Landau, and, ever since the vast improvements brought to the theory of superfluidity in the mid-twentieth century, the question of why this is the case remained. Landau's approach for liquid helium is

[3]Even if the Landau criterion was originally developed for liquid helium without an obstacle, it also treats the elementary excitations of the system.

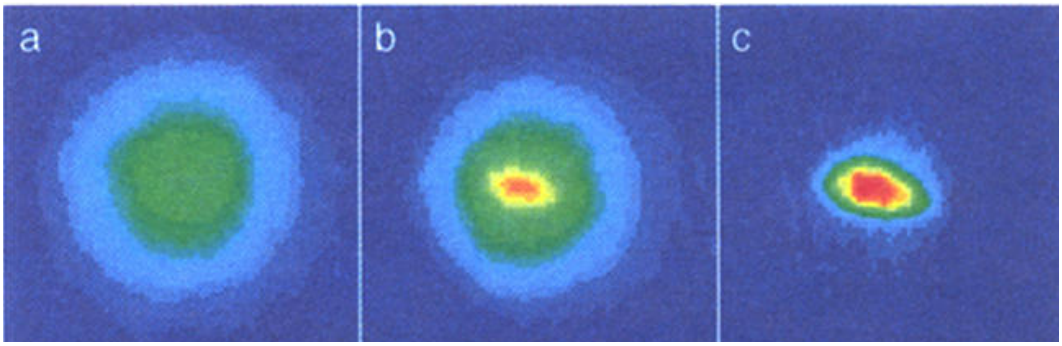

Figure 6: False color image of the velocity distribution of a cloud of sodium atoms in a trap. In (a) the cloud is cooled to temperatures just above the transition. (b) is obtained just after the condensate appeared, and (c) is the condensate after the evaporative cooling. In this experiment, the temperature of the cloud after condensation is ~ 2 μK, and the number of atoms is around 5×10^5, for densities exceeding 10^{14} cm^{-3}. Figure from [9].

indeed only applicable to weakly interacting quantum fluids if the impurities are weak enough so that the fluid is only minimally disturbed by their presence, as stronger impurities can create excitations even at $v_\infty < v_c$. The critical velocity for superfluidity is then necessarily lower than the speed of sound. Still, its precise determination is nontrivial and continues to challenge theoreticians, mostly because of the interactions between particles.

Most of the time, the Gross-Pitaevskii equation does not admit a simple analytical solution in the presence of an external potential, and numerical investigations are needed to determine the critical velocity. Yet, in some very special cases, it is possible to analytically treat the problem, and obtain exact expressions for the critical velocity for superfluidity going beyond the previous results given by Landau. This is the case for example in one-dimensional systems when the obstacles within the fluid are simple: Narrow [45–47] or wide [45, 48, 49] compared to the healing length, and even random potentials [48, 50, 51]. In one dimension, the breakdown of superfluidity typically manifests through the repeated emission of solitons from the obstacle [19, 45, 47, 52], which are the one-dimensional counterpart of the vortices predicted by Feynman [53] in higher dimensions. This notably explains the presence of a nonzero drag force [47, 54–57], characteristic of a nonsuperfluid flow regime.

Because of the complexity of the equations in dimensions higher than one, the vast majority of the studies have been carried out numerically, and most of the analytical results in two dimensions were obtained for wide obstacles of simplified geometries [49, 58–61]. This breakdown of superfluidity results in the repeated emission of vortices from the obstacle [62–64].

The long-awaited observation of BEC

The theoretical framework for BEC was established, and the next logical step was to obtain an experimental proof of its existence, as theorized long ago in the 1920s [65]. While studying superfluidity in liquid helium was straightforward experimentally but challenging to model due to the strong interactions, weakly interacting Bose gases offered ideal platforms for theoretical studies of superfluidity, but had still not been observed because of the complexity of the experimental setups. They were a *grail* for researchers as their quasi-100% condensed fraction constituted a much better deal than the $\sim 10\%$ liquid helium previously provided.

By the mid-1990s, the stage was set for the observation of Bose-Einstein condensates thank to the development of new experimental techniques. The significant progress in laser cooling, coupled with the innovation of magnetic traps for confining and manipulating ultracold atoms, played a pivotal role in the creation of magneto-optical traps (MOTs) [66]. This was then further improved with evaporative cooling methods [67], which allowed to cool the

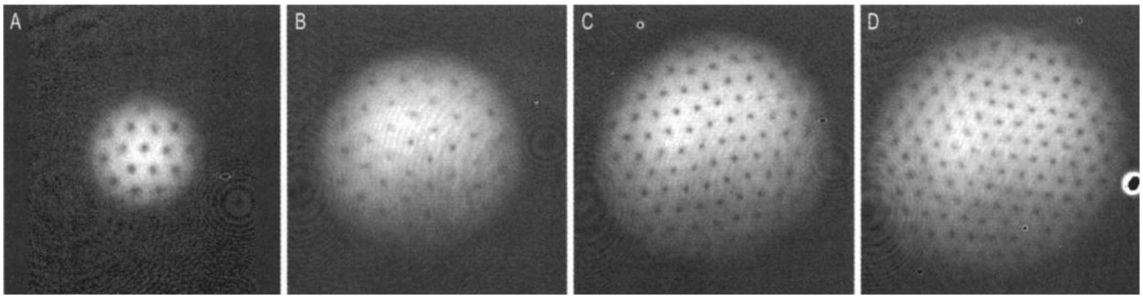

Figure 7: Observation of an Abrikosov vortex lattice in an atomic BEC after different stirring times with a laser beam. The lattices are respectively composed of 16 (A), 32 (B), 80 (C) and 130 (D) vortices. Figure from Ref. [72]

atoms down to temperatures close to absolute zero, making the quantum mechanical nature of the particles appear. Eventually, the groups of Cornell and Wieman at Boulder, and Ketterle at MIT managed to reach the required temperatures (below 170 nK) and densities for monoatomic alkali gases to undergo a phase transition and enter the BEC state [8, 9] (see Fig. 6). Their groundbreaking discovery earned them the 2001 Nobel Prize *"for the achievement of Bose–Einstein condensation in dilute gases of alkali atoms, and for early fundamental studies of the properties of the condensates"*, paving the way for decades of research on cold atoms.

Following these improvements, the study of superfluidity slowly migrated to cold atoms, for which the Gross-Pitaevskii theory provides a really accurate framework. Many setups with atomic BEC were developed, some focusing on creating quasi-2D or quasi-1D BECs by tightly confining the particle with the aid of a shallow trap in one or two directions, resulting in "pancake" or "cigar"–shaped BECs. The existence of a critical velocity has for instance been experimentally observed in alkaline condensates [68–71]. As a result many theoretical investigations of the critical velocity for superfluidity emerged in the past decades [45–51], leading to the state of the art as we know it today.

An unconventional rotation

Building upon previous works in the 1950s by Penrose and Onsager [15, 16], Ginzburg and Pitaevskii [73], later followed by Feynman [53], introduced the concept of a macroscopic wavefunction $\psi = \sqrt{n}e^{i\phi}$, where n represents the density and ϕ the phase of the system. The superfluid velocity is related to the gradient of the phase as $\boldsymbol{v} = \frac{\hbar}{m}\nabla\phi$, resulting in the superfluid being irrotational, thereby deviating from conventional rotation. The circulation on a closed loop $\mathscr{C}$ is then

$$\Gamma = \oint_{\mathscr{C}} \boldsymbol{v}\cdot\boldsymbol{dl} = \frac{\hbar}{m}\oint_{\mathscr{C}} \nabla\phi = \frac{h}{m}k, \tag{16}$$

with k an integer. Rotation in quantum physics is really a peculiar phenomenon: In the celebrated "rotating bucket" experiment (i.e. an experiment putting a quantum fluid on rotation), no motion of the superfluid is observed for small enough rotation frequency. Beyond a certain rotation velocity, the circulation can only increase in discrete steps of h/m, leading to the appearance of an integer number k of particular topological structures known as vortices [53].

Following the first experimental detection of a quantum of circulation around a fine wire in liquid helium II [74], many experiments similar to the rotating bucket experiment were developed in which the fluid is stirred with a laser beam, leading to the observation of the formation of vortex arrays in BEC for given stirring frequencies [70, 72, 75, 76] (see Fig. 7), and to further studies on vortices properties [77, 78] (for a complete description, refer to Ref.

[79]). Interestingly, the vortices organize into a triangular array to maximize the distance between them, following the same structure as predicted by Abrikosov for superconductors [80–82].

Vortices are then an important feature of superfluids, but they do not only appear when rotating a quantum fluid: More generally, they can be emitted in the wake of an obstacle. The emission of said quantized vortices is crucial as it is one of the mechanisms leading to a critical velocity lower than Landau's prediction: Once the critical velocity is exceeded, pairs of vortices with opposing circulation – the analog of dark solitons in 1D – will emerge downstream of the obstacle [83, 84], causing dissipation and a nonzero drag force [85]. This is notably the criterion used in Chap. 3 to determine whether the system is superfluid or not. The precise determination of the critical velocity for superfluidity is however highly nontrivial in 2D as the periodic shedding of vortices strongly depends on the parameters of the obstacle in the fluid [61, 62, 86].

Beyond the superfluid regime

When the velocity of the fluid is slightly above the critical velocity for superfluidity, a nonstationary regime takes place, in which the energy dissipation is nontrivial. This regime strongly differs from the superfluid regime: No analytical solutions are possible, and it exhibits really different features.

Depending on the dimensionality of the system and its parameters, a whole zoology of nonlinear structures can appear repeatedly within the fluid, such as trains of solitons [87, 88], vortices [55, 62, 70, 89–92], snake instabilities [55, 92–94], vortex tangles [95, 96], shock waves [97–100], etc. In 2D, the dissipation mechanism in the nonstationary regime can for example lead to the irregular vortex shedding, or possibly more intriguing shedding patterns such as the Bénard-von Kármán vortex street [101–103]. The dynamics of such structures is however highly nontrivial and chaotic, and is the object of the study of quantum turbulence [95, 104–107]. Its study has been made easier with the high control one now has on the main characteristics of the experiments (interactions, density, number of atoms, trapping configurations...), but also strongly relies from the theoretical side on numerical simulations.

At some point, the velocity is so high that it exceeds a second important threshold [52, 108, 109] – the supersonic separatrix, referred to as v_s in this manuscript – and the fluid enters yet again another regime of transport. Just like the superfluid regime, it is stationary but corresponds to another family of solutions to the time-independent Gross-Pitaevskii equation [52]. v_s then determines the separation between the nonstationary turbulent regime previously defined, and the stationary supersonic regime we are now interested in.

In this regime of transport, the flow almost behaves like a BEC without interactions because the kinetic energy is so high that we can virtually neglect them. The transmission of the fluid across a barrier is not perfect, and there is a nonzero drag force meaning energy dissipation. Yet, in some very restricted cases, it is possible to have a perfect transmission coefficient even in the nonsuperfluid phase, due to resonant transport [110–113] – this is however not the norm. Contrarily to the superfluid regime in which the fluid was only perturbed around the obstacle, the density profile is now characterized by the emission of long-range nonlinear excitations only in the wake of the obstacle.

To conclude, in the presence of a localized obstacle, several regimes of transport can exist depending on the velocity of the fluid, the amplitude of the obstacle, its width, etc. They exhibit really different characteristics, whether be it for the type of excitations emitted, the density profile, or the energy dissipation. As an example, we provide an overview of the conditions leading to these different regimes in Fig. 8, for a $\delta-$peak obstacle [47]. It is a phase diagram representing the injection velocity vs. the amplitude of the considered obstacle.

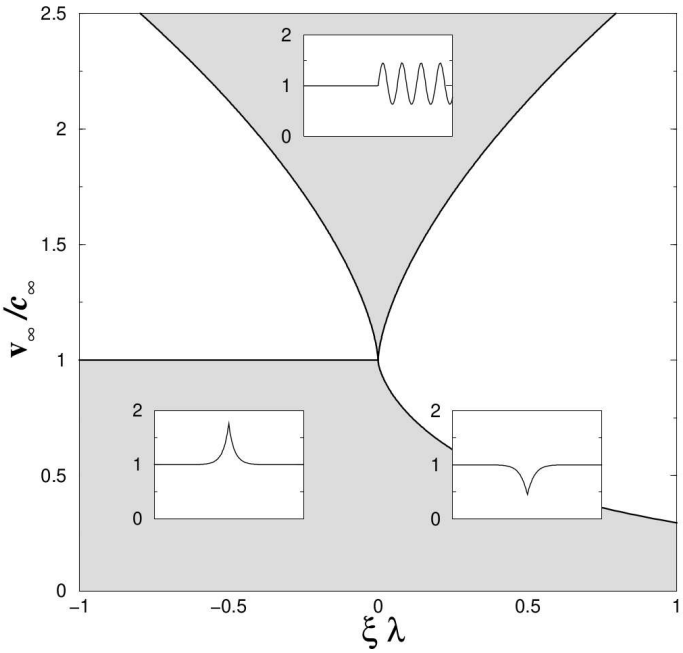

Figure 8: Phase diagram of the possible regimes for a quantum fluid in the presence of a $\delta-$peak obstacle, as a function of the injection velocity v_∞ and the dimensionless parameter $\xi\lambda$, with λ the amplitude of the obstacle. The grey shaded areas correspond to the domain of existence of the stationary solutions: The bottom one is the superfluid regime, the top one is the stationary supersonic regime, and the white in-between zone is the nonstationary regime. The insets represent the typical density profiles obtained for the corresponding flow parameters. Figure from Ref. [47].

The dawn of a new era for quantum fluids

The emergence of new experimental platforms: Quantum fluids of light

While superfluidity was historically observed in liquid helium and later demonstrated in Bose-Einstein condensates, it is important to recognize that this phenomenon is not exclusive to atomic systems: It is only required that the system present a large number of indiscernible particles, and exhibit collective behaviors and a macroscopic coherence. Many examples arise in the domain of condensed matter and do not necessarily require low temperatures. Among them stand superconductors, lasers [114, 115], neutron stars [116, 117], nuclear systems [117], etc.

The exploration of superfluidity thus extends beyond traditional contexts, and in recent decades, significant strides have been made in its understanding in unconventional media. Superfluidity of light – one of the systems of interest in this manuscript, along with BECs – has for instance been a focus of exploration in the past decades, first with exciton-polaritons fluid[4] in a planar semiconductor microcavity [118–120], laying the groundwork for the emergence of the field. What about the interactions, since photons are not supposed to interact with each other? In such systems, photons couple to excitons to form polaritons, and it is the interactions between the excitons that induce effective interactions between the polaritons. As for their mass, photons are indeed mass-less particles, but since light is confined within a microcavity structure, it leads to a parabolic-like dispersion relation, giving an effective mass to exciton-polaritons. The quasi-particles thus adopt a collective behavior and form a quantum fluid of light [121], in which one can for example observe the formation of a polariton Bose-Einstein condensate [118, 122] (and this at higher temperatures than for atomic

[4]Photons are confined and strongly coupled to excitons.

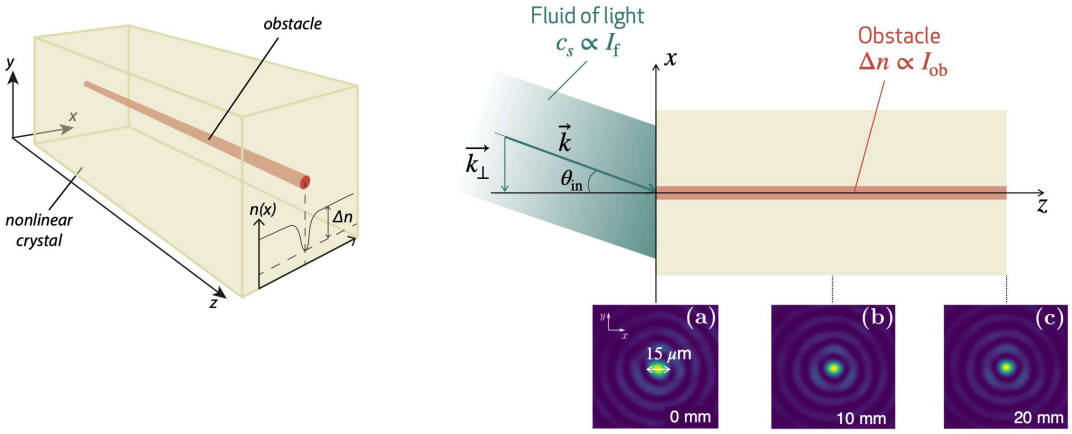

Figure 9: Sketch of the experimental setup. The narrow red beam creates a $z-$invariant localized optical defect which acts as an obstacle in the transverse plane (x, y). The large green beam creates a 2D fluid of light evolving along the $z-$axis. The input angle θ_{in} of the green beam with respect to the red one is linked to the input velocity of the fluid, and can be experimentally tuned via a spatial spatial light modulator. Figures (a), (b) and (c) represent three numerical simulations of the typical evolution of the 2D fluid of light across the nonlinear crystal. The propagation coordinate z plays the role of time. Figure courtesy of Claire Michel.

systems[5]), or many other hydrodynamic features such as solitons [119], vortices [123], the apparition of turbulence, etc.

Even though quantum fluids of light were historically studied with exciton-polaritons, the main drawback of such systems is that losses can be important (cavity losses coming from the mirrors, absorption, decay of the polaritons, etc.), and the system needs to be continuously pumped to compensate for them. This adds a lot of complexity, and one needs a more elaborate model to describe the dynamics of the system.

Subsequent experiments in nonlinear optics have thus been implemented to bypass the need for a cavity (therefore the very short lifetime of the polaritons[6]), reducing losses in the system: Such conservative fluids of light are closer to the dynamics described by the Gross-Pitaevskii equation. For instance, one can observe the superfluidity of light in atomic vapors [42, 43, 124, 125], as well as in setups consisting in nonlinear photorefractive crystals [54, 55, 99, 100, 126, 127], or nonlinear liquid materials [44, 128–130]. These devices notably allow to precisely control the photon interactions strength, as well as the type of nonlinearity.

Focus on a setup: Nonlinear photorefractive crystals

In the present manuscript, the systems we are particularly interested in are quantum fluids of light in propagating geometries [131–133], such as in nonlinear crystals [54, 55], or in hot atomic vapors [42, 124, 134].

We chose to exemplify the results presented in this manuscript for the former, as performed in Nice by Michel and Bellec [54, 55]. The experimental setup is represented in Fig. 9: In the considered system, the fluid is generated using a laser (green beam) propagating in a nonlinear crystal (Strontium-Barium Niobate in the present case). The obstacle encountered by the fluid is a non-permanent optical defect generated via photorefractive effect: Another laser (red beam) is included into the setup to locally modify the optical properties of the material. As it propagates, it induces a redistribution of electrons and holes in the crystal,

[5]The exciton-polaritons are bosonic quasi-particles which are much lighter than alkali atoms, and for which condensation occurs at standard cryogenic temperatures.

[6]The mirrors delimiting the cavity are not perfectly reflecting and do not trap light with a 100% efficiency.

creating a non-uniform charge distribution along its path. This, in turn, locally modifies the refractive index of the medium where it is the strongest. A repulsive obstacle is thus created as the refractive index is decreased along the path of the laser, creating a local potential barrier for photons. This makes it a platform reusable at will because as soon as the laser is turned off, the charge distribution returns to its initial form, and the refractive index becomes constant again in the crystal, "erasing" the obstacle.

By modifying the characteristics of the laser acting as the fluid (namely, the intensity and the input angle of the green beam), it is possible to highlight different intensity regimes and thus to study the superfluid transition. As a result, it is possible to observe superfluidity in such systems, for instance through the observation of dispersive shock waves [98, 99], the optical equivalent of drag force [54], or even the emergence of quantized vortices [55].

After earlier efforts to characterize light as a gas of photons [135], potentially exhibiting a superfluid behavior under specific assumptions [115, 136], subsequent theories emerged to describe light superfluidity with the nonlinear Schrödinger equation (see Ref. [121] for a whole overview).

An analogy with atomic systems

Such systems in their easiest form can be described by a weak interaction theory, just like atomic systems, leading to a hydrodynamic description of light [121, 132]. The propagation in the z direction of a continuous laser beam along a nonlinear photorefractive crystal and across an optical obstacle is ruled by the 2D nonlinear Schrödinger equation for the complex envelope of the optical field $\mathcal{E}(\boldsymbol{r} = (x, y), z)$ [137]

$$i\partial_z \mathcal{E} = \underbrace{-\frac{1}{2kn_e}\nabla^2_{\boldsymbol{r}}\mathcal{E}}_{\text{kinetic}} \underbrace{- k\delta n\left(|\mathcal{E}_{\text{obst}}|^2\right)\mathcal{E}}_{\text{potential}} \underbrace{- k\Delta n\left(|\mathcal{E}|^2\right)\mathcal{E}}_{\text{interactions}} \underbrace{- \frac{i\alpha}{2}\mathcal{E}}_{\text{losses}}. \tag{17}$$

More formally, this equation derives from the Maxwell equations, leading to the Helmholtz equation for the electric field. Several approximations (scalar, paraxial and monochromatic approximations) are then needed to obtain NLS, and can be found in Refs. [137, 138] for the full derivation.

It is notable that there is a direct correspondence between the nonlinear Schrödinger equation describing such optical systems and the Gross-Pitaevskii equation for atomic systems: The same terms are accounted for, albeit from different origins. The main differences are as follow.

- **Evolution term**: The temporal evolution is replaced by a spatial evolution along the propagation axis (denoted z here).
- **Wavefunction**: The equation pertains to the envelope $\mathcal{E}$ of the optical field instead of the usual ψ. Where we once had the density defined as $n = |\psi|^2$, it is now the intensity that is expressed as $\mathcal{I} = |\mathcal{E}|^2$. This wavefunction is a complex number, and can be decomposed into its modulus $\sqrt{\mathcal{I}}$ and a phase. The gradient of the optical phase $\arg(\mathcal{E})$ gives the local velocity $\boldsymbol{v} = \nabla_{\boldsymbol{r}} \arg(\mathcal{E})/n_e k$, with n_e the refractive index of the crystal, i.e. the optical analog of the mass. In the paraxial limit, this simplifies to $v \approx \theta_{\text{in}}/n_e$, with θ_{in} the angle between the green beam and the propagation axis.
- **Kinetic energy**: The relevant dynamics takes place in the (x, y) plane. The propagation constant $k = 2\pi/\lambda$ of the fluid (represented by the green beam in the setup depicted in Fig. 9) plays the role of an effective mass in the transverse plane.
- **Potential energy**: δn is the $z-$invariant refractive index depletion induced by the obstacle (represented by the red beam in Fig. 9). It represents an obstacle whose amplitude and width depend respectively on $\mathcal{I}_{\text{obst}}$ and the diameter of the red beam.

- **Interaction energy**: We work with $\Delta n < 0$, responsible for the defocusing nonlinear response of the crystal, and which induces photon-photon interactions. This equation perfectly mimics a Bose gas in weak repulsive interactions, in the presence of an obstacle. The expression of Δn is unspecified here but can take different forms, and acts as a "signature" for the system. In the photorefractive nonlinear crystals as studied in [54, 55] it is given by a saturable nonlinearity $\frac{g|\mathcal{E}|^2}{|\mathcal{E}|^2+\mathcal{E}_{\rm sat}^2}$, with $\mathcal{I}_{\rm sat}$ the saturation intensity of the material. On the other hand in hot atomic vapors [42, 43, 124, 125], it is given by none other than the Kerr nonlinearity $g|\mathcal{E}|^2$, which is the same as in BECs.

- **Losses**: This term describes possible losses during the propagation inside the crystal, due to the absorption of the material.

It is also possible to define an analog healing length ξ_∞, and an analog speed of sound c_∞, for which the expressions will slightly differ depending on the type of system considered.

In the end, Eq. (17) is just a reformulation of the Gross-Pitaevskii equation: Quantum fluids of light are formally analogous to Bose-Einstein condensates, and really good candidates to explore the physics of quantum fluids, and more generally of low-temperature physics. As a result, the interest in such full-optical systems is steadily growing, both theoretically and experimentally, as they offer a deeper understanding of light propagation in diverse media.

Setups to simulate quantum physics and beyond

All in all, these various experimental platforms offer a thorough insight into the underlying physical mechanisms at low temperature. They can serve as quantum simulators [139–141] as they provide a vast field of possibilities to mimic many-body physics with light [142] or matter [143], for systems whose properties are still generally unknown. This is achievable because experimentalists have now a complete control over many parameters of the system such as the interactions, the temperature, the geometry in which the system is trapped, the number of particles, etc.

They also facilitate the replication of physics beyond the reach of traditional experimentation, such as, for example, analog black holes and the Hawking effect [144–149]. They thus form versatile platforms, really convenient for investigating numerous phenomena.

TOOLBOX

For the reader to have a better grasp on the different concepts, we provide in this section the various tools necessary to follow the different chapters. They notably include the dimensionless equation used to describe both BECs and quantum fluids of light, and the types of nonlinearities one can expect when working with these systems.

Dimensionless equation

In this manuscript, the main equation is the previously defined Gross-Pitaevskii equation (or its analog NLS), which can be used to describe the dynamics of various systems including atomic BECs or quantum fluids of light. The most general expression one can think of is

$$iA\partial_T\psi(\boldsymbol{r},T) = -\frac{B}{2}\nabla^2\psi(\boldsymbol{r},T) + U(\boldsymbol{r})\psi(\boldsymbol{r},T) + \varepsilon\left(|\psi|^2\right)\psi(\boldsymbol{r},T) - \frac{i\alpha}{2}\psi(\boldsymbol{r},T), \tag{18}$$

with $n(\boldsymbol{r},T) = |\psi(\boldsymbol{r},T)|^2$. All the quantities A, B, T, $U(\boldsymbol{r})$, $\varepsilon(n)$ and α permit to characterize the type of system one is working with. Here, the Laplacian is D–dimensional, making Eq. (18) valid in any dimension.

In order to have a more general theory, we want to work with a dimensionless form of this equation so that, in the end, we only need to specify the expression of the nonlinearity to determine what type of system we are working with. A way to do that is to perform the following change of variables

$$t = \frac{\mu_\infty T}{A}, \quad \tilde{\boldsymbol{r}} = \frac{\boldsymbol{r}}{\xi_\infty}, \quad \tilde{\psi}(\tilde{\boldsymbol{r}},\tau) = \frac{\psi(\boldsymbol{r},T)}{\sqrt{n_\infty}}, \quad \tilde{U}(\tilde{\boldsymbol{r}}) = \frac{U(\boldsymbol{r})}{\mu_\infty}, \quad \tilde{\varepsilon}(\tilde{n}) = \frac{\varepsilon(n)}{\mu_\infty} \quad \text{and} \quad \tilde{\alpha} = \frac{\alpha}{\mu_\infty}.$$

To simplify the treatment of the problem, we consider that the system is homogeneous at infinity, far from the perturbation induced by the external potential $U(\boldsymbol{r})$. We can thus define quantities such as the uniform density n_∞, the chemical potential $\mu_\infty = \varepsilon'(n_\infty)n_\infty$ (the typical energy of the system), and the healing length $\xi_\infty = \sqrt{\frac{B}{\mu_\infty}}$, which we use to rescale the problem. Now, the lengths, densities and energies will respectively be expressed in units of ξ_∞, n_∞ and μ_∞.

The dimensionless form that we derive from this change of variables in order to describe all these situations reads[a]

$$i\partial_t\tilde{\psi} = -\frac{1}{2}\nabla^2\tilde{\psi} + \tilde{U}(\tilde{\boldsymbol{r}})\tilde{\psi} + \tilde{\varepsilon}(\tilde{n})\tilde{\psi} - \frac{i\tilde{\alpha}}{2}\tilde{\psi}, \tag{19}$$

with $\tilde{n}(\tilde{\boldsymbol{r}},t) = |\tilde{\psi}(\tilde{\boldsymbol{r}},t)|^2$ being the density (intensity) associated with the dimensionless wavefunction $\tilde{\psi}(\tilde{\boldsymbol{r}},t)$.
We will more often than not work with this dimensionless equation, in which the only parameter determining the type of system we are working with is the nonlinearity $\tilde{\varepsilon}(\tilde{n})$.

[a] For the sake of simplicity, we will drop the tildes in the different chapters.

Reducing the dimensionality of the problem

In this manuscript, a focus is directed towards the physics of low-dimensional interacting quantum systems, which are fascinating in the sense that they are forced to adapt, and adopt

new behaviors that are not the norm in three dimensions. The confinement to reduced dimensions induces a change of dynamics, enhancing effects like interactions and correlations. Superfluidity is no exception, and its properties are well impacted by a change of dimensionality. Notably, quantum gases, whether of matter or of light, appear as particularly suitable platforms for observing this type of physics as a high degree of control is now attained by experimentalists.

If the Gross-Pitaevskii equation was first derived in three dimensions in the 1960s, this theory is quite general and remains applicable in lower dimensions. A 2D version is for example provided in Eq. (17) to describe the dynamics of a paraxial fluid of light in a photorefractive crystal [54, 55]. Changing the dimension in the mathematical description is an easy feat, as it does not have an impact on the structure of the equation. The main change is that the equation will apply to the transverse wavefunction $\psi(\boldsymbol{r} = (x, y), t)$ for 2D systems, and the wavefunction along the propagation axis $\psi(z, t)$ for 1D systems; It will also change the value of the coupling constant g[7]. Experimentally speaking, it is however more complicated to reduce the dimension of the system: If the concepts are basically the same for 1D and 2D systems, different setups are required depending on the desired outcome. This is usually performed by confining the system in harmonic traps of frequencies tailored to freeze the dynamics in one or two dimensions, leading to systems of peculiar geometries, such as "pancake"–shaped [8, 9, 150] or "cigar"–shaped BECs [69], whose dynamics are respectively quasi−2D and quasi−1D.

What type of nonlinearities

An important feature of the model we use with the Gross-Pitaevskii equation (19) is that it is possible to describe the dynamics of very different physical systems depending on the expression of the nonlinear interactions $\varepsilon(|\psi|^2)$ between the particles.

All along this manuscript, we will work with an unspecified expression for $\varepsilon(|\psi|^2)$, allowing us to derive a general theory. Yet, our results will often be exemplified for several types of systems, among which stand BECs and quantum fluids of light in photorefractive crystals. We present here different possibilities for the expression of the nonlinear interaction potential $\varepsilon(|\psi|^2)$, and the systems they are associated with.

Ultracold atomic Bose gases The most general nonlinearity used to describe ultracold atomic Bose gases is the powerlaw nonlinearity, given by the Hartree-Fock potential $\varepsilon(n) = gn^\nu$, and which scales as a positive power of the density $n(\boldsymbol{r}, t) = |\psi(\boldsymbol{r}, t)|^2$. Depending on the dimensionality and the dilution regime of the system, the value of the exponent ν will differ:

- In the one-dimensional regime, when the system is dilute such that $na_s \ll 1$ (with a_s the s-wave scattering length of the two-body interaction potential), one has $\nu = 1$ and $\varepsilon(n) = gn$. This is the original expression of the nonlinear interaction potential, derived from the quartic interaction Hamiltonian in the Gross-Pitaevskii theory.

- Still in 1D but in the other dilution regime $na_s \gg 1$, $\nu = 1/2$ leading to $\varepsilon(n) = gn^{1/2}$ [151, 152]: This is the radial Thomas-Fermi regime, in which the kinetic energy term can be neglected in comparison with the mean-field interaction energy.

- In 2D when the system is dilute enough, i.e. $na_s^2 \ll a_s/l$[8] with l the typical length of the harmonic trap used to reduce the dimension of the system, one has $\nu = 1$ leading to $\varepsilon(n) = gn$.

[7] This is of no importance in our treatment as the dimensionless form of the nonlinearity does not involve the value of g.

[8] But also larger than $(a_s/l)^2 \exp\left[-\sqrt{2\pi} l/a_s\right]$ to prevent the gas from entering the 2D analog of the Tonks-Girardeau regime, in which case $\varepsilon(n) = g|\ln(nl^2)|/n$.

- On the contrary in the high density limit in 2D, i.e. $na_s^2 \gg a_s/l$, one has $\nu = 2/3$, and thus $\varepsilon(n) = gn^{2/3}$ [153].

Quantum fluids of light As a first approximation, quantum fluids of light can generally be described using a saturable nonlinearity $\varepsilon(n) = gn/(n+n_{\text{sat}})$ with n_{sat} the saturation intensity. This is for example characteristic of saturable medium like the nonlinear photorefractive crystals as used in Ref. [54, 55]. Here, the g coefficient is such that $g = \pi N^3 r_{33} E_0/\lambda_0$, with N and r_{33} respectively the mean refractive index and the electro-optic coefficient of the crystal along the extraordinary axis, E_0 the amplitude of an electric field applied along the $c-$axis, and λ_0 the wavelength of the laser representing the fluid in free space.

For a saturated system such that $n \ll n_{\text{sat}}$, this expressions reduces to $\varepsilon(n) = gn$. This limit can be encountered in nonlinear optics, in which case it is referred to as Kerr nonlinearity. This is the case for example in quantum fluids of light with condensed exciton-polaritons [154], or in hot atomic vapors [42, 124], in which it describes the phenomenon where the refractive index of a media locally and instantaneously changes as a response to the electric field as it passes through it. We only study the self-defocusing case in this manuscript (positive $\varepsilon(n)$).

Focus on the 2 systems of interest in this manuscript

In this section, we provide the relevant ways to obtain Eq. (19) when starting from the equations expressed in their natural units. We do so for the 2 main nonlinearities used in this manuscript.

Atomic BECs Even if the results of this manuscript are usually given for the original $\varepsilon(n) = n$, some results may also be provided for the general powerlaw nonlinearity. We thus derive the dimensionless equation for $\varepsilon(n) = gn^\nu$. The original equation reads

$$i\hbar\partial_t\psi = -\frac{\hbar^2}{2m}\nabla^2\psi + U(\boldsymbol{r})\psi + \varepsilon\left(|\psi|^2\right)\psi. \tag{20}$$

Note that we did not consider losses in ultracold atomic gases. We obtain the dimensionless Eq. (19) with the parameters

$$A = \hbar, \quad B = \frac{\hbar^2}{m}, \quad \tau = \frac{\mu_\infty T}{\hbar}, \quad \tilde{\varepsilon}(\tilde{n}) = \frac{\tilde{n}^\nu}{\nu} \quad \text{and} \quad \xi_\infty = \frac{\hbar}{\sqrt{m\mu_\infty}}.$$

The healing length is also given by $\xi_\infty = \hbar/mc_\infty$, leading to $\mu_\infty = mc_\infty^2 = \varepsilon'(n_\infty)n_\infty$, and thus defining the speed of sound for a powerlaw nonlinearity

$$c_\infty = \sqrt{\frac{\nu g n_\infty^\nu}{m}}. \tag{21}$$

Paraxial fluids of light As previously explained, the propagation of a quantum fluid of light in a photorefractive crystal is ruled by NLS, an analog of the Gross-Pitaevskii equation. The expression of the nonlinearity is $\varepsilon(n) = gn/(n+n_{\text{sat}})$, with n_{sat} the saturation intensity. The original equation reads

$$i\partial_z\psi = -\frac{1}{2k}\nabla^2\psi + U(\boldsymbol{r})\psi + \varepsilon\left(|\psi|^2\right)\psi - \frac{i\alpha}{2}\psi, \tag{22}$$

where we have included photonic losses as performed in Ref. [55], as they are not negligible and can play an important role in the dynamics of the system. Through misuse of language,

we also have replaced the electric field $\mathcal{E}$ (and the intensity $\mathcal{I}$) by respectively ψ and n. One recovers the dimensionless form (19) using the same change of variables, with

$$A = 1, \quad B = \frac{1}{k}, \quad \tau = \mu_\infty z, \quad \tilde{\varepsilon}(\tilde{n}) = \left(1 + \frac{1}{\tilde{n}_{\rm sat}}\right)^2 \frac{\tilde{n}}{1 + \tilde{n}/\tilde{n}_{\rm sat}} \quad \text{and} \quad \xi_\infty = \sqrt{\frac{1}{k\mu_\infty}},$$

and with $\tilde{n}_{\rm sat} = n_{\rm sat}/n_\infty$. One can re-express the healing length as $\xi_\infty = 1/kc_\infty$, leading to $\mu_\infty = kc_\infty^2 = \varepsilon'(n_\infty)n_\infty$, and allowing us to define an analog speed of sound

$$c_\infty = \sqrt{\frac{\varepsilon'(n_\infty)n_\infty}{k}} = \sqrt{\frac{g\tilde{n}_{\rm sat}}{k}} \frac{1}{1 + \tilde{n}_{\rm sat}}. \tag{23}$$

Thesis outline

As the reader can attest, this manuscript centers on the breakdown of superfluidity in low-dimensional quantum fluids, with a particular emphasis on the critical velocity for superfluidity. This theme is central to the research presented here, and is the focus of two of the three chapters in this thesis, specifically in the context of one-dimensional and two-dimensional systems. The manuscript is divided as follows:

- **Chapter 1**: We begin by establishing the theoretical framework for one-dimensional systems, revisiting important preliminary results from the linear-response theory, that are essential for the nonperturbative treatment we perform. A detailed report is provided on how to obtain the critical velocity v_c for quantum fluids in the presence of obstacles of various geometries, using both analytical and numerical methods. Additionally, we incorporate losses due to absorption into our model, and treat them analytically, offering a thorough description of the breakdown of superfluidity in the one-dimensional mean-field regime.

- **Chapter 2**: This chapter is dedicated to exploring another velocity of interest – the supersonic separatrix v_s – that demarcates the boundary between the superfluid and the nonstationary regimes. Employing a Hamiltonian approach, we derive results for the supersonic separatrix in systems similar to those studied in the previous chapter. A focus is also shed to quantum fluids in the presence of attractive obstacles, leading to the characterization of possible resonances in v_s.

- **Chapter 3**: We extend the one-dimensional model to two dimensions, starting with an analysis of the limitations of the linear-response theory in 2D. A new method is introduced to derive exact analytical results for v_c in 2D systems. In this context, the fluid is now allowed to pass through the obstacle while another part circumvents it – a phenomenon not observed in one-dimensional systems. This behavior results in different mechanisms for the breakdown of superfluidity, depending on the amplitude of the obstacle.

Chapter 1

Critical velocity for superfluidity in one dimension

Sommaire

The goal of this chapter is to perform a complete study of the critical velocity v_c for superfluid motion of a quantum fluid past a localized obstacle in the one-dimensional Gross-Pitaevskii regime. This study is not restricted to weakly perturbative obstacles, yielding results going beyond the celebrated Landau criterion. In addition, we generalize the Gross-Pitaevskii equation to possibly nonquartic interaction Hamiltonians, allowing us to derive results for general nonlinear interaction schemes, regardless of the nature of the considered quantum fluid. This allows, for example, for a treatment of superfluidity in the so-called paraxial fluids of light in saturable media, a system of interest in this manuscript. We also take one-photon absorption into account as they can play an important role in the dynamics of such optical systems, and treat them with an adiabatic approach. Our generic results provide a very broad picture of the critical velocity for superfluidity in the one-dimensional mean-field regime.

Article linked to the chapter:

J. Huynh, M. Albert and P.-É. Larré, "Critical velocity for superfluidity in the one-dimensional mean-field regime: From matter to light quantum fluids" – Phys. Rev. A **105**, 023305 (2022)

1.1 One-dimensional mean-field regime

1.1.1 1D Gross-Pitaevskii equation

In this section, we delve into the exploration of superfluidity within a one-dimensional quantum fluid of bosonic particles flowing along the $x-$axis, whose dynamics is captured by the 1D reduction of the introduced Gross-Pitaevskii equation provided in the introduction. In this framework, all particles are assumed to be in the same quantum state, characterized by a single one-dimensional wavefunction $\psi(x,t)$, verifying

$$i\partial_t\psi = \left[-\frac{1}{2}\partial_x^2 + U(x) + \varepsilon(n)\right]\psi^{1}, \tag{1.1}$$

where $n(x,t) = |\psi(x,t)|^2$ is the linear density of the system.

- The potential $U(x)$ describes a static localized obstacle within the fluid. We take it in the form $U(x) = U_0 f(|x|/\sigma)$ is, with U_0 its single extremum located at $x = 0$, and σ its typical range, so that the extremum of $f(|x|/\sigma)$ is $f(0) = 1$, and $f \to 0$ as $|x| \gg \sigma$. Depending on the sign of U_0, this obstacle will be either repulsive ($U_0 > 0$) or attractive ($U_0 < 0$).
- The nonlinear term $\varepsilon\left(|\psi|^2\right)$ describes interactions between the particles constituting the quantum fluid. It is often known to be of the form $\varepsilon(n) = n$, but we consider it here as a generic, local and instantaneous function of the density to describe various types of quantum fluids, including the so-called quantum fluids of light. We refer the reader to the TOOLBOX section provided in the introduction for the possible expressions for the nonlinearity.

1.1.2 Validity of the one-dimensional Gross-Pitaevskii equation

The Mermin-Wagner theorem of statistical physics states that no phase transition leading to the formation of a single-particle mean-field state ψ can occur in one dimension at finite temperature. Yet, provided certain conditions are met, the 1D Gross-Pitaevskii equation (1.1) still provides an accurate description of the system. In this subsection, we clarify the validity of Eq. (1.1) for a 1D atomic Bose gas characterized by the usual $\varepsilon(n)$, and in the absence of obstacle $U(x)$, to represent a system without impurities.

Condition on the size of the system We start this discussion with the quantum many-body Hamiltonian in one dimension

$$\hat{H} = \int dx\, \hat{\Phi}^\dagger(x)\left[-\frac{1}{2}\partial_x^2 + \frac{1}{2}\hat{\Phi}^\dagger(x)\hat{\Phi}(x)\right]\hat{\Phi}(x). \tag{1.2}$$

The Gross-Pitaevskii approach to this 1D description consists in neglecting all quantum fluctuations of the Bose field $\hat{\Phi}$, and replace it with the classical field $\psi(x) = \langle\hat{\Phi}(x)\rangle$. To see the validity of this approach, we express $\hat{\Phi}$ as $\hat{\Phi}(x) = \exp\{i\hat{\theta}(x)\}\sqrt{\hat{n}(x)}$, with $\left[\hat{n}(x), \hat{\theta}(x')\right] = i\delta(x-x')$, and calculate the one-body density matrix (OBDM) $\rho(x,x') = \langle\hat{\Phi}^\dagger(x,t)\hat{\Phi}(x',t)\rangle$. Several hypothesis are required to further simplify the OBDM for a homogeneous system, namely

- Being in the weakly interacting regime.
- A low temperature such that $k_\mathrm{B}T < \sqrt{\mu k_\mathrm{B} T_d}$, with $T_d = \hbar^2 n^2/m$ the temperature of quantum degeneracy. Here n is the typical density of the homogeneous system.

[1] This equation will later be refined in Sec. 1.3.4 by adding a term corresponding to particle losses.

- Looking at the long-range behavior such that $|x - x'| \gg 1$.

Provided these conditions are met, the OBDM can be expressed as [18]

$$\rho(x, x') \approx \sqrt{n(x)n(x')} \exp\left\{-\mathscr{F}_T(x - x') - \mathscr{F}_Q(x - x')\right\}, \tag{1.3}$$

where

$$\mathscr{F}_T(x) = \frac{k_\mathrm{B}T}{\sqrt{\mu k_\mathrm{B}T_d}} \frac{|x|}{\xi}, \tag{1.4a}$$

$$\mathscr{F}_Q(x) = \frac{1}{\pi}\sqrt{\frac{\mu}{k_\mathrm{B}T_d}} \ln\left\{\frac{|x|}{\xi}\right\}. \tag{1.4b}$$

The fluctuations can then be separated into two components

- $\mathscr{F}_T$, which originates from the thermal fluctuations, and are responsible for the exponential decay of the one-body density matrix. They are however negligible in the low-temperature regime when $k_\mathrm{B}T \ll \sqrt{\mu k_\mathrm{B}T_d}$.
- The remaining term $\mathscr{F}_Q$, which originates from the phase fluctuations of $\hat{\Phi}$ at $T = 0$, leads to an algebraic decrease of the OBDM. Yet, this behavior is negligible for systems of size L such that

$$\frac{1}{\pi}\sqrt{\frac{\mu}{k_\mathrm{B}T_d}} \ln\left\{\frac{L}{\xi}\right\} \ll 1, \tag{1.5}$$

  i.e.

$$L \ll l_\phi = \xi \exp\left\{\pi\sqrt{\frac{k_\mathrm{B}T_d}{\mu}}\right\}. \tag{1.6}$$

One can observe long-range coherence in such conditions for the temperature and the size of the system: This is the criterion formulated by Penrose and Onsager [15]. The description of $\hat{\Phi}$ as a classical field ψ is then possible because the fluctuations disappear, and the use of the one-dimensional reduction of the Gross-Pitaevskii equation is justified.

What about the interactions in 1D**?** In general, the temperature of a quantum fluid is not necessarily low, nor are the interactions weak. Many other regimes can exist depending on the value of the temperature and the interactions. Figure 1.1 provides a brief overview of these regimes as a function of the temperature T and the number of atoms N (linked to the interactions) for a quantum fluid in a harmonic trap of transverse frequency ω.

The regime of interest for us is one of a dilute Bose gas of typical density n, but also of weak interactions. The interaction parameter γ is obtained by comparing the interaction energy $E_i = n$ (as we consider Bose gases) vs. the kinetic energy E_k. In one dimension, the usual density of the system is proportional to the inverse of its size, such that $L = 1/n$, leading to

$$E_k \sim \frac{\hbar^2}{mL^2} \propto n^2 \to \gamma = \frac{E_i}{E_k} \sim \frac{1}{n}.$$

When corroborating it with Fig. 1.1, this indeed means that the regime of interest for us is the one represented in the top-left corner of Fig. 1.1. In the end, the validity of our model relies on a gas dilute enough to reduce the collisions between atoms (and then the kinetic energy) and to be ultracold, but also not too dilute to remain in the weakly interacting regime.

1.1.3 A few basic solutions with obstacle

We conclude this discussion on the validity of the mean-field approach for 1D Bose gases, and from now on, we will stay within the framework of an unspecified nonlinear interaction potential $\varepsilon(n)$. It is first instructive to look at a few elementary solutions of Eq. (1.1) in the presence of a defect $U(x)$.

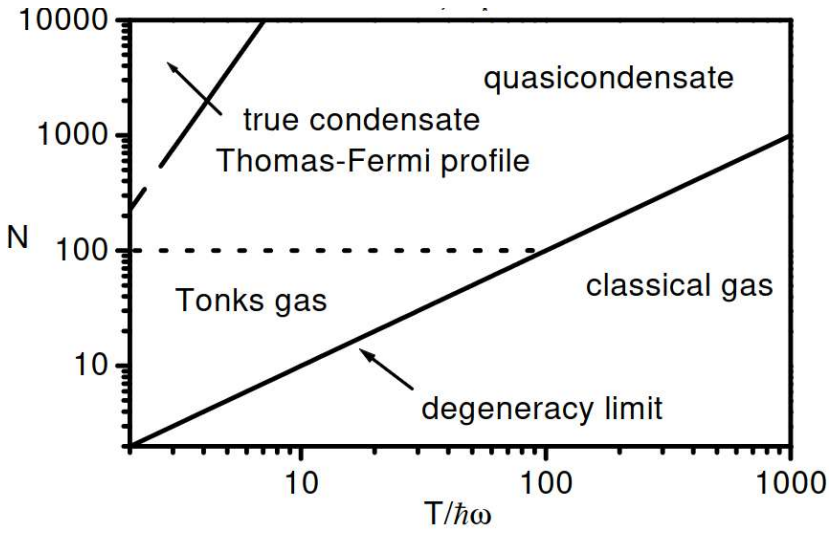

Figure 1.1: Phase diagram for a one-dimensional Bose gas in a harmonic trap of transverse frequency ω. It is represented as a function of the temperature and the number of atoms. The regime of interest in this manuscript corresponds to the top-left corner, in which a true condensate is possible. Figure from Ref. [18].

Quantum fluid trapped in a box

It is possible to exactly solve Eq. (1.1) for a BEC trapped in a box, such that $U(x) = 0$ for $x \in [0, L]$, and is infinite otherwise. In the absence of interactions, all the particles occupy the ground state of the trap, which is a sine wave. However, once the interactions come into play, this scenario cannot persist: The density tends to become uniform under the effect of collisions between particles. Gradually, the density flattens, approaching near homogeneity far from the trap walls, but always drops abruptly to zero at the edges of the box, over a characteristic length ξ_∞. This provides a physical interpretation for the healing length: It is the length necessary for the fluid to have a fully-recovered density after being perturbed.

It is pretty straightforward to obtain the exact analytical expression for the wavefunction for the first half of the box $\psi(x) = \sqrt{n_\infty}\tanh(x/\xi_\infty)$, with $\xi_\infty = \sqrt{1/\mu_\infty}$ (the second half of the solution being the mirror to this first solution). This solution is illustrated in Fig. 1.2.

Thomas-Fermi approximation

Things are a bit more complicated when there is no restriction on the obstacle $U(x)$, but it remains possible to obtain approximate solutions to Eq. (1.1). Usually, the number of particles in the experiment is very large, and the chemical potential μ_∞, representing the interaction energy between the particles, is much more important than the kinetic energy. In that case, it is possible to obtain an analytical solution of Eq. (1.1) for the density by neglecting the kinetic term. It is indeed legitimate to make such an assumption because as the repulsive interactions become more important, the condensate will expand and become spatially uniform (except close to the boundaries of the system), thus minimizing its kinetic energy. One is then left with the implicit relation defining the density

$$n(x) = \varepsilon^{-1}\left(\mu_\infty - U(x)\right), \tag{1.7}$$

for an arbitrary nonlinear interaction potential $\varepsilon(n)$. The "usual" density profile one has when working with this standard nonlinearity is $n(x) = \mu_\infty - U(x)$, with μ_∞ the chemical potential stemming from the time-dependent part of the wavefunction $\exp\{-i\mu_\infty t/\hbar\}$. This is the Thomas-Fermi approximation [19], which provides a simple and intuitive way to understand the density distribution of quantum fluids in trapping potentials without requiring a

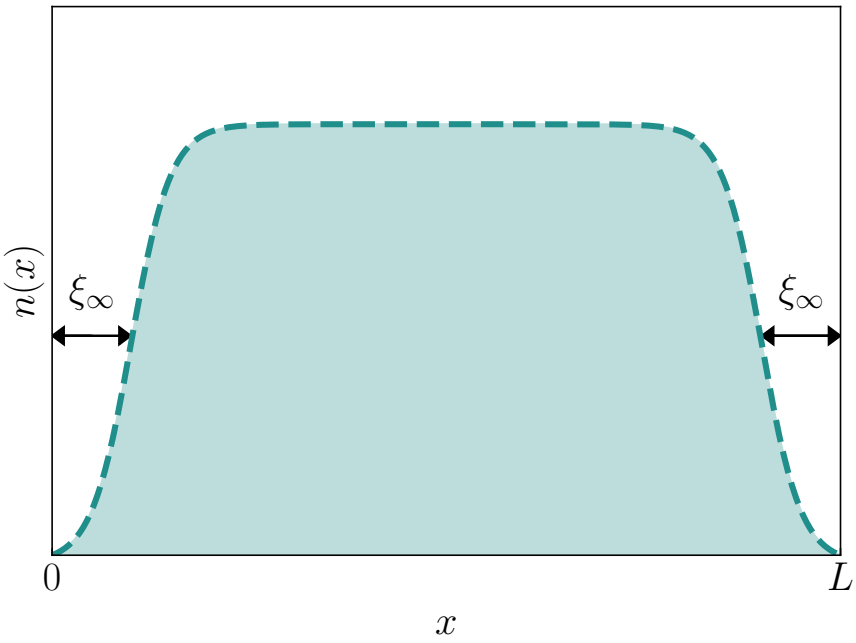

Figure 1.2: Density profile $n(x) = |\psi(x)|^2$ of a BEC trapped in a box of size L. The density is uniform everywhere except close to the boundaries of the system, where it abruptly drops to zero, over a characteristic distance corresponding to the healing length ξ_∞.

detailed knowledge of the wavefunction. Note that even though we bring up the topic of the Thomas-Fermi approximation in this chapter on the one-dimensional case, it remains valid in dimensions higher than one.

Even if the Thomas-Fermi approximation neglects the kinetic part of Eq. (1.1), it still provides an accurate analytical prediction for the density, which must vanish at the so-called Thomas-Fermi radius R, solution of $U(R) = \mu_\infty$. It is however important to note that this approximation is not valid anymore in the vicinity of R, in which case a full resolution of Eq. (1.1) is necessary, allowing for the removal of the discontinuity of the derivative of the density at this point. This can be seen for example in Fig. 1.3, in which the Thomas-Fermi approximation shows an abrupt cancellation of the density for $x = R$.

1.1.4 Hydrodynamic description

Let us go back to the Gross-Pitaevskii equation (in the absence of losses), without any assumptions on its contributions. We look for the evolution of the density and the phase of the quantum fluid, and re-express Eq. (1.1) into equations on the velocity and density fields, which can be done with the Madelung transform, using a phase-density representation for the wavefunction $\psi(x,t) = \sqrt{n(x,t)}e^{i\theta(x,t)}$. The velocity field $v(x,t)$ is linked to the phase $\theta(x,t)$ through its derivative: $v(x,t) = \partial_x\theta(x,t)$.

This makes it possible to cast the 1D Gross-Pitaevskii equation into two coupled hydrodynamics equations for the velocity and density fields

$$\partial_t v = -\partial_x \left(\frac{v^2}{2} + U(x) + \varepsilon(n) - \frac{1}{2}\frac{\partial_x^2\sqrt{n}}{\sqrt{n}} \right) \tag{1.8a}$$

$$\partial_t n + \partial_x (nv) = 0. \tag{1.8b}$$

These equations are analogous to those found in classical hydrodynamics, allowing us to draw parallels and interpret the dynamics of our quantum fluid through the lens of hydrodynamics.

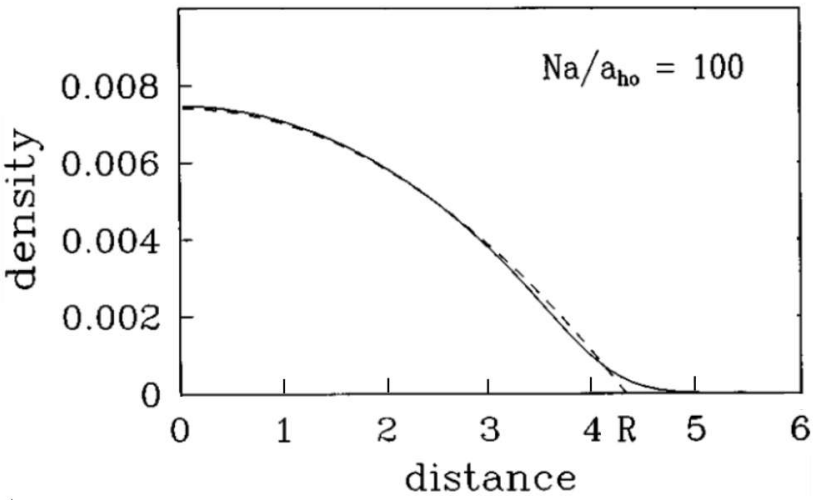

Figure 1.3: Density profile of atoms interacting with repulsive forces in a spherical trap, as a function of the distance from the center of the trap in units of a_{ho} (the typical size of the spherical trap). Solid line: Solution of the stationary Gross-Pitaevskii equation. Dashed line: Thomas-Fermi approximation. Figure from Ref. [155].

Equation (1.8a) is similar to the Euler equation for a classical inviscid fluid, with the exception that it contains an additional term proportional to $\partial_x^2\sqrt{n}/\sqrt{n}$. In ultracold gases, this term is called the "quantum pressure" and is of quantum origin, whereas it stems from paraxial diffraction in the context of quantum fluids of light. Equation (1.8b) is the continuity equation for the number of particles, as there are no losses yet: The number of particles in the system is conserved.

How to obtain v_c from there? Many criteria to determinate whether a system is superfluid or not are possible (presence of a long-range order, of vortices, existence of a drag force, etc.). In the present manuscript, we study the response of a quantum fluid to an obstacle via the hydrodynamic equations (1.8b). Our criteria for a superfluid flow are

- A stationary solutions for the velocity and density fields $v(x,t) = v(x)$ and $n(x,t) = n(x)$.
- Unperturbed profiles far away from the obstacle, such that $v(|x| \gg \sigma) = v_\infty$ and $n(|x| \gg \sigma) = n_\infty$.

We search for the conditions of existence of the solutions of Eqs. (1.8) meeting these criteria. The existence of said solutions is conditioned by the value of the injection velocity v_∞: The last value of v_∞ for which such solutions for a superfluid flow exist is the critical velocity for superfluidity v_c.

1.2 The perturbative approach

Before going into a detailed calculation of the critical velocity for superfluidity v_c for generic parameters of obstacles, it is instructive to investigate the dynamics of the system when it is weakly excited. This is necessary to lay the foundations of this manuscript, and will provide a first value for v_c in the perturbative regime.

The most straightforward approach to obtain the low energy excitations involves solving the hydrodynamic equations (1.8) employing a perturbative method. In the absence of obstacle $U(x)$, it is easy to obtain a stationary and uniform solution (n_∞, v_∞). Let us assume now

that a really small obstacle is present in the fluid, with typical amplitude U_0 much smaller than the chemical potential μ_∞, so that it only slightly modifies the homogeneous stationary solution $(n_\infty + \delta n(x,t), v_\infty + \delta v(x,t))$ via elementary excitations. By linearizing Eqs. (1.8) around the equilibrium state (n_∞, v_∞), an approximate solution for this small perturbation can be derived.

In this manuscript, we often derive results for Gaussian obstacles. We do so for several reasons: In most quantum fluid experiments (both of matter or light), the laser beams used to generate the obstacle often have a Gaussian transverse profile. Such an obstacle also has the advantage of being easily numerically represented as it presents no discontinuity, and yields simple analytical developments in the limits of wide and narrow σ (in the latter, we recover a $\delta-$peak obstacle).

1.2.1 From superfluid subsonic motion to supersonic wave resistance

We consider an obstacle in the fluid of the form $U(x,t) = U(x)e^{\eta t}$, with $\eta \ll 1$. The obstacle is then really slowly switched on (on a time scale much bigger than any other characteristic time in the system), so that the fluid can gradually adapt to the changes induced, without generating anything else than elementary excitations. In this adiabatic approach, the fluid is almost at equilibrium at each time, and one can use the linear-response theory. This allows us to derive the differential equations for the phase and density variations

$$\partial_t \begin{pmatrix} \delta n \\ \delta\theta \end{pmatrix} = \begin{pmatrix} -k_\infty \partial_x & -n_\infty \partial_x^2 \\ -\varepsilon'(n_\infty) + \frac{1}{4n_\infty}\partial_x^2 & -k_\infty \partial_x \end{pmatrix} \begin{pmatrix} \delta n \\ \delta\theta \end{pmatrix} + \begin{pmatrix} 0 \\ -U(x) \end{pmatrix}, \tag{1.9}$$

with $\theta(x,t) = -\eta t + k_\infty x + \delta\theta(x,t)$. These equations are then solved in Fourier space, which yields both the Bogoliubov dispersion relation [19]

$$E_B(k) = \sqrt{\frac{k^2}{2}\left(\frac{k^2}{2} + 2\varepsilon'(n_\infty)n_\infty\right)} \tag{1.10}$$

after diagonalizing the system with the chemical potential $\mu_\infty = \varepsilon'(n_\infty)n_\infty$. The expression of the density corrections $\delta n(x)$ in the fluid become [156]

$$\delta n(x,t) = \frac{2n_\infty}{4\pi^2}\int dk\, d\omega\, \frac{k^2}{2}\frac{\hat{U}(k,\omega)}{(v_\infty k - \omega)^2 - E_B^2(k)} e^{i(kx-\omega t)}. \tag{1.11}$$

The Fourier transform of the obstacle is easily obtained: $\hat{U}(k,\omega) = 2\pi U_0 \hat{f}(k)\delta(\omega - i\eta)$, and simplifies the density corrections to a stationary expression[2]

$$\frac{\delta n(x)}{n_\infty} = \int dy\, U(y)\chi(x-y), \tag{1.12}$$

where $\chi(x-y)$ is the linear-response function (or Green's function, or susceptibility), given by

$$\chi(x-y) = \frac{1}{2\pi^2}\int dk\, \frac{k^2}{2}\frac{e^{ik(x-y)}}{(v_\infty k - i0^+)^2 - E_B^2(k)}. \tag{1.13}$$

It admits different expressions depended on whether the system is subsonic or supersonic.

[2]The integration over ω will have two consequences: It will change ω into $i\eta$ in the denominator, which is then transformed into a $i0^+$ term in Eq. (1.13); And it will yield a $e^{\eta t}$ prefactor, which is close to 1 since $\eta \ll 1$. The time dependence is then neglected in the following.

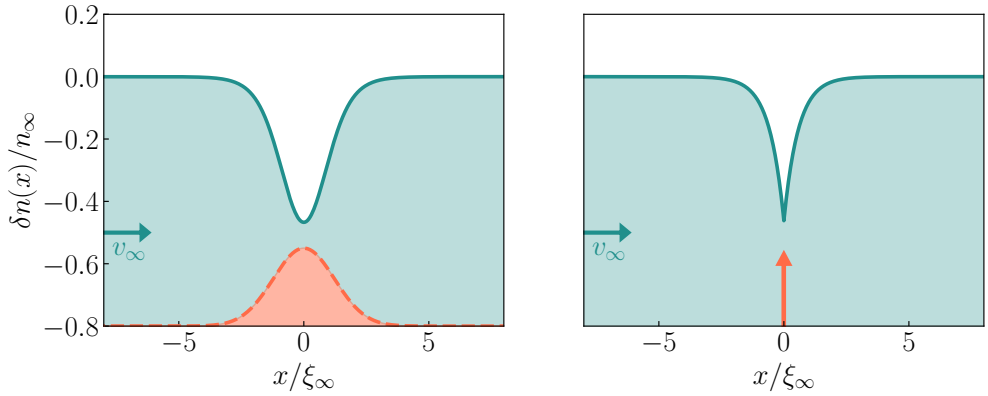

Figure 1.4: Density corrections $\delta n(x)/n_\infty$ in units of U_0/μ_∞ (left) and λ/μ_∞ (right) in the subsonic regime for an input fluid velocity $v_\infty = 0.5c_\infty$. The obstacle is considered to be a Gaussian of amplitude $U_0/\mu_\infty \ll 1$ and width $\sigma \sim \xi_\infty$ (in orange) in the left panel, whereas the right panel represents the density variation for a $\delta-$peak obstacle of amplitude λ. For a $\delta-$peak, the density dip is localized around the obstacle, and is compensated over a distance of order ξ_∞. On the other hand, the perturbation takes place over a length comparable to the typical width σ for a Gaussian obstacle.

Subsonic flow

In the subsonic regime, the Green's function admits two purely imaginary poles given by $k_\pm = \pm\frac{2i\varkappa}{\xi_\infty} - i0^+$, with $\varkappa = \sqrt{1-\frac{v_\infty^2}{c_\infty^2}}$. One then has

$$\chi(x-y) = \frac{1}{2\pi^2}\int_{-\infty}^{+\infty} dk\, \frac{k^2}{2}\frac{e^{ik(x-y)}}{(v_\infty k - i0^+)^2 - E_B^2(k)} = -\frac{1}{\pi\mu_\infty\varkappa}e^{-2\varkappa|x-y|/\xi_\infty}. \tag{1.14}$$

The integral over k in Eq. (1.13) has been solved in the complex plane using the residue theorem. This then yields exact analytical results for the density variations when specifying the form of the obstacle:

$$\frac{\delta n(x)}{n_\infty} \propto -\frac{\lambda}{\mu_\infty}\frac{1}{\varkappa}e^{-2\varkappa|x|/\xi_\infty} \tag{1.15}$$

for a $\delta-$peak obstacle of amplitude $\lambda = U_0 F(\sigma)$ in the subsonic regime, with $F(\sigma)$ being the integral of the typical shape of the obstacle $f(|x|/\sigma)$ over the whole real axis. In that particular case, $\delta n(x)$ simply corresponds to the linear-response function $\chi(0)$ (the same applies by extension to $\delta v(x)$, albeit with a different Green's function).

For a Gaussian obstacle of amplitude U_0, the expression for the density variations reads

$$\frac{\delta n(x)}{n_\infty} \propto -\frac{U_0}{\mu_\infty}\frac{e^{(\varkappa\sigma/\xi_\infty)^2}}{\varkappa}\left\{e^{-2\varkappa x/\xi_\infty}\left[1+\mathrm{erf}\left(\frac{x}{\sigma}-\frac{\varkappa\sigma}{\xi_\infty}\right)\right] + e^{2\varkappa x/\xi_\infty}\mathrm{erfc}\left(\frac{x}{\sigma}+\frac{\varkappa\sigma}{\xi_\infty}\right)\right\}. \tag{1.16}$$

These analytical expressions reveal that the density corrections not only depend on the obstacle parameters, but also on the rescaled initial velocity of the fluid v_∞/c_∞ through the dependence in $\varkappa$. In the subsonic regime, the presence of a repulsive obstacle potential will generate a localized density hole around the obstacle when $v_\infty/c_\infty < 1$. The density profile is then described by evanescent waves with the healing length ξ_∞ as a characteristic range around the obstacle. This is illustrated in Fig. 1.4 for a $\delta-$peak (right) as well as for a Gaussian obstacle (left), where the dimensionless fluctuations are expressed in units of λ/μ_∞ and U_0/μ_∞, very small units in the perturbative approach. Schematics of the obstacles are represented in orange and are expressed in units of μ_∞.

These very weak density corrections are rapidly compensated, and an unperturbed profile is restored over a distance of the order of the healing length for a $\delta-$peak, and σ for a Gaussian obstacle. Thus, we are indeed in the superfluid regime: The presence of the obstacle has no long-range influence on the fluid.

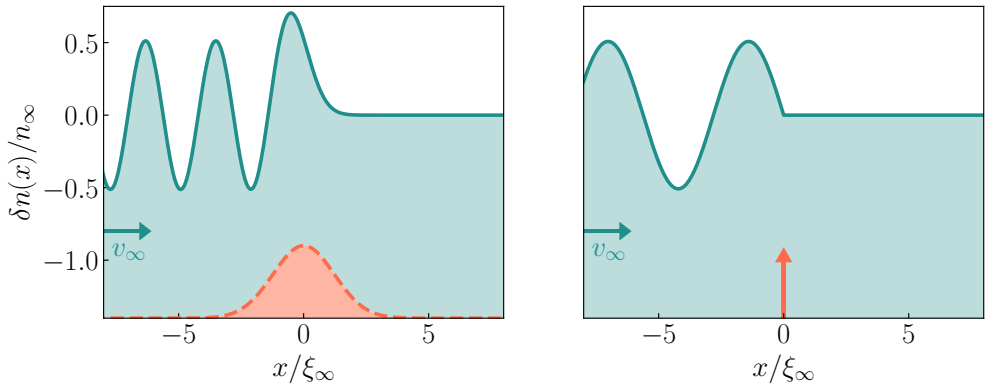

Figure 1.5: Density corrections $\delta n(x)/n_\infty$ in units of U_0/μ_∞ (left) and λ/μ_∞ (right) in the supersonic regime for a perturbative Gaussian obstacle of width $\sigma \sim \xi_\infty$ (in orange) in the left panel, and an input velocity $v_\infty = 1.5c_\infty$. The right panel represents the same thing but for a $\delta-$peak obstacle. Long-range excitations are emitted in the wake of the obstacle.

Supersonic flow

Similarly to the subsonic case, we can determine the density correction associated with the presence of the obstacle using Eq. (1.12). The only difference lies in the fact that the Green's function will differ: Its poles in the supersonic regime are now mostly real, with a really small imaginary part, such that $k_\pm = \pm\frac{2\kappa}{\xi_\infty} - i0^+$, with $\kappa = \sqrt{\frac{v_\infty^2}{c_\infty^2} - 1}$. It is now given by

$$\chi(x-y) = \frac{1}{2\pi^2}\int_{-\infty}^{y} dk\, \frac{k^2}{2}\frac{e^{ik(x-y)}}{(v_\infty k - i0^+)^2 - E_B^2(k)} = \frac{1}{2\pi\mu_\infty\kappa}\sin\left[\frac{2\kappa(x-y)}{\xi_\infty}\right]. \tag{1.17}$$

As the poles are located in the inferior half-plane, the integration for $x > y$ is null. The residue theorem is used again for the integration over $x < y$, and yields for the density corrections

$$\frac{\delta n(x)}{n_\infty} \propto \frac{\lambda}{\mu_\infty}\frac{1}{\kappa}\sin\left[\frac{2\kappa x}{\xi_\infty}\right]\Theta(-x) \tag{1.18}$$

for a $\delta-$peak obstacle, and with $\Theta(x)$ the Heaviside step function. Following the same method, one can also obtain the expression for a Gaussian obstacle

$$\frac{\delta n(x)}{n_\infty} \propto \frac{U_0}{\mu_\infty}\frac{e^{-(\kappa\sigma/\xi_\infty)^2}}{\kappa}\mathfrak{Im}\left\{e^{2i\kappa x/\xi_\infty}\mathrm{erfc}\left(\frac{x}{\sigma} + \frac{i\kappa\sigma}{\xi_\infty}\right)\right\}. \tag{1.19}$$

While these density corrections exhibit dependencies on v_∞/c_∞ (through κ) and on the obstacle parameters similar to the subsonic scenario, the solution takes on a distinctive form. It is important to note that we are no longer in the superfluid regime, as the fluid velocity surpasses the critical velocity, but a regime of stationary flow still exists [52]. The presence of the obstacle significantly influences the density profile, which is fundamentally different to that in the subsonic regime as can be seen in Fig. 1.5. In that case the radiation condition [157] imposes for the wake to be located ahead of the obstacle (upstream), and the fluid remains unperturbed downstream. This explains the constant density far from the obstacle for $x > 0$. In other words, the velocity of the obstacle is larger than the velocity of the Bogoliubov excitations, which provide an estimate of the speed of sound, thus explaining why no wave can radiate downstream. Mathematically, this is linked to the presence of the $-i0^+$ term in the poles of the response function $\chi(x-y)$: As there are no poles in the upper half-plane, the density corrections are null for $x > 0$. This is a classical phenomenon not restricted to quantum fluids, that can be evidenced in many systems such as ship waves (this

Figure 1.6: Illustration of a classical supersonic fluid encountering an obstacle in its path. The white arrow indicates the direction of the flow, and the velocity of the water is larger than the speed of the waves at the surface, since there are no excitations downstream. Photo courtesy of Quentin Glorieux.

is the Kelvin wake pattern [158]), or even a simple stick in a water flow as can be seen in Fig. 1.6.

Upstream, the emission of long-wavelength waves is observed, with the wavelength decreasing as the fluid velocity increases. This phenomenon is known as Bogoliubov-Čerenkov radiation [159]. The term draws an analogy with the Čerenkov effect in electromagnetism, where a charged particle moving faster than the speed of light in a medium emits long-range light radiation [160]. However, the concept of Čerenkov radiation can be extended to any system in which the source moves uniformly through a homogeneous medium at a speed greater than a critical value. Exceeding the speed of sound, much like surpassing the speed of light, leads to specific phenomena. For instance, when an aircraft exceeds Mach 1, it generates a characteristic supersonic boom. In the present case, the sound waves depicted in Fig. 1.5 are emitted upstream of the flow, traveling at a speed lower than that of the fluid. These waves serve as the linear counterpart to shock waves produced by a supersonic aircraft.

Given the results in the previous paragraphs, the critical velocity for superfluidity in the perturbative approach is given by the speed of sound c_∞. This is the same velocity as the one predicted by the Landau criterion, which seems coherent as, even if he considered a system without obstacle, he also treated the case of elementary excitations.

The drag force as indicator for superfluidity

By definition, the superfluid-nonsuperfluid transition is characterized by the sudden emission of excitations, which are at the origin of dissipation in quantum fluids. This results in a nonzero drag force experienced by the obstacle for velocities larger than the critical velocity for superfluidity. If a particle moves within a superfluid with a velocity lower than the critical velocity, its motion is non-dissipative. The superfluid regime is then usually associated with the cancellation of the drag force experienced by the obstacle, as studied in ultracold atomic gases [161] or cavity exciton-polaritons [56, 162, 163]. On the other hand, the nonsuperfluid regime is characterized by the presence of a nonzero drag force. While the first experiments often relied on indirect measures of a heating in the system [156, 164], more recent setups have been developed, which now provide a direct method to obtain the drag force. For example in Ref. [54], the authors extract a direct analog of the drag force exerted by a fluid of light and measured the associated displacement of the obstacle; Which has also more recently been done in hot atomic vapors in Ref. [134].

The force experienced by the obstacle subjected to the quantum fluid is expressed as

$F_\mathrm{d} = \langle\psi|\,\partial_x U(x)\,|\psi\rangle = \int dx\, n(x,t)\partial_x U(x)$ [47], where the average is taken over the condensed state. This expression for the drag force comes from Ehrenfest theorem for a fluid particle of wavefunction ψ experiencing a potential $U(x)$. The integral with the constant part n_∞ of the density is null, and the only contribution to the drag force will come from the density corrections previously derived.

In the subsonic case, a step-to-step analytical calculation of F_d with the expressions (1.15) or (1.16) (for the $\delta-$peak or the Gaussian respectively) shows that one is left with the integral of an odd function over a symmetric interval. The drag force in the subsonic regime is then necessarily zero since the density corrections are symmetrical, implying that the obstacle has no influence on the flow, which remains superfluid.

The supersonic regime is fundamentally different from the subsonic regime: When the fluid velocity exceeds the critical superfluidity velocity c_∞, this force arises due to the possibility of emitting elementary Bogoliubov excitations. A detailed calculation starting from the expression of the density corrections defined in Eq. (1.17) shows that the drag force for supersonic velocities is not null (as the density variations are not symmetrical anymore), and reads

$$F_\mathrm{d} = i\frac{n_\infty U_0^2}{\mu_\infty}\int_{-\infty}^{+\infty} dx\,dk\,\frac{k e^{ikx}}{(k-k_-)(k-k_+)} f\circ f(x) \tag{1.20}$$

with $\circ$ the composition operator, which is the same as Eq. (41) from Ref. [163]. For large values of κ (i.e. $v_\infty \gg c_\infty$), this reduces to

$$F_\mathrm{d} = \frac{2n_\infty U_0^2}{\mu_\infty}\left|\hat{f}\left(\frac{2\kappa}{\xi_\infty}\right)\right|^2. \tag{1.21}$$

In this regime, the drag force is nonzero and generally decreases as $|\hat{f}(2\kappa/\xi_\infty)|^2$ [47, 163], where $\hat{f}(k)$ is the Fourier transform of the obstacle potential. Specific calculations show that the drag force is constant for a $\delta-$peak

$$F_{\mathrm{d},\delta} = \frac{2n_\infty \lambda^2}{\mu_\infty}. \tag{1.22}$$

It is interesting to note that this expression does not depend on the ratio v_∞/c_∞: This saturation of the drag force to a constant value is an artifact of the $\delta-$peak. A full derivation of the drag force for a $\delta-$peak obstacle when the constraint $\lambda \ll \mu_\infty$ is lifted (i.e. the nonperturbative regime) is provided in Sec. 2.2.2.

For a Gaussian obstacle, one obtains

$$F_{\mathrm{d},G} = \frac{2n_\infty U_0^2}{\mu_\infty}\frac{e^{-2(\kappa\sigma/\xi_\infty)^2}}{\kappa}\mathfrak{Im}\left\{\int dx\, e^{-(x-i\kappa\sigma/\xi_\infty)^2}\mathrm{erfc}\left(x+\frac{i\kappa\sigma}{\xi_\infty}\right)\right\}, \tag{1.23}$$

the exponential decay $e^{-2(\kappa\sigma/\xi_\infty)^2}$ being recovered through Eq. (1.21) with the expression of the obstacle. These different expressions for the drag force are represented in Fig. 1.7 as a function of v_∞/c_∞, in units of $n_\infty U_0^2/\mu_\infty$.

An in-depth study of density corrections in the supersonic regime reveals that as v_∞ increases, the amplitude of the emitted waves becomes smaller. Indeed, as the fluid velocity increases, so does the kinetic energy. At a certain point, it surpasses the energy barrier created by the obstacle: The obstacle is increasingly less perceived by the fluid, leading to a reduction in the amplitude of the waves generated by the obstacle. Consequently, $F_\mathrm{d} \to 0$ in the limit of a velocity much greater than the speed of sound. One must however be careful because this close-to-zero drag force for supersonic velocities is not synonymous with a return to a superfluid regime: For high velocities, the kinetic energy is so big that the dynamics of the quantum fluid is as if the interactions were not present. Superfluidity is thus prevented by kinetic effects.

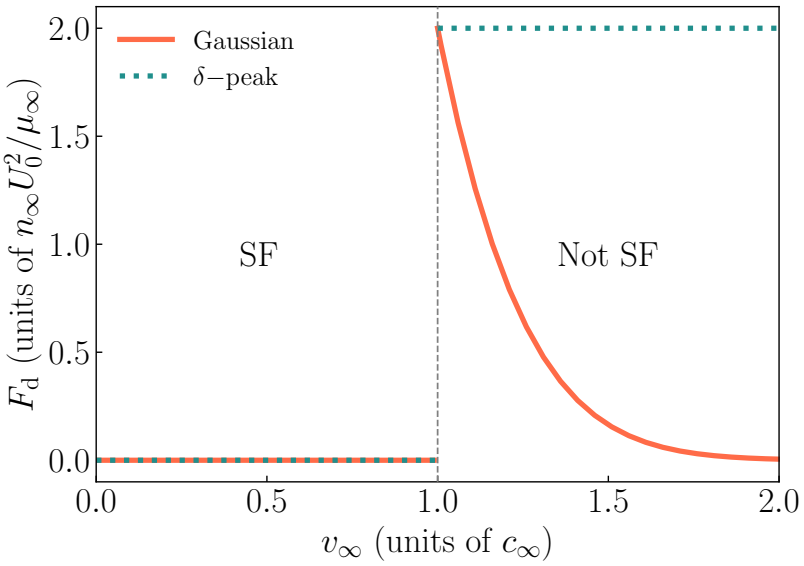

Figure 1.7: Drag force experienced by a Gaussian obstacle of typical width of $\sigma \sim \xi_\infty$ ($\delta-$peak obstacle) in plain orange (dashed blue) line, as a function of the velocity of the fluid. F_d is expressed in units of $n_\infty\lambda^2/\mu_\infty$ for the $\delta-$peak, and $n_\infty U_0^2/\mu_\infty$ for the Gaussian obstacle. In the superfluid regime, there is no dissipation, ergo $F_\mathrm{d} = 0$, whereas when $v_\infty > c_\infty$, this force becomes nonzero and depends on the shape of the obstacle.

1.2.2 Validity of the perturbative approach

To establish the range of validity of the perturbation theory, we treat the extreme case where there is a really deep density dip close to the obstacle, i.e. when the density fluctuations deviate significantly from the unperturbed density. We then look at the results obtained with the response function evaluated at $x - y = 0$[3]. For the perturbation theory to remain applicable, a crucial requirement is that $|\delta n(x = 0)|/n_\infty \ll 1$. Utilizing the outcomes from Eq. (1.15), this condition can be expressed as

$$\epsilon := \frac{\lambda/\mu_\infty}{\sqrt{1-(v_\infty/c_\infty)^2}} \ll 1. \tag{1.24}$$

Contrary to intuition, this parameter is not solely determined by the amplitude of the obstacle (which must necessarily remain small compared to the interactions), but also by the fluid velocity. This velocity dependence imposes a significant constraint on the system, and the condition (1.24) may not be satisfied for all fluid velocities. When the velocity of the fluid approaches the speed of sound, the Bogoliubov excitations will pile up in the vicinity of the obstacle, resulting in nonlinear waves of high amplitude, that cannot be treated within the perturbation theory [52, 163] as $|\delta n(x = 0)|/n_\infty$ is no longer small. Hence, we exit the domain of validity of the linear-response theory when approaching velocities close to the speed of sound.

However, credit must be given to the perturbative approach, which allows for the distinction between two types of flow: Subsonic superfluid and supersonic nonsuperfluid. The critical velocity marking the boundary between these two regimes is that of sound, aligning with what Landau's criterion predicts for the weakly interacting Bogoliubov regime.

[3]This is equivalent to work with the results obtained for a $\delta-$peak obstacle.

1.3 Beyond the perturbative approach

Predicted by Landau, the existence of a critical velocity below which the system is superfluid has found validation in numerous experimental works [68–71] and has become a cornerstone in the study of superfluidity. Yet, these studies have shown that the actual critical velocity is usually lower than the one predicted by Landau, as noticed by Landau himself concerning ^{4}He superfluidity [165]. Indeed, Landau's method provides the same results as the perturbative approach, in which we assume that the perturbation induced by the obstacle is small. This is however not usually the case in experimental setups.

Theoretical investigations have thus been led to gain more insight into this phenomenon, and exact analytical results have been obtained in the one-dimensional case [45, 47]. In these papers, the authors investigate the flow of a BEC through localized obstacles of different geometries, in terms of the obstacle's parameters and of the velocity of the fluid. They obtain exact expressions for the critical velocity for superfluidity through the existence (or not) of a steady flow solution unperturbed far away from the localized obstacles considered in their work, as well as the drag force.

The main motivation of this chapter is to, in a similar way to what has been done before, derive analytical expressions for the critical velocity for superfluidity of a quantum fluid flowing past a localized nonperturbative obstacle. However, our results go beyond previous works: By considering a generic nonlinearity $\varepsilon\left(|\psi|^2\right)$, we are in principle able to derive the value of the critical velocity for many types of systems. We give specific results for various expressions of the nonlinear interaction potential, namely a powerlaw nonlinearity $\varepsilon(n) = n^\nu$ (often exemplified for $\nu = 1$), and quantum fluids of light in saturable media $\varepsilon(n) = n/(n+n_{\mathrm{sat}})$ (refer to the TOOLBOX for more details). In addition, while most of the previous studies have been performed for the two extreme cases of obstacles of characteristic range smaller or larger than the healing length ξ_∞ of the homogeneous fluid, the present manuscript provides a description that ranges from narrow (Sec. 1.3.1) to wide obstacles (Sec. 1.3.2), with a numerical study to interpolate the behavior of the critical velocity in between these two extreme regimes (Sec. 1.3.3). Finally, some systems call for taking losses into account, as it is the case for experiments on light superfluidity in which losses are caused by photonic absorption. Particle losses, if present, are accounted for and are analytically treated within an adiabatic approximation, which is numerically verified in Sec. 1.3.4.

In this section, we characterize the critical velocity for superfluidity as a function of the obstacle's parameters (its amplitude U_0 and width σ), and notably obtain $v_c(\sigma)$ for any value of U_0, starting from the hydrodynamic equations (1.8) with our criteria for a superfluid flow.

In the stationary regime, it is possible to combine the two Eqs. (1.8) into a single one: The continuity equation (1.8b) yields an expression for the velocity $v(x) = v_\infty n_\infty/n(x)$, which is then injected into Eq. (1.8a). This yields

$$\frac{1}{2}\frac{\partial_x^2\sqrt{n}}{\sqrt{n}} + \frac{v_\infty^2}{2}\left(1-\frac{1}{n^2}\right) + \varepsilon(1) - \varepsilon(n) = U(x), \tag{1.25}$$

where $n(x) \to 1$ as $|x| \gg \sigma$. The superfluid stationary regime exists as long as this equation admits solutions: The last velocity v_∞ for which there exists a stationary solution is the critical velocity for superfluidity.

After linearizing Eq. (1.25) for large $|x|$ with $n(x) = 1 + \delta n(x)$ (and keeping the terms proportional to δn), one is left with the equation $\partial_x^2\delta n(x) - 4(\varepsilon'(1) - v_\infty^2)\delta n(x) = 0$. This equation admits vanishing solutions if $v_\infty < \varepsilon'(1)$, meaning that the system is superfluid provided the flow is subsonic. This imposes a huge constraint on the range of possible v_∞'s

in the following study, namely that superfluidity only occurs at subsonic speeds $v_\infty < 1$[4].

1.3.1 Narrow obstacle

If the range of the obstacle is much smaller than the healing length (in the dimensionless units, $\sigma \ll 1$), the potential $U(x)$ can be approximated with a Dirac delta function: $U(x) = U_0 F(\sigma)\delta(x)$, with for example $F(\sigma) = \sqrt{\pi}\sigma$ for a Gaussian obstacle with $f(|x|/\sigma) = \exp\{-x^2/\sigma^2\}$. We provide detailed calculations leading to the critical velocity for superfluidity v_c for such a narrow obstacle. The main equation to solve is

$$\frac{1}{2}\frac{\partial_x^2\sqrt{n}}{\sqrt{n}} + \frac{v_\infty^2}{2}\left(1 - \frac{1}{n^2}\right) + \varepsilon(1) - \varepsilon(n) = 0, \tag{1.26}$$

except at $x = 0$, where the $\delta-$peak obstacle is located, and for which one obtains a condition on the derivative [52]

$$\frac{\partial_x n(0^+) - \partial_x n(0^-)}{4n_0} = U_0 F(\sigma). \tag{1.27}$$

The resolution of Eq. (1.26) for $x \neq 0$ yields

$$\frac{(\partial_x n)^2}{8n} + \frac{v_\infty^2}{2}\left(n + \frac{1}{n}\right) + n\varepsilon(1) - \mathcal{E}(n) = E, \tag{1.28}$$

with $\mathcal{E}(n) = \int dn\, \varepsilon(n)$ and $E = v_\infty^2 + \varepsilon(1) - \mathcal{E}(1)$ the integration constant defined with the density $n = 1$ at $|x| \to \infty$. This yields the value of the derivative of the density evaluated at $x = 0$

$$\partial_x n(0^\pm) = \pm\sqrt{8n_0}\left[-n_0\frac{v_\infty^2}{2}\left(1 - \frac{1}{n_0}\right)^2 - n_0\varepsilon(1) + \varepsilon(1) - \mathcal{E}(1) + \mathcal{E}(n_0)\right]^{\frac{1}{2}}. \tag{1.29}$$

As the velocity is lower than the speed of sound, we will necessarily have a dip in the density at $x = 0$ for repulsive obstacles. As a result, the density at $x = 0$ is $n_0 < 1$, and its derivatives are respectively $\partial_x n(0^-) < 0$ and $\partial_x n(0^+) > 0$. The situation is the opposite for attractive obstacles: There is a density bump at $x = 0$ such that $n_0 > 1$, and so $\partial_x n(0^-) > 0$ and $\partial_x n(0^+) < 0$. Combining Eqs. (1.27) and (1.29), one is left with

$$\mathscr{U}(n_0, v_\infty) := \mathrm{sgn}(1 - n_0)\sqrt{2}\left[-\frac{v_\infty^2}{2}\left(1 - \frac{1}{n_0}\right)^2 - \varepsilon(1) + \frac{\varepsilon(1) - \mathcal{E}(1) + \mathcal{E}(n_0)}{n_0}\right]^{\frac{1}{2}} = U_0 F(\sigma). \tag{1.30}$$

We represent Eq. (1.30) in Fig. 1.8 for $\varepsilon(n) = n$ and $v_\infty = 0.5$. Note that it remains qualitatively the same for other values of $v_\infty < 1$, and for a powerlaw nonlinearity (the case of the saturable nonlinearity is peculiar, and will be explained at the end of the section). We can see that, when $U_0 > 0$, Eq. (1.30) admits solutions provided that $U_0 F(\sigma) < \mathscr{U}_{\max} = \mathscr{U}(n_{0,\min})$ as there is always at least one intersection with the curve. $n_{0,\min}$ is defined such that it is solution of $\partial_{n_0}\mathscr{U}(n_{0,\min}) = 0$. We obtain the implicit relation

$$\frac{n_{0,\min}}{1 - n_{0,\min}}\left[\varepsilon(1) - \mathcal{E}(1) + \mathcal{E}(n_{0,\min}) - \varepsilon(n_{0,\min})n_{0,\min}\right] = v_\infty^2. \tag{1.31}$$

As $\mathscr{U}_{\max}(v_\infty)$ is a decreasing function of v_∞, the condition $U_0 F(\sigma) < \mathscr{U}_{\max}(v_\infty)$ to admit solutions is equivalent to $v_\infty < v_c$, where the critical velocity v_c is implicitly given by

$$\mathscr{U}_{\max}(v_c) = U_0 F(\sigma). \tag{1.32}$$

[4]It is important to note that stationary solutions to Eq. (1.25) do exist for $v_\infty > 1$ but for another family of solutions, which will lead to another regime of transport for the fluid (not superfluid anymore). This is the object of Chap. 2.

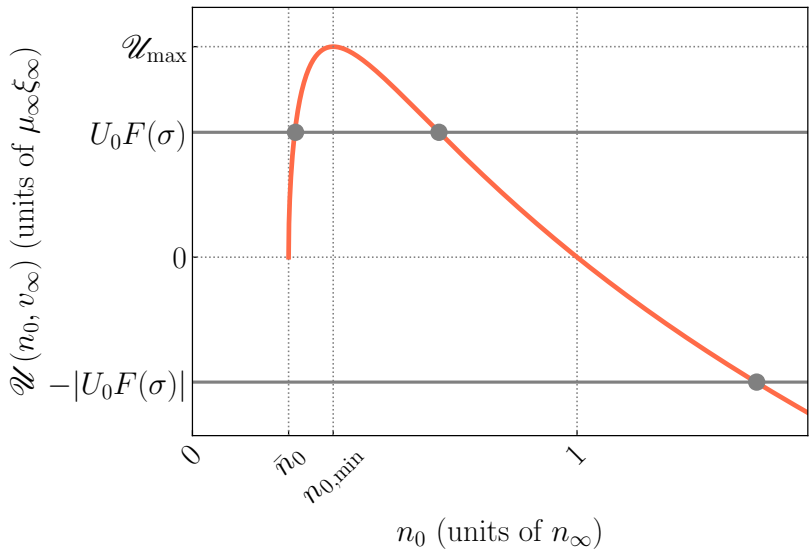

Figure 1.8: Fictitious potential $\mathscr{U}(n_0, v_\infty)$ as a function of n_0, for $v_\infty = 0.5$ and $\varepsilon(n) = n$. When the obstacle is repulsive ($U_0F(\sigma) > 0$), it is graphically shown that Eq. (1.30) admits up to two solutions (the physical one being the larger, as the density is supposed to go to 1 as the obstacle vanishes). Superfluidity is lost for the value of v_∞ for which there is no crossing between $U_0F(\sigma)$ and $\mathscr{U}(n_0, v_\infty)$. Concerning attractive obstacles, superfluidity is never lost (at least for $\varepsilon(n) = n$) as Eq. (1.30) always admits one solution, and so $v_c = 1$.

In the end, the equations defining the critical velocity for superfluidity for a $\delta-$peak obstacle are the following

$$U_0F(\sigma) = \sqrt{2}\left[-\frac{v_c^2}{2}\left(1 - \frac{1}{n_{0,c}}\right)^2 - \varepsilon(1) + \frac{\varepsilon(1) - \mathcal{E}(1) + \mathcal{E}(n_{0,c})}{n_{0,c}}\right]^{\frac{1}{2}}, \tag{1.33a}$$

$$\frac{n_{0,c}}{1 - n_{0,c}}\left[\varepsilon(1) - \mathcal{E}(1) + \mathcal{E}(n_{0,c}) - \varepsilon(n_{0,c})n_{0,c}\right] = v_c^2. \tag{1.33b}$$

Repulsive obstacles

Simplified expressions (albeit still implicit) can be derived from these implicit equations when specifying the nonlinearity characterizing the system. We then obtained the following expression for $\varepsilon(n) = n$ [45, 52]

$$\frac{\left[1 - 20v_c^2 - 8v_c^4 + (1 + 8v_c^2)^{\frac{3}{2}}\right]^{\frac{1}{2}}}{2\sqrt{2}v_c} = U_0F(\sigma). \tag{1.34}$$

No easy analytical expression can be derived for a saturable nonlinearity or a general powerlaw nonlinearity on the other hand, as it would not be possible to invert Eq. (1.33b) to obtain $n_{0,c}$, and these equations must be solved numerically. These critical velocities are represented in Fig. 1.9 for $\varepsilon(n) = n$ (in blue) and saturable nonlinearities with saturation intensities $n_{\text{sat}} \in \{0.1, 1, 10\}$ (in orange). It can be seen that as the amplitude of the obstacle gets smaller, the critical velocity tends to $v_c = 1$: This is in accordance with the Landau criterion. On the contrary when $U_0F(\sigma)$ increases, v_c tends to 0. This is expected as the stronger the obstacle, the easier it is to break superfluidity.

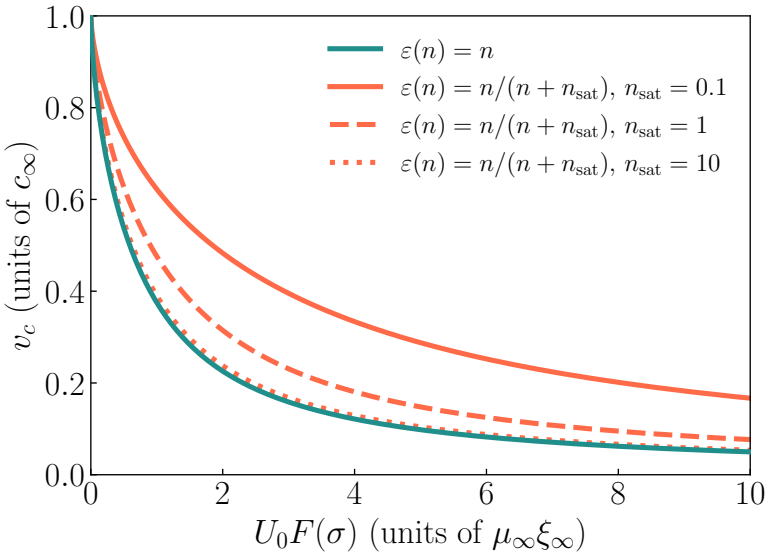

Figure 1.9: Critical velocity for superfluidity for a repulsive $\delta-$peak obstacle. These results are shown for a different nonlinearities as indicated in the legend.

Attractive obstacles

For attractive obstacles ($U_0 < 0$), stationary solutions always exist for $\varepsilon(n) = n$ and superfluidity is never lost: The flow can be superfluid for all $v_\infty < 1$ (there is always an intersection between $-|U_0F(\sigma)|$ and $\mathscr{U}(n_0, v_\infty)$ as shown in Fig. 1.8), hence the critical velocity in that case is equal to Landau's critical speed $v_c = 1$ in our dimensionless units.

On the other hand it is not the case for a saturable nonlinearity: For some parameters, the fictitious potential $\mathscr{U}(n_0, v_\infty)$ tends to a plateau at $-\sqrt{2 + 2n_{\rm sat} - v_\infty^2}$ for large values of n_0, so that there is no intersection between $U_0F(\sigma)$ and the curve. This is conditioned by the value of the saturation intensity, such that if $n_{\rm sat} < v_\infty^2/2 - 1$, the system is not superfluid anymore. As shown in Fig. 1.10, the larger $n_{\rm sat}$, the larger the range of negative values of $\mathscr{U}(n_0, v_\infty)$ for which superfluidity exists: The saturation intensity needs to be really small for superfluidity to be broken. In practice, this condition is not really restrictive as it is possible to experimentally tune the value of $n_{\rm sat}$ to large values (as is the case in the experiment of [55]), making it possible to observe the superfluid regime.

Density profile

The density profile is sharp at $x = 0$ for a narrow obstacle, with a discontinuous derivative. It can be shown that the fundamental solution is formed by two portions of grey solitons (as the interactions are repulsive, there is a density dip), whose centers are located at $\pm x_0$.

More generally, dark solitons are a solution of the 1D Gross-Pitaevskii equation with repulsive interactions. They consist in waves, very robust against perturbations, that can propagate over long distances without deformation. This interesting property is possible thanks to the competition between the dispersive and nonlinear terms in the Gross-Pitaevskii equation. Solitons can appear and are studied in many domains, among which stands classical hydrodynamics [166, 167] (in which they were originally discovered [168]) or nonlinear optics [138, 169]. More importantly in this context, they can exist in quantum fluids such as Bose-Einstein condensates [170–173] or quantum fluids of light [121, 174].

The analytical solution for such a soliton for $\varepsilon(n) = n$ was originally proposed in Ref. [175], and can also be found in Refs. [19, 176]. It reads

$$n(x \pm x_0) = n_\infty \left[v_\infty^2 + \left(1 - v_\infty^2\right) \tanh^2 \left\{ \sqrt{1 - v_\infty^2}(x \pm x_0) \right\} \right]. \tag{1.35}$$

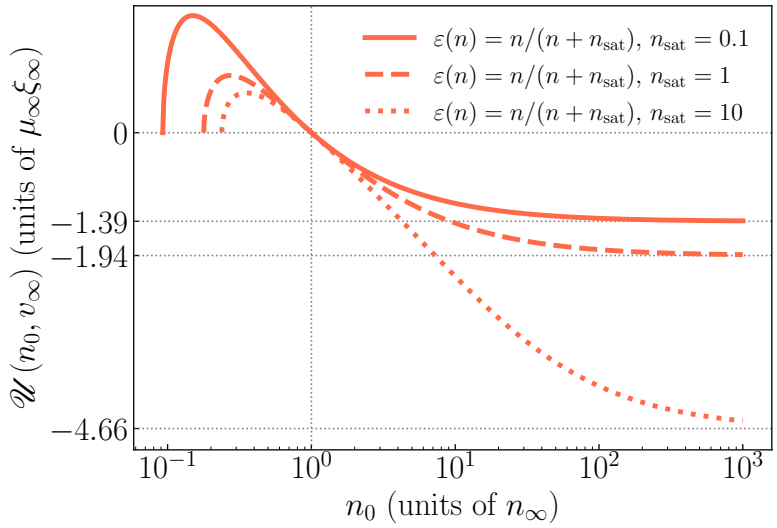

Figure 1.10: Fictitious potential $\mathscr{U}(n_0, v_\infty)$ as a function of n_0, for $v_\infty = 0.5$ and a saturable nonlinearity. For repulsive obstacles, the observed behavior is the same as for $\varepsilon(n) = n$; The change lies in the case of attractive obstacles. A saturation to a plateau at $\mathscr{U}(n_0, v_\infty) = -\sqrt{2 + 2n_{\rm sat} - v_\infty^2}$ is observed for large values of n_0, as shown in grey dashed lines for various values of $n_{\rm sat}$. The curves saturate to $\mathscr{U}(n_0, v_\infty) = -1.39$ for $n_{\rm sat} = 0.1$, -1.94 for $n_{\rm sat} = 1$ and -4.66 for $n_{\rm sat} = 10$, and superfluidity is thus broken when $|U_0 F(\sigma)|$ is larger than these plateaux.

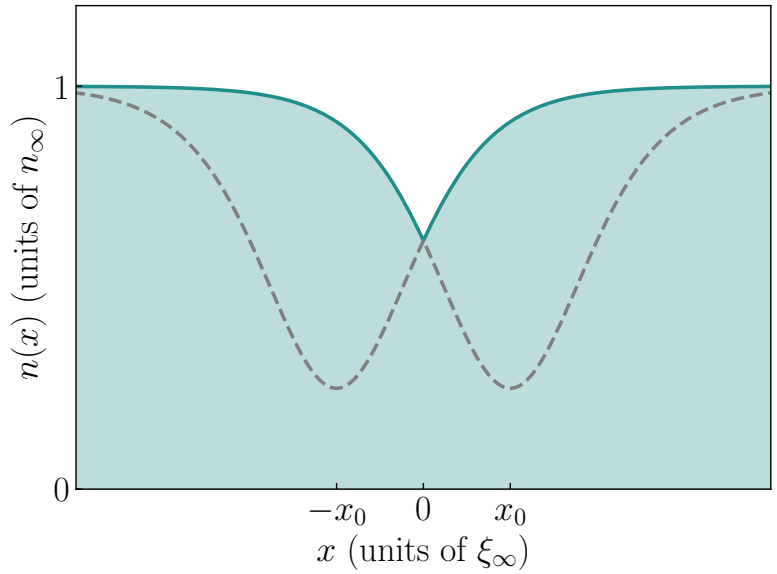

Figure 1.11: Density profile in the case of a $\delta-$shaped obstacle, for $v_\infty = 0.5$. The physical solution (plain line) is formed by two portions of grey solitons (dashed lines), centered at $x = x_0$.

This density profile is represented in Fig. 1.11. Equation (1.35) shows that the density dip gets deeper as v_∞ decreases. In the limit of $v_\infty = 0$, one has a motionless black soliton, whereas when $v_\infty = 1$, the soliton totally disappears. The velocity of the soliton is then bounded by the speed of sound.

It is interesting to note that Eq. (1.34) can also be derived from the expression of the solitonic density profile provided in Eq. (1.35). Following the calculations performed in [45], we present this method, starting from expression of the density Eq. (1.35). This, together with the condition on the derivative given in Eq. (1.27), leads implicitly to the possible values

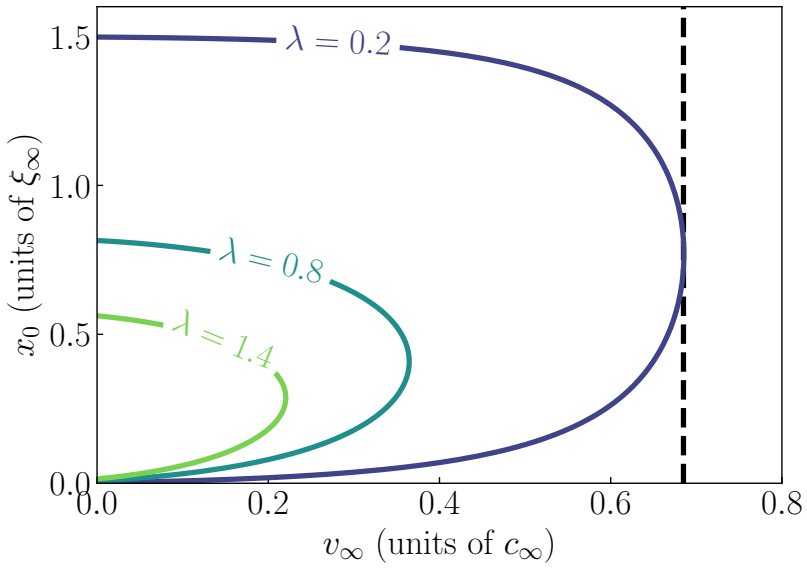

Figure 1.12: 2D representation of Eq. (1.36) as a function of v_∞ and x_0, for several values of $\lambda = U_0 F(\sigma) \in \{0.2, 0.8, 1.4\}$. For example, one can see with the black dashed line that when $v_\infty/c_\infty > 0.68$, Eq. (1.36) with $\lambda = 0.2$ has no solutions anymore for x_0, defining the critical velocity for this given amplitude. This v_c coincides with the results obtained in Fig. 1.9.

of x_0 through the relation

$$\lambda = U_0 F(\sigma) = \frac{(1-v_\infty^2)^{3/2} \tanh\left(\sqrt{1-v_\infty^2}x_0\right) \operatorname{sech}^2\left(\sqrt{1-v_\infty^2}x_0\right)}{v_\infty^2 + (1-v_\infty^2)\tanh^2\left(\sqrt{1-v_\infty^2}x_0\right)}, \tag{1.36}$$

which is represented in Fig. 1.12. One can see that for a given value of $\lambda = U_0 F(\sigma)$, there are up to two possible values for x_0 depending on the injection velocity v_∞. As long as v_∞ is lower than a critical value (namely, v_c), there are two solutions and superfluidity can exist. The value of v_∞ for which there is no solution anymore for x_0 defines v_c.

Equation (1.36) can be re-expressed as a polynomial after the change of variable $X = \tanh\left(\sqrt{1-v_\infty^2}x_0\right)$ (note that $X > 0$ as $x_0 > 0$), which yields

$$X^3 + \lambda(1-v_\infty^2)^{-1/2}X^2 - X + \lambda v_\infty^2(1-v_\infty^2)^{-3/2} = 0. \tag{1.37}$$

This can in turn be simplified into

$$\tilde{X}^3 + p\tilde{X} + q = 0, \tag{1.38}$$

with

$$\tilde{X} = X + \frac{\lambda}{3}(1-v_\infty^2)^{-1/2}, \tag{1.39a}$$

$$p = -\left(1 + \frac{\lambda}{3}(1-v_\infty^2)^{-1/2}\right), \tag{1.39b}$$

$$q = \frac{1}{3} + \left(v_\infty^2 + \frac{2\lambda^2}{27}\right)(1-v_\infty^2)^{-1/2}. \tag{1.39c}$$

Equation (1.38) can be analytically solved and one can obtain its roots $\tilde{X}$ using Cardano's formula, but it is only necessary to study its discriminant Δ to obtain v_c. Equation (1.38) has three distinct real roots when $\Delta > 0$, and one real and two complex-valued conjugate roots

if $\Delta < 0$. This change in the nature of the solutions for $\Delta = 0$ exactly gives the condition to derive v_c. This condition reads

$$\frac{q^2}{4} + \frac{p^3}{27} = 0, \tag{1.40}$$

and transforms after calculation into

$$\lambda = \frac{\left[1 - 20v_c^2 - 8v_c^4 + (1 + 8v_c^2)^{\frac{3}{2}}\right]^{\frac{1}{2}}}{2\sqrt{2}v_c}. \tag{1.41}$$

One recovers Eq. (1.34) from the main text, which implicitly gives the critical velocity for superfluidity in the case $\varepsilon(n) = n$.

1.3.2 Wide obstacle

In the case of slowly-varying obstacles, i.e. when the typical size of $U(x)$ is much larger than the healing length ($\sigma \gg \xi_\infty$), the gradients of the obstacle are so small that the fluid can almost be considered uniform. It is (as a first approximation) as if the obstacle were flat, neglecting all dependence on σ. It is then possible to perform an analytical expansion of the potential around its maximum value U_0 such that $U(x) = U_0\left(1 - |\partial_x^2 f(0)|x^2/2\sigma^2\right)$. The critical velocity can be obtained as being a constant for a given value of U_0, to which we add a small perturbation which includes the dependence on σ: $v_c(U_0, \sigma) = v_{c,0}(U_0) + \delta v_c(U_0, \sigma)$.

We will first treat the case of $v_{c,0}(U_0)$, which is the part of the critical velocity that does not depend on the width σ of the obstacle: This is called the hydraulic approach, in which the dispersion term can be neglected. We then perform a Taylor expansion of the various observables around the hydraulic solutions in order to take into account the gradients of the obstacle as performed in Ref. [45], allowing us to obtain an analytical expression for the small correction in σ. Finally, we tackle the problem of the critical velocity for obstacles of really large amplitude, which goes beyond the hydraulic approach as the density depletion becomes really important, and requires a specific treatment. The combination of these results will provide a good description for the critical velocity for wide obstacles.

Hydraulic approach

As a first approximation, we consider the obstacle to be constant everywhere, taking its maximum value U_0. The density is then constant as well, and takes the value $n(x) = n(x = 0) = n_0$. As the obstacle is flat, Eq. (1.25) reduces to

$$U_0 = \frac{v_\infty^2}{2}\left(1 - \frac{1}{n_0^2}\right) + \varepsilon(1) - \varepsilon(n_0) := \mathscr{V}(n_0, v_\infty). \tag{1.42}$$

Solving this equation for a given nonlinearity gives an expression for $v_{c,0}$, the critical velocity to the zeroth order in σ, as a function of U_0. In a similar fashion to what has been done for narrow obstacles, we can graphically solve this equation as represented in Fig. 1.13. $\mathscr{V}(n_0, v_\infty)$ is here represented as a function of n_0 in the case of $\varepsilon(n) = n$ (though nothing fundamentally changes for a saturable nonlinearity).

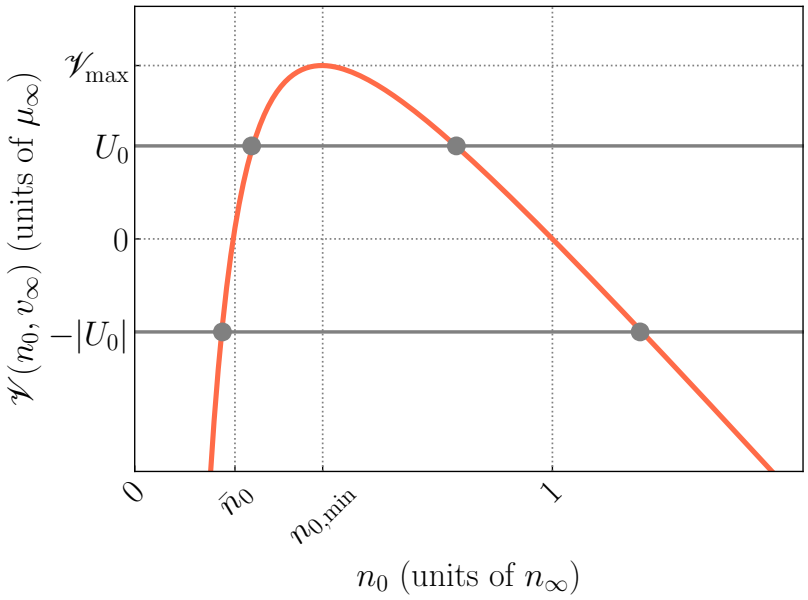

Figure 1.13: Fictitious potential $\mathscr{V}(n_0, v_\infty)$ as a function of n_0 for $v_\infty = 0.3$ and $\varepsilon(n) = n$. For repulsive obstacles, Eq. (1.42) admits up to two solutions, and superfluidity is again lost for the value of v_∞ for which there are no solutions anymore. Concerning attractive obstacles, superfluidity is never lost as Eq. (1.42) always admits two solutions no matter the expression of $\varepsilon(n)$.

Again, we search for the values of v_∞ for which this equation has solutions for the density. As shown graphically in Fig. 1.13, solutions exist as long as $U_0 < \mathscr{V}_{\max} = \mathscr{V}(n_{0,\min}, v_\infty)$. $n_{0,\min}$ gives the position of the maximum of $\mathscr{V}(n_0, v_\infty)$: $\partial_{n_0}\mathscr{V}(n_{0,\min}, v_\infty) = 0$, which yields the relation

$$v_{c,0}^2 = \varepsilon'(n_{0,\min}) n_{0,\min}^3. \tag{1.43}$$

This equation, combined with Eq. (1.42), and applied to the critical parameters $v_{c,0}$ and $n_{0,\min}$, yields

$$\frac{v_{c,0}^2}{2}\left(1 - \frac{1}{n_{0,\min}^2}\right) + \varepsilon(1) - \varepsilon(n_{0,\min}) = U_0. \tag{1.44}$$

This provides the implicit relations necessary to obtain the hydraulic approximation for the critical velocity for superfluidity. $v_{c,0}$ is represented in Fig. 1.14 as a function of the amplitude of the obstacle.

It is easily seen in Fig. 1.14 that, for the two considered nonlinearities at least, $v_{c,0}(U_0)$ always abruptly goes to zero for any form of $\varepsilon(n)$, but for different values of U_0. The maximum value possible for U_0 before completely losing superfluidity depends on the value of the saturation intensity n_{sat}. A more thorough study of Eq. (1.44) reveals indeed that the hydraulic approach is valid only if $U_0 < U_{0,\max} = \varepsilon(1)$. For the nonlinearities used in this manuscript, we found that $U_{0,\max} = 1$ for $\varepsilon(n) = n$, and $U_{0,\max} = (1 + n_{\text{sat}})/n_{\text{sat}}$ for a saturable one. Beyond this threshold values, the obstacle transforms into an infinitely large classical barrier, the density becomes null and the fluid is separated into two independent parts on both sides of the obstacle. In reality for a finite-sized obstacle, v_c is not strictly null and the barrier can be crossed via tunneling even if its amplitude exceeds the maximum value because of the quantum pressure. The question of how to obtain results for obstacles larger than $U_{0,\max}$ is however not captured within this hydraulic approach as the quantum pressure is neglected, and is the object of another part of this section, albeit only for $\sigma \gg 1$.

Concerning attractive obstacles ($U_0 < 0$), one can see that Eq. (1.42) always admits two

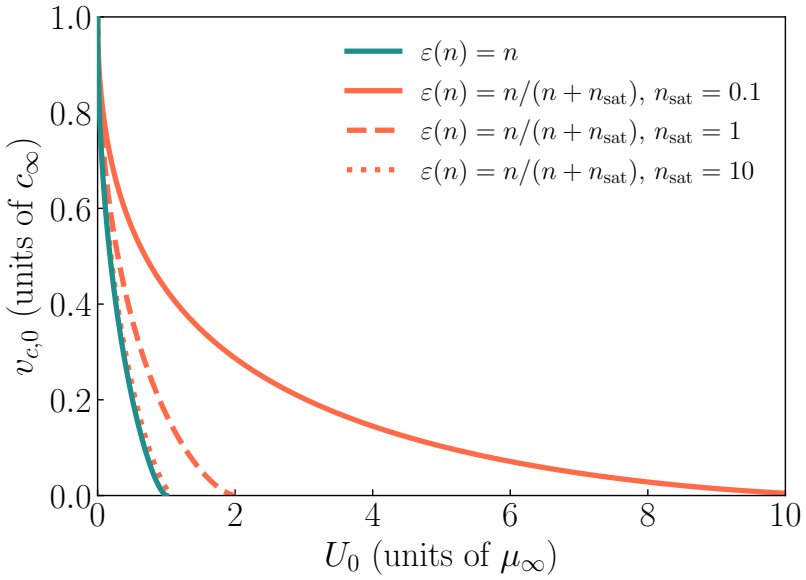

Figure 1.14: Critical velocity for superfluidity $v_{c,0}$ obtained in the hydraulic approximation, for a wide repulsive obstacle. These results are shown, as for the narrow obstacle, for various nonlinearities as indicated in the legend. Each curve drops to zero for $U_0 = U_{0,\rm max}$, respectively given by $U_{0,\rm max} \in \{1, 10, 1.1, 2\}$ for $\varepsilon(n) = n$ and saturable nonlinearities with $n_{\rm sat} \in \{0.1, 1, 10\}$.

solutions, meaning that superfluidity is never lost: The critical velocity for superfluidity is given by the Landau criterion $v_c = c_\infty$ (1 in our dimensionless units). It is interesting to note that this criterion is also valid for a saturable nonlinearity, which was not always the case for a $\delta-$peak obstacle as shown in the previous section.

When the obstacle $U(x)$ is smooth enough (i.e. its gradients are small), the fluid behaves almost as if it were uniform, and it becomes possible to define quantities at each point x such as the local speed of sound $c(x) = [\varepsilon'(n)n(x)]^{1/2}$: This is the local density approximation (LDA) [48, 177].
The local Landau criterion states that as long as the velocity of the fluid does not exceed this local speed of sound, the system is superfluid: This translates to $v(x) < c(x)$. Using the continuity equation, this condition can be re-expressed as

$$v_\infty < v_{c,\rm LL} = \left[\varepsilon'(n)n^3\right]^{1/2}. \tag{1.45}$$

Given that there is a different speed of sound at each point x, superfluidity will be broken where this local speed of sound $c(x)$ is minimal, i.e. where the obstacle is maximal, and thus where the density is minimal. Equation (1.43) is then just a reformulation of the local Landau criterion for the point where the density is minimal, such that $n(x) = n_{0,\rm min}$.

Correction to the hydraulic approach

The critical velocity can be more precisely defined when taking into account the gradients of the obstacle to the lowest order in $1/\sigma$, that were so far neglected in the hydraulic approach [108]. Following the method proposed in [45], we improve the hydraulic expression $v_{c,0}$ by a correction proportional to a power of σ, and generalize it to other types of nonlinearities. To treat that case, we perform Taylor expansions of the various relevant quantities in powers of

$1/\sigma \to 0$ around the hydraulic solution $(n_{0,\min}, v_{c,0})$ but with yet unknown dependencies on σ. The solution is of the form

$$v_c = v_{c,0} + \delta v_c \sigma^a, \tag{1.46a}$$

$$n = n_{0,\min} + \delta n \sigma^b, \tag{1.46b}$$

$$U = U_0 \left(1 - \frac{|\partial_x^2 f(0)|}{2} x^2 \sigma^c\right), \tag{1.46c}$$

$$x = y\sigma^d. \tag{1.46d}$$

The various coefficients are adapted to have a coherent Taylor development, and are given by $a = -4/3$, $b = -2/3$, $c = -4/3$ and $d = 1/3$. After solving Eq. (1.25) order by order in σ taking into account Eqs. (1.46), one obtains

- Order σ^0

$$\frac{v_{c,0}^2}{2}\left(1 - \frac{1}{n_{0,\min}^2}\right) + \varepsilon(1) - \varepsilon(n_{0,\min}) = U_0. \tag{1.47}$$

This is the equation obtained in the hydraulic approach, treated in the previous section.

- Order $\sigma^{-2/3}$

$$v_{c,0}^2 = \varepsilon'(n_{0,\min}) n_{0,\min}^3. \tag{1.48}$$

We recover the local Landau criterion.

- Order $\sigma^{-4/3}$

This is the equation to solve to obtain the correction to the hydraulic approach, as it is the first order for which δv_c appears in the expansion. The first intermediate step in the calculations leads to

$$\partial_y^2 \delta n = A\delta n^2 + B\delta v_c - Cy^2, \tag{1.49}$$

with the coefficients

$$A = 2\left[3\varepsilon'(n_{0,\min}) + n_{0,\min}\varepsilon''(n_{0,\min})\right], \tag{1.50a}$$

$$B = 4v_{c,0}\left[\frac{1}{n_{0,\min}} - n_{0,\min}\right], \tag{1.50b}$$

$$C = 2U_0 n_{0,\min} |\partial_x^2 f(0)|. \tag{1.50c}$$

Equation (1.49) can be further simplified and transforms to

$$\partial_z^2 \Delta n = \Delta n^2 + \Delta v_c - z^2, \tag{1.51}$$

with the change of variables $z = (AC)^{\frac{1}{6}} y$, $\Delta n = A^{\frac{2}{3}} C^{-\frac{1}{3}} \delta n$ and $\Delta v_c = A^{\frac{1}{3}} B C^{-\frac{2}{3}} \delta v_c$.

This simplified equation describes a saddle-node bifurcation. Its two solutions depend on the value of Δv_c, and exist as long as $-\infty < \Delta v_c < \Delta v_{c,\mathrm{crit}}$. Analytical expressions for these solutions are given for $|\Delta v_c| \gg 1$ in Ref. [45], and are plotted in Fig. 1.15. As Δv_c approaches the critical value, these asymptotic solutions are no longer valid and one has to solve Eq. (1.51) numerically. The two solutions get closer until they merge, and the superfluid transition occurs when $\Delta v_c = \Delta v_{c,\mathrm{crit}}$, which is determined numerically as $\Delta v_{c,\mathrm{crit}} \approx 1.466$.

Finally, by taking into account the variations of the obstacle, we are able to obtain the small correction to the hydraulic approach

$$\delta v_c = \frac{1.466\, C^{\frac{2}{3}}}{A^{\frac{1}{3}} B}, \tag{1.52}$$

which leads to

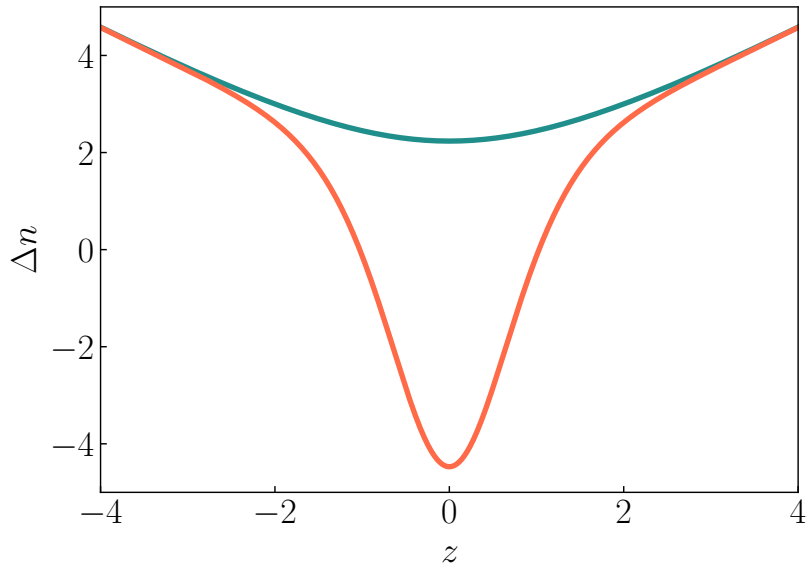

Figure 1.15: Two asymptotic solutions of Eq. (1.51) as given in Ref. [45] for $\Delta v_c = -5$. As Δv_c increases and approaches its critical value, the two solutions get closer. They merge for $\Delta v_{c,\mathrm{crit}} \approx 1.466$, in which case Eq. (1.51) no longer has a solution. The consequence in our case is that superfluidity is lost.

$$v_c = v_{c,0}(U_0) + \frac{1.466}{2^{\frac{5}{3}}} \frac{\left(U_0 |\partial_x^2 f(0)| n_{0,\min}\right)^{\frac{2}{3}}}{v_{c,0}\left(\frac{1}{n_{0,\min}} - n_{0,\min}\right)\left[3\varepsilon'(n_{0,\min}) + n_{0,\min}\varepsilon''(n_{0,\min})\right]^{\frac{1}{3}}} \frac{1}{\sigma^{\frac{4}{3}}}. \quad (1.53)$$

The critical velocity for superfluidity mainly depends on the part determined to the zeroth order in σ, i.e. $v_{c,0}(U_0)$, and so its main dependence is on U_0, the amplitude of the obstacle. The shape of the obstacle is only important for the correction to $v_{c,0}$ via its second derivative at $x = 0$ and its width: The larger σ, the smaller this correction. This means that for a really large obstacle, the critical velocity tends to $v_{c,0}(U_0)$, the value obtained in the hydraulic approach. Going from a flat obstacle to the "real" obstacle implies that the potential seen by the fluid will be less important, and as a result v_c increases[5]: The quantum pressure is then favorable to superfluidity.

Josephson treatment of the problem for a wide obstacle

So far, the method used in the previous sections to determine the critical velocity for a very wide obstacle presents a problem when U_0 approaches its maximum value $U_{0,\max}$, which is the amplitude of the obstacle for which the fluid is exactly separated in two independent parts in the zero gradient approximation, and for which superfluidity breaks down. In practice, these gradients can no longer be neglected, especially close to the obstacle, where the density depletion is pretty important and the variation of density not negligible. In reality, the critical velocity for $U_0 \geqslant U_{0,\max}$ is not strictly zero, although it is really small. With the amplitude of the obstacle greater than the energy E of the stationary state, the system now consists of two quantum reservoirs isolated from each other by the potential; We tackle this problem as a Josephson junction.

[5]This is indeed demonstrated by the fact that the correction in $\sigma^{-4/3}$ is positive as $n_{0,\min} < 1$.

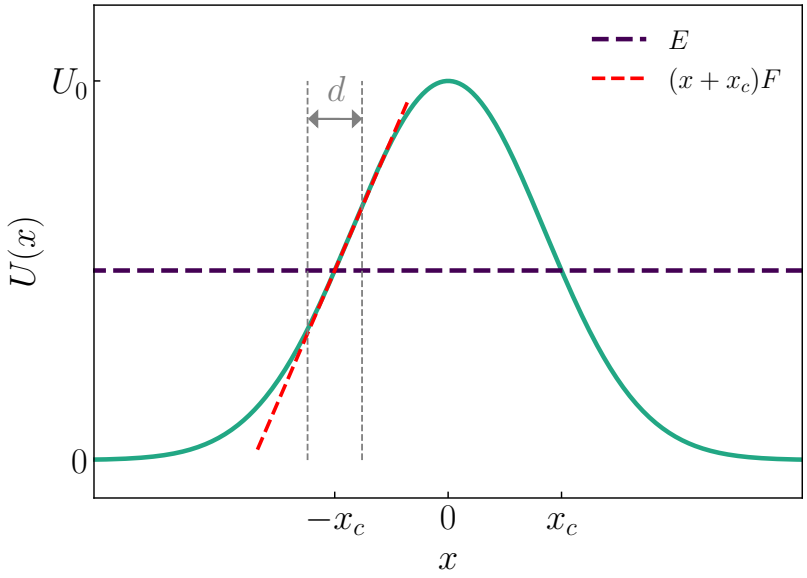

Figure 1.16: Schematics of the obstacle potential in green, both of large width σ and large amplitude U_0. A linear expansion is performed close to the classical turning points $-x_c$, such that $U - E \approx (x + x_c)F$ (in red). This approximation is valid on a layer of width d.

We assimilate our system to two reservoirs (called left and right) of typical energy E, but of different phases θ_{L} and θ_{R}, separated by the previously defined barrier. Given this phase difference between the two reservoirs, a current of particles is established through tunneling. It is defined in the Josephson approach as $j = j_c \sin(\theta_{\mathrm{R}} - \theta_{\mathrm{L}})$, with $j = i(\psi\partial_x\psi^* - \psi^*\partial_x\psi)/2$, and j_c being the critical current. This current j is proportional to the velocity through the relation $j = n(x)v(x) = v$ ($n_\infty = 1$ in our dimensionless units), so finding the critical current is equivalent to finding the critical velocity.

The calculation of the critical velocity in this approach will be two-fold. We first need to compute the total wavefunction of the system, which is composed of the wavefunction coming from each reservoir. Only then will it be possible to compute the critical velocity with the expression of the current in the Josephson approach. These calculations are exemplified for a nonlinear interaction potential of the form $\varepsilon(n) = n^\nu$, but remain quite similar for a saturable nonlinearity.

Calculation of the wavefunction As the system is considered superfluid, we start from the time-independent 1D Gross-Pitaevskii equation

$$-\frac{1}{2}\partial_x^2\psi + (U - E)\psi + \varepsilon\left(|\psi|^2\right)\psi = 0. \tag{1.54}$$

Let now $\pm x_c$ be the classical turning points, i.e. the boundaries of the obstacle such that $E = U(\pm x_c)$. In the following, we compute the left solution by working around $-x_c$, and the right solution is deduced by symmetry. A sketch of this is presented in Fig. 1.16. Close to that boundary, one can carry out a linear expansion of the obstacle such that locally $U(x) - E = (x + x_c)F$, as performed in [155], where F is the modulus of the external force $F = \partial_x U$ at $x = -x_c$. Equation (1.54) then transforms into

$$-\frac{1}{2}\partial_x^2\psi + (x + x_c)F\psi + \varepsilon\left(|\psi|^2\right)\psi = 0. \tag{1.55}$$

To further simplify it, we introduce another space variable $\chi = (x+x_c)/d$, such that $2Fd^3 = 1$, in which d is a typical thickness of the boundary. The new rescaled Gross-Pitaevskii equation

takes the form

$$-\partial_\chi^2\psi + \chi\psi + 2d^2\varepsilon\left(|\psi|^2\right)\psi = 0. \tag{1.56}$$

In the following, it is convenient to specify the expression of the nonlinear interactions. Let us explicitly treat the case of a powerlaw nonlinearity with $\varepsilon(n) = n^\nu$. With the rescaling $\psi = (2d^2)^{-\frac{1}{2\nu}}\phi$, Eq. (1.56) simplifies to

$$-\partial_\chi^2\phi + \chi\phi + \phi^{1+2\nu} = 0. \tag{1.57}$$

To solve this equation and obtain the wavefunction for a wide obstacle of large amplitude, we will need to make some approximations on the system. Depending on whether we treat the problem inside or outside of the barrier, different terms will be neglected.

- Classically allowed region: $U < E$

Outside the potential barrier, the gradients of the obstacle are so small that the kinetic term is much smaller than the interactions. One can use the Thomas-Fermi approximation, leading to the relation

$$\phi_{\text{out}} = (-\chi)^{\frac{1}{2\nu}}, \tag{1.58}$$

which, with the proper rescaling, transforms into

$$\psi_{\text{out}} = \left(-\frac{\chi}{2d^2}\right)^{\frac{1}{2\nu}} = (E - U(x))^{\frac{1}{2\nu}}. \tag{1.59}$$

- Classically forbidden region: $U > E$

Inside the barrier, the obstacle is so strong that the nonlinear term can be neglected, and Eq. (1.57) turns into the Airy equation, whose asymptotic solution is

$$\phi_{\text{in}} = \frac{A}{2\sqrt{\pi}\chi^{1/4}}\exp\left\{-\frac{2}{3}\chi^{3/2}\right\}, \tag{1.60}$$

with A a numerical constant. This is equivalent to using the WKB approximation [178] with $1/\sigma \to 0$ (instead of the usual $\hbar \to 0$), with the classical turning points satisfying $U(x) = E$. Using the same change of variable as before, this solution transforms into

$$\psi_{\text{in}} = \frac{A}{2\sqrt{\pi}d(2d^2)^{\frac{1}{2\nu}}}\frac{1}{[2(U-E)]^{\frac{1}{4}}}\exp\left\{-\sqrt{2}\int dx'\,\sqrt{(U-E)}\right\}. \tag{1.61}$$

One recovers the usual wavefunction obtained in the WKB approximation.

We now have two asymptotic limits for the solutions inside and outside the obstacle. In order to find the complete wavefunction, we numerically solve the dimensionless equation (1.57) using a RK4 algorithm. This can be seen in Fig. 1.17, on which is represented the numerical solution of the dimensionless wavefunction, as well as both asymptotic solutions. The value of A is numerically defined and comes from an ad hoc adjustment of ϕ_{in} in order to have the best fit possible with the numerical solution inside the obstacle.

The fact that the obstacle has both a large amplitude and width will have two consequences: First, the interactions between particles described by the nonlinear potential $\varepsilon(n)$ become negligible, simplifying the model. The left and right wavefunctions can then be approximated with the asymptotic expressions we found in the classically forbidden region[6] with

[6] Even if we do not use the previous results for the classically allowed region, they were necessary in order to compute the value of the constant A.

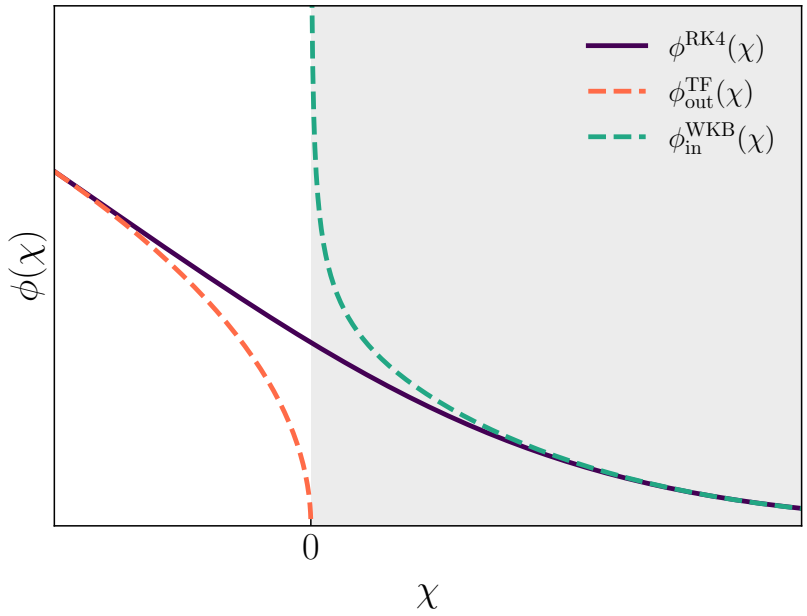

Figure 1.17: Rescaled left wavefunction as a function of the dimensionless variable χ for $\varepsilon(n) = n$. The orange (green) curve is the analytical solution obtained in the Thomas-Fermi (WKB) approximation to treat the problem outside (inside) the obstacle. The purple curve is the numerical solution of Eq. (1.57) obtained with a RK4 algorithm. A is chosen to yield the best fit possible with the numerical solution. The white zone corresponds to the classically allowed region, whereas the grey one is the forbidden region inside the obstacle.

the WKB approximation. Additionally, there is no overlap in the obstacle between the wavefunction of each reservoir, making it so that the total wavefunction is a linear combination of these two wavefunctions: It then reads $\psi = \psi_{\mathrm{R}} + \psi_{\mathrm{L}}$, with

$$\psi_{\mathrm{R}} = \frac{A}{2\sqrt{\pi d}(2d^2)^{\frac{1}{2\nu}}} \frac{1}{[2(U-E)]^{\frac{1}{4}}} \exp\left\{-\sqrt{2}\int_x^{x_c} dx' \sqrt{(U-E)}\right\} e^{i\theta_{\mathrm{R}}}, \tag{1.62a}$$

$$\psi_{\mathrm{L}} = \frac{A}{2\sqrt{\pi d}(2d^2)^{\frac{1}{2\nu}}} \frac{1}{[2(U-E)]^{\frac{1}{4}}} \exp\left\{-\sqrt{2}\int_{-x_c}^{x} dx' \sqrt{(U-E)}\right\} e^{i\theta_{\mathrm{L}}}. \tag{1.62b}$$

The prefactor highly depend on the parameters of the obstacle $U(x)$ and E, which are also hidden in the expression of d.

Now that we have an analytical expression for the wavefunction, it is possible to use the expression of the current in order to estimate the critical velocity for superfluidity. After calculation, one finds

$$j = \frac{A^2}{2\pi d(2d^2)^{\frac{1}{\nu}}} \exp\left\{-\sqrt{2}\int_{-x_c}^{x_c} dx' \sqrt{(U-E)}\right\} \sin(\theta_{\mathrm{R}} - \theta_{\mathrm{L}}), \tag{1.63}$$

and then

$$v_c = \frac{A^2}{2\pi d(2d^2)^{\frac{1}{\nu}}} \exp\left\{-\sqrt{2}\int_{-x_c}^{x_c} dx' \sqrt{(U-E)}\right\}. \tag{1.64}$$

This critical velocity is proportional to a nontrivial prefactor involving the parameters of the system, and the numerical parameter A, but the most important part is the exponential decay. The value of the critical velocity for superfluidity in the case of a wide obstacle of large amplitude is then exponentially small, and is ruled by the physics taking place on the tunnel path between the two classical turning points.

Case of a saturable nonlinearity For a saturable nonlinearity of the form $\varepsilon(n) = n/(n+n_{\rm sat})$ with $n_{\rm sat}$ the saturation intensity, the calculations are more tricky as the equivalent of Eq. (1.57) includes a nontrivial nonlinear form for the interaction potential

$$-\partial_\chi^2\phi + \chi\phi + \frac{\phi^3}{1+\phi^2/K} = 0, \tag{1.65a}$$

$$K = 2d^2\frac{(1+n_{\rm sat})^2}{n_{\rm sat}}. \tag{1.65b}$$

Nevertheless, an in-depth study of K shows that it scales as

$$\frac{(1+n_{\rm sat})^2}{n}\left[\sqrt{\frac{E}{\sigma}}\ln\frac{U}{E}\right]^{-\frac{4}{3}}. \tag{1.66}$$

Even for its minimum value for $n_{\rm sat} = 1$, K remains really large provided σ and U_0 are large. Equation (1.65a) then transforms into Eq. (1.57), and one can follow the same approach for the calculations as for $\varepsilon(n) = n$. This yields

$$v_c^{\rm sat} = \sqrt{n_{\rm sat}}v_c, \tag{1.67}$$

with v_c given by Eq. (1.64).

1.3.3 Obstacle of arbitrary width

So far, we have obtained analytical results in both limits $\sigma \ll 1$ and $\sigma \gg 1$. We now focus on the in-between case of obstacles of arbitrary width σ – which is not analytically solvable – and treat it numerically, allowing us to interpolate our previous limits.

To solve the stationary problem defined by Eq. (1.25), we treat it with a imaginary-time numerical method via a relaxation algorithm, which will then be studied for long evolution times. We start the integration with a solution that has the right asymptotic properties $n(x, \tau = 0) = 1$ and let it evolve in "time" through the following fictitious dynamical system

$$\partial_\tau n = \underbrace{\frac{1}{2}\frac{\partial_x^2\sqrt{n}}{\sqrt{n}}}_{QP[n]} + \underbrace{\frac{v_\infty^2}{2}\left(1-\frac{1}{n^2}\right) + \varepsilon(1) - \varepsilon(n)}_{\mathscr{U}[n]} - U(x), \tag{1.68}$$

with τ a fictitious-evolution numerical time. If the superfluid solution exists, it should be an attractor of Eq. (1.68), and if not, the system is not superfluid. The critical velocity is given by the value of v_∞ for which the algorithm does no longer converge towards an attractor with the correct boundary conditions at infinity.

Following the explicit Euler method with an unperturbed density profile as initial condition, this approach enables us to determine the density profile for specified values of U_0 and σ. Knowing $n(x)$, it is an easy task to derive v_c: The larger v_∞, the more depleted the density will be at the position of the obstacle, and the solution disappears when v_∞ exceeds v_c. This is represented in Fig. 1.18. The goal of our simulation is to find this v_c as a function of σ, for a given value of U_0 and various nonlinearities.

In the following, it becomes necessary to specify the shape of the obstacle, which we chose as a Gaussian obstacle $U(x) = U_0 e^{-x^2/\sigma^2}$. The numerical approach then allows us to obtain Fig. 1.19, in which all the different results are encompassed. It represents the critical velocity for superfluidity with respect to the width of the obstacle, for a given amplitude $U_0 = 0.5$. The blue and orange markers (squares, dots, crosses) stand respectively for $\varepsilon(n) = n$ and a saturable nonlinearity with $n_{\rm sat} \in \{0.1, 1, 10\}$, and the black dotted and dashed lines represent the analytical limits previously obtained for the limiting cases $\sigma \ll 1$ and $\sigma \gg 1$. These limits

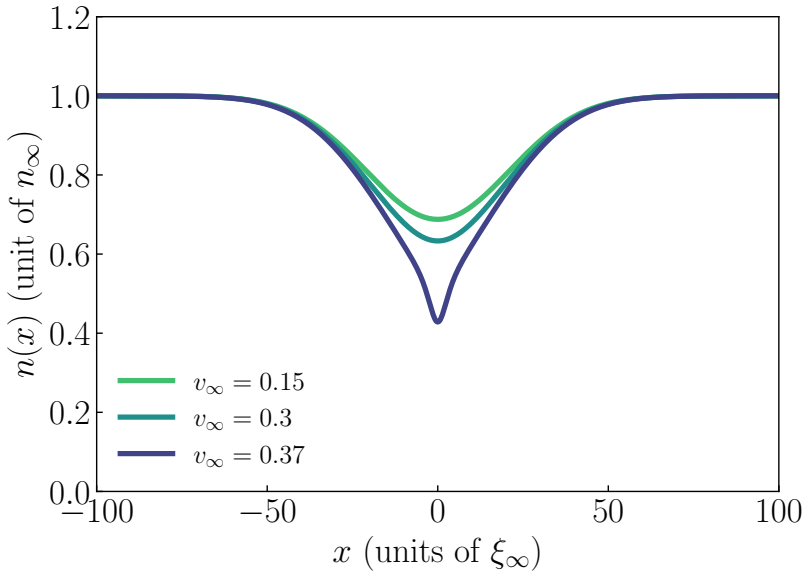

Figure 1.18: Density profiles obtained with our algorithm, for $\varepsilon(n) = n$, $U_0 = 0.3$, $\sigma = 30$ and different initial velocities $v_\infty \in \{0.15, 0.3, 0.37\}$. The larger the velocity, the more impacted the density profile around the obstacle. The solution disappears beyond $v_\infty = 0.37$, meaning that it is the critical velocity for superfluidity. Note that this is also the result obtained with the hydraulic approach for large obstacles.

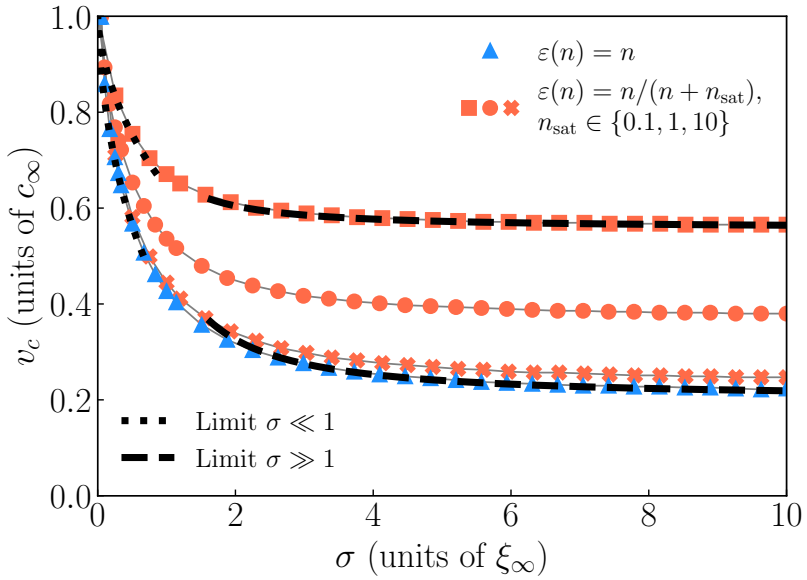

Figure 1.19: Critical velocity for superfluidity as a function of the width of the Gaussian obstacle $U(x) = U_0 \exp\{-x^2/\sigma^2\}$, for $U_0 = 0.5$. v_c is plotted for different expressions of $\varepsilon(n)$ as indicated in the legend. The asymptotic results previously obtained in the limits $\sigma \ll 1$ and $\sigma \gg 1$ are also included in black dotted and dashed lines, and are in agreement with the numerical simulation.

are in agreement with the numerical results obtained with our algorithm, which gives credit to the relaxation method used. For the sake of clarity, these limits are only represented for $\varepsilon(n) = n$ and $\varepsilon(n) = n/(n + n_{\rm sat})$ with $n_{\rm sat} = 0.1$, but it has been verified that the results for $n_{\rm sat} = 1$ and $n_{\rm sat} = 10$ are also in agreement with the numerics.

The critical velocity shows a monotonic behavior in σ between the two different limits of narrow and wide obstacles, going from $v_c = 1$ for $\sigma \to 0$, to the limit obtained in the hydraulic approximation for large values of σ. Surprisingly enough, these limits seem to be

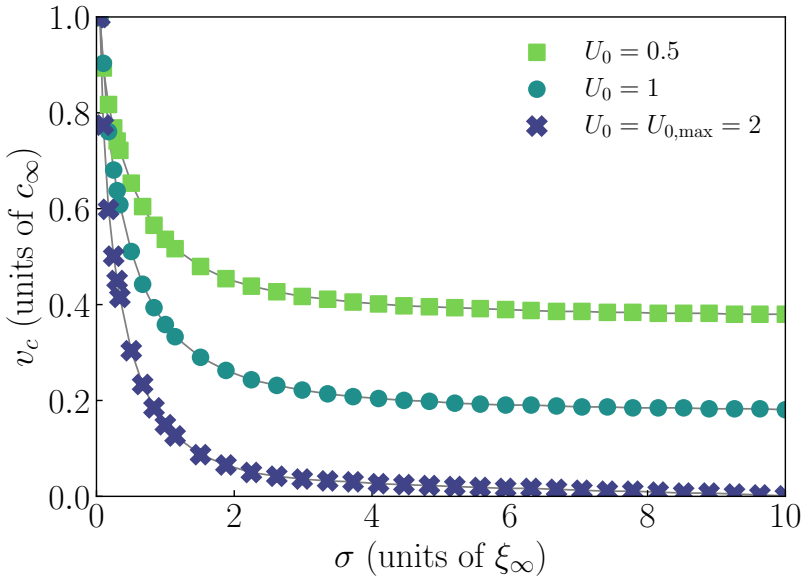

Figure 1.20: Critical velocity for superfluidity as a function of the width of the Gaussian obstacle $U(x) = U_0 \exp\{-x^2/\sigma^2\}$, for various $U_0 \in \{0.5, 1, 2\}$. v_c is plotted for $\varepsilon(n) = n/(n + n_{\rm sat})$ with $n_{\rm sat} = 1$. When $U_0 = U_{0,\max}$, v_c drops to zero for large values of σ. The Josephson treatment of the case $(\sigma, U_0) \gg 1$ is not represented here as the correction is exponentially small and would not be visible.

valid for almost the whole range of σ values, except between $\sigma \in [1, 2]$, in which case the numerical simulation links these asymptotic results. Note that in the limit $n_{\rm sat} \gg 1$, one recovers the results obtained for $\varepsilon(n) = n$, which makes sense as the saturable nonlinearity becomes proportional to the density if $n_{\rm sat} \gg 1$.

Figure 1.20 also represents the critical velocity as a function of σ for a Gaussian obstacle, a saturable nonlinearity with $n_{\rm sat} = 1$, but this time for various values of U_0 (see legend). When comparing the results for these different U_0, one can see that the higher the barrier, the lower v_c. The range of velocities for which it is possible to observe superfluidity then gets more and more restricted as U_0 increases. In the limit where U_0 is above its maximum value ($U_0 = U_{0,\max} = (1 + n_{\rm sat})/n_{\rm sat}$ for a saturable nonlinearity), superfluidity is broken, at least in the small gradients approximation. Even though the Josephson treatment for $\sigma \gg 1$ and $U_0 > U_{0,\max}$ shows that the critical velocity is not strictly null, in practice the result obtained for v_c is exponentially small and cannot be represented with the vertical scale used in Fig. 1.20.

All in all, these figures allow us to make the distinction between two different regimes of transport: The various curves represent separatrices between superfluid and nonsuperfluid regimes, and correspond to the disappearance of the stationary solutions of Eq. (1.25). In other words, for a given set of parameters (v_∞, σ, U_0), the system can either be superfluid (under the different curves), or nonstationary and not superfluid anymore (above it).

1.3.4 Treatment of the losses

So far, we have considered conservative systems. We are now interested in the effect of losses on the dynamics of the quantum fluid. The Gross-Pitaevskii equation describing the system becomes

$$i\partial_t\psi = \left[-\frac{1}{2}\partial_x^2 + U(x) + \varepsilon\left(|\psi|^2\right) - \frac{i\alpha}{2}\right]\psi, \tag{1.69}$$

with α representing the rate of the photonic absorption. The hydrodynamic Eqs. (1.8) will be consequently modified, especially Eq. (1.8b) which now acquires a negative source term:

$$\partial_t n + \partial_x (nv) = -\alpha n, \tag{1.70}$$

meaning that the number of particles is not conserved in the presence of particle losses. The critical velocity for superfluidity having a strong nontrivial dependence on $n(x)$, it will obviously be impacted. The treatment of losses might differ depending on the experimental setup, but they are usually unavoidable when dealing with quantum fluids of light, and have been shown to lower the critical velocity for superfluidity [56, 162, 163].

In the experiments described in [54, 55], photon absorption along the photorefractive crystal is described by linear homogeneous losses, and are estimated to represent about 30% of the initial light intensity after propagation through the crystal. Yet, superfluidity remains even with such losses. We chose to use an adiabatic treatment of the losses [43, 179] (which will be detailed further on), and compare it to the critical velocity obtained after a brute force numerical integration of the time-dependent Gross-Pitaevskii equation. Both approaches are detailed in the following paragraphs, with a comparison of their results.

Adiabatic approach

In this paragraph, we explain the adiabatic approximation we used to derive the critical velocity for superfluidity from the fictitious dynamical system depicted in Eq. (1.68). If the losses manifest on a time scale $1/\alpha$ much larger than any other time scale in the problem, it is reasonable to assume that the dynamics of the fluid must adiabatically follow the time variations of its unperturbed density, which decays exponentially as $n_\infty(t) = n_\infty(0)\exp\{-\alpha t\}$. This is equivalent to treat the fluid as if it were in a stationary state at each time t, and all the quantities used to define the dimensionless problem must be replaced with their instantaneous unperturbed counterparts derived from $n_\infty(t)$. The number of particles will then decrease in time because of the absorption, and as a result, all the other quantities will be modified. For $\varepsilon(n) = n$, one has:

- $c_\infty(t) = \sqrt{n_\infty(t)} = c_\infty(0)\exp\{-\alpha t/2\}$,
- $\mu_\infty(t) = n_\infty(t) = \mu_\infty(0)\exp\{-\alpha t\}$,
- $\xi_\infty(t) = \hbar/\sqrt{n_\infty(t)} = \xi_\infty(0)\exp\{\alpha t/2\}$.

As a consequence, the width and amplitude of the obstacle are also rescaled as

- $U_0/\mu_\infty(t) = U_0\exp\{\alpha t\}/\mu_\infty(0)$,
- $\sigma/\xi_\infty(t) = \sigma\exp\{-\alpha t/2\}/\xi_\infty(0)$.

In the end, the results will certainly strongly depend on the loss rate α, but also on the arbitrarily chosen integration time t.

Our adiabatic approach then amounts to compute v_c through the same algorithm as before, used in the absence of losses, but with rescaled values for U_0 and σ as we work with a given integration time t. We present results for $t = 75$ and $\alpha \in \{0, 0.002, 0.01\}$ (respectively in units of $\hbar/\mu_\infty(0)$ and $\mu_\infty(0)/\hbar$) and for $\varepsilon(n) = n$. For example when $\alpha = 0.01$ and $U_0/\mu_\infty(0) = 0.2$, the fictitious problem must be solved with the rescaled quantities $U_0/\mu_\infty(t) = 0.232$ and $\sigma/\xi_\infty(t) = 0.928\sigma/\xi_\infty(0)$. This leads to v_c as a function of σ, which is later represented in Fig. 1.22 in plain lines for values of $\alpha \in \{0, 0.002, 0.01\}$. This time integration $t = 75$, along with the chosen loss rates, corresponds to a situation of adiabatic transport and is in agreement with experiments of Ref. [54], as it amounts to losses around 30% of the initial light intensity after a propagation in the crystal for the largest value of α we considered here.

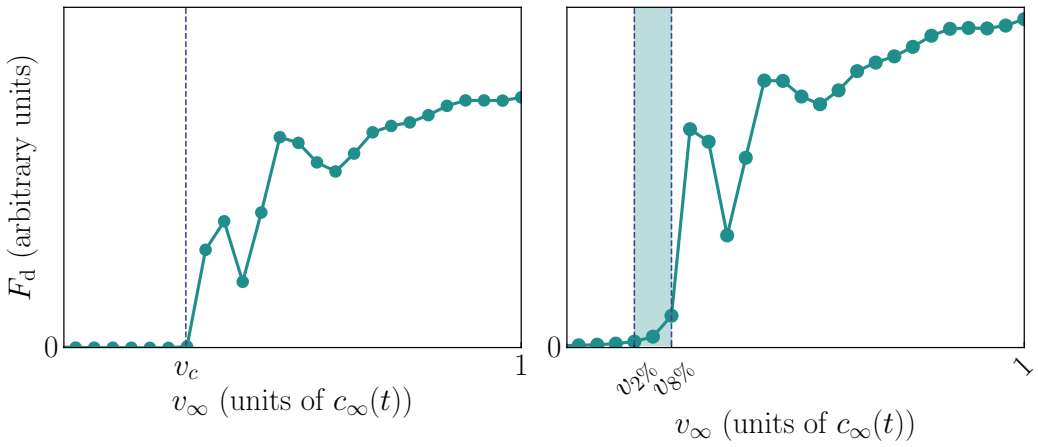

Figure 1.21: Computation of the instantaneous drag force F_d at the final evolution time $t = 75$, for a Gaussian obstacle of amplitude $U_0 = 0.2$, as a function of the injection velocity v_∞, both without and with losses (respectively left $\alpha = 0$ and right $\alpha = 0.001$). On the left panel, the critical velocity is well defined because the transition in the drag force is sharp. On the right panel, the losses blur the transition and v_c is hardly definable. We arbitrarily chose it to be around the velocity for which F_d amounts to 5% of its value at $v_\infty = c_\infty(t)$.

Numerical integration

Another method to obtain v_c is performed in the reference frame of the moving obstacle, obtained after the Galilean transformation $U(x,t) = U_0 \exp\{-(x + v_\infty t)^2/\sigma^2\}$, which is equivalent to the configuration studied so far. We numerically integrate the time-dependent Gross-Pitaevskii equation with such a moving obstacle, compute the drag force, and extract v_c from its behavior. Indeed, when F_d is null (or negligible) the system is superfluid, and superfluidity is broken when $F_d \neq 0$. The velocity at which this transition in the drag force occurs is v_c. We represent in Fig. 1.21 the instantaneous drag force at a given time t, which is sufficient to observe the superfluid-nonsuperfluid transition and deduce v_c from there. In practice, one would need to average several instantaneous measures over a sufficient integration time to obtain a "well-defined" drag force, thus getting rid of the the important variations from one point to the other.

In the configuration where losses are neglected, this transition is sharp and well defined: The drag force is null until $v_\infty = v_c$, and then it increases. On the other hand when losses are included, the situation is more complicated: The drag force is not zero even at small velocities, and assigning a value to the critical velocity is not possible anymore. The losses will smooth the transition, and the well-defined critical velocity transforms into a crossover zone [56, 162, 163] , going from a regime where the drag force is negligible to a regime of wave resistance, in which the drag force does impact the system. These two situations are roughly depicted in Fig. 1.21.

In order to have a good approximation of v_c in the presence of losses, we arbitrarily choose the superfluid crossover to occur around the value of v_∞ for which the drag force experienced by the obstacle corresponds to 5% of its value at $v_\infty = c_\infty(t)$ (the zone in which we gradually go from a superfluid to a nonsuperfluid regime occurs between $v_{2\%}$ and $v_{8\%}$ with our criterion). This yields a pretty good approximation for $v_c(\sigma)$ for a given value of U_0, which is depicted in Fig. 1.22 with different markers for the various loss rates $\alpha \in \{0, 0.002, 0.01\}$.

Comparison between the two approaches

In order to see if our use of the adiabatic approximation is relevant of not, we compare in Fig. 1.22 the critical velocities obtained either through the adiabatic approximation (plain

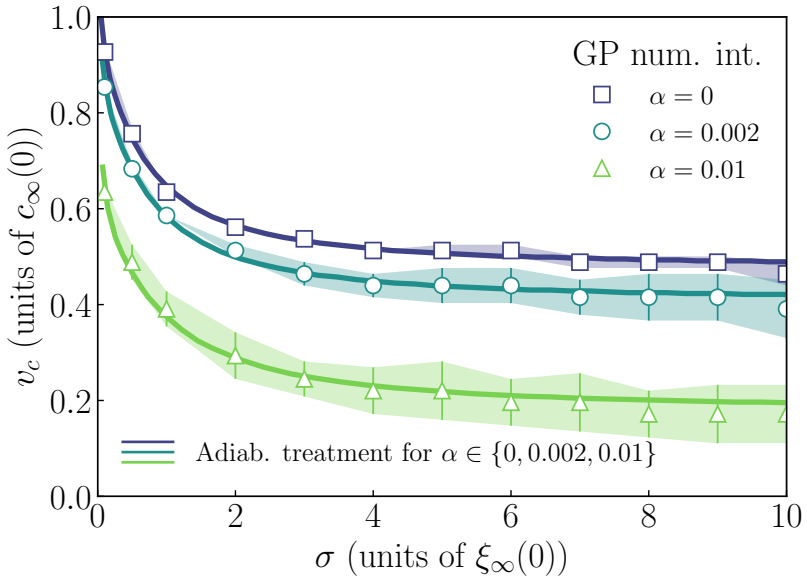

Figure 1.22: Critical velocity for superfluidity as a function of the width of the Gaussian obstacle $U(x) = U_0 \exp\{-x^2/\sigma^2\}$, for $\varepsilon(n) = n$, and in the presence of losses with rate $\alpha \in \{0, 0.002, 0.01\}$. The dimensionless propagation time is chosen to be $t = 75$, and the obstacle height without losses is $U_0/\mu_\infty(0) = 0.2$. The various markers correspond to the critical velocity obtained after the brute force numerical integration of the Gross-Pitaevskii equation with absorption. The critical velocity is now replaced by a crossover zone of given extension, accounting for the smoothness of the transition in the drag force experienced by the obstacle (for more explanations, see main text). The curves represent the critical velocity deduced from the numerical integration of Eq. (1.68) with our adiabatic approach.

lines), or through a computation of the drag force after the brute force numerical integration of the Gross-Pitaevskii equation (markers and shaded areas). Note that in addition to the drag force, we also computed the density profile in order to validate the crossover zone we found, to see if excitations were emitted or not. These critical velocities are represented in Fig. 1.22, both for an integration time of $t = 75$ and the values of the loss rate previously provided.

As we can see, the agreement between the shaded areas and the curves obtained after numerical integration of the out-of-equilibrium problem in the adiabatic evolution approximation is excellent. This adiabatic approach is then valid (at least for the small values of α we used), and allowed us to account for an analytical description of the dissipation induced by the absorption of the media in which the fluid propagates. It is interesting to note that this treatment of the losses in the adiabatic evolution approximation is valid in any dimension D, and thus also applies to the bidimensional case discussed in Chap. 3. Consequently, the approach will not be reiterated in subsequent chapters to avoid redundancy.

1.4 Conclusion

This chapter was dedicated to the determination of the critical velocity for superfluidity v_c of a generic quantum fluid encountering a localized obstacle, for which we obtained an analytical expression as a function of the parameters of the obstacle (i.e. its width σ and amplitude U_0). This was done within the framework of the 1D Gross-Pitaevskii equation. The results we obtained are several-fold, and go beyond the Landau criterion, which validity is restricted to the perturbative regime, by working with obstacles of arbitrary amplitudes. Our study extends beyond the conventional one-dimensional Gross-Pitaevskii equation, allowing us to

treat various types of quantum fluids described by different expression for the nonlinear interaction potential. Most of our results are exemplified for the usual nonlinearity $\varepsilon(n) = n$, and for a saturable nonlinearity characteristic of superfluids of light in saturable media, which is relevant for ongoing experiments on hot atomic vapors or photorefractive nonlinear crystals.

We derive analytical results for the critical velocity for superfluidity in the limiting cases of narrow and wide obstacles, which were tackled with diverse approaches, for other nonlinearities than the usual $\varepsilon(n) = n$. In addition, these limits were numerically interpolated by addressing the case of obstacles of arbitrary widths with an original algorithm treating the problem as a fictitious dynamical system. This yields results consistent with the previously derived analytical limits, providing a complete description of $v_c(\sigma)$ for a given amplitude U_0. Lastly, we also go beyond previous works by incorporating losses effect in our theoretical model, and obtained accurate results for the critical velocity for systems subject to losses through an adiabatic approach.

Interestingly, our theoretical model also exhibits the existence of another family of stationary solutions for the Gross-Pitaevskii equation, but meeting different criteria than our requirements for superfluidity (notably, the density profile is now perturbed close to the obstacle). This heralds the existence of another important separatrix, this time in the supersonic regime, which characterizes the transition between a nonstationary and a stationary regime. The next logical step would then be to continue the study in one dimension, derive this separatrix and characterize the other types of stationary transport existing for velocities higher than the critical velocity for superfluidity. This is the subject of Chap. 2. In addition, a few perspectives on the one-dimensional case will be addressed in the general conclusion.

Chapter 2

One-dimensional stationary transport at supersonic velocities

Sommaire

This second chapter is dedicated to the study of another regime of transport for quantum fluids in one dimension, which is also stationary, but does not exhibit superfluid characteristics, as stated by the presence of a nonzero drag force. We focus on the properties of this regime at velocities much larger than the speed of sound, and characterize the critical supersonic velocity v_s marking the separation between this regime and the nonstationary turbulent regime. Unexpectedly, this regime exhibits a possible superfluid-like behavior for given sets of parameters (U_0, v_∞), but only for attractive obstacles. This is linked to the presence of resonances in the transmission spectrum of the system, for which we provide a complete study. We also characterize this other stationary regime via an exact calculation of the drag force for narrow obstacles, obtaining results going beyond previous studies.

Article linked to the chapter:

J. Huynh, F. Hébert, P.-É. Larré and M. Albert, "Stationary transport above the critical velocity in a one-dimensional superflow past an obstacle" – EPL **143**, 46005, (2023)

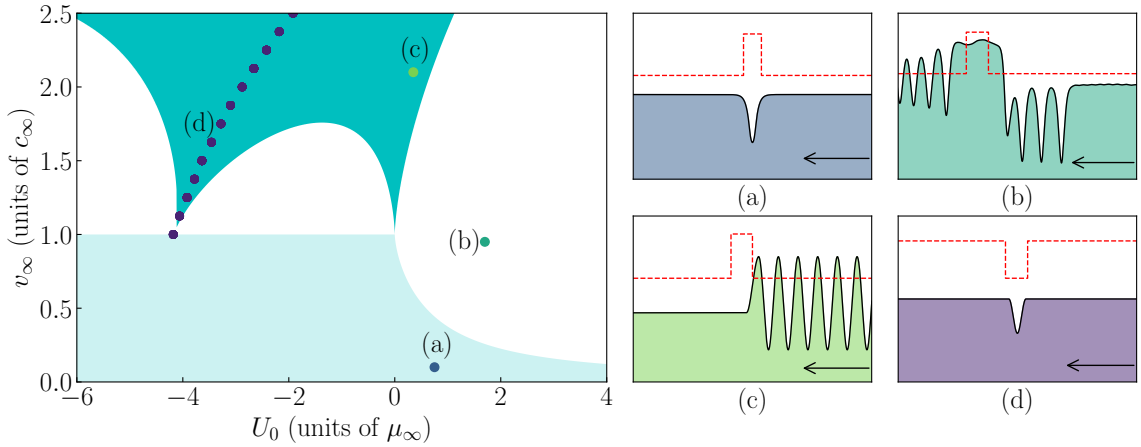

Figure 2.1: Typical phase diagram of the possible stationary flows in the presence of a localized obstacle (represented in red in the insets), as a function of the injection velocity v_∞ and the amplitude of the obstacle U_0. The asymptotic flow is here from right to left, as depicted by the left-pointing arrows in panels (a-d). The different regimes range from superfluid (light blue), to nonstationary nonsuperfluid (white), to stationary nonsuperfluid (dark blue). The dotted curve in the left panel corresponds to the set of parameters (U_0, v_∞) leading to a superfluid-like solution in the supersonic phase. Panels (a), (b), (c) and (d) represent the density profiles $n(x)$ associated with each point in the main figure, and were obtained after a numerical simulation with $\varepsilon(n) = n$ and for a rectangular obstacle potential, as represented in red dashed line in panels (a–d).

The transport properties described by the Gross-Pitaevskii equation (1.1) are much richer than only the superfluid behavior presented in Chap. 1: Three different regimes of transport are indeed possible for a quantum fluid moving at velocity v_∞ across an obstacle – all along this chapter, the asymptotic flow is from right to left (see Fig. 2.1) – and the determination of whether the system is in one regime or another highly depends on the parameters of said obstacle. These regimes are represented in Fig. 2.1, along with the associated density profiles corresponding to each point (a), (b), (c) and (d). Chapter 1 focuses on what happens below the critical velocity for superfluidity v_c, showing that the flow is stationary and only perturbed close to the obstacle: This is the superfluid regime, presented in Fig. 2.1 (a). When the velocity is higher than v_c, two different regimes can take place, neither being superfluid.

- At velocities slightly above v_c, the flow is no longer stationary, and one can observe the repeated emission of nonlinear excitations [52, 55, 69, 180] such as solitons. This situation is depicted in Fig. 2.1 (b), where the quantum fluid is partially reflected and transmitted by the obstacle, leading to the appearance of nonlinear structures in both directions. Superfluidity is thus broken, and quantum turbulence may potentially arise for extreme parameters [95, 104–107].

- When the velocity of the obstacle exceeds yet another threshold, referred to as the supersonic separatrix v_s in this manuscript [52, 108, 109], the fluid enters a new regime of stationary transport. In this regime, the kinetic energy is so high compared to the interaction energy that the dynamics could almost be described by the linear Schrödinger equation: Part of the fluid is transmitted through or reflected by the obstacle. This creates a standing wave with a density modulation upstream, as shown in Fig. 2.1 (c). In our case, the fluid moves from right to left past an obstacle at $x = 0$, so that the perturbation appears upstream in the positive$-x$ region of space.

  Interestingly, the possibility of perfect transmission remains due to resonant transport [110–112]. There indeed exists a given set of parameters (U_0, v_∞) for which backscattering is suppressed, as shown in Fig. 2.1 (d). Even if this dynamics mimics the superfluid

regime [113], it remains however debatable to say whether it is truly superfluid or not, as it occurs at supersonic velocities.

While several of the results presented in this chapter were already discussed in Ref. [52], we re-derive them with different methods and provide explicit expressions for concrete cases, relevant for experimental studies of transport properties of quantum fluids described by a generalized Gross-Pitaevskii equation. We thus provide the reader with a comprehensive study, yielding a clear map of the different possible regimes of transport for a quantum fluid.

While Chap. 1 treated the superfluid regime (light blue in Fig. 2.1), the present chapter particularly deals with the supersonic stationary regime (dark blue), for which the analytical treatment does not entirely deviate from the methods used in Chap. 1. We thus obtain exact analytical expressions for the supersonic separatrix v_s for different obstacle parameters and fluid velocities. We again derive asymptotic results for various nonlinear interaction potentials, for obstacles of characteristic width either much smaller or much larger than the healing length, and for both positive and negative amplitudes this time. A focus is shed on the case of attractive obstacles, which exhibit resonances and the possibility for a regime of perfect transport at these supersonic velocities. We numerically and analytically characterize these resonances for a toy model consisting in a supersonic flow of a lossless Gross-Pitaevskii quantum fluid with $\varepsilon(n) = n$, past a square-well obstacle potential of arbitrary depth and width.

2.1 A Hamiltonian-like formulation

The system we consider in this chapter is the exact same as in Chap. 1, to the exception that the velocity of the fluid is now supersonic, i.e. $v_\infty > c_\infty$, leading to another regime of stationary transport. In our model, the dynamics of the system is also ruled by the Gross-Pitaevskii equation (1.1) for the order parameter ψ, but we do not take particle losses into account in this chapter. The considered obstacles will also mostly be Gaussian obstacles, though we will illustrate the phenomenon of resonances in Sec. 2.5 for attractive obstacles through a simpler model consisting of a squared obstacle $U(x) = U_0\Theta(\sigma/2 - |x|)$, for which tractable analytical results are possible. Both types of obstacles have a single extremum U_0 (positive or negative) at $x = 0$, and are localized such that $U(x)$ vanishes for $|x| \gg \sigma$, with σ the typical range of the obstacle. While small quantitative differences will obviously arise between the study of these two obstacles, the transport through a square well is qualitatively similar to that observed in the more realistic (from an experimental point of view) case of a Gaussian obstacle.

A hydrodynamic description of the problem is again obtained through the Madelung representation $\psi(x,t) = A(x)e^{i\phi(x)}e^{-i\mu_\infty t}$, with $n(x) = A(x)^2$ the local density, $v(x) = \partial_x\phi$ the local velocity and μ_∞ the energy of the stationary state. From this description, the Gross-Pitaevskii equation transforms into an imaginary and a real part, yielding the system

$$n(x)v(x) = j, \tag{2.1a}$$

$$\partial_x^2 A = 2\left[U(x) + \varepsilon(n) + \frac{j^2}{2A^4} - \mu_\infty\right]A. \tag{2.1b}$$

As previously explained in Sec. 1.2, the radiation condition [157] imposes the boundary conditions of the system: The density profile $n(x)$ must remain unperturbed downstream ($x \to -\infty$ in our case, since the fluid flows from right to left) with density n_∞ and velocity v_∞ (and thus a current $j = n_\infty v_\infty$), and the perturbation occurs upstream. This is different from the superfluid case, in which the fluid needed to remain unperturbed everywhere but at the vicinity of the obstacle. This asymptotic condition at $x \to -\infty$ imposes $\partial_x A = 0$ at this point, defining a typical energy scale $\mu_\infty = \varepsilon(1) + v_\infty^2/2$.

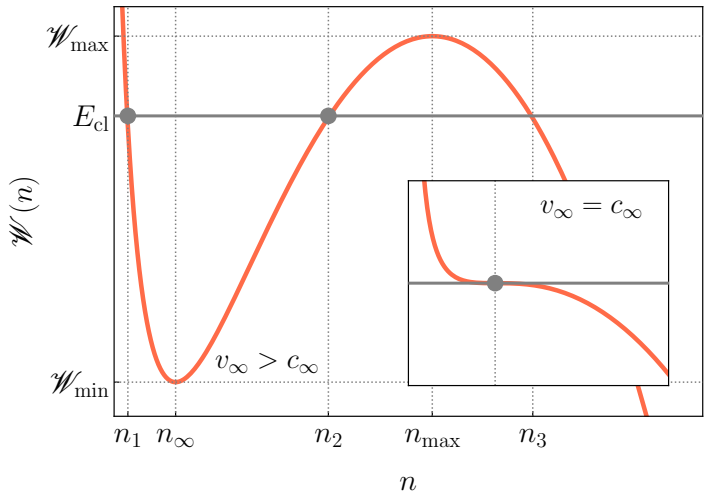

Figure 2.2: Schematic behavior of the fictitious potential $\mathscr{W}(n)$ as a function of n for $v_\infty > c_\infty$, and $\varepsilon(n) = n$. When the fictitious particle has an energy $E_{\rm cl}$, the density of the fluid will oscillate between n_1 and n_2. The inset displays the special case $v_\infty = c_\infty$, in which case the fictitious particle is at rest if its energy is that of the saddle-point.

Interestingly enough, this can be rephrased in terms of a Hamilton-like problem describing the dynamics of a fictitious classical particle of position $A(x) = \sqrt{n(x)}$ and momentum $p(x) = \partial_x A(x)$ at effective time x [52, 181]. The equation of motion of the system given by Eq. (2.1b) arises from the Hamilton-like equations of motion

$$\partial_x A = \partial_p \mathscr{H}, \tag{2.2a}$$

$$\partial_x p = -\partial_A \mathscr{H}, \tag{2.2b}$$

with the associated Hamiltonian

$$\mathscr{H}(A,p) = \frac{p^2}{2} + \mathscr{W}(A^2) - U(x)A^2, \tag{2.3}$$

and the fictitious potential

$$\mathscr{W}(A^2 = n) = \frac{v_\infty^2}{2}\left(n + \frac{1}{n}\right) + n\varepsilon(1) - \mathcal{E}(n), \tag{2.4}$$

with $\mathcal{E}(n) = \int dn\, \varepsilon(n)$. The typical shape of the fictitious potential $\mathscr{W}(n)$, conditioned by the values of the chemical potential μ_∞ and the flux j, is depicted in Fig. 2.2 for $\varepsilon(n) = n$ and $v_\infty \geqslant c_\infty$. It is usually such that $\lim_{n\to 0} \mathscr{W}(n) = +\infty$ and $\lim_{n\to+\infty} \mathscr{W}(n) = -\infty$, with a local minimum $\mathscr{W}_{\min}$ (maximum $\mathscr{W}_{\max}$) obtained for $n_\infty = 1$ ($n_{\max} > 1$). The solutions $A(x)$ of the Hamiltonian problem then coincide with "classical" trajectories in the potential $\mathscr{W}(n)$, with corresponding energy $E_{\rm cl}$.

This grey box is crucial for the comprehension of Chap. 2, as our study relies on a classical approach to solving a wave problem. We encourage the reader to keep in mind that, in the fictitious particle picture, $A(x)$ is the equivalent of the position and x of the effective time.

In some configurations (viz. for a saturable nonlinearity) the local maximum $\mathscr{W}_{\max}$ vanishes. This obviously impacts the determination of v_s, but does not prevent the system from entering this stationary regime. The only requirement is that the fictitious potential always admit a local minimum.

How to determine v_s?

In the absence of an external potential, the Hamiltonian given by Eq. (2.3) is time-independent and the energy $E_{\rm cl}$ of the classical particle is conserved. The free solutions of the Gross-Pitaevskii equation can be obtained from the possible trajectories of the classical particle in the potential $\mathscr{W}(A^2 = n)$. One can then obtain an analytical expression for the supersonic separatrix v_s by solving the Hamilton equations with the energy $E_{\rm cl}$ associated with the considered obstacle.
As long as $\mathscr{W}_{\rm min} < E_{\rm cl} < \mathscr{W}_{\rm max}$, the particle will oscillate in $\mathscr{W}(n)$: This is the supersonic stationary regime. This is no longer the case if $E_{\rm cl} < \mathscr{W}_{\rm min}$ or $E_{\rm cl} > \mathscr{W}_{\rm max}$ because the particle would not be trapped anymore and the density could take any possible value: The dynamics is no longer stationary, and excitations are continuously generated. The boundary between these two cases is by definition given by the supersonic separatrix v_s, and corresponds to the last stationary solution, linking a nonstationary regime to a stationary one as shown in Fig. 2.1. The supersonic separatrix v_s is then characterized by $E_{\rm cl} = \mathscr{W}_{\rm max}$.

What happens for weak obstacles?

When $U(x) = 0$, solutions with $E_{\rm cl} = \mathscr{W}_{\rm min}$ or $E_{\rm cl} = \mathscr{W}_{\rm max}$ (i.e. $n = n_\infty$ or $n = n_{\rm max}$) correspond respectively to the supersonic and the subsonic superfluid solutions. As v_∞ approaches c_∞, these two critical velocities v_s and v_c merge and become identical and equal to the speed of sound c_∞, as shown in Fig. 2.1 for $U_0 = 0$. This is linked to the structure of the fictitious potential $\mathscr{W}(n)$, that now exhibits a saddle-point for $v_\infty = c_\infty$ (see the inset of Fig. 2.2). The presence of a weak obstacle with $U_0 \ll 1$ will not alter the structure of this saddle-node bifurcation, but will instead trigger the instability. This bifurcation between two behaviors can be seen in Fig. 2.1 for $U_0 \ll 1$.

Density profile

In the presence of a scattering potential $U(x)$, the density profile of the quantum fluid in the supersonic stationary regime is linked to the shape of the fictitious potential $\mathscr{W}(n)$, and exhibits the presence of nonlinear waves upstream. Classically speaking, the dynamics of the particle inside this potential is as follows: It starts unperturbed at $x = -\infty$ (where $U(x) = 0$) with density $n_\infty = 1$ ($A(-\infty) = 1$), and experiences a kick of energy when meeting the obstacle. Its energy then goes from $\mathscr{W}_{\rm min}$ to $E_{\rm cl}$, and the particle oscillates between n_1 and n_2 (the first two solutions of $\mathscr{W}(n) = E_{\rm cl}$) after this encounter. Graphically, the "particle" will evolve on the orange line between the two grey dots represented in Fig. 2.2. Concerning the density profile, this means that between $x = -\infty$ and the obstacle, the flow is unperturbed, and $n(x)$ is a (possibly nonlinear) wave oscillating between n_1 and n_2 upstream. This situation is roughly depicted in the inset (c) of Fig. 2.1.

As in Chap. 1, the aim of this chapter is to obtain a complete phase diagram representing the supersonic separatrix v_s as a function of the parameters of the obstacle inside the fluid (either the amplitude, or the width). To do so, we first derive analytical results in the two opposite limits of narrow and wide obstacles, which are then interpolated by a numerical simulation of the Gross-Pitaevskii equation.

2.2 Narrow obstacle

The study of narrow obstacles will be twofold: We will first derive the analytical expression of the supersonic separatrix v_s, and then provide the full calculations leading to the expression of the drag force for obstacles of arbitrary amplitudes, going beyond previous results obtained in the perturbative regime. The results obtained in this section for v_s and the drag force, put together with those of Sec. 1.3.1, will provide a complete vision of the different existing stationary regimes for the system in the presence of a narrow obstacle.

2.2.1 Supersonic separatrix

In a similar fashion to what has been derived in Sec. 1.3.1 (see also Refs. [45, 47, 52]), we treat the case of a narrow obstacle by replacing it with a $\delta-$peak obstacle of amplitude $U_0F(\sigma)$ such that $U(x) = U_0F(\sigma)\delta(x)$, with $F(\sigma) = \sigma$ being the integral of $\Theta(\sigma/2 - |x|)$ over the whole real axis. One can then obtain an analytical expression for the supersonic separatrix by searching for the solutions of Eq. (2.1b) (which is actually the same as Eq. (1.26)). The same approach is employed by separating the integration space into different parts: downstream ($x < 0$), $x = 0$, and upstream ($x > 0$).

- Downstream ($x < 0$): Because of the radiation condition [157], the density perturbation is null everywhere for $x < 0$, and the density profile is flat.
- At $x = 0$, one obtains the same condition on the derivative given by Eq. (1.27), except that $\partial_x n(0^-) = 0$. This condition can be simplified to [52]

$$\partial_x n(0^+) = 4n_0U_0F(\sigma) \tag{2.5}$$

- Upstream ($x > 0$): We obtain

$$\frac{(\partial_x n)^2}{8n} + \mathscr{W}(n) = E_{\mathrm{cl},\delta}, \tag{2.6}$$

with $E_{\mathrm{cl},\delta} = 2U_0^2F^2(\sigma) + v_\infty^2 + \varepsilon(1) - \mathcal{E}(1)$ defined thanks to the condition (2.5) with $n_0 = 1$. From this, it is now possible to obtain an analytical expression for the supersonic separatrix v_s. Several methods can be employed, and are detailed in the following paragraphs.

Method 1: Graphical resolution

The first method we present to obtain v_s from Eq. (2.6) is basically the same employed as in Chap. 1, and is based on a study of the fictitious potential $\mathscr{W}(n)$ displayed in Fig. 2.2. The procedure is as follows

- Obtain $n_{\max}(v_s)$ through $\partial_n\mathscr{W}(n_{\max}) = 0$.
- Inject $n_{\max}(v_s)$ into $\mathscr{W}(n)$ to obtain $\mathscr{W}_{\max}$.
- Solve $E_{\mathrm{cl},\delta}(v_s) = \mathscr{W}_{\max}$.

In the end, this method yields an implicit relation for the supersonic separatrix as a function of the amplitude $\lambda = U_0 F(\sigma)$ of the $\delta-$peaked obstacle

$$|\lambda| = \frac{1}{\sqrt{2}}\left[\frac{v_s^2}{2}\left(\sqrt{n_{\max}(v_s)} - \frac{1}{\sqrt{n_{\max}(v_s)}}\right)^2 + \varepsilon(1)[n_{\max}(v_s) - 1] + \mathcal{E}(1) - \mathcal{E}(n_{\max}(v_s))\right]^{\frac{1}{2}}. \quad (2.7)$$

It is important to note that Eq. (2.7) is valid no matter the sign of $\lambda = U_0 F(\sigma)$, meaning that the supersonic separatrix will be the same whether the obstacle is attractive or repulsive. This symmetry[1] is a peculiarity of the $\delta-$peak model, and will be broken as σ increases, or in other words, when the velocity of the flow is large enough so that the associated de Broglie wavelength is small enough to resolve the details of the potential. This will notably lead to the appearance of resonances for v_s, and will be the object of Sec. 2.5.

Exact analytical results can be derived from this method when specifying the expression of the nonlinear interaction potential. For example, for $\varepsilon(n) = n$, one has

$$n_{\max}(v_s) = \frac{v_s^2 + v_s\sqrt{v_s^2 + 8}}{4}, \quad (2.8)$$

which leads to the implicit relation for v_s [52]

$$|\lambda| = \frac{\sqrt{v_s(v_s^2+8)^{3/2} + v_s^4 - 20v_s^2 - 8}}{4\sqrt{2}}. \quad (2.9)$$

The derivation is however more complex when looking at a more complicated nonlinearity such as the saturable one, for which $\varepsilon(n) = n/(n + n_{\text{sat}})$. In the latter case, it is still possible to obtain $n_{\max}$ analytically:

$$n_{\max}(v_s) = \frac{v_s^2(1+n_{\text{sat}}) + v_s\sqrt{8n_{\text{sat}}(1+n_{\text{sat}}) + v_s^2(1-n_{\text{sat}})^2}}{2(2 + 2n_{\text{sat}} - v_s^2)}, \quad (2.10)$$

but the last step, i.e. the resolution of $E_{\text{cl},\delta} = \mathscr{W}_{\max}$, has to be performed numerically to obtain v_s. These results are encompassed in Fig. 2.3, in which v_s is represented as a function of the amplitude of the $\delta-$peak for the nonlinearities indicated in the legend. As Eq. (2.9) involves the absolute value of the amplitude of the $\delta-$peak, the supersonic separatrix v_s is an even function of $\lambda \lessgtr 0$.

One can see that although $\varepsilon(n) = n$ is supposed to be a limiting case of the saturable nonlinearity when $n_{\text{sat}} \gg 1$, important deviations can be observed between the blue and orange dotted curves. As a matter of fact, for saturable systems, the potential $\mathscr{W}(n)$ may be such that it has no local maximum depending on the value of n_{sat}, leading to the saturation of v_s at large $U_0 F(\sigma)$. This saturation is all the more quickly reached as the saturation intensity n_{sat} is low (see, e.g., the $n_{\text{sat}} = 0.1$ curve in Fig. 2.3). Figure 2.4 displays the corresponding fictitious potential $\mathscr{W}(n)$ for this precise value of n_{sat}. One can see that for velocities lower than $v_\infty = \sqrt{2 + 2n_{\text{sat}}}$, the fictitious potential $\mathscr{W}(n)$ has the same behavior as for $\varepsilon(n) = n$ (i.e it goes to $-\infty$ as $n \to +\infty$). However, when the injection velocity exceeds that threshold, $\mathscr{W}(n)$ has no local maximum anymore, and the fictitious particle is always trapped no matter its energy. It will then always oscillate around the minimum of $\mathscr{W}(n)$, and all the solutions

[1] Symmetry not present for the critical velocity for superfluidity v_c, as it is always equal to the speed of sound for attractive obstacles.

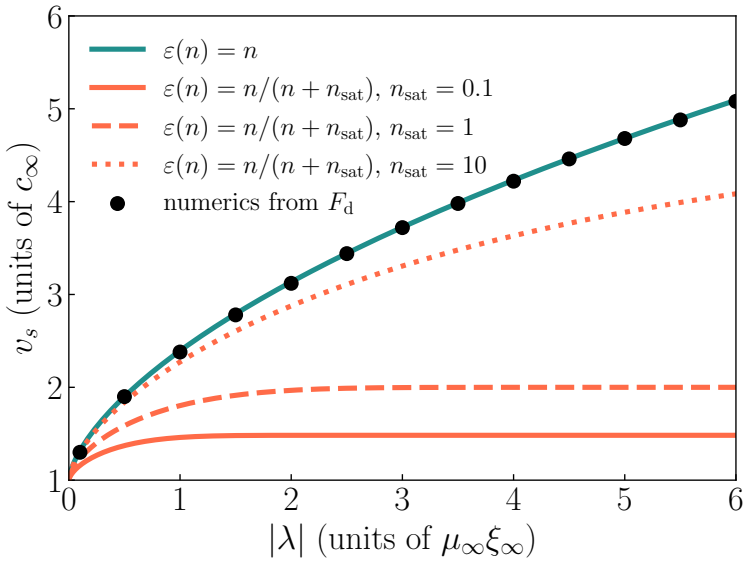

Figure 2.3: Supersonic separatrix v_s as a function of the absolute value of the amplitude of a $\delta-$peak. These results are shown for various nonlinearities, as indicated in the legend. The curves are the analytical results we obtained, whereas the black dots come from a numerical simulation, and correspond to the value of the velocity for which the drag force (in the stationary regime) becomes nonzero, for given values of $|\lambda|$.

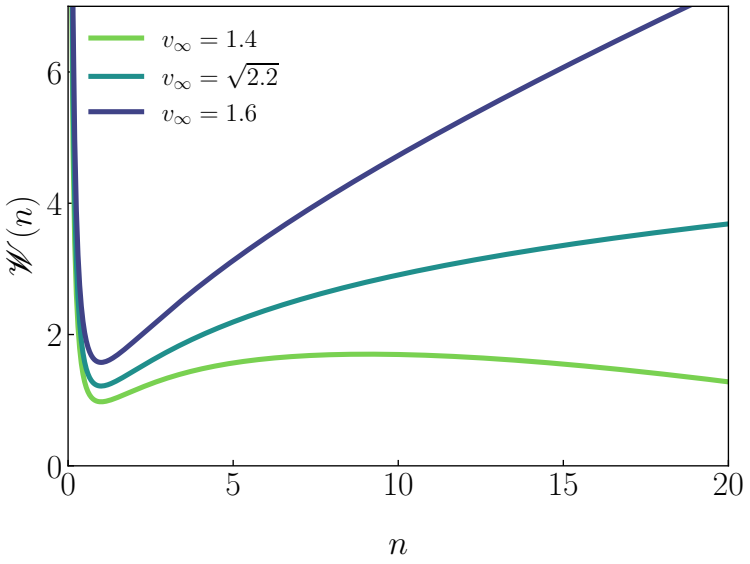

Figure 2.4: Fictitious potential $\mathscr{W}(n)$ for a saturable nonlinearity with $n_{\rm sat} = 0.1$. The various colors represent this potential for different values of $v_\infty \in \{1.4, \sqrt{2.2}, 1.6\}$. These three velocities lead each to different cases: For $v_\infty = 1.4$, the fictitious potential behaves as the one for $\varepsilon(n) = n$; whereas for $v_\infty = 1.6$, it has no local maximum anymore. The value separating these two cases is $v_\infty = \sqrt{2 + 2n_{\rm sat}} = \sqrt{2.2}$, which is the saturation value of v_s as can be seen in Fig. 2.3 in plain orange line.

for $n_{\rm sat}$ satisfying this condition are stationary. This notably translates into the saturation of v_s at large values of $|U_0 F(\sigma)|$, explaining the plateaux seen in Fig. 2.3 for $n_{\rm sat} = 0.1$ and $n_{\rm sat} = 1$, with respective values of $v_s = \sqrt{2.2}$ and $v_s = 2$ (note that there also exists a plateau for $n_{\rm sat} = 10$ at $v_s = \sqrt{22}$, which is not displayed here, as it happens at larger $|U_0|$).

Method 2: The "polynomial way" for a powerlaw nonlinearity $\varepsilon(n) = n^\nu/\nu$, $\nu \in \mathbb{N}$

As previously explained, the solutions of Eq. (2.6) are fixed by the condition $\mathscr{W}(n_{\max}) = E_{\mathrm{cl},\delta}$, which admits i roots. These roots $0 \leq n_1 \leq n_2 \leq \cdots \leq n_i$ are solutions of

$$2n\mathcal{E}(n) - 2n^2\mu_\infty + 2nE_{\mathrm{cl},\delta} - v_\infty^2 = 0, \tag{2.11}$$

with $\mu_\infty = v_\infty^2/2 + \varepsilon(1)$ and $E_{\mathrm{cl},\delta} = 2\lambda^2 + v_\infty^2 + \varepsilon(1) - \mathcal{E}(1)$. These i roots must be real for the regime to be stationary, and, as a result, the discriminant of Eq. (2.11) must be positive. This imposes a condition on the value of $U_0F(\sigma)$, and this is what defines the supersonic separatrix v_s.

To solve Eq. (2.11), it is convenient to work with a nonlinearity $\varepsilon(n)$ whose antiderivative $\mathcal{E}(n)$ is expressed as an integer-valued polynomial. For example for a powerlaw nonlinearity, one gets $\mathcal{E}(n) = n^{1+\nu}/(\nu + \nu^2)$ and in that case Eq. (2.11) is a polynomial $P(n)$ of degree $2 + \nu$

$$P(n) = an^{2+\nu} + bn^2 + cn + d = 0, \tag{2.12}$$

with the coefficients

$$a = \frac{2}{\nu(1+\nu)}, \tag{2.13a}$$

$$b = -\left(v_\infty^2 + \frac{2}{\nu}\right), \tag{2.13b}$$

$$c = 2v_\infty^2 + 4\lambda^2 + \frac{2}{1+\nu}, \tag{2.13c}$$

$$d = -v_\infty^2. \tag{2.13d}$$

Finally, the supersonic separatrix is implicitly given by the condition on the discriminant of Eq. (2.12)

$$\Delta_P = \frac{\nu(1+\nu)}{2}(-1)^{\frac{(2+\nu)(1+\nu)}{2}}\mathrm{Res}_n(P, \partial_n P) > 0, \tag{2.14}$$

with $\mathrm{Res}_n(P, \partial_n P)$ being the resultant of $P(n)$ and $\partial_n P(n)$, i.e. the determinant of their Sylvester matrix $S_{P,\partial_n P}$ [182], whose size is $(3 + 2\nu) \times (3 + 2\nu)$.

Results for $\nu = 1$: We test this method for $\varepsilon(n) = n$, and verify if these results are in accordance with the ones obtained with the previous method. The polynomial given by Eq. (2.11) is now

$$P(n) = n^3 - \left(v_\infty^2 + 2\right)n^2 + \left(2v_\infty^2 + 4\lambda^2 + 1\right)n - v_\infty^2 = 0, \tag{2.15}$$

which is the same as Eq. (A12) from [183]. It is of order 3 and its derivative is of order 2, meaning that the Sylvester matrix associated with these two polynomials is of size 5×5, and reads

$$S_{P,\partial_n P} = \begin{pmatrix} 1 & b & c & d & 0 \\ 0 & 1 & b & c & d \\ d & 0 & 1 & b & c \\ 3 & 2b & c & 0 & 0 \\ 0 & 3 & 2b & c & 0 \end{pmatrix}. \tag{2.16}$$

Its discriminant, given by Eq. (2.14), reads

$$\Delta_P = -16\left\{16\lambda^6 + \left(-v_\infty^4 + 20v_\infty^2 + 8\right)\lambda^4 - (v_\infty^2 - 1)^3\lambda^2\right\} > 0. \tag{2.17}$$

This equation has 6 solutions for λ, among which two are null, two are purely imaginary, and two are real and with opposite signs. When plotting Eq. (2.17) in Fig. 2.5 for an arbitrary

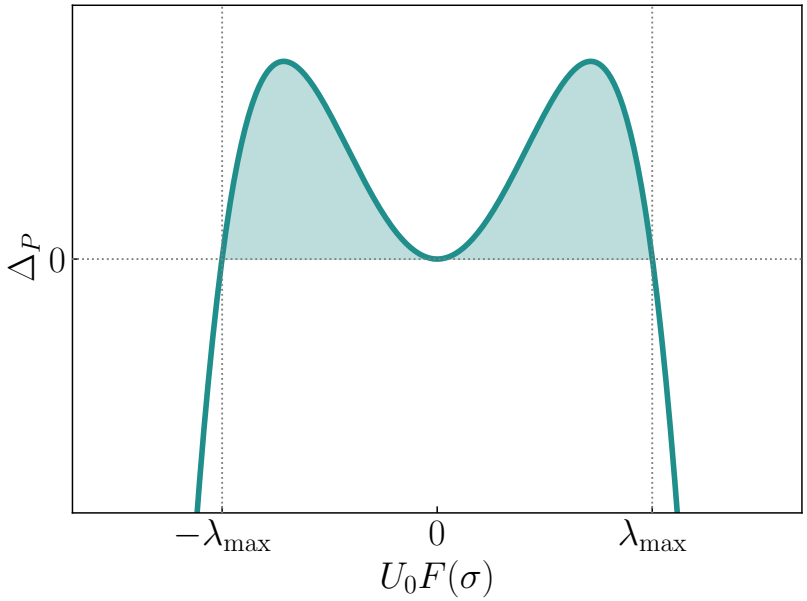

Figure 2.5: Typical discriminant Δ_P as defined by Eq. (2.17), for $v_\infty > c_\infty$. The shaded area corresponds to the domain of validity of the equation $\Delta_P > 0$. The supersonic separatrix is defined by the last value of $U_0F(\sigma)$ for which $\Delta_P > 0$, i.e. $\pm\lambda_{\max}$.

value $v_\infty > c_\infty$, one can realize that this condition is satisfied provided $|\lambda| \in [0, \lambda_{\max}]$. In the end, the supersonic separatrix is defined by $|\lambda| = \lambda_{\max}$, whose expression is found to be

$$|\lambda| = \frac{\sqrt{v_s(v_s^2+8)^{3/2} + v_s^4 - 20v_s^2 - 8}}{4\sqrt{2}}. \tag{2.18}$$

This is the exact same expression that was obtained with the previous method.

The concepts behind this more mathematical method might seem easier to grasp than those of the previous section, but this method also has its limitations. Its ingenuity lies on the fact that by choosing a powerlaw nonlinearity, one is left with only a polynomial. In addition to that, it is not necessary to solve it, only to obtain its discriminant[2]. In theory, it would then be possible to solve the problem for any powerlaw nonlinearity, even though the resolution gets harder because of the size of the Sylvester matrix. However, the advantage of this method is also its main drawback: It only stands for a powerlaw nonlinearity with ν an integer. Some systems of interest described by a powerlaw nonlinearity but with a noninteger ν (refer to the TOOLBOX in the introduction) are thus not described by this method. Treating the case of the saturable nonlinearity is also not feasible since we would not have a polynomial to solve.

Method 3: A numerical v_s from the calculation of the drag force

Another way to obtain the supersonic separatrix v_s is to compute the drag force experienced by the obstacle as a function of the injection velocity $v_\infty > c_\infty$, and to extract from these data the first value of v_∞ for which this drag force admits a well-defined stationary expression. Even though the calculations are much more complicated as the drag force is a highly non-trivial function of the amplitude of the obstacle, it remains possible to numerically determine this limit. Detailed calculations are provided in Sec. 2.2.2 for $\varepsilon(n) = n$, and the supersonic separatrix v_s computed from the drag force is represented in Fig. 2.3 in black markers for several values of $\lambda = U_0F(\sigma)$. The results provided via this method are in perfect accordance with previous results obtained with methods 1 and 2.

[2]This is quite convenient as so far, only polynomials only up to degree 4 have known analytical solutions.

2.2.2 Exact expression for the drag force

While many studies to determine the drag force in weakly interacting quantum fluids have been led [47, 57, 156, 184, 185], these results rely on the linear-response theory and then only treat the case of obstacles of small amplitudes. This yields a single critical velocity (the Landau critical speed), separating two stationary regimes of transport: A superfluid one with zero drag, and a regime of wave resistance with a nonzero drag (see Chap. 1).

In this section, we provide the full calculations leading to the analytical expression of the drag force in the stationary supersonic regime for a repulsive $\delta-$shaped obstacle of arbitrary amplitude $\lambda = U_0 F(\sigma)$, and for $\varepsilon(n) = n$. We recall the expression of the drag force exerted by the fluid onto the obstacle, as provided in Chap. 1

$$F_{\mathrm{d}} = \int_{-\infty}^{+\infty} dx\, n(x,t)\partial_x U(x). \tag{2.19}$$

Based on this, a natural way to compute it[3] is to first derive the density profile, and the calculations are then pretty straightforward given the simplicity of the obstacle. It yields, as shown in this section, a highly nontrivial function of the parameters of the system.

We remind that in the perturbative regime (i.e. when the amplitude of the obstacle is really small compared to the chemical potential) – as already demonstrated in Sec. 1.2 – the drag force is a Heaviside step function for a $\delta-$shaped obstacle [47, 57, 163], and its value for $v_\infty > c_\infty$ is $F_{\mathrm{d,pert.}} = 2\lambda^2$. In this section, we improve this result by going beyond the limits imposed by the linear-response theory.

Calculation of the density

The first step to obtain the expression of the drag force from Eq. (2.19) is to derive the exact expression of the density $n(x)$. For a $\delta-$peak obstacle, this density profile differs a lot depending on the considered position x. The radiation condition imposes that the wake must be located upstream, where the density is highly perturbed and exhibits the presence of nonlinear waves. On the other hand, the fluid is unperturbed downstream. We remind the equation to obtain the upstream density of the quantum fluid in the presence of a $\delta-$peak obstacle, provided at the beginning of the chapter

$$\frac{(\partial_x n)^2}{8n} + \mathscr{W}(n) = E_{\mathrm{cl},\delta}, \tag{2.20}$$

with $\mathscr{W}(n) = \frac{v_\infty^2}{2}\left(n + \frac{1}{n}\right) + n - \frac{n^2}{2}$ and $E_{\mathrm{cl},\delta} = 2\lambda^2 + v_\infty^2 + 1/2$ for $\varepsilon(n) = n$. The equation $\mathscr{W}(n) = E_{\mathrm{cl},\delta}$ admitting three roots $0 < n_1 < n_2 < n_3$ (see Fig. 2.2), one can re-express Eq. (2.20) as

$$\left(\frac{\partial_x n}{2}\right)^2 = n^3 - 2n^2\mu_\infty + 2nE_{\mathrm{cl},\delta} - v_\infty^2 = (n-n_1)(n-n_2)(n-n_3), \tag{2.21}$$

with

$$\mu_\infty = \frac{n_1+n_2+n_3}{2} = \frac{v_\infty^2}{2} + 1, \tag{2.22a}$$

$$E_{\mathrm{cl},\delta} = \frac{n_1n_2 + n_1n_3 + n_2n_3}{2}, \tag{2.22b}$$

$$v_\infty^2 = n_1n_2n_3. \tag{2.22c}$$

One can recover the values of n_1, n_2 and n_3 as functions of λ and v_∞, which, in the end, are the only unknown parameters here. We search for bounded solutions of Eq. (2.21), as we

[3] Note that it is also possible to compute the drag force through the stress tensor (see [47, 163]).

know that the density in the stationary supersonic regime will necessarily oscillate between n_1 and n_2 (see Fig. 2.2). This equation, derived from the Gross-Pitaevskii equation, admits spatially periodic stationary solutions which were first studied by Tsuzuki [186], Korteweg and de Vries [187]: They are called "cnoidal waves" because they can be expressed in terms of the Jacobi elliptic cosine function. The density profile then takes this form, and reads [188]

$$n(x) = n_1 \cos^2\left[\phi(x)\right] + n_2 \sin^2\left[\phi(x)\right], \tag{2.23}$$

which leads to

$$\partial_x n = (n_2 - n_1) \sin\left[2\phi(x)\right] \frac{d\phi}{dx}. \tag{2.24}$$

Combining Eqs. (2.23) and (2.24) in Eq. (2.21), one then obtains

$$\partial_x n = (n_2 - n_1) \sin\left[2\phi(x)\right] \sqrt{\frac{(n_2 - n_1)\cos\left[2\phi(x)\right] + 2n_3 - n_1 - n_2}{2}}, \tag{2.25}$$

and so by identification,

$$\frac{d\phi}{dx} = \sqrt{\frac{(n_2 - n_1)\cos\left[2\phi(x)\right] + 2n_3 - n_1 - n_2}{2}}. \tag{2.26}$$

The solution for the phase is given by the Jacobi amplitude [189]

$$\phi(x) = \mathrm{am}\left[\sqrt{n_3 - n_1}x + \mathrm{C}, k\right], \tag{2.27a}$$

$$k = \frac{n_2 - n_1}{n_3 - n_1} \in [0, 1[, \tag{2.27b}$$

leading to the density profile [188]

$$n(x) = n_1 + (n_2 - n_1)\,\mathrm{sn}^2\left[\sqrt{n_3 - n_1}x + \mathrm{C}, k\right]. \tag{2.28}$$

Here $\mathrm{sn}\left[x, k\right] = \sin\left[\mathrm{am}(x, k)\right]$ is the Jacobi elliptic sine function, and C a constant chosen to match the density on either side of the obstacle. One finds that $\mathrm{C} = -\mathrm{K}/2$, with

$$\mathrm{K} = \int_0^1 \frac{dt}{\sqrt{1 - t^2}\sqrt{1 - kt^2}}, \tag{2.29}$$

where the period of the $\mathrm{sn}\left[x, k\right]$ function is 4K [190]. This density profile in the supersonic regime is a cnoidal-wave solution, and is represented in Fig. 2.6.

Calculation of the drag force

Once we have the density profile, it is pretty straightforward to compute the drag force from its expression, with a $\delta-$peaked obstacle $U(x) = \lambda\delta(x)$, and the expression of the density profile previously provided in Eq. (2.28) with n_1, n_2 and n_3 being functions of λ and v_∞.

However, as this expression for the density is valid in the stationary supersonic regime only, the input velocity v_∞ must be larger than the supersonic separatrix $v_s(\lambda)$ implicitly given by Eq. (2.9). In the end, the only free parameter in the problem is the amplitude λ of the obstacle.

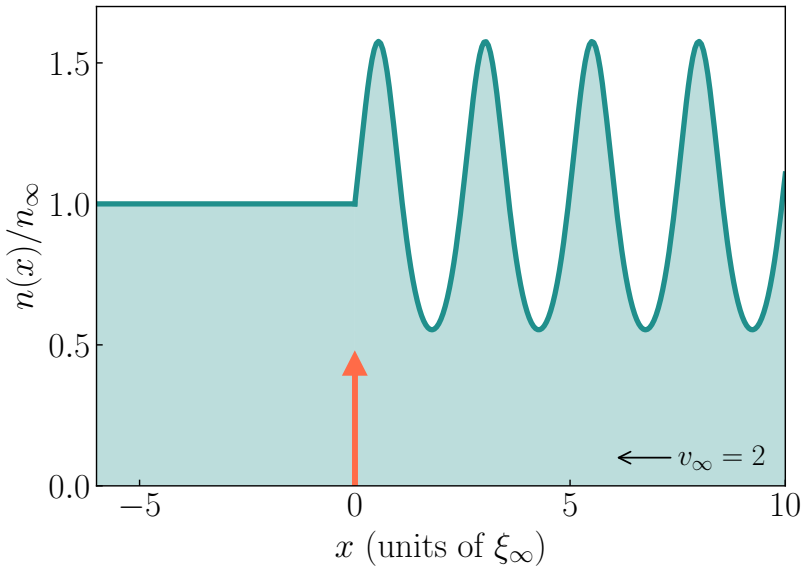

Figure 2.6: Density profile $n(x)/n_\infty$ in the supersonic regime for a $\delta-$peak obstacle of amplitude $\lambda = 0.5$. As imposed by the radiation condition, cnoidal waves given by Eq. (2.28) are emitted upstream, whereas the density profile is flat downstream.

The calculation of the drag force leads to

$$F_{\rm d}(x) = \lambda(n_2 - n_1)\sqrt{n_3 - n_1}\,\mathrm{cn}\left[-\frac{\mathrm{K}}{2}, k\right]\mathrm{sn}\left[-\frac{\mathrm{K}}{2}, k\right]\mathrm{dn}\left[-\frac{\mathrm{K}}{2}, k\right], \tag{2.30}$$

valid for

$$|\lambda| < \frac{\sqrt{v_s(v_s^2+8)^{3/2} + v_s^4 - 20v_s^2 - 8}}{4\sqrt{2}}, \tag{2.31}$$

with $\mathrm{cn}\,[x,k]$, $\mathrm{sn}\,[x,k]$ and $\mathrm{dn}\,[x,k]$ being respectively the Jacobi elliptic cosine, Jacobi elliptic sine and the Jacobi delta amplitude. Equation (2.30) provides a simple explicit expression for the drag force experienced by a point-like obstacle immersed in a stationary supersonic 1D quantum flow. To the best of our knowledge, this has not been explicited yet in the literature on quantum transport.

We represent this drag force in Fig. 2.7 (normalized by $2\lambda^2$, its constant value at supersonic speeds obtained in Chap. 1 within the linear-response theory) for several amplitudes $\lambda \in \{0.1, 1, 2, 4\}$ as a function of the input velocity v_∞, and for $\varepsilon(n) = n$. These results give credit to the drag force obtained in the perturbation theory as one can see that as the amplitude of the obstacle decreases, the supersonic separatrix tends to Landau's critical speed ($v_s/c_\infty \to 1$), and the drag force above this velocity threshold tends to the result of the linear-response theory, i.e. $F_{\rm d}/2\lambda^2 \to 1$.

A larger amplitude λ will shift the maximum of the drag force towards higher values of v_∞, which is logical as the higher the amplitude of the obstacle, the higher the supersonic separatrix. Based on these results, one can recover the curve of the supersonic separatrix as a function of the amplitude λ by looking at the values v_∞ for which Eq. (2.30) (defined in the stationary regime) exists, for a given value of λ. The simulation for various amplitudes of obstacle permits to reconstruct the curve of $v_s(\lambda)$ (see the black dots in Fig. 2.3), which is in perfect agreement with the theoretical expression for v_s provided by Eq. (2.9), giving credit to our analytical expression for the drag force.

Another consequence of an increasing λ is that the maximum value of the drag force will

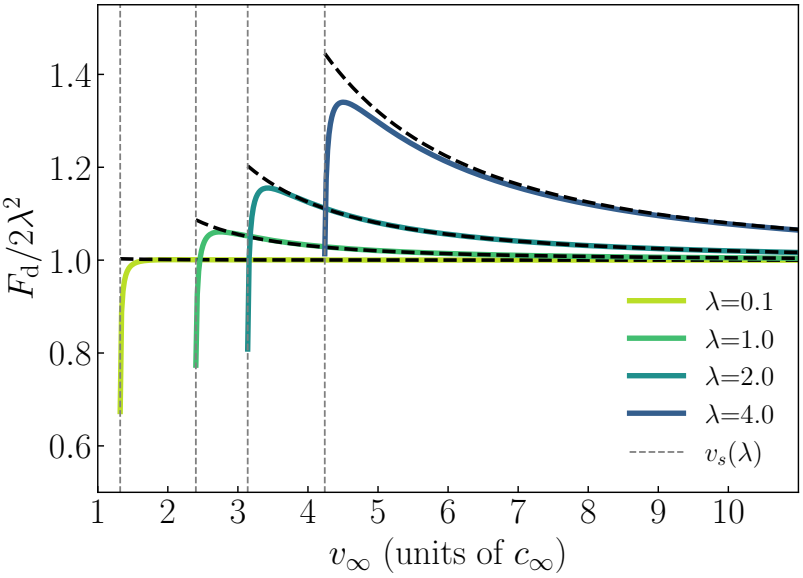

Figure 2.7: Drag force F_d rescaled by its perturbative value $F_{d,pert.} = 2\lambda^2$ as a function of the injection velocity v_∞, for different amplitudes $\lambda \in \{0.1, 1, 2, 4\}$. The black dashed lines represent the asymptotic limit for $v_\infty \gg 1$, but remain valid for intermediate velocities. The higher λ, the higher the maximum of the drag force and the velocity for which the drag force starts. This velocity is represented in grey dashed line for each value of λ, and corresponds to the supersonic separatrix v_s.

also increase. Concerning the algebraic decrease at large velocity, an asymptotic development of Eq. (2.30) for $v_\infty \gg 1$ shows that

$$F_d = 2\lambda^2 + \frac{\lambda^4}{v_\infty^2} = F_{d,pert.}\left[1 + \frac{1}{2}\left(\frac{\lambda}{v_\infty}\right)^2\right]. \tag{2.32}$$

This is represented in black dashed lines in Fig. 2.7, and yields a really good fit to represent the decreasing portion of the drag force. The resistance is thus larger for an obstacle of large amplitude than a perturbative one, explaining the bump in the drag force for velocities slightly above v_s. At high velocity, the kinetic energy possibly exceeds the barrier and the obstacle is less and less perceived, making the perturbative treatment relevant. The drag force then decreases to its value $F_d = F_{d,pert.}$ obtained in the linear-response theory.

Summary

To conclude this section on the drag force for $\delta-$shaped obstacles of arbitrary amplitudes λ, we gather all the results we have concerning v_c, v_s and F_d and plot them together. These results are encompassed in Fig. 2.8, and are presented for given amplitudes of obstacle ($\lambda = 1$ in the top row, and $\lambda = 4$ in the bottom row). The left column represents the phase diagram (λ, v_∞) with the different separatrices: The critical velocity for superfluidity v_c (Eq. (1.34)) for $v_\infty < 1$, and the supersonic separatrix v_s (Eq. (2.9)) for $v_\infty > 1$. The right column corresponds to the associated rescaled drag force given by Eq. (2.30). It admits different behaviors depending on the regime, which are as follows:

- In the stationary subsonic regime, the drag force is found to be null as long as $v_\infty < v_c$: This characterizes a superfluid flow, as detailed in Chap. 1.
- In the stationary supersonic regime (for $v_\infty > v_s$), the analytical expression of F_d is given by Eq. (2.30). The drag force suddenly increases for $v_\infty = v_s(\lambda)$, and reaches its maximum close to this value. The way it decreases is then dictated by Eq. (2.32), until

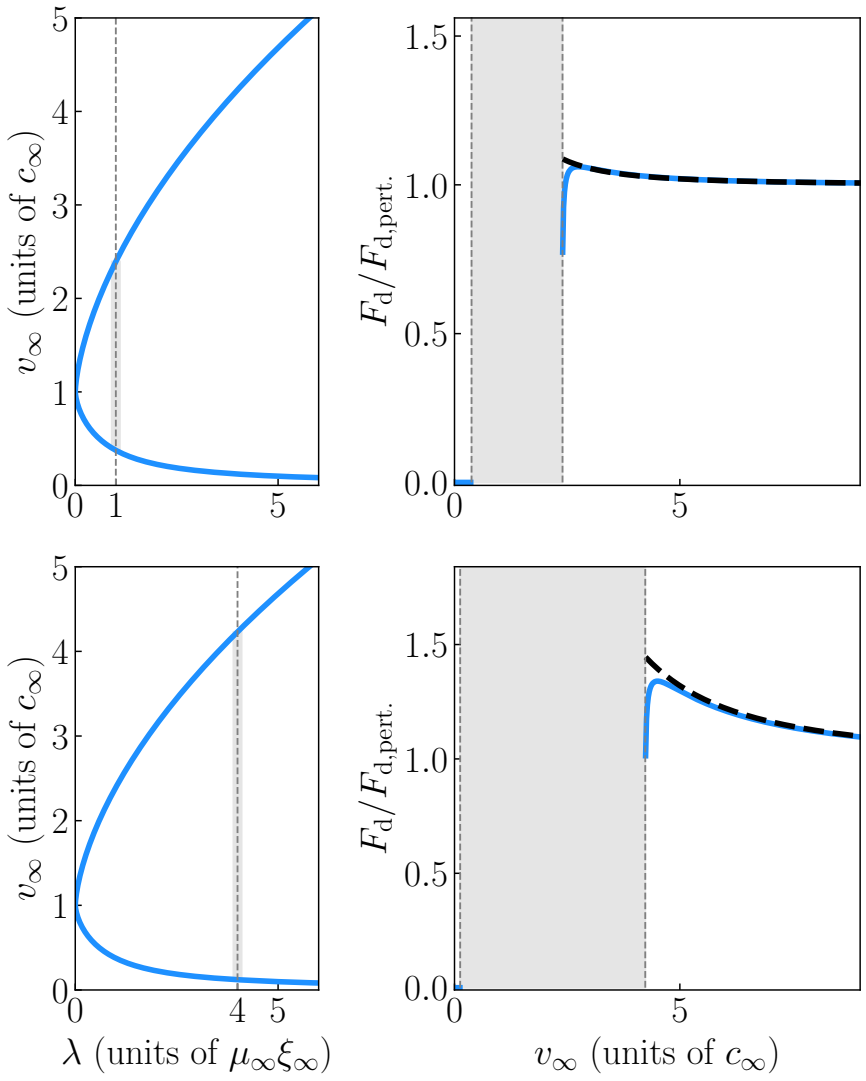

Figure 2.8: Left column: Phase diagram (λ, v_∞) with the subsonic and supersonic separatrices respectively for $v_\infty < 1$ and $v_\infty > 1$. Right column: Drag force as a function of the injection velocity, with the asymptotic limit for $v_\infty \gg 1$ in black dashed lines. The grey area is the nonstationary regime. The two rows both stand respectively for $\lambda = 1$ and $\lambda = 4$.

it reaches a constant value for $v_\infty \gg 1$ – the value obtained in the perturbative regime: $F_\mathrm{d,pert.} = 2\lambda^2$.

- What about the nonstationary regime for velocities between v_c and v_s? In that case, the system displays a complicated time-dependent evolution associated with a quasiperiodic nucleation of nonlinear excitations such as solitons in the present 1D setting, and the expression for the drag force provided in Eq. (2.30) is not valid anymore as it relies on stationary solutions. In this intermediate regime, the drag force fluctuates a lot but can be evaluated numerically in average, over a large integration time so as to capture a large number of dissipative events, as performed in Ref. [47] in 1D, or Ref. [183] in 2D. This nonstationary regime is represented by the shaded grey area in Fig. 2.8, and one can see that the higher λ, the bigger the gap created by the nonstationary regime in the drag force.

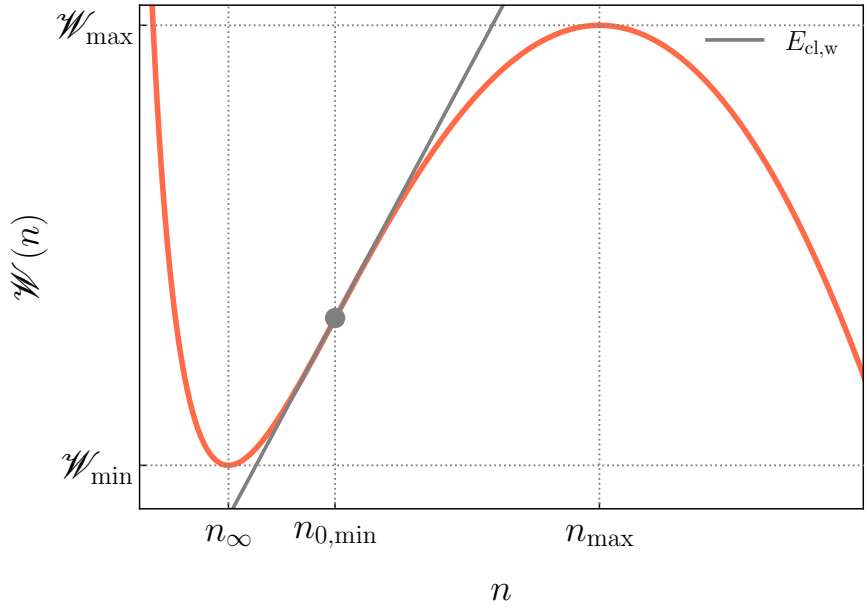

Figure 2.9: Schematic behavior of the fictitious potential $\mathscr{W}(n)$ as a function of n for $v_\infty > c_\infty$ and $\varepsilon(n) = n$, obtained in the Hamiltonian approach. The classical energy of the fictitious particle in the wide obstacle regime is not constant anymore, and $n_{0,\min}$ corresponds to the inflection point of $\mathscr{W}(n)$.

2.3 Wide obstacle

Back to the supersonic separatrix, we now derive results in the case of wide obstacles such that $\sigma \gg 1$. This can be done within both frameworks of the Hamiltonian approach provided in the previous section, or even the method used in Sec. 1.3.2.

Method 1: Using the Hamiltonian formulation

The Hamiltonian approach in terms of the fictitious particle in the potential $\mathscr{W}(n)$ is still valid for a wide obstacle. In that case, the fictitious particle would adiabatically follow the slow variations of the effective potential $\mathscr{W}_U(n) := \mathscr{W}(n) - U(x)n$, and would remain at its minimum as long as it exists. It is then only a matter of finding the saddle-node of the equation, which yields $n_{0,\min}$, and inserting it in Eq. (2.34), thus obtaining $v_{s,0}(U_0)$. This time, the only difference is that $E_{\mathrm{cl,w}} = U_0 n_{0,\min} + \mathrm{C}$.

Graphically speaking, v_s is obtained for the values of (U_0, C) such that $E_{\mathrm{cl,w}}$ is tangent to the fictitious potential $\mathscr{W}(n)$ at its inflection point $n_{0,\min}$, as represented in Fig. 2.9. The procedure to obtain v_s is the following

- Define the inflection point $n_{0,\min}$ through the condition $\partial_x^2 \mathscr{W}(n_{0,\min}) = 0$.
- Solve $E_{\mathrm{cl,w}}(v_s) = \mathscr{W}(n_{0,\min})$.

Method 2: The hydraulic approximation

We momentarily leave the Hamilton formulation of the problem, and go back to the method used in Sec. 1.3.2: We perform a series expansion of the obstacle in powers of the width σ, such that $U(x) = U_0 - |\partial_x^2 U_0| x^2/2\sigma^2$, and first treat the hydraulic case of the flat obstacle following the same method.

The stationary equation to solve is then given by the fictitious potential $\mathscr{V}(n_0, v_\infty) = U_0$ defined in Eq. (1.42), and represented in Fig. 2.10. This equation admits two stationary solutions, the first one $v_{c,0} < 1$ being the critical velocity for superfluidity, with $n_{0,\min} < 1$

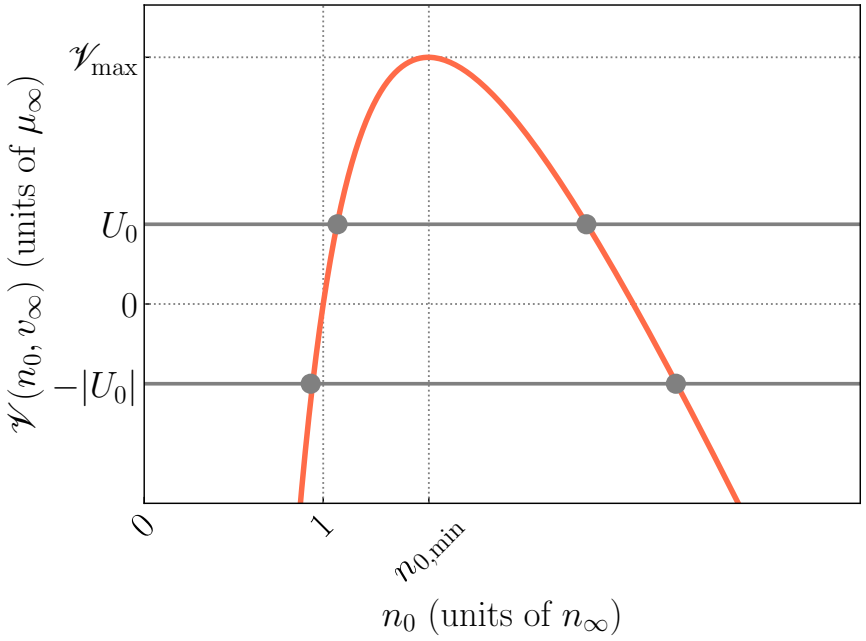

Figure 2.10: Fictitious potential $\mathscr{V}(n_0, v_\infty)$ as a function of n_0 for $v_\infty = 2$ and $\varepsilon(n) = n$. For repulsive obstacles, there are up to two solutions, and the supersonic separatrix $v_{s,0}$ is obtained for the value of v_∞ for which there are no solutions anymore. Concerning attractive obstacles, there are always two solutions.

the density at $x = 0$. The other solution is the one we are interested in in this chapter: It is obtained for supersonic velocities such that $v_{s,0} > 1$, which yields $n_{0,\min} > 1$, characteristic of the emission of long wavelength waves.

Again, we solve this equation for a given nonlinearity, which yields the expression for the supersonic separatrix $v_{s,0}$ as a function of U_0 in the hydraulic approach. This equation has solutions as long as $U_0 < \mathscr{V}_{\max} = \mathscr{V}(n_{0,\min}, v_\infty)$.

This yields the implicit equation necessary to obtain $v_{s,0}$ as a function of U_0

$$\frac{v_{s,0}^2}{2}\left(1 - \frac{1}{n_{0,\min}}\right) + \varepsilon(1) - \varepsilon(n_{0,\min}) = U_0, \tag{2.33}$$

with

$$v_{s,0}^2 = \varepsilon'(n_{0,\min}) n_{0,\min}^3, \tag{2.34}$$

which is actually the same as for the critical velocity for superfluidity $v_{c,0}$, except that now we need supersonic solutions.

Note that Eq. (2.33) defines the same fictitious potential as in Sec. 1.3.2, but the range of reachable n_0 changes due to the constraint $v_{s,0} > 1$. It is represented in Fig. 2.10 for $\varepsilon(n) = n$ and $v_\infty = 2$. It is interesting to see that the values of possible densities at $x = 0$ are not bound this time, as $n_{0,\min}$ can take any value larger than 1.

In then end, this hydraulic method is just a re-expression of the Hamiltonian approach previously explained. The condition $\mathscr{V}_{\max}(n) = U_0$ is nothing but the derivative of $E_{\mathrm{cl,w}} = \mathscr{W}(n)$ (i.e. the condition in the Hamiltonian approach) with respect to n, evaluated at $n = n_{0,\min}$. It is thus normal to recover the exact same result for $v_{s,0}$.

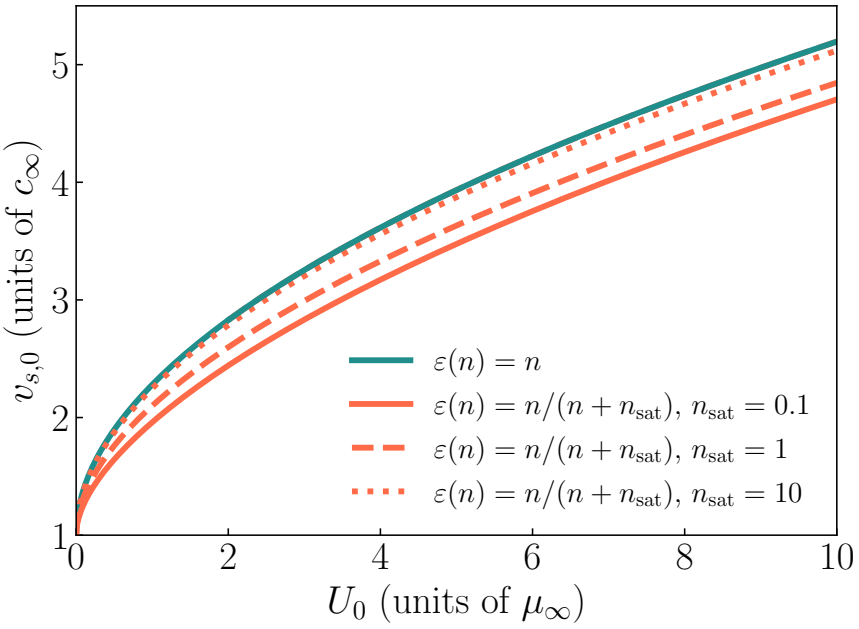

Figure 2.11: Supersonic separatrix $v_{s,0}$ as a function of the amplitude of a repulsive obstacle of large σ. The results are obtained for the nonlinearities provided in the legend.

2.3.1 Repulsive obstacles

It is possible to obtain exact analytical results for $v_{s,0}$ with respect to the amplitude of the obstacle (as the width is supposed to be large) for $\varepsilon(n) = n$

$$v_{s,0} = \left[2(U_0 - 1) + 3\left(U_0 - 1 + \sqrt{U_0(U_0 - 2)}\right)^{-\frac{1}{3}} + 3\left(U_0 - 1 + \sqrt{U_0(U_0 - 2)}\right)^{\frac{1}{3}}\right]^{\frac{1}{2}}. \quad (2.35)$$

Similar results were obtained numerically for a saturable nonlinearity.

The solutions for $v_{s,0}$ are represented in Fig. 2.11 as a function of the amplitude U_0 of the wide obstacle, for the same nonlinearities as in the previous sections. One can see that as U_0 increases, the supersonic separatrix $v_{s,0}$ takes on higher values: A bigger obstacle will induce more nonlinear emissions inside the fluid, making the transition towards a stationary solution more complicated. When comparing Fig. 2.11 with the allure of v_s for the $\delta-$peak, one can see that $v_{s,0}$ does not reach a plateau to a given value when working with a saturable nonlinearity. This behavior is then really an artifact of the $\delta-$peak. It is also interesting to note that the deviation with the curve for $\varepsilon(n) = n$ (blue curve) is less pronounced than for the superfluid case (see Fig. 1.13).

Concerning the possible correction to the following order in σ, the method used in Sec. 1.3.2 (and in Refs. [45, 191]) is not applicable anymore as it relies on the fact that $n(x) = n_{0,\min} + \delta n(x)$, with $\delta n/n_{0,\min} \ll 1$, i.e small density fluctuations around $x = 0$. This is not the case as $n_0 \in [1, n_{0,\min}]$, and there is no restriction on the value of $n_{0,\min}$, since v_∞ can take any value larger than 1. A comparison with the numerical simulation of the problem shows that if it exists, this correction is actually negligible when $\sigma \gg 1$, and the hydraulic approach is sufficient. It will be numerically demonstrated in the following Sec. 2.4 that when σ diminishes, this correction slowly increases, thus reducing the value of v_s[4].

[4]This is the opposite of the superfluid regime, in which this correction tended to increase the value of the critical velocity for superfluidity. The gradient of the potential $U(x)$ thus favor the stationarity of the flow.

2.3.2 Attractive obstacles

For the case of attractive obstacles, the fictitious potential presented in Fig. 2.10 shows that, again, there is always a solution to the equation $\mathscr{V}(n_0, v_\infty) = U_0$ no matter the value of the input velocity: $v_{s,0} = 1$ for wide attractive obstacles. This, combined with the result of the previous chapter $v_{c,0} = 1$, shows that the stationary regime is never broken for wide attractive obstacles: One goes continuously from a superfluid regime to a stationary nonsuperfluid one, never encountering turbulence. This is however not true anymore for obstacles of arbitrary width, as it has been shown in the previous section that the supersonic separatrix for a narrow obstacle is the same for repulsive or attractive obstacles.

2.4 Gaussian obstacle of arbitrary width

As in the superfluid case, the width of the obstacle has an important impact on the shape of the supersonic separatrix, and we have to numerically solve the problem in order to obtain the shape of this separatrix for obstacles of arbitrary widths. This study allows us to interpolate the two different asymptotic results obtained in both limits of $\sigma \ll 1$ and $\sigma \gg 1$.

We numerically solve the Hamilton equations Eqs. (2.2) with the Hamiltonian defined in Eq. (2.3) with a RK4 algorithm, which is equivalent to solving the following system

$$\partial_x A = p, \tag{2.36a}$$

$$\partial_x p = \frac{v_\infty^2}{A^3} - 2\left(\frac{v_\infty^2}{2} - U(x) + \varepsilon(1) - \varepsilon\left(A^2\right)\right) A, \tag{2.36b}$$

with $(A(-\infty) = 1, \partial_x A(-\infty) = 0)$ as initial condition, meaning that the density profile is flat far downstream from the obstacle, and equal to n_∞. The numerical resolution of Eqs. (2.36) with the RK4 algorithm provides the density of the quantum fluid everywhere in space for a given value of v_∞, and of the potential $U(x)$. Our criterion to obtain the supersonic separatrix from that is to run several simulations with a decreasing v_∞ (starting from a point in the phase space far in the stationary region), and then to look for the first value of v_∞ for which the density diverges or becomes negative at the position of the obstacle, meaning that the regime is not stationary anymore.

2.4.1 Repulsive obstacles

We run the simulation for a Gaussian obstacle $U(x) = U_0 e^{-x^2/\sigma}$, $U_0 = 1$, and various expressions of $\varepsilon(n)$, yielding the results for the supersonic separatrix v_s as a function of σ represented in Fig. 2.12. The supersonic separatrix is an increasing function of U_0, until it reaches its value obtained in the hydraulic approach when $\sigma \gg 1$.

The analytical limits found in the previous sections are again in perfect agreement with the numerical results obtained after solving the Hamiltonian problem. For the sake of clarity, the results for the saturable nonlinearity are only represented for $n_{\text{sat}} \in \{0.1, 1\}$. It is interesting to note that for saturable systems, the range of validity of the analytical limits depends on the value of n_{sat}: The smaller n_{sat} (i.e., the more saturated the system), the shorter the validity range of our analytical result in the limit $\sigma \ll 1$. This can be clearly seen in Fig. 2.12, in which the limit for $\sigma \ll 1$ (black dotted line) starts to deviate from the numerical solution for $n_{\text{sat}} = 0.1$.

We also represent this supersonic separatrix in the bottom part of Fig. 2.12 for the same Gaussian obstacle as a function of σ for different values of $U_0 \in \{0.1, 0.5, 1, 2\}$, and for a saturable nonlinearity. After comparing the curves for these different U_0, one can clearly see that the higher the barrier, the higher the supersonic separatrix, meaning that range of values of the parameters (σ, v_∞) leading to a nonstationary regime is more important than

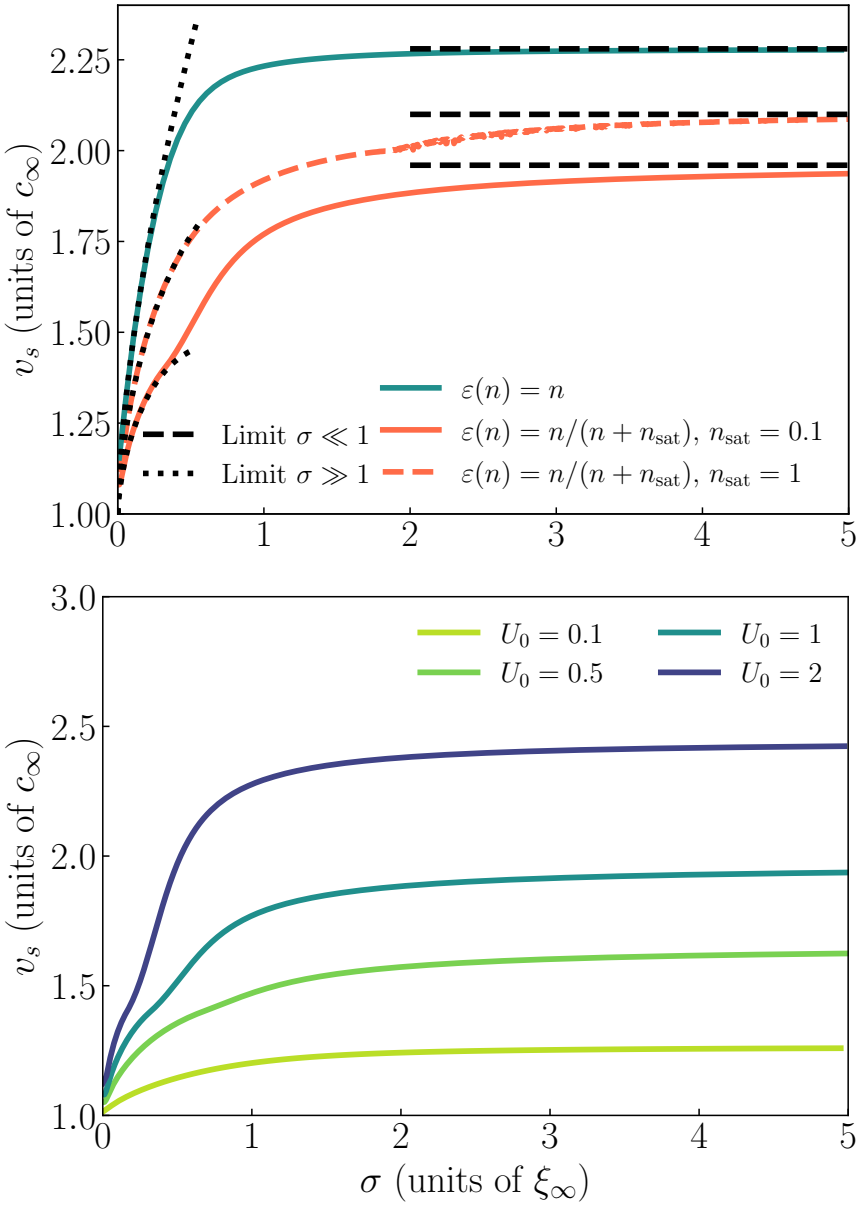

Figure 2.12: Top: Supersonic separatrix v_s as a function of the width σ of a Gaussian obstacle of amplitude $U_0 = 1$, for different expressions of $\varepsilon(n)$ (see legend). The asymptotic results obtained in both limits of narrow and wide obstacles are represented in black dotted and dashed lines. The agreement with the numerical results is good, but their validity span for narrow obstacles is smaller as $n_{\rm sat}$ decreases in the case of a saturable system. Bottom: Supersonic separatrix v_s as a function of the width for Gaussian obstacles of various amplitudes $U_0 \in \{0.1, 0.5, 1, 2\}$. v_s is plotted for $\varepsilon(n) = n/(n + n_{\rm sat})$ with $n_{\rm sat} = 0.1$.

for a smaller U_0. This was also the case in the subsonic regime: In the end, the bigger (U_0, σ), the easier it is for the system to be in a nonstationary regime.

2.4.2 Resonances for attractive obstacles

The numerical simulation for attractive obstacles reveals that $v_s(\sigma) = 1$ for many values of σ: We call this "resonances" in a sense that these points where $v_s = 1$ are associated with a perfect transmission across the obstacle, as will be demonstrated in Sec. 2.5. The top part of Fig. 2.13 – representing v_s as a function of σ for different nonlinearities – also shows that the number of resonances gets larger as σ increases, and that the curve of v_s can be delimited

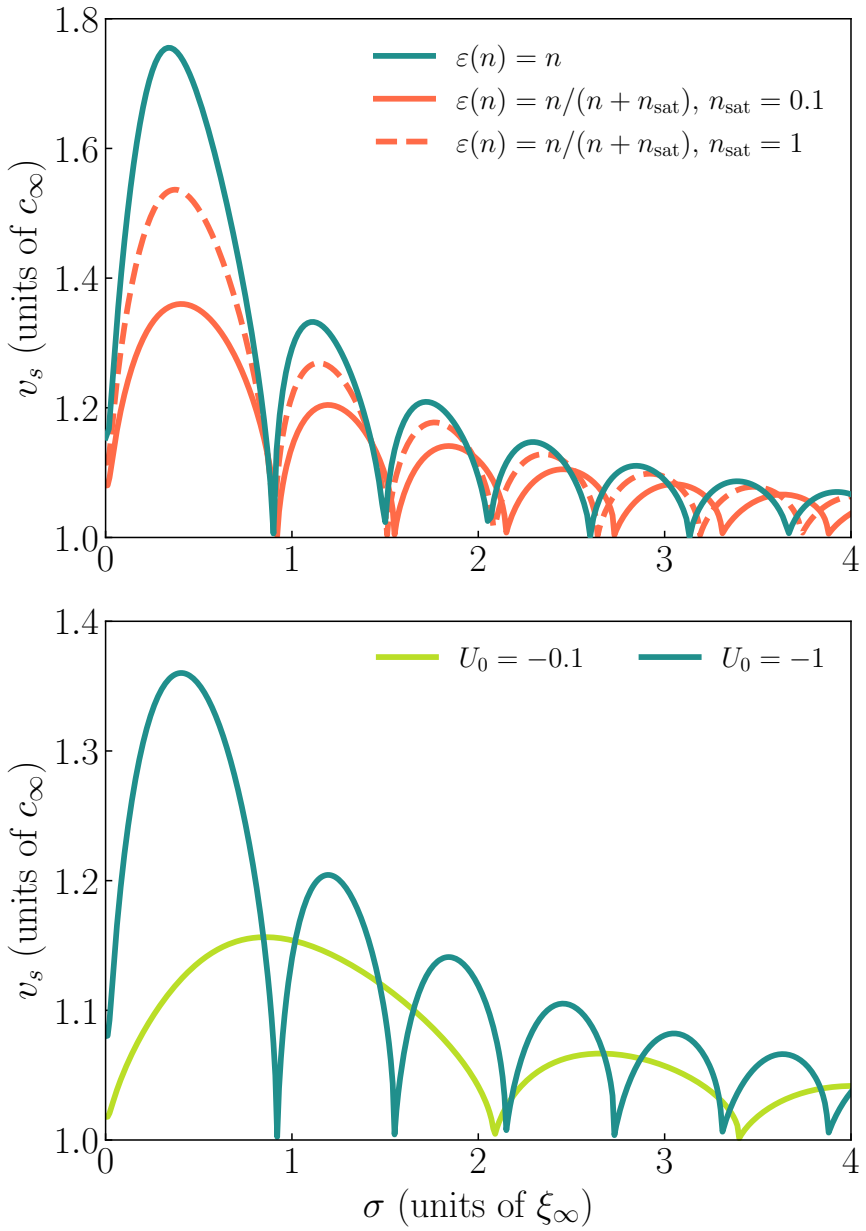

Figure 2.13: Top: Supersonic separatrix v_s as a function of the width σ of an attractive Gaussian obstacle of amplitude $U_0 = -1$, for different expressions of $\varepsilon(n)$ (see legend). One can see the appearance of resonances for given values of σ, that are slightly shifted as σ increases and $n_{\rm sat}$ decreases. Bottom: Supersonic separatrix v_s as a function of the width for Gaussian obstacles of various amplitudes $U_0 \in \{-1, -0.1\}$. v_s is plotted for $\varepsilon(n) = n/(n + n_{\rm sat})$ with $n_{\rm sat} = 0.1$.

by an envelope structure, which expression is undefined yet.

The bottom part of Fig. 2.13 represents the supersonic separatrix, again as a function of σ and for a saturable nonlinearity, but for various values of U_0. For the sake of clarity, we only have represented it for $U_0 \in \{-1, -0.1\}$. One can see that the effect of U_0 on the envelope v_s and the position of the resonances is also important: The larger U_0, the more numerous the resonances and the higher the envelope of v_s. The supersonic separatrix is thus highly nontrivial for such a Gaussian obstacle, as the position of the resonances and the envelope of v_s will both vary with σ, U_0 and $\varepsilon(n)$ (and $n_{\rm sat}$ for a saturable nonlinearity).

This phenomenon of resonances is quite peculiar, and necessitates further investigation to better understand their nature: What is their origin? How are they distributed? We provide

in Sec. 2.5 a thorough characterization of these resonances and the envelope of v_s, focusing on a simpler obstacle – a square-well potential instead of an attractive Gaussian defect – making it possible to derive analytical results.

2.5 Characterizing the resonances for attractive obstacles

Gaussian attractive obstacles lead to an interesting shape for v_s by exhibiting the presence of nonlinear-resonances. We show in this section that these resonances are associated with lines of perfect transmission across the attractive obstacle, and that this can be assimilated to "superfluid-like" solutions for supersonic velocities, connecting the superfluid regime to the supersonic one, never leaving the stationary regime. These solutions are of great interest, but only exist on specific curves in the (U_0, v_∞) diagram, and do not form a continuous family of solutions like in the subsonic superfluid regime.

While several of the results we present were already discussed in Ref. [52], the resonances we characterize in this section were not the main focus of those authors. Here, we provide a comprehensive approach that leads to various explicit results, highlighting the implications of these resonances on the dynamics of the system.

In this section, we use the Hamiltonian approach provided in Sec. 2.1 and predict the existence of these resonances in terms of the fictitious potential $\mathscr{W}(n)$. We derive these results for a toy-model consisting in squared obstacles $U(x) = U_0\Theta(\sigma/2 - |x|)$ of arbitrary amplitude U_0 and width σ, and for $\varepsilon(n) = n$. This simpler system allows us to derive exact analytical results for the characterization of the resonances.

2.5.1 Origin of the resonances

We first provide a complete study of the lobe structure corresponding to resonances seen for attractive obstacles, meaning the shape of the envelope of v_s, and the fact that these resonances are associated with lines of prefect transmission in the (U_0, v_∞) plane.

Transmission coefficient

The transmission and reflection coefficient of a plane wave diffracted by a square well are usually well known in the linear case (i.e. $\varepsilon(n) = 0$), leading to an easy description of the position of the resonances [178], for which the reflection is suppressed. This is however not the case anymore when including the interactions between particles, as it is generally not possible to separate the incoming and reflected waves. Yet, it remains possible to obtain a good description of these coefficients, as well as the positions of the resonances in the weak backscattering limit where $\delta n/n_\infty \ll 1$ [181, 192]. In this approximation, the transmission coefficient reads [181]

$$T = \left(1 + \frac{\Delta E}{2(v_\infty^2 - 1)}\right)^{-1}, \tag{2.37}$$

with ΔE the energy difference of the fictitious particle between its final ($x = +\infty$) and initial ($x = -\infty$) states: $\Delta E = \mathscr{H}[A, p]|_{x=+\infty} - \mathscr{H}[A, p]|_{x=-\infty}$, with an initial profile corresponding to the equilibrium $A = 1$ and $p = 0$ (flat density profile).

The numerical results based on Eq. (2.37) are summarized in Fig. 2.14, where the color bar shows the transmission coefficient of the fluid of a function of the injection velocity v_∞ and the amplitude $U_0 < 0$ of the rectangular well, for a given value of σ. The colored zone corresponds to the stationary regime, and clearly exhibits resonances. It is separated from white zones of undefined transmission by the supersonic separatrix v_s. The lines of perfect transmission are shown to follow exactly the nontrivial structure of the stability diagram and are drawn as orange dotted curves, while the white dashed curve represents the envelope of v_s.

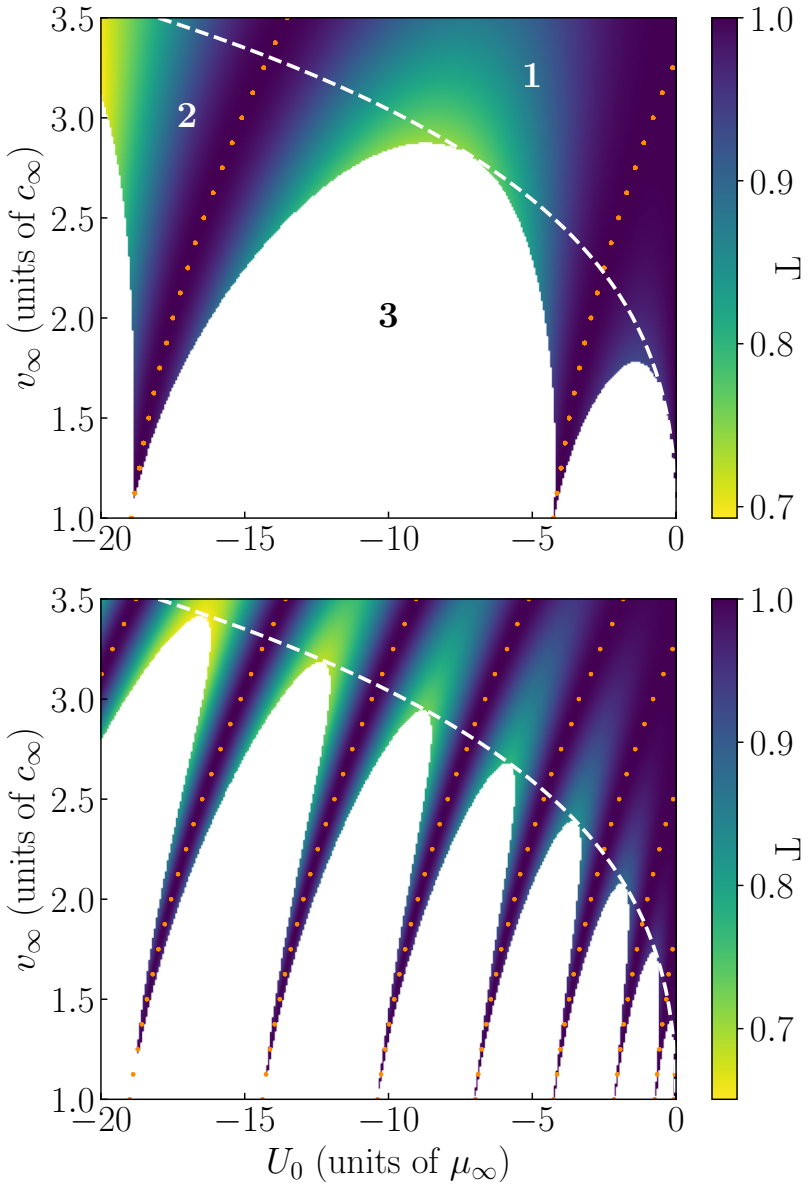

Figure 2.14: Phase diagram (U_0, v_∞) (in the natural units of the superfluid) of a quantum fluid flowing across attractive square well potentials of respective widths $\sigma = 1$ (top) and $\sigma = 4$ (bottom), and for $\varepsilon(n) = n$. The transmission across the barrier is associated with the color bar and is maximum along the orange dotted curves, which determine the position of the resonances. The white dashed line represents the envelope of v_s. The tag numbers **1**–**3** are associated with three cases: Above the envelope, below it but in the stationary regime, and below it in the nonstationary regime. These different regimes will be explained in the following sections.

When comparing the top and bottom figures (respectively, for $\sigma = 1$ and $\sigma = 4$), one can see that the number of resonances gets larger as σ increases. At some point, for an arbitrarily large value of σ, the resonances are so thin and numerous that they are not distinguishable from one another anymore, to the extent that the supersonic separatrix would be given by $v_s = 1$ in the limit $\sigma \gg 1$, closing the nonstationary gap. One can also see that for such an obstacle, the envelope of v_s bears no dependence on σ as it remains the same while the width increases. This is different to the previous case of the Gaussian obstacle, for which this envelope was a decreasing function of σ.

Analytical results can be obtained for both the envelope of v_s and the lines of perfect transmission, and rely on the thorough study of the fictitious potential $\mathscr{W}(n)$. Depending on

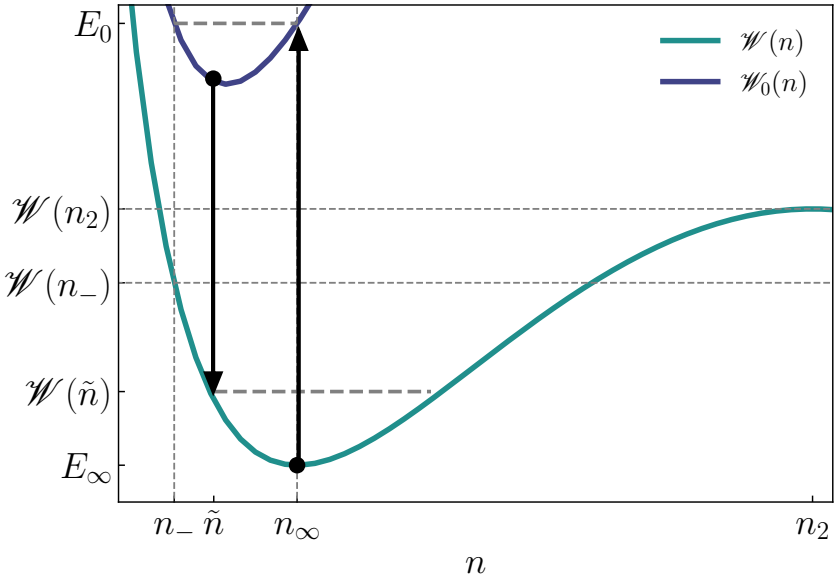

Figure 2.15: Classical fictitious potentials $\mathscr{W}(n)$ and $\mathscr{W}_0(n)$ in the case of an attractive square well in the configuration **1**. $\mathscr{W}(n)$ is for $|x| > \sigma/2$, and $\mathscr{W}_0(n)$ for $x \in [-\sigma/2, \sigma/2]$ inside the well.

its shape (and on the value of U_0 and v_∞), one can be in either the configurations **1**, **2** or **3** presented in Fig. 2.14. An explanation is provided in terms of the fictitious particle within this potential.

Before the excitations caused by the square well potential, the fictitious particle is at rest from $x = -\infty$ to $x = -\sigma/2$ with constant density n_∞ and energy $E_\infty = \mathscr{W}(n_\infty)$, and is located at the bottom of the fictitious potential $\mathscr{W}(n)$. As x increases, it reaches the well and undergoes a kick of energy $\Delta E = E_0 - E_\infty$, going from (n_∞, E_∞) to (n_∞, E_0) in the new fictitious potential $\mathscr{W}_0(n) = \mathscr{W}(n) + |U_0|n$. This corresponds for example to the right vertical arrow in Fig. 2.15. As it is not at equilibrium in $\mathscr{W}_0$, it will oscillate between n_∞ and n_- (the other solution of $\mathscr{W}_0(n_-) = E_0$) as it progresses in the obstacle, and will return to $\mathscr{W}$ with density $\tilde{n}$ when $x = \sigma/2$, as represented by the left vertical arrow in Fig. 2.15.

Following Ref. [52], we define $\tilde{L}$, corresponding to the distance between n_∞ and $\tilde{n}$ performed in $\mathscr{W}_0$, and L_0 the distance of a round-trip between n_∞ and n_-, i.e. the period of the oscillations of the fictitious particle in $\mathscr{W}_0$

$$\tilde{L} = \frac{1}{\sqrt{2}} \int_{\sqrt{\tilde{n}}}^{\sqrt{n_\infty}} \frac{dA}{\sqrt{E_0 - \mathscr{W}_0(A)}}, \tag{2.38a}$$

$$L_0 = \sqrt{2} \int_{\sqrt{n_-}}^{\sqrt{n_\infty}} \frac{dA}{\sqrt{E_0 - \mathscr{W}_0(A)}}. \tag{2.38b}$$

Several cases leading to different dynamics for the fluid are then possible depending on the values of U_0, v_∞ and σ.

Case 1: Periodic orbits above the envelope of v_s

Stationary solutions always exist no matter U_0, σ and v_∞ when the energy of the fictitious particle at $x = \sigma/2$, i.e. $\mathscr{W}(\tilde{n})$, is such that $\mathscr{W}(\tilde{n}) < \mathscr{W}(n_-) < \mathscr{W}(n_2)$. That way, the fictitious particle is confined and oscillates as shown in Fig. 2.15, leading to a periodic orbit.

In the configuration where $\tilde{n} = n_-$, one has $\mathscr{W}(\tilde{n}) = \mathscr{W}(n_-) = \mathscr{W}(n_2)$: The fictitious particle returns to the fictitious potential $\mathscr{W}$ with exactly the energy of the local maximum of $\mathscr{W}(n)$. This defines the envelope of v_s, separating two cases: One where stationary solutions

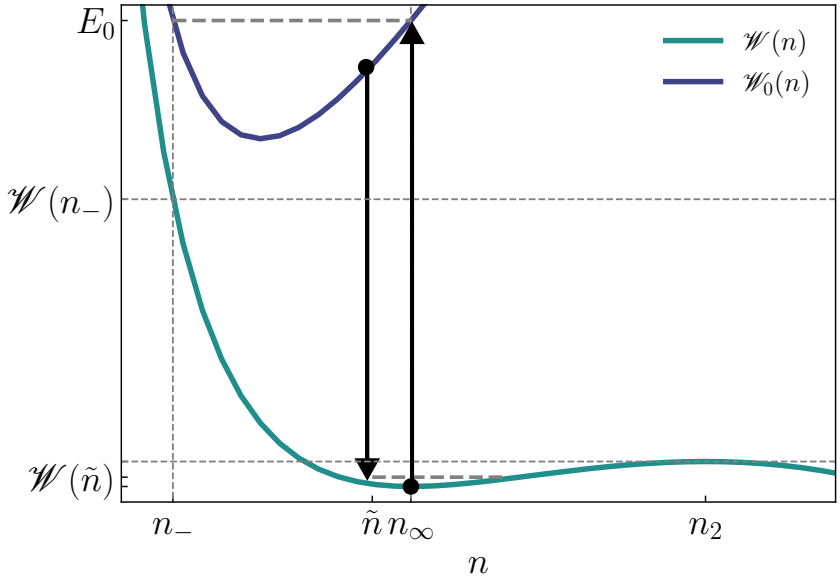

Figure 2.16: Same caption as Fig. 2.15 but for the configuration **2**.

always exist (as illustrated by the tag number **1** of Fig. 2.14), and one where the existence of such solutions is conditioned by the value of σ. An analytical expression can be obtained for that envelope and can be found in Eqs. (34) and (35) of Ref. [52]

$$1 - \frac{F(v_\infty)}{2U_0} = G(v_\infty, U_0), \tag{2.39a}$$

$$F(v_\infty) = \left[\frac{v_\infty^2}{4}\left(1 + \sqrt{1 + \frac{8}{v_\infty^2}}\right) - 1\right] \times \left[\frac{5v_\infty^2}{4} + 1 - \frac{3v_\infty^2}{4}\sqrt{1 + \frac{8}{v_\infty^2}}\right], \tag{2.39b}$$

$$G(v_\infty, U_0) = \frac{v_\infty^2 + 1}{2} + U_0 - \left[\left(\frac{v_\infty^2 + 1}{2} + U_0\right)^2 - v_\infty^2\right]^{\frac{1}{2}}. \tag{2.39c}$$

Given Eqs. (2.39), we have the confirmation that the envelope of v_s does not depend on σ for an attractive square well obstacle. The resonances will then never disappear, and the envelope will always be the same no matter the width of the obstacle. This is different for a Gaussian obstacle, for which the envelope of v_s does depend on σ, and decreases until it is not distinguishable anymore from $v_c = 1$. It stems from the fact that when the fictitious particle is excited after encountering $\mathscr{W}_0(n)$ at $x = -\sigma/2$, it will either experience a flat obstacle, or an obstacle which amplitude depends on σ (Gaussian obstacle). Since the structure of the resonances is linked to the shape of the fictitious potential $\mathscr{W}_0(n)$ (and of $U(x)$), it is then normal that the envelope of the resonances depends on σ for a Gaussian obstacle.

Case 2: Periodic orbits below the envelope of v_s

Figure 2.16 shows the other configuration possible for stationary states to exist, subjected to the condition $\mathscr{W}(\tilde{n}) < \mathscr{W}(n_2) < \mathscr{W}(n_-)$. It translates to the fact that the distance traveled by the fictitious particle in $\mathscr{W}_0$ is such that the energy $\mathscr{W}(\tilde{n})$ of the particle at $x = \sigma/2$ is still lower than the maximum of $\mathscr{W}$, so periodic orbits can exist. On the other hand, $\mathscr{W}(\tilde{n})$ could in principle be larger than $\mathscr{W}(n_2)$ for other values of σ. Stationary solutions exist for values of σ associated with distances performed in $\mathscr{W}_0(n)$ comprised in the interval $[0, \tilde{L}] \cup [L_0 - \tilde{L}, L_0 + \tilde{L}] \cup [2L_0 - \tilde{L}, 2L_0 + \tilde{L}] \ldots$, describing the lobe-like shape seen in Fig. 2.14, and corresponding to the tag number **2**.

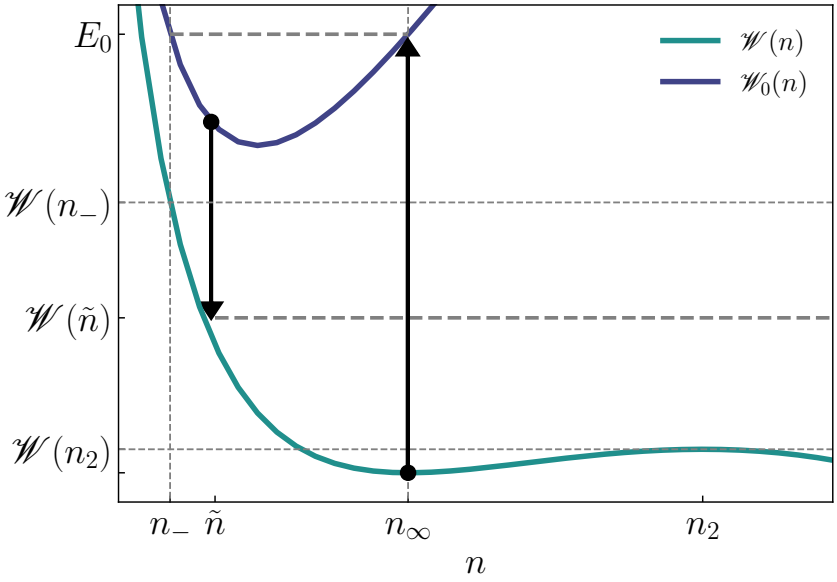

Figure 2.17: Same caption as Fig. 2.15 but for the configuration **3**. In that case, there are no stationary solutions anymore.

Concerning the exact position of the resonances, they first appear on the line $v_\infty = 1$ and link the superfluid regime to "superfluid-like" solutions in the supersonic regime, making the transition continuous and never leaving the stationary regime. They are obtained when the two extrema of the fictitious potential $\mathscr{W}(n)$ merge in a unique saddle-point located at $n = n_\infty$. The fictitious particle cannot oscillate anymore, and the only possibility for a stationary state to exist is when the excited fictitious particle exits $\mathscr{W}_0(n)$ with the same density it had when entering it, meaning $\tilde{L} = 0$.

More generally, when the fictitious particle performs an arbitrary number of round-trips in the excited potential $\mathscr{W}_0(n)$ so that its energy after exiting the obstacle is exactly the one it had before the excitation, a resonance forms between the width of the obstacle and the wavelength of the cnoidal wave of the oscillating particle, causing a perfect transmission, and linking the superfluid regime to the stationary nonsuperfluid one. The equation of these lines of perfect transmission, represented in orange dotted curves in Fig. 2.14, is then given by $\alpha L_0 = \sigma$, with α an integer.

Case 3: Free states in the nonstationary regime

When $\mathscr{W}(n_2) = \mathscr{W}(\tilde{n}) = \mathscr{W}(n_-)$, the energy of the fictitious particle is above the one of the local maximum of $\mathscr{W}(n)$ as can be seen in Fig. 2.17. No oscillation in $\mathscr{W}$ is possible, and no periodic orbits can exist: The system is not stationary anymore, corresponding to the white zones in Fig. 2.14, associated with the tag number **3**.

2.5.2 Separation between the resonances

We further characterize the resonances by looking at their starting point on the line $v_\infty = 1$: We want to see if their distribution in the nonlinear case $\varepsilon(n) = n$ follows the same distribution as in the linear case, i.e. for $\varepsilon(n) = 0$. It is not possible to analytically define them when $\varepsilon(n) = n$ because the usual approach in terms of incident and reflected waves is not possible anymore. In that case, the positions of the resonances are slightly shifted compared to the linear case as discussed in Refs. [110, 111]. We numerically compute them using Eq. (2.37).

When neglecting the interactions between particles however, it is possible to define the

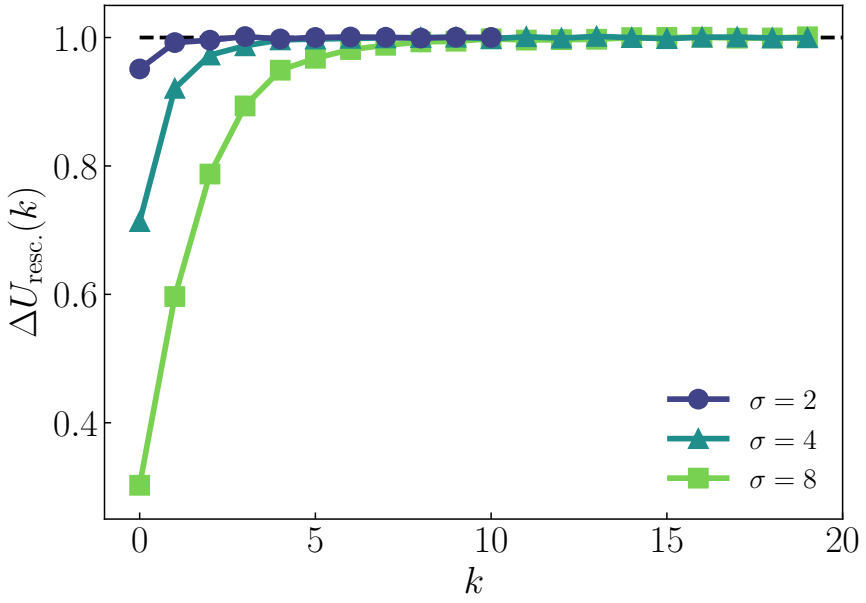

Figure 2.18: Rescaled value of the separation between the resonances for a square well obstacle as a function of the index k of the resonance. The colored dots, triangles and squares stand respectively for $\sigma = \in \{2, 4, 8\}$ in the nonlinear regime $\varepsilon(n) = n$, and are obtained after a numerical simulation of Eq. (2.37). The black dashed curve is the theoretical value for the linear case $\varepsilon(n) = 0$.

exact position of the resonances because the transmission coefficient is easily tractable [193]

$$T = \left(1 + \frac{U_0^2}{4E(E-U_0)\sin^2\left[\sqrt{2(E-U_0)}\sigma\right]}\right)^{-1}. \tag{2.40}$$

A resonance occurs when the transmission coefficient $T = 1$, leading to the condition on the amplitude of the obstacle

$$U_{0,k} = E - \frac{k^2\pi^2}{2\sigma^2}, \tag{2.41}$$

with k the number of the resonance. To get rid of the energy offset, we focus on the distance between two consecutive resonances, and thus introduce the rescaled separation between each consecutive resonances

$$\Delta U_{\text{resc.}}(k) = \frac{2\sigma^2}{(2k+1)\pi^2}\left|U_{0,k+1} - U_{0,k}\right|. \tag{2.42}$$

We plot this rescaled separation in Fig. 2.18 as a function of the index k. This function is constant in the linear case and is represented in black dashed line, whereas the various markers are numerically obtained for different values of σ in the nonlinear case (see legend). As Eq. (2.42) gets rid of the $\sigma-$dependence, the curves for the various σ are supposed to collapse on the curve for the linear case. This is the case as one can see in Fig. 2.18, but for larger and larger values of k as σ increases. The deviation from the black curve is clear for small values of k (all the more that σ is large), meaning that the separation between the two first resonances (for example) in the nonlinear case is really different from that obtained in the linear case. Note that we have less data for $\sigma = 2$ than for the rest because such an obstacle leads to less resonances in the numerical integration we performed.

2.5.3 Resonances in the density profile of the fluid

We numerically obtained the density profiles of the fluid for obstacles of fixed $\sigma = 4$ but varying U_0, and for a constant velocity $v_\infty = 3.5$. Based on the data provided in Fig. 2.14,

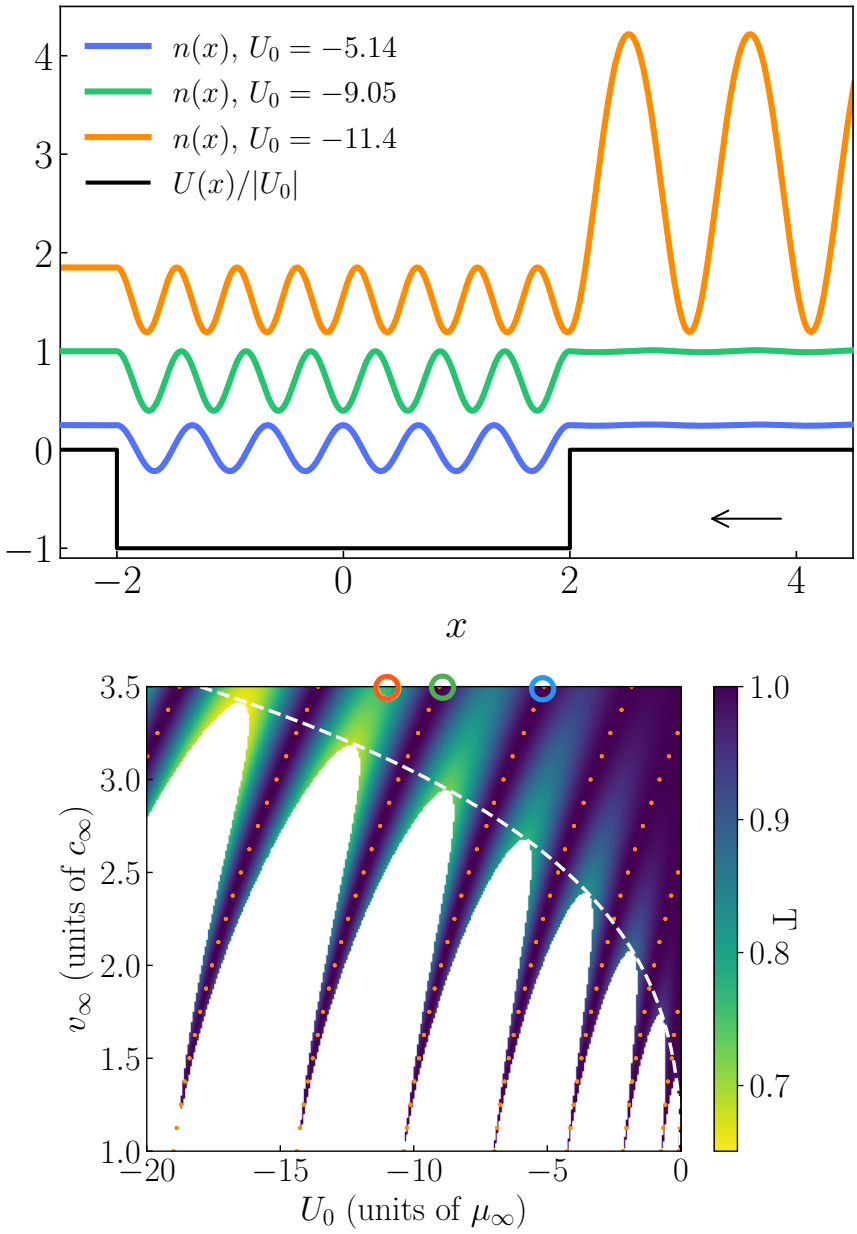

Figure 2.19: Top: Density profiles for several chosen parameters in the (U_0, v_∞) plane (for the sake of clarity, the different curves are shifted to avoid overlapping). The flow goes from right to left with constant velocity $v_\infty = 3.5$, and encounters a square-well obstacle of width $\sigma = 4$ and varying amplitudes $U_0 \in \{-5.14, -9.05, -11.4\}$. For $U_0 = -5.14$ and $U_0 = -9.05$, one is almost located on the sixth and seventh lines of perfect transmission, as circled in blue and green in the bottom part of the figure – There are indeed respectively 6 and 7 oscillations in the well. The orange curve is obtained for $U_0 = -11.4$, which does not correspond to a perfect transmission (see the orange circle in the bottom figure): This can be seen in the density profile, which is a nonlinear wave upstream. Bottom: We recall the value of the transmission coefficient as a function of U_0 and v_∞: The orange, green and blue circle define the values we are interested in, and are respectively associated with the density profile in the top part.

we chose values of U_0 representing different dynamics (refer to the orange, green and blue circles in the bottom part of Fig. 2.19). This is represented in the top part of Fig. 2.19, where the blue and green lines stand respectively for $U_0 = -5.14$ and $U_0 = -9.05$, both supposedly located on the sixth and seventh line of perfect transmission ($k = 6$ and $k = 7$). In these cases, the density is locally perturbed at the position of the obstacle, and is flat otherwise:

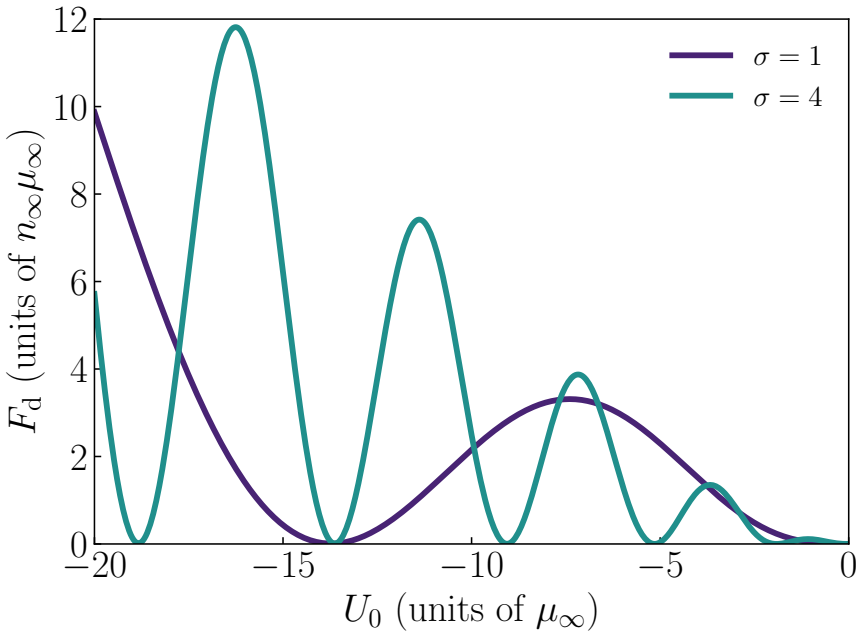

Figure 2.20: Friction force exerted by a fluid of supersonic velocity $v_\infty = 3.5$ on a square obstacle as a function of its amplitude, for two different widths $\sigma = 1$ and $\sigma = 4$. The values of U_0 for which $F_{\mathrm{d}} = 0$ are located on the lines of perfect transmission.

This is a superfluid-like dynamics. The only difference between the two is that as k increases, so does the number of nodes and oscillations in the density profile.

For $U_0 = -11.4$, the transmission coefficient is lower than one and does not correspond to a resonance anymore. The density profile, represented in orange, is thus similar to the one in the supersonic regime when $U_0 > 1$: It corresponds to cnoidal waves. Their period can be determined within our approach with the fictitious potential $\mathscr{W}$, and is given by the time taken by the fictitious particle to go from $\tilde{n}$ to the second solution to $\mathscr{W}(n) = \mathscr{W}(\tilde{n})$ (see Fig. 2.15 for example).

2.5.4 Resonances associated with a zero drag force in the supersonic regime

We also characterized the friction exerted onto the obstacle by numerically evaluating the drag force, as given by Eq. (2.19). We used for this the density profiles computed in the previous section. Contrarily to the $\delta-$peak, for which F_{d} was close to be constant (except for v_∞ really close to v_s), the drag force for attractive obstacles is now an ever-oscillating function. It is represented in Fig. 2.20 as a function of U_0, for $v_\infty = 3.5$, and for $\sigma = 1$ and $\sigma = 4$, and clearly exhibits resonances for given values of U_0.

For example for $\sigma = 4$, the force drops to zero for $U_0 = -5.14$ and $U_0 = -9.05$, which corresponds indeed to the density profiles obtained in Fig. 2.19. When the force drops to zero, the transmission is maximum: The fluid experiences no friction along these lines of perfect transmission, leading to a "superfluid-like" behavior for supersonic velocities.

2.6 Conclusion

In a similar fashion to Chap. 1, in which treated the superfluid regime, the present chapter was mostly dedicated to the determination of the supersonic separatrix v_s, i.e., the separation between the nonstationary regime, and the second regime of stationary transport at higher velocities. Using several methods (Hamilton approach or hydraulic approximation which, in the end, are equivalent), we derive exact analytical results for v_s for repulsive and attractive

Gaussian obstacles of various widths and amplitudes, and also for different expressions of the nonlinear interaction potential $\varepsilon(n)$. A detailed study of the drag force exerted by the fluid onto a narrow obstacle is also performed, providing results going beyond the linear-response theory.

These results, put together with those obtained in Chap. 1, allow us to complete the phase diagrams of the different critical velocities v_c and v_s in the (U_0, v_∞) and (σ, v_∞) planes, and have a complete description of the different regimes of transport possible for the quantum fluid. We respectively encompass v_c and v_s in Figs. 2.21 as a function of the amplitude of the obstacle, for $\sigma \ll 1$ (top), $\sigma = 1$ (middle) and $\sigma \gg 1$ (bottom). These different v_c's and v_s's are represented for $\varepsilon(n) = n$ in blue, and the associated blue shaded area represents the stationary regime (either subsonic or supersonic). For the sake of completeness, the results for a saturable nonlinearity are also represented in orange, albeit only in the two analytical limits $\sigma \ll 1$ (top) and $\sigma \gg 1$ (bottom), for readability concerns. Here are the main characteristics of each systems, depending on the width of the obstacle.

- $\sigma \ll 1$: The supersonic separatrix for repulsive obstacles is, similarly to v_c in the superfluid regime, a monotone function of U_0 whose lowest value is provided by the hydraulic limit (bottom). v_s is a symmetric function of the amplitude of the obstacle as it only depends on $|U_0 F(\sigma)|$; This symmetry is later broken when σ increases. Finally, it exhibits a saturation in the case of a narrow obstacle, which is also interpreted as an artifact of the $\delta-$distribution.

- $\sigma \sim 1$: A new interesting behavior is observed for attractive obstacles: The symmetry in v_s provided by the $\delta-$peak is broken as soon as we leave the limit of narrow obstacle, and the attractive part of the phase diagram exhibits the presence of resonances in $v_s(U_0)$. An in-depth characterization of these resonances is provided in Sec. 2.5 for an attractive rectangular defect, in which we derive both their position and the envelope of the supersonic separatrix. This allows us to make the distinction between 3 zones in which the dynamics will differ in the phase diagram provided in Fig. 2.14. Above the envelope of v_s where the solution is always stationary, and under it where the solution is either stationary (between the lobe structure and the envelope) or not (under the lobe structure). The density profile becomes symmetric for these resonances, and the friction disappears as the quantum fluid is totally transmitted through the obstacle: Such solutions are reminiscent of a superfluid regime, which normally occurs only at subsonic velocities. Interestingly, Ref. [113] also shows the presence of such resonances for peculiar values of $v_\infty > v_c$, for which the excitations are fully suppressed, leading to a "superfluid-like" behavior at supersonic velocities. These velocities are close to the velocities leading to a perfect transmission across the obstacle in the linear case (i.e. when $\varepsilon(n) = 0$), thus assimilating these resonances to a nonlinear counterpart of the Ramsauer-Townsend effect [178]. These results were however derived for repulsive square obstacles, but are actually not contradictory with this manuscript. Indeed, the lines of perfect transmission we derived in Sec. 2.5 are slightly curved and thus still exist for positive values of U_0, even if their origin stems form negative values of U_0.

- $\sigma \gg 1$: For a Gaussian obstacle, these resonances, associated with lines of perfect transmission – and so with superfluid-like solutions – slowly disappear in the limit $\sigma \gg 1$ (bottom)[5]. In the end for attractive obstacles, one goes continuously from $v_s > 1$ to $v_s = 1$ as σ increases, via the appearance of resonances. In the limit $\sigma \gg 1$, the resonances are so numerous and their envelope is so low that it becomes impossible to differentiate it from $v_s = 1$: The supersonic separatrix v_s is then identical to the critical velocity for superfluidity v_c, and the nonstationary regime totally disappears.

[5]Note that for a square well obstacle, the resonances always exist since the envelope of v_s does not merge with $v_c = 1$, but the resonances are so numerous that the nonstationary regime is not distinguishable anymore.

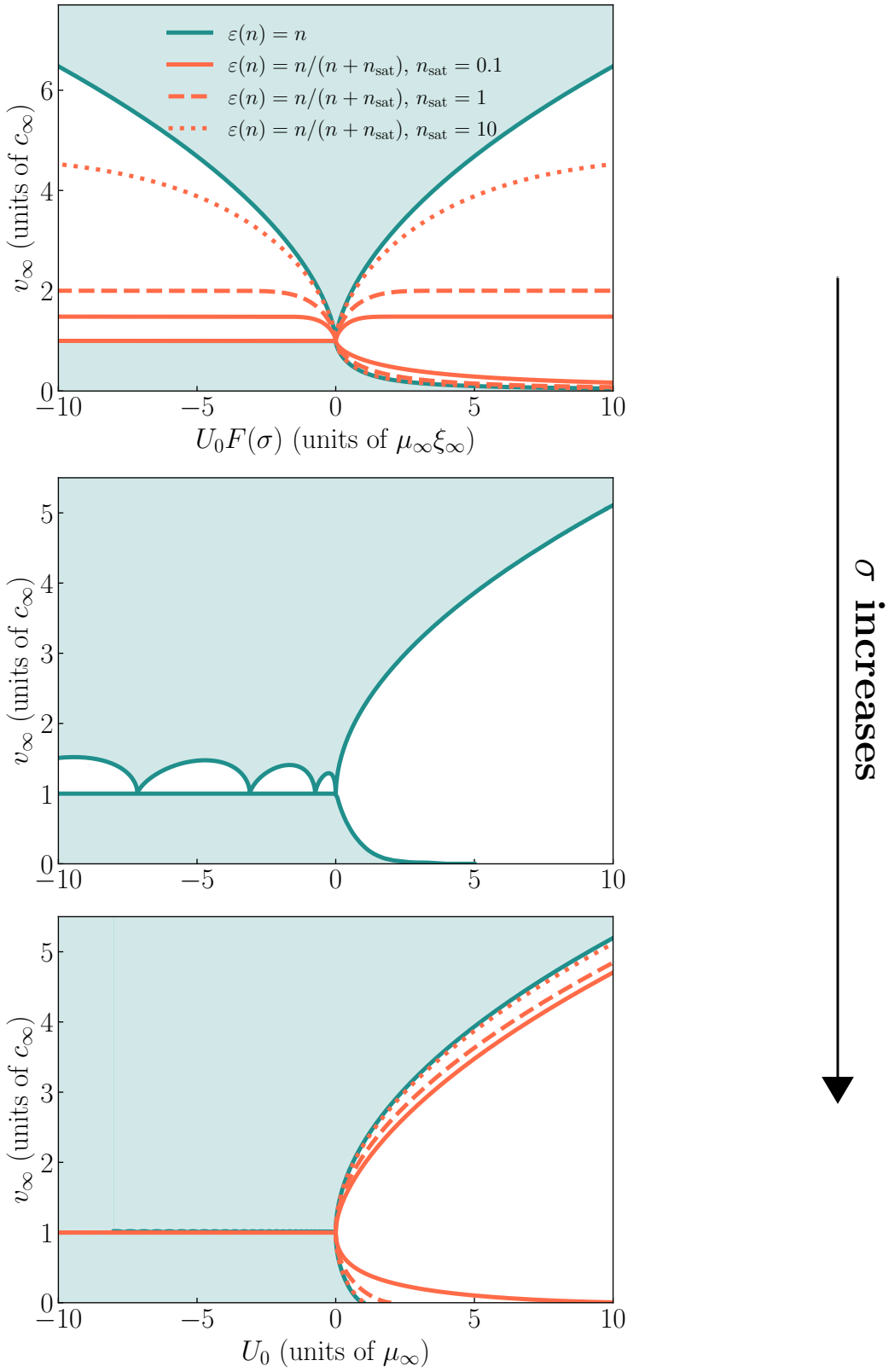

Figure 2.21: Critical velocities as a function of the amplitude of a narrow (top), moderately wide (middle, $\sigma \sim 1$) and wide (bottom) Gaussian obstacle, for the various nonlinearities indicated in the legend. The frontier in the subsonic regime $v_\infty < 1$ corresponds to the critical velocity for superfluidity v_c, whereas the frontier in the supersonic regime $v_\infty > 1$ is the supersonic separatrix v_s. The shaded area corresponds to the stationary regimes for $\varepsilon(n) = n$, whereas the white one is the nonstationary regime, in which solitons are repeatedly emitted for a repulsive obstacle. All the results in the top and bottom figures are analytical, whereas those for $\sigma \sim 1$ were obtained numerically.

Chapter 3

Critical velocity for superfluidity in two dimensions

Sommaire

In strong contrast to the 1D geometry studied in Chap. 1, the continuity equation is not integrable in 2D. In this dimension, different analytical approaches of the quantum hydrodynamic equations are thus in order to evaluate the critical velocity for superfluid motion. These approaches rely on Janzen-Rayleigh expansions of the velocity potential and appropriate continuity conditions for the flow fields at the boundary of the obstacle. Supported by numerical simulations, they reveal that for a wide obstacle, the critical speed is a nontrivial nonmonotonic function of the amplitude of the obstacle, with two different branches depending on whether the obstacle is penetrable or not, and corresponding to two distinct mechanisms for the breakdown of superfluidity. The present chapter is devoted to detailing these results.

Article linked to the chapter

J. Huynh, F. Hébert, M. Albert and P.-É. Larré, "Critical velocity of a two-dimensional superflow past a potential barrier of arbitrary penetrability" – Phys. Rev. A **105**, 013317 (2024)

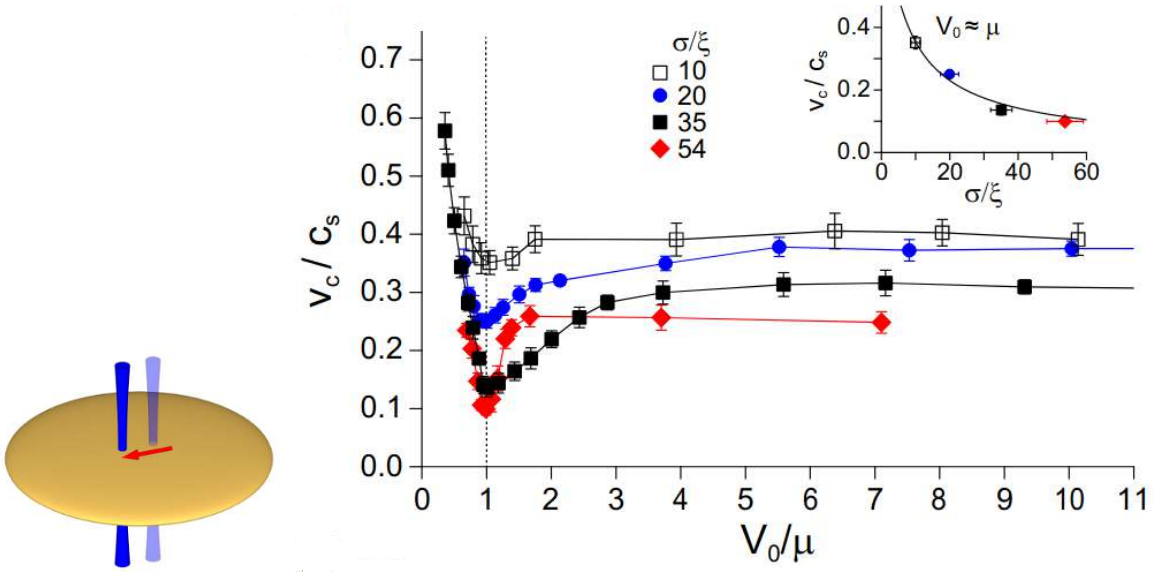

Figure 3.1: Left: Schematics of the experimental setup of Ref. [195]. The obstacle is generated by a repulsive Gaussian beam (blue) that moves within the condensate with constant velocity. Right: Critical velocity v_c/c_s (with c_s the speed of sound) with respect to the relative amplitude of the barrier V_0/μ, for various widths σ/ξ of obstacle (see the inset for $v_c(\sigma)$). The critical velocity reaches a minimum around $V_0 = \mu$, and increases to reach a plateau for large V_0, which depends on σ. Interestingly, the minimum exhibited around $V_0 = \mu$ disappears as σ decreases. Figures from Ref. [195].

Historically, the study of superfluidity in systems described by the Gross-Pitaevskii theory regained momentum with the long-awaited experimental realization of BECs in atomic systems in 1995 [8, 9]. Following this, subsequent experiments appeared, particularly in three dimensions [39, 68, 69], which explored superfluidity by stirring the quantum fluid using an external laser beam. This method has also been applied to two-dimensional setups, as demonstrated in Ref. [164] for a disk-shaped Bose gas. The authors examine the heating rate of the Bose gas in response to the local perturbation caused by the laser beam, and correlate this heating with the transition from a superfluid state to a normal gas. The authors of Ref. [194] even go further, showing that the onset of heating occurs due to the creation of vortex-antivortex pairs.

In a simpler setup – a planar quantum fluid flowing against a rigid obstacle, similar to the original experiments with liquid helium – Frisch *et al.* developed one of the earliest theoretical models to calculate the critical speed of superfluid motion [58]. In this reference, the authors used the Gross-Pitaevskii framework to derive the well-known critical value $v_c = \sqrt{2/11}$ (in units of the speed of sound) for wide impenetrable disks. This study also revealed that the transition to the nonsuperfluid regime in 2D is marked by the emission of vortex-antivortex pairs, rather than solitons as observed in 1D systems. The dynamics of these vortices after emission depends heavily on the parameters of the system, paving the way for the study of quantum turbulence. Rica later refined this method in Ref. [59] – the very same method we employ in this chapter – leading to a more precise value $v_c = 0.369773$.

In Ref. [195], the authors experimentally realize the previously-mentioned setup to study the critical velocity for vortex shedding in a BEC, or in other words v_c. Their experiment involves sweeping an obstacle of amplitude V_0 and width σ, generated by a repulsive Gaussian laser beam within a highly oblate BEC (as illustrated in the right part of Fig. 3.1), and then identifying the velocity at which vortices are emitted. The critical velocity for superfluidity is then determined from the probability distribution of vortex dipole formation in the BEC. For one of the first times, the authors provide results for penetrable obstacles ($V_0 < \mu$ the

chemical potential), thereby going beyond Frisch's results, which apply only to impenetrable obstacles. This is also one of the main objectives of this chapter – obtaining $v_c(V_0)$. As shown in the right part of Fig. 3.1, they find that the critical velocity does not vanish as $V_0 \to \mu$, unlike the 1D case. Instead, it reaches a nonzero minimum and then increases to a plateau. The value of this plateau depends solely on σ (as shown in the inset), validating the results of Refs. [58, 59] for $V_0 > \mu$. Interestingly, they attribute these two distinct behaviors in v_c to different mechanisms of vortex shedding, which depend on the penetrability of the obstacle. This concept will also be explored later in this chapter.

In recent decades, numerous theoretical studies have sought to explain experimental observations related to the breakdown of superfluidity in two-dimensional atomic systems. Many of these studies have focused on the nucleation of vortices in quantum fluids [63, 101, 196–198], while other have extended the analysis to obtain v_c as a function of the width of the obstacle [49, 60, 101, 199, 200]. Very recently, Ref. [61] provided a numerical study of v_c as a function of the amplitude of the obstacle, building upon previous experimental results from the same team [195], described in the previous paragraph. This study extends beyond the rigid obstacle model developed in Ref. [58] by considering penetrable obstacles, of amplitude not necessarily larger than the chemical potential of the gas (impenetrable-obstacle regime of Frisch, Rica, Josserand, Pomeau and coworkers) and possibly lower than the latter (penetrable-obstacle regime). This approach is particularly relevant for experimentalists working with cold atoms (but also quantum fluids of light), where the obstacles are often generated by lasers with intensities comparable to the chemical potential of the system.

The study of superfluidity however extends beyond atomic systems, with significant experiments also conducted on polaritons in semiconductor microcavities [41, 201–203], later resulting in the clear evidence of superfluid motion in Ref. [118]. The authors observed the suppression of scattering from the defect when the velocity of the fluid is lower than the speed of sound, giving credit to the Landau criterion in such systems. In the nonsuperfluid state, the density profile of the system exhibits Čerenkov nonlinear radiations upstream and a Mach cone in the wake of the obstacle. Subsequent theoretical works aimed to explain these results in nonlinear optical systems [121, 162], further exploring superfluidity in polaritons in microcavities. These systems are analyzed within the mean-field Gross-Pitaevskii framework, leading to similar results to those observed for Bose gases, albeit within the context of quantum fluids of light. Various experimental setups have also been explored: Following Frisch's pioneering work, Ref. [204] focuses on the dynamics of a resonantly driven exciton-polariton flowing against an obstacle, demonstrating vortex emission when the velocity exceeds a certain threshold. This configuration is particularly relevant to our study, as it is similar to the one studied in this chapter.

More recently, new types of quantum fluids of light have been developed to bypass the need for a cavity and reduce losses in the system. In this manuscript, we particularly focus on quantum fluids of light in propagating geometries, such as photorefractive crystals [54, 55]. These experiments notably observed a vanishing drag force as the velocity approaches v_c, as well as the absence of long-range wave emission and the presence of vortices in the wake of the obstacle above that threshold (see the top part of Fig. 3.2, representing the intensity of the fluid for specific values of the velocity). Ultimately, these observations provide an experimental basis for estimating v_c. This critical velocity, as represented in the bottom part of Fig. 3.2, will be the central focus of Chap. 3, particularly in the case of wide obstacles. Here, v_c is illustrated as a function of the width d/ξ of the defect, revealing a spectrum of nonlinear structures that emerge when crossing the superfluid threshold. The associated intensity profiles represented in the top part of Fig. 3.2 further illustrate the fluid's behavior above v_c.

Yet, while v_c has been extensively studied through simulations and experiments, few analytical results aside from Ref. [61] exist when considering the penetrability of the obstacle,

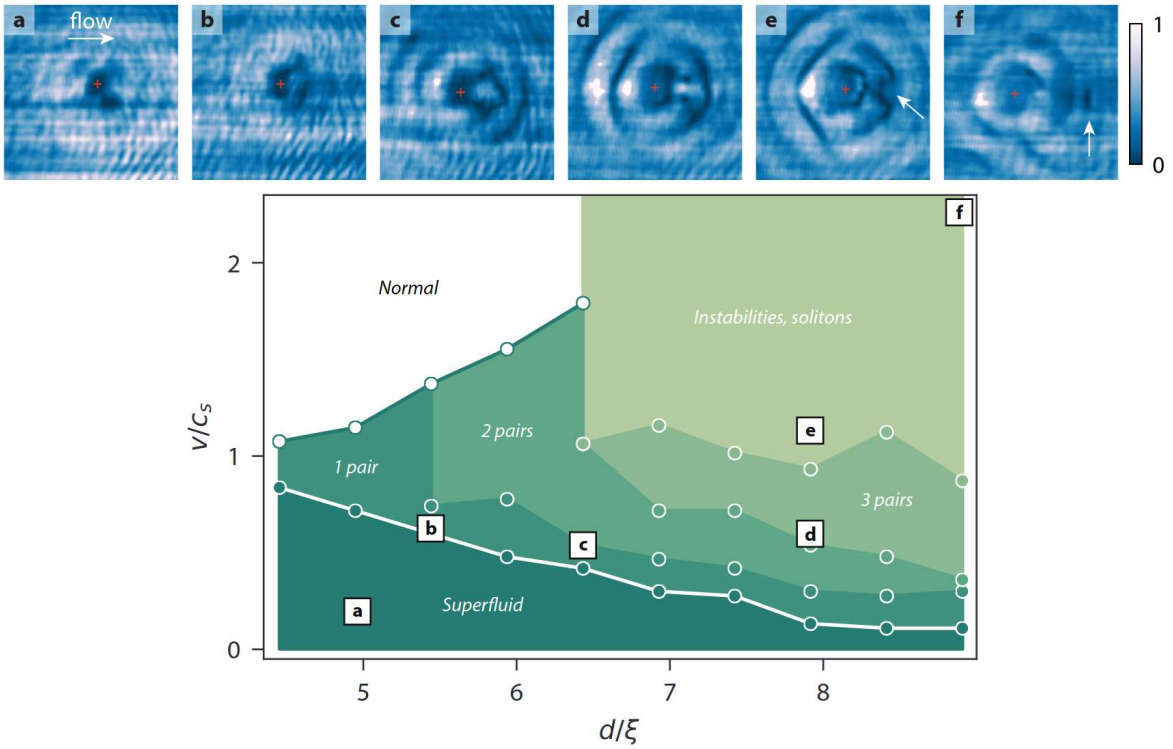

Figure 3.2: Top: Intensity of the 2D fluid of light in the transverse plane at the output of the nonlinear photorefractive crystal (for more details, we invite the reader to refer to the introduction of the manuscript). The fluid of light is here generated by a tilted laser beam propagating through a nonlinear photorefractive crystal, while the obstacle is created by another laser beam that locally modifies the refractive index. Insets (a–f) are obtained for various values of the input velocity and diameter of the obstacle, as indicated by the red cross. Bottom: Experimental diagram of the various phases of the fluid of light passing by an obstacle, as a function of the velocity v/c_s of the fluid, and the diameter d/ξ of the obstacle (c_s being the sound velocity in this case). The main focus of the present chapter is on the lower separatrix. The various regimes range from normal (white) to superfluid (dark green). The green scale in between separated by the circles corresponds to the observation of turbulent coherent structures: Vortex pairs, snake instabilities and solitons. Tags (a–f) are associated with the intensity profiles in the top part. Figures courtesy of Claire Michel, extracted from [55].

and even less for nonlinearities different from the standard $\varepsilon(n) = n$, i.e. those describing quantum fluids other than BECs, such as paraxial superfluids of light for instance. The aim of this chapter is to complement our results in 1D discussed in Chap. 1, and develop a new model to describe v_c for these more realistic obstacles (albeit with large width σ), thereby going beyond Frisch's results. Additionally, we extend this model to various types of nonlinearities to account for different experimental setups, ranging from BECs with a powerlaw nonlinearity, to the quantum fluids of light with a saturable nonlinearity that are central to this manuscript.

3.1 Two-dimensional mean-field regime

This section is part of a broader study in Chap. 3, which explores superfluidity in a two-dimensional quantum fluid of bosonic particles. While the dynamics of the system does not change much compared to the one-dimensional case, the shift to two dimensions introduces significant analytical challenges. We provide in this section the detailed model of our system – later used to derive the critical velocity for superfluidity in this more complex setting – as well as some preliminary results from the linear-response theory.

3.1.1 Analytical model and hydrodynamic equations

The dynamics of our system is, similarly to Chap. 1, ruled out by the Gross-Pitaevskii equation, in the absence of losses. We now focus on its two-dimensional reduction

$$i\partial_t\psi(\boldsymbol{r},t) = \left[-\frac{1}{2}\nabla^2 + U(\boldsymbol{r}) + \varepsilon(n)\right]\psi(\boldsymbol{r},t), \tag{3.1}$$

where $n(\boldsymbol{r},t) = |\psi(\boldsymbol{r},t)|^2$ is the density of the quantum fluid. We again derive the hydrodynamic equations using the Madelung transformation, in order to obtain equations on the density and velocity fields. The Gross-Pitaevskii equation thus transforms into the following system

$$\partial_t\boldsymbol{v} + \nabla\left[\frac{v^2}{2} + U(\boldsymbol{r}) + \varepsilon(n) - \frac{1}{2}\frac{\nabla^2\sqrt{n}}{\sqrt{n}}\right] = 0, \tag{3.2a}$$

$$\partial_t n + \nabla\cdot(n\boldsymbol{v}) = 0, \tag{3.2b}$$

where the velocity $\boldsymbol{v}(\boldsymbol{r},t) = \nabla\phi(\boldsymbol{r},t)$ is expressed in units of the speed of sound $c_\infty = \sqrt{n_\infty\varepsilon'(n_\infty)/m}$ or k. The interpretation of these equations is the same as in Chap. 1, and we invite the reader to refer to Sec. 1.1.4 for more details.

Finally, different condition are expected for a superfluid motion. The solutions must be stationary, which removes the dependence in time in Eqs. (3.2) and leads to time-independent density and velocity fields $n(\boldsymbol{r})$ and $\boldsymbol{v}(\boldsymbol{r})$. The fluid must also be devoid of any hydrodynamic disturbance far away from the obstacle [58]. At infinity, one then has $n(\boldsymbol{r}) = n_\infty = 1$ and $\boldsymbol{v}(\boldsymbol{r}) = \boldsymbol{v}_\infty = (v_\infty, 0)$ with $v_\infty > 0$ (the flow is from left to right). With these different assumptions, the hydrodynamic equations (3.2) simplify to

$$\frac{v^2}{2} + U(\boldsymbol{r}) + \varepsilon(n) - \frac{1}{2}\frac{\nabla^2\sqrt{n}}{\sqrt{n}} = \frac{v_\infty^2}{2} + \varepsilon(1), \tag{3.3a}$$

$$\nabla\cdot(n\boldsymbol{v}) = 0, \tag{3.3b}$$

Contrary to the method used in Chap. 1, the continuity equation (3.3b) does not simplify into a simple condition, and cannot be injected into Eq. (3.3a) to characterize the system with a single equation, yielding the critical velocity as the last solution of this equation: The system is not integrable anymore. We then use an analog method inspired from classical fluid mechanics to derive v_c, as performed in [58, 59]. This method is several-fold, and its different steps will later be detailed in Sec. 3.2.

3.1.2 The perturbative approach

Let us first study two-dimensional systems within the linear-response theory. In a similar approach to that performed in Chap. 1, we begin the study of superfluidity in 2D by examining the simplest case: A very small obstacle. This allows us to apply the linear-response theory for a weakly perturbating obstacle, as we did in one dimension in Sec. 1.2. The density fluctuations of the quantum fluid in this framework are given by

$$\frac{\delta n(\mathbf{r})}{n_\infty} = \int d\boldsymbol{r}\, U(\boldsymbol{r}')\chi\left(|\boldsymbol{r}-\boldsymbol{r}'|\right), \tag{3.4}$$

where the Green's function of the system is

$$\chi(\boldsymbol{r}-\boldsymbol{r}') = \frac{1}{2\pi^2}\int d\boldsymbol{k}\frac{k^2}{2}\frac{e^{i\boldsymbol{k}\cdot(\boldsymbol{r}-\boldsymbol{r}')}}{(\boldsymbol{v}_\infty\cdot\boldsymbol{k} - i0^+)^2 - E_B^2(k)}, \tag{3.5}$$

and the Bogoliubov dispersion relation is

$$E_B(k) = \sqrt{\frac{k^2}{2}\left[\frac{k^2}{2} + 2gn_\infty\right]}. \tag{3.6}$$

The passage in higher dimension complicates the problem, as the Green's function now involves a double integral of a complex function, which is in general hard to solve analytically. After converting the problem to polar coordinates and changing variables to $q = k\xi_\infty$, the response function becomes

$$\chi(|\boldsymbol{r}-\boldsymbol{r'}|) = -\frac{2}{\pi^2}\mathfrak{Re}\left\{\int_{-\pi/2}^{\pi/2} d\theta \int_0^{+\infty} dq\, \frac{q e^{i\frac{q}{\xi_\infty}|\boldsymbol{r}-\boldsymbol{r'}|\cos(\theta-\phi)}}{q^2-q_*^2}\right\}, \tag{3.7}$$

with ϕ being the angle between $\boldsymbol{k}$ and $\boldsymbol{r}-\boldsymbol{r'}$. As in Sec. 1.2, the poles of the integral are $q_* = \pm 2\sqrt{1-\frac{v_\infty^2}{c_\infty^2}\cos^2\theta} - i0^+$. These poles are either real (with a small imaginary part) for supersonic velocities, or purely imaginary for subsonic velocities. Even if Eq. (3.7) seems hard to solve analytically, it remains possible to provide the next step of the calculations of the Green's function. Equation (3.7) thus transforms to

$$\chi(|\boldsymbol{r}-\boldsymbol{r'}|) = -\frac{2}{\pi^2}\mathfrak{Re}\left\{-\frac{1}{2}\int_{-\pi/2}^{\pi/2} d\theta\, \left(e^{\alpha q_*}\mathrm{Ei}[-\alpha q_*] + e^{-\alpha q_*}\mathrm{Ei}[\alpha q_*]\right)\right\}, \tag{3.8}$$

with $\alpha = \frac{|\boldsymbol{r}-\boldsymbol{r'}|}{\xi_\infty}\cos(\theta-\phi)$.

It is interesting to look at the specific value of $\chi(\boldsymbol{r})$ at the origin, as the Green's function is actually the response function of the system to the perturbation caused by a $\delta-$peaked obstacle at $\boldsymbol{r}=\boldsymbol{0}$. By performing a Taylor expansion of the integrand around $|\boldsymbol{r}-\boldsymbol{r'}| \to 0$, i.e. $\alpha \to 0$, one can deduce its behavior close to the origin. The Green's function simplifies to

$$\chi(|\boldsymbol{r}-\boldsymbol{r'}|) = -\frac{2}{\pi}\mathfrak{Re}\left\{-\gamma - 2\int_0^{\pi/2} d\theta\, \ln[\alpha q_*]\right\}. \tag{3.9}$$

Let us now study more in details this simplified Green's function for a specific value of the velocity. We start off with the easiest analytical case possible for Eq. (3.7), i.e. the system at rest with $v_\infty = 0$ (and the angle $\phi = 0$). In that case, the density profile is symmetric, but this symmetry arises solely because the velocity of the fluid is null; As soon as the fluid begins to move, this symmetry is broken. The density fluctuations are localized around the $\delta-$peak obstacle $U(x) = \lambda\delta(x)$, with $\lambda = U_0 F(\sigma)$ its amplitude. The numerical integration leads to

$$\frac{\delta n(\boldsymbol{r})}{n_\infty} = -\frac{2\lambda}{\pi}\mathrm{K}_0\left[\frac{2|r|}{\xi_\infty}\right], \tag{3.10}$$

with K_0 the modified Bessel function of the second kind, and of order zero. This result is then validated by our calculations, since Eq. (3.9) reduces to

$$\chi(|\boldsymbol{r}-\boldsymbol{r'}|) = -\frac{2}{\pi}\left(-\gamma - \ln\left[\frac{|\boldsymbol{r}-\boldsymbol{r'}|}{\xi_\infty}\right]\right), \tag{3.11}$$

which is nothing more than the series expansion of $-\frac{2}{\pi}\mathrm{K}_0\left[\frac{2|\boldsymbol{r}-\boldsymbol{r'}|}{\xi_\infty}\right]$ around $|\boldsymbol{r}-\boldsymbol{r'}| \to 0$, with γ the Euler-Mascheroni constant.

These density fluctuations at zero velocity are illustrated in Fig. 3.3, where one can see a clear divergence at the origin, which is logarithmic. This divergence was indeed predicted given that the density of a fluid perturbed by a $\delta-$peak obstacle must necessarily be null at the origin in dimension higher than one [205]. Whenever the velocity of the fluid increases and is not zero anymore, this divergence still does not vanish: In the extreme case $v_\infty = c_\infty$, the Green's function presents the same divergence in $-\ln\left[\frac{|\boldsymbol{r}-\boldsymbol{r'}|}{\xi_\infty}\right]$. This presents a significant issue, as the validity of the linear-response theory relies on the fact that $|\delta n(\boldsymbol{r})/n_\infty| \ll 1$ everywhere – a condition that is unfortunately not satisfied here, even more so that the

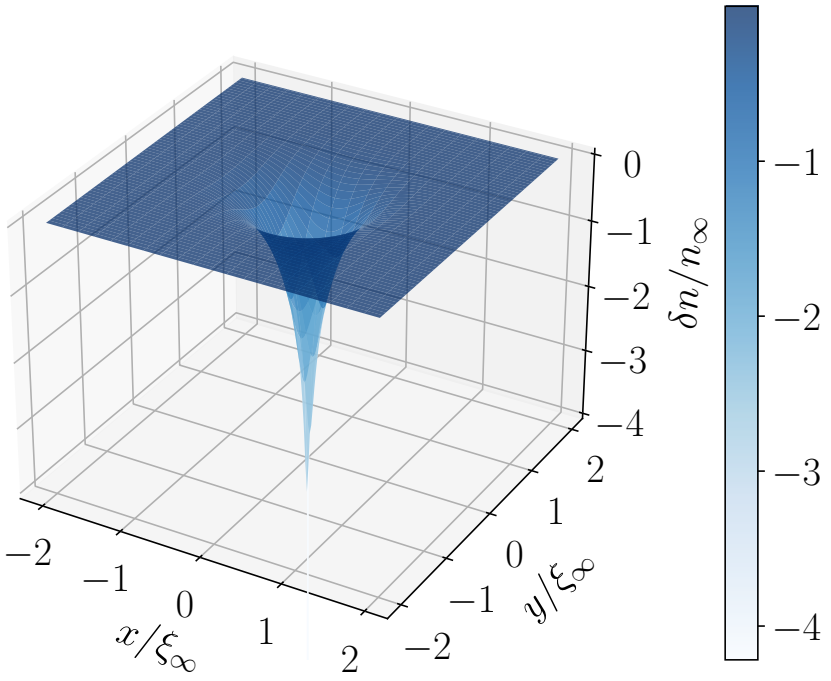

Figure 3.3: Density fluctuations of the fluid in the presence of a $\delta-$peak obstacle of amplitude $\lambda = 0.1$ and zero velocity, as given by Eq. (3.10). The profile is symmetric and exhibits a singularity at the origin, making it so that the linear-response theory fails.

corrections are such that $|\delta n(\boldsymbol{r})/n_\infty| > 1$, and the density fluctuations exhibit a singularity at $\boldsymbol{r} = \boldsymbol{0}$.

Ultimately, the linear-response theory inevitably fails for a $\delta-$peak in two-dimensions because the density must be zero at the origin, which contradicts the assumptions of this approach. This is different from the one-dimensional case, where the system's geometry forces the fluid to cross the obstacle in order to maintain the current continuity. This ensures that the density is never null, making the perturbative treatment valid.

Nevertheless, the perturbation theory yields acceptable results far away from the origin, and it is ultimately in this region of space that one can determine whether energy radiation occurs or not. Two different behaviors arise depending on the velocity of the fluid:

- If $v_\infty < c_\infty$: There are no density fluctuations for $r \to \infty$ and the density is flat, i.e. $n(r) = n_\infty = 1$.

- If $v_\infty > c_\infty$: Following Ref. [206], it can be shown that, upstream, Čerenkov radiations are emitted outside a cone; For example if one considers a cut at $y = 0$, then the density along x upstream of the obstacle reads

$$n(x) = 2U_0 \sqrt{\frac{\left(\frac{v_\infty^2}{c_\infty^2} - 1\right)^{1/2}}{\pi\left(\frac{2v_\infty^2}{c_\infty^2} + 1\right)|x|}} \cos\left[-2\sqrt{\frac{v_\infty^2}{c_\infty^2} - 1}x - \frac{\pi}{4}\right]. \tag{3.12}$$

Despite the logarithmic divergence at the origin, the linear-response theory predicts a drastic change of behavior in the density profile at $v_\infty = c_\infty$ far from the obstacle. This denotes a superfluid transition in agreement with the Landau criterion.

3.2 The method to obtain the critical velocity for superfluidity

Building on the analytical model presented at the beginning of the present chapter, we now extend the analysis to encompass nonperturbative obstacles of arbitrary amplitude and width, thus going beyond the linear-response theory. In this section, we provide the method to obtain an analytical expression for the critical velocity for superfluidity in two dimensions, which is composed of several steps. This method is then applied to the two different cases of impenetrable and penetrable obstacles, leading to the emergence of two mechanisms for the breakdown of superfluidity.

3.2.1 Step 1: Superfluid condition in the hydraulic approach

In Chap. 1, we derived a condition for superfluidity by obtaining an implicit expression for the density through the "Euler"-like equation, integrating the continuity equation, and then combining the two. This resulted into a single equation on the density, parametrized by v_∞. The critical velocity for superfluidity corresponded to the first velocity v_∞ for which the stationary solutions to that equation disappeared. However, this method is not possible anymore in two dimensions, because the continuity equation is not integrable as it is presented in Eq. (3.3b). Therefore, we must develop a different approach to determine the condition for superfluid motion in 2D.

Fortunately, it is still possible to exploit the dependence of $n(\boldsymbol{r})$ on $v(\boldsymbol{r})$ in 2D, obtained from Eq. (3.3a) by re-expressing the continuity equation in the hodograph plane [207], where it transforms into a linear PDE in the new coordinates (v, θ)

$$\partial_v^2 \Phi + \frac{1}{nv} \partial_v (nv) \partial_v \Phi + \frac{1}{nv^2} \partial_v (nv) \partial_\theta^2 \Phi = 0, \tag{3.13}$$

where $\Phi(\boldsymbol{v}) = \boldsymbol{v} \cdot \boldsymbol{r} - \phi(\boldsymbol{r})$ is the Legendre transform of the velocity potential $\phi(\boldsymbol{r})$. The full derivation of Eq. (3.13) is provided in Appendix A.1.

Equation (3.13) is then studied with the method of characteristics, to determine a condition on n and v for which no perturbation can propagate along a characteristic curve whose equation $\theta = \theta(v)$ is provided by the relation

$$\frac{\mathrm{d}\theta}{\mathrm{d}v} = \pm \sqrt{-\frac{1}{nv^2} \partial_v (nv)}. \tag{3.14}$$

The calculations leading to this result are provided in Appendix A.2. For the motion to be superfluid, Eq. (3.14) must be complex-valued for all v, in which case Eq. (3.13) is elliptic. Since n and v are always positive, the condition for superfluid motion is

$$\partial_v (nv) > 0. \tag{3.15}$$

Generalized local Landau criterion
Equation (3.3a) can be rearranged in the form

$$E(n) = \varepsilon(n) + \mathcal{Q}(n) = \varepsilon(1) - U(\boldsymbol{r}) - \frac{v^2 - v_\infty^2}{2}, \tag{3.16}$$

where $\mathcal{Q}(n) = -\frac{1}{2}\frac{\nabla^2\sqrt{n}}{\sqrt{n}}$ is the quantum pressure. Differentiating this equation with respect to $v(\boldsymbol{r})$, one gets

$$\partial_v n = -\left[\partial_n E(n)\right]^{-1} v = -\left[\partial_n \varepsilon(n) + \partial_n \mathcal{Q}(n)\right]^{-1} v, \tag{3.17}$$

which yields

$$\partial_v(nv) = n + v\partial_v n = n\left(1 - v\left[n\partial_n\varepsilon(n) + n\partial_n\mathcal{Q}(n)\right]^{-1} v\right) > 0 \tag{3.18}$$

for the superfluid condition (3.15). Identifying $n\partial_n\varepsilon(n)$ to the square of the local speed of sound $c(\boldsymbol{r})$, one finally obtains the superfluid condition in the form

$$v(\boldsymbol{r})\left[c^2(\boldsymbol{r}) + n(\boldsymbol{r})\partial_n\mathcal{Q}\left(n(\boldsymbol{r})\right)\right]^{-1} v(\boldsymbol{r}) < 1, \tag{3.19}$$

valid $\forall \boldsymbol{r}$. This is nothing but the local Landau criterion at zero quantum pressure. Condition (3.19) extends the latter criterion beyond the hydraulic approach, with a renormalization of the square of the local speed of sound by the operator

$$n(\boldsymbol{r})\partial_n\mathcal{Q}(n(\boldsymbol{r})) = n(\boldsymbol{r})\frac{1}{4}\left[\frac{1}{n(\boldsymbol{r})}\nabla\left(\frac{\nabla n(\boldsymbol{r})}{n(\boldsymbol{r})}\right) - \nabla\left(\frac{\cdot}{n(\boldsymbol{r})}\right)\right]. \tag{3.20}$$

In this chapter, we work within the hydraulic approach, i.e. $\mathcal{Q}(n) \to 0$. With this assumption, the condition for superfluid motion (3.19) reduces to the well-known result $v^2(\boldsymbol{r}) < c^2(\boldsymbol{r})$, with $c(\boldsymbol{r}) = \sqrt{n(\boldsymbol{r})\partial_n\varepsilon}$ the local speed of sound. This constraint is also equivalent to the same inequality with $v(\boldsymbol{r})$ and $c(\boldsymbol{r})$ respectively replaced by their maximum $v_{\max}$ and minimum $c_{\min}$, reached where the density of the quantum fluid is minimum. In the end, this means

$$v_{\max}^2 < n_{\min}\partial_n\varepsilon(n_{\min}). \tag{3.21}$$

This condition is valid if $\partial_n\varepsilon(n)$ is a monotonically increasing function, which is verified for the nonlinearities we considered in this manuscript. In the end, the condition $v(\boldsymbol{r}) < c(\boldsymbol{r}) \Leftrightarrow \partial_v(n\boldsymbol{v}) > 0$: The local Landau criterion is not merely phenomenological – It also has a mathematical foundation as it is formally obtained from the ellipticity of the continuity equation (3.15).

In the hydraulic approach, the density profile is implicitly given by

$$\varepsilon(n(\boldsymbol{r})) = \varepsilon(1) - U(\boldsymbol{r}) - \frac{v^2(\boldsymbol{r}) - v_\infty^2}{2}. \tag{3.22}$$

The density $n_{\min}$ used in the local Landau criterion (3.21) is obtained when $U(\boldsymbol{r})$ and $v(\boldsymbol{r})$ are maximum, such that

$$\varepsilon(n_{\min}) = \varepsilon(1) - \max\left[U(\boldsymbol{r})\right] - \frac{v_{\max}^2 - v_\infty^2}{2}. \tag{3.23}$$

In the end, one only needs to find the maximum velocity $v_{\max}(v_\infty, \max\left[U(\boldsymbol{r})\right])$ to obtain the superfluid condition from Eq. (3.21).

What type of obstacle? In order to obtain the expression of $v_{\max}$, one has to solve the continuity equation (3.3b), which notably requires specifying the shape of the obstacle in our model. We consider it as one of the simplest possible: A disk, i.e. a constant piece-wise obstacle. We thus treat the problem using polar coordinates, simplifying the calculations, and allowing us to derive exact results. We also consider that the typical radius σ of the obstacle is really large compared to the healing length ξ_∞, thus justifying the use of the hydraulic approximation. The obstacle is then defined by

$$U(\boldsymbol{r}) = \begin{cases} U_0 & \text{if } r < \sigma, \\ 0 & \text{otherwise.} \end{cases} \tag{3.24}$$

A Gaussian-shaped obstacle would have been ideal for our model, given its common use in real experiments with BECs or with paraxial fluids of light. However, such a potential does not allow for a full analytical treatment beyond a certain point. Additionally, we found that these results obtained from a Gaussian potential are similar to those from our simpler model. Therefore, our disk-shaped obstacle is well-suited, and provides an appropriate framework for v_c in 2D, yielding results consistent with those obtained from more realistic obstacles.

We can now derive the condition for superfluid motion for the same nonlinearities as before, which are as follows.

Powerlaw nonlinearity $\varepsilon(n) = n^\nu/\nu$: Equation (3.21) becomes

$$1 - \nu U_0 + v_\infty^2 \left[\frac{\nu}{2} - \frac{v_{\max}^2}{v_\infty^2} \left(1 + \frac{\nu}{2} \right) \right] > 0. \tag{3.25}$$

Saturable nonlinearity $\varepsilon(n) = (1+\beta)^2 \frac{n}{1+\beta n}$ with $\beta = 1/n_{\text{sat}}$: The condition for superfluid motion is more complicated, and reads

$$4\Big[(1+\beta)^2 - \left(1-\beta^2\right) U_0 - \beta\, U_0^2\Big] - 2v_\infty^2 \left[\frac{v_{\max}^2}{v_\infty^2} \left(3 + 2\beta(U_0+2) + \beta^2 \right) - 1 - 2\beta\, U_0 + \beta^2 \right] - \beta v_\infty^4 \left(\frac{v_{\max}^2}{v_\infty^2} - 1 \right)^2 > 0. \tag{3.26}$$

After deriving the value of $v_{\max}$, the condition for superfluidity is nothing more than a polynomial in v_∞, which resolution leads to $v_\infty < v_c$.

3.2.2 Step 2: Solving the hydrodynamic equations in the incompressible approximation

Now that we have specified a condition for superfluid motion, we need to find the expression of the maximum velocity $v_{\max}$ in the fluid in order to derive the critical velocity for superfluidity. To do so, we must solve the hydrodynamic equations (3.3), again treated in the hydraulic approximation ($\mathcal{Q}(n(\boldsymbol{r})) \to 0$) – This is an important assumption, which is also one of the limitations of our model.

Following the treatment performed in Ref. [58], we assume that the typical radius σ of the obstacle is such that $\sigma \gg \xi_\infty$. In this problem, the healing length ξ_∞ is an important scale that enters into play twice: It determines the typical radius of a vortex core, as well as the thickness of the boundary layer that forms around the obstacle. As the radius σ of the disk is large compared to ξ_∞, one can deduce as a first approximation an asymptotic solution in which the quantum pressure term is neglected in Eq. (3.3a): This amounts to neglecting

what happens in the boundary layer. From there, one can infer an analytical expression for the density field of the quantum fluid moving at velocity $\boldsymbol{v}(\boldsymbol{r})$

$$n(\boldsymbol{r}) = \varepsilon^{-1}\left[\varepsilon(1) - U_0 - \frac{\chi}{2}\left(\frac{|\nabla\phi(\boldsymbol{r})|^2}{v_\infty^2} - 1\right)\right], \tag{3.27}$$

where $\chi = v_\infty^2$ denotes the asymptotic compressibility [19] of the superfluid in units of $1/(\text{mass} \times v_\infty^2)$. In the incompressible limit $\chi \to 0$, the density given by Eq. (3.27) is a constant piece-wise function that reads

$$n(\boldsymbol{r}) = \begin{cases} \varepsilon^{-1}\left[\varepsilon(1) - U_0\right] & \text{if } r < \sigma, \\ 1 & \text{otherwise.} \end{cases} \tag{3.28}$$

In this case, $\nabla \cdot \boldsymbol{v}(\boldsymbol{r}) = 0$, and the velocity potential ϕ (defined as $\boldsymbol{v} = \nabla\phi$) satisfies the Laplace equation, a well-known problem for incompressible potential flows around a circular cylinder in classical fluid mechanics. Given the shape of the obstacle, we can provide the exact analytical expression of the density profile in the incompressible limit, for two different nonlinear interaction potentials (in their rescaled forms).

Powerlaw nonlinearity $\varepsilon(n) = n^\nu/\nu$**:**

$$n(\boldsymbol{r}) = \left[1 - \nu U_0\right]^{\frac{1}{\nu}}. \tag{3.29}$$

Saturable nonlinearity $\varepsilon(n) = (1+\beta)^2 \frac{n}{1+\beta n}$ **with** $\beta = 1/n_{\text{sat}}$**:**

$$n(\boldsymbol{r}) = \frac{\frac{1}{1+\beta}\left[1 - \frac{U_0}{1+\beta}\right]}{1 - \frac{\beta}{1+\beta}\left[1 - \frac{U_0}{1+\beta}\right]}. \tag{3.30}$$

We remind that we need to solve the continuity equation (3.3b) to obtain $v_{\max}$, and then the critical velocity for superfluidity. This equation can be re-expressed as

$$n(\boldsymbol{r})\nabla^2\phi_0(\boldsymbol{r}) + \nabla n(\boldsymbol{r})\nabla\phi_0(\boldsymbol{r}) = 0, \tag{3.31}$$

which is nothing but the Laplace equation $\nabla^2\phi_0(\boldsymbol{r})$ since the density profile is constant in the hydraulic approach.

The boundary conditions We complement this problem with the proper boundary conditions. Two types of boundary conditions are used: The asymptotic boundary condition at infinity; And the boundary condition at the interface of the obstacle, which strongly depends on the value of U_0.

Far from the obstacle ($r \gg \sigma$), the fluid must remain unperturbed, i.e. $n(\boldsymbol{r}) = n_\infty = 1$, and the asymptotic boundary condition is always the same no matter the amplitude of the obstacle. We have a uniform flow upstream $\boldsymbol{v}(r \gg \sigma) = (v_\infty, 0)$, meaning that in polar coordinates the velocity potential is

$$\phi(r \gg \sigma) = v_\infty r\cos\theta \quad \text{for} \quad r \gg \sigma. \tag{3.32}$$

Different dynamics can then take place depending on whether the obstacle is impenetrable, or penetrable. It is important to treat these different cases with the proper boundary conditions at $x = \sigma$. They strongly differ depending on the amplitude U_0 of the obstacle, and are provided in Secs. 3.3 and 3.4, in which we derive exact analytical results for v_c for both the impenetrable and the penetrable regimes respectively, and for two different nonlinearities.

How is the penetrability of the obstacle accounted for in the equations?
To determine whether an obstacle is penetrable or not, one argument is to impose that the density must always be positive in the incompressible approximation. Referring to Eq. (3.27) with $\chi = 0$, one can see that the density is positive if

$$\varepsilon(1) - U_0 > 0, \tag{3.33}$$

leading to $U_0 < \varepsilon(1)$, an upper bound for the penetrability of the obstacle. In the end, $U_0 < \varepsilon(1)$ means a penetrable obstacle, and $U_0 > \varepsilon(1)$ an impenetrable one.

After solving the Laplace equation $\nabla^2\phi_0(\boldsymbol{r})$ with the proper boundary conditions, one obtains ϕ_0, deduces $v_{\max}$, and solves the superfluid condition to obtain the critical velocity for superfluidity in the incompressible approximation.

3.2.3 Step 3: Solving the hydrodynamic equations beyond the incompressible approximation using Janzen-Rayleigh expansions

As a matter of fact, using the approximation $\chi \to 0$ is not entirely justified because the fluid is not strictly incompressible. One has to take into account the fact that the density field will drastically change in the vicinity of the obstacle and possibly cross it, but these changes will take place continuously and not abruptly. It is then not possible to neglect the spatial dependence of the density. We derive these "new" density profiles for the previously-stated nonlinearities, which are as follows.

Powerlaw nonlinearity $\varepsilon(n) = n^\nu/\nu$:

$$n(\boldsymbol{r}) = \left[1 - \nu U_0 - \frac{\nu\chi}{2}\left(\frac{|\nabla\phi(\boldsymbol{r})|^2}{v_\infty^2} - 1\right)\right]^{\frac{1}{\nu}}. \tag{3.34}$$

Saturable nonlinearity $\varepsilon(n) = (1+\beta)^2 \frac{n}{1+\beta n}$ with $\beta = 1/n_{\text{sat}}$:

$$n(\boldsymbol{r}) = \frac{\frac{1}{1+\beta}\left[1 - \frac{U_0}{1+\beta} - \frac{\chi}{2(1+\beta)}\left(\frac{|\nabla\phi(\boldsymbol{r})|^2}{v_\infty^2} - 1\right)\right]}{1 - \frac{\beta}{1+\beta}\left[1 - \frac{U_0}{1+\beta} - \frac{\chi}{2(1+\beta)}\left(\frac{|\nabla\phi(\boldsymbol{r})|^2}{v_\infty^2} - 1\right)\right]}. \tag{3.35}$$

The variations we add to the density profile $n(\boldsymbol{r})$ compared to the incompressible approximation provided in Eqs. (3.29) and (3.30), albeit nonnegligible, are still small enough that we can treat them perturbatively through an expansion of the velocity potential in powers of $\chi \ll 1$.

This problem of a potential compressible flow over a circular obstacle was first tackled by Janzen and Rayleigh in the 1910s [208, 209]. Following Ref. [59], we refine the results obtained for the incompressible approximation by searching for the velocity potential in the Janzen-Rayleigh form, i.e. a power series in χ to the highest order possible:

$$\phi(\boldsymbol{r}) = \phi_0(\boldsymbol{r}) + \phi_1(\boldsymbol{r})\chi + ... + \phi_k(\boldsymbol{r})\chi^k + ..., \tag{3.36}$$

with $\chi \ll 1$ and $k \geqslant 0$ being the index of the expansion in powers of χ. This expansion of the velocity potential in powers of χ is then injected into the expression of $n(\boldsymbol{r})$ provided in Eq. (3.27), leading to an expansion of the density around the incompressible solution, for $\chi \ll 1$. Ultimately, the higher the value of k, the more accurate the correction to the critical velocity added to the incompressible solution. However, it is still important to note that while

Janzen-Rayleigh expansions offer a nonnegligible corrections to v_c, these corrections are still smaller than those that could be obtained by incorporating the quantum pressure term to go beyond the hydraulic approximation.

Additionally, Janzen-Rayleigh expansions can sometimes exhibit oscillatory behaviors as the number of terms in the expansion increases. This oscillation arises from the perturbative nature of the method, where higher-order terms in the series can grow larger, causing oscillations around the exact solution. In conclusion, even though the expansion provided a meaningful correction to v_c, it would not be advisable to extend the expansion to significantly higher orders.

One now almost has all the tools to solve the differential problem, and obtain an analytical expression for the $v_{c,k}$'s taking into account the Janzen-Rayleigh expansion. The only missing part is the maximum velocity $v_{\max}$, which must be injected into the condition for superfluid motion (3.15) to obtain the critical velocity.

Knowing the density profile with the Janzen-Rayleigh expansion, it is now possible to obtain the equation describing the dynamics of the quantum fluid in the presence of the cylindrical obstacle. It is given by the continuity equation (3.3b), which develops into

$$n(\boldsymbol{r})\nabla^2\phi(\boldsymbol{r}) + \nabla n(\boldsymbol{r})\nabla\phi(\boldsymbol{r}) = 0, \tag{3.37}$$

with $n(\boldsymbol{r})$ defined in Eq. (3.27), and $\phi(\boldsymbol{r})$ in Eq. (3.36). This equation must then be solved order by order in χ.

We now provide the explicit expression of the continuity equation for two different nonlinearities. These equations are computed order by order in χ, which leads to the establishment of recurrence relations between the different $\phi_k(\boldsymbol{r})$'s of the Janzen-Rayleigh expansion. From there, one can find the expression of the maximum velocity for a given k, given by $v_{\max,k} = |\nabla\phi_k(\sigma, \pi/2)|$, and the total maximum velocity is given by $v_{\max} = v_{\max,0} + v_{\max,1}\chi + ... + v_{\max,k}\chi^k$.

Powerlaw nonlinearity $\varepsilon(n) = n^\nu/\nu$: Equation (3.37) becomes

$$\left[1 - \nu U_0 - \frac{\nu\chi}{2}\left(\frac{v^2}{v_\infty^2} - 1\right)\right]\nabla^2\phi = \frac{\chi}{2v_\infty^2}\nabla(v^2)\nabla\phi. \tag{3.38}$$

When expanding this equation order by order in the compressibility χ in the density and velocity potential, one can deduce a recurrence relation between the different ϕ_k's

$$(1 - \nu U_0)\nabla^2\phi_{k+1} = -\frac{\nu}{2}\nabla^2\phi_k + \frac{1}{2v_\infty^2}\sum_{j=0}^{k}\left[\nabla\phi_{k-j}\cdot\nabla(v^2)_j + \nu\nabla^2\phi_{k-j}(v^2)_j\right], \tag{3.39}$$

where we introduced $(v^2)_k = \sum_{j=0}^{k}\nabla\phi_{k-j}\nabla\phi_j$ for the sake of readability. The resolution of these Poisson equations for each ϕ_k will lead to the different $v_{\max,k}$ we are searching for.

Saturable nonlinearity $\varepsilon(n) = (1+\beta)^2\frac{n}{1+\beta n}$ with $\beta = 1/n_{\text{sat}}$: For a saturable nonlinearity, Eq. (3.37) becomes

$$\left[A - B\chi\left(\frac{v^2}{v_\infty^2} - 1\right) - C\chi^2\left(\frac{v^2}{v_\infty^2} - 1\right)^2\right]\nabla^2\phi = \frac{\chi}{2v_\infty^2}\nabla(v^2)\nabla\phi, \tag{3.40}$$

with

$$A = 1 - \frac{U_0(1-\beta)}{1+\beta} - \frac{\beta U_0^2}{(1+\beta)^2}, \tag{3.41a}$$

$$B = \frac{1 + 2\beta U_0 - \beta^2}{2(1+\beta)^2}, \tag{3.41b}$$

$$C = \frac{\beta}{4(1+\beta)^2}. \tag{3.41c}$$

The expression for the recurrence relation between the various $\nabla\phi_k$'s is given by

$$A\nabla^2\phi_{k+2} = -B\nabla^2\phi_{k+1} + C\nabla^2\phi_k + \frac{1}{2v_\infty^2}\sum_{j=0}^{k+1}\left[\nabla\phi_{k+1-j}\cdot\nabla(v^2)_j + 2B\nabla^2\phi_{k+1-j}(v^2)_j\right] - \frac{2C}{v_\infty^2}\sum_{j=0}^{k}\nabla^2\phi_{k-j}(v^2)_j + \frac{C}{v_\infty^4}\sum_{j=0}^{k}\nabla^2\phi_{k-j}\left(\sum_{i=0}^{j-i}(v^2)_i(v^2)_j\right). \tag{3.42}$$

Similarly, we deduce the values of each $v_{\max,k}$ from the different expressions of ϕ_k obtained after solving the Poisson equation for each k.

3.2.4 In short...

As the reader can attest, the procedure to analytically derive the critical velocity for superfluidity involves several important steps and various mathematical methods. The present section provides a short account of the method used to derive the critical velocity for superfluidity up to an arbitrary order in the compressibility.

- Using a Janzen-Rayleigh expansion of the velocity potential around the incompressible solution to solve the problem, we perturbatively solve the hydrodynamic equations in the hydraulic approximation for a disk-shaped obstacle of arbitrary amplitude to obtain the expression of the velocity potential $\phi_k(\boldsymbol{r})$ for each k.
- The maximum velocity is that at the poles of the obstacle: By injecting it to the new condition for superfluid motion – strictly equivalent to the local Landau criterion – we can obtain an exact analytical expression for the critical velocity for superfluidity for a given order in the perturbative expansion.

3.3 Impenetrable obstacles $U_0 > \varepsilon(1)$

As previously shown in Chap. 1 for one-dimensional systems, the critical velocity for superfluidity becomes exponentially negligible when the obstacle amplitude gets larger than $\varepsilon(1)$, regime within which the defect is classically impenetrable and the fluid is, in the hydraulic approach, cut into two disconnected part. This is not the case anymore in a 2D setting, in which the fluid is able to go around the obstacle, yielding a possibly nonzero critical speed v_c. The case of the two-dimensional impenetrable obstacle was first studied in 1992 by Frisch *et al.* in Ref. [58], in which the authors obtained the expression of the critical velocity for superfluidity for a supposedly impenetrable disk-shaped obstacle in the incompressible approximation, yielding $v_{c,0} = \sqrt{2/11}$ for $\varepsilon(n) = n$ (and corresponding to the order $k = 0$ of the Janzen-Rayleigh expansion, though this method was not used at the time). A few years later, this model was refined by Rica in Ref. [59], in which he presented the inclusion of the compressibility via the Janzen-Rayleigh expansion for low χ, computed order by order the full superfluid flow around the disk, and derived a refined value of the critical velocity for superfluidity. This paper provides $v_{c,k}$'s up to the 11^{th} order in χ, converging to $v_{c,11} = 0.369$ for $\varepsilon(n) = n$.

In this section, we go beyond these previous results that stood for the impenetrable regime only by deriving exact analytical expressions for $v_{c,k}$ for a powerlaw or a saturable nonlinearity. Using the method previously explained, we compute results respectively up to order $k = 6$ and $k = 4$ in the Janzen-Rayleigh method, and verified their correspondence with the results obtained by Rica in Ref. [59] in the appropriate limits.

3.3.1 Boundary condition at $r = \sigma$

Since the obstacle is impenetrable, the dynamics of the system is as follows: The fluid cannot cross it and is forced to go around it, which is only possible because the system is bidimensional. As a result, the density for $r < \sigma$ is null (but not necessarily at $r = \sigma$), and the Gross-Pitaevskii equation (3.1) only applies for $r > \sigma$, in which case $U_0 = 0$.

The boundary condition we implement for the impenetrable obstacle pertains to the derivative of the velocity potential, and must be valid for each order k of the Janzen-Rayleigh expansion. It is quite simple – making it valid no matter the expression of the nonlinear interaction potential $\varepsilon(n)$ – and reads

$$\partial_r \phi_k(\sigma) = 0 \quad \forall\theta, \tag{3.43}$$

i.e. the normal velocity is null at $r = \sigma$ since the flow cannot cross the obstacle. The velocity of the fluid is thus purely tangential at $r = \sigma$: This is the no-slip boundary condition of classical hydrodynamics [207], generally used for solid boundaries.

This case is reminiscent of the dynamics of a potential flow around a disk in classical fluid mechanics, with the same stagnation points at the rear side and the front side of the obstacle ($r = \sigma$, $\theta \in \{0, \pi\}$). The point of maximum velocity is obtained at the poles of the obstacle, i.e. $v_{\max} = v(\sigma, \pm\pi/2)$, as we explicitly show below.

3.3.2 The incompressible solution

The case of the incompressible solution for an impenetrable obstacle is peculiar in a sense that almost all the results are the same no matter the expression of the nonlinear interaction potential $\varepsilon(n)$: They obey the same continuity equation with same boundary conditions, thus leading to same velocity potential $\phi_0(\boldsymbol{r})$, and maximum velocity $v_{\max,0}$. The only difference when changing $\varepsilon(n)$ will be the condition for superfluidity, which will be provided by Eqs. (3.25) or (3.26) for a powerlaw or a saturable nonlinearity respectively. Since the obstacle is impenetrable, the fluid is restricted to the region $r > \sigma$ where the obstacle is null. Consequently, the hydrodynamic equations (3.2) must be solved without obstacle, which greatly simplifies the problem as it is equivalent to formally consider $U_0 = 0$. As a result, the critical velocity $v_{c,0}$ will not depend on the parameters of the obstacle but rather only the parameters of $\varepsilon(n)$ (i.e. ν for the powerlaw nonlinearity, or β for the saturable nonlinearity).

To obtain the zeroth-order critical velocity $v_{c,0}$, one first has to solve the continuity equation with $\chi = 0$, which reduces to $\nabla \cdot \boldsymbol{v}(\boldsymbol{r}) = 0$, and by extension to Laplace's equation

$$\nabla^2 \phi_0(\boldsymbol{r}) = 0, \tag{3.44}$$

which, in polar coordinates, reads

$$\frac{1}{r}\partial_r \left(r \partial_r \phi_0\right) + \frac{1}{r^2}\partial_\theta^2 \phi_0 = 0. \tag{3.45}$$

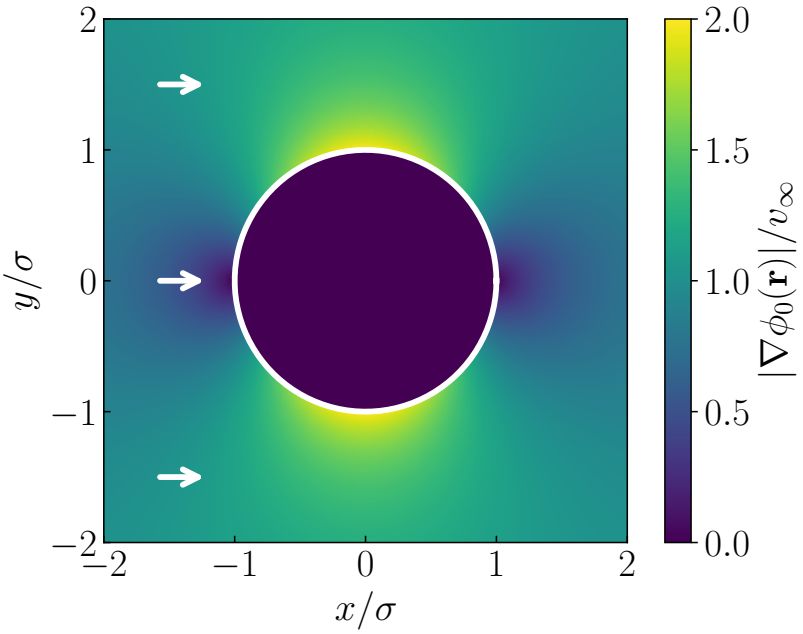

Figure 3.4: Norm of the velocity field $\boldsymbol{v}_0(\boldsymbol{r}) = \nabla\phi_0(\boldsymbol{r})$ in the incompressible approximation ($k = 0$) and for an impenetrable obstacle. $\boldsymbol{v}_0(\boldsymbol{r})$ is derived from the expression of the velocity potential provided in Eq. (3.47), valid for any $\varepsilon(n)$. The boundary condition implemented imposes that the normal velocity must be null at $r = \sigma$, leading to $v_0(\sigma, \{0, \pi\}) = 0$, corresponding to the stagnation points of classical hydrodynamics. Similarly, the maximum of velocity is obtained at the poles of the obstacle and is $v_{\mathrm{max},0} = v_0(\sigma, \pm\pi/2) = 2v_\infty$. The obstacle is represented by a disk of radius σ.

The resolution of Laplace's equation in polar coordinates is a well-known problem of classical physics that can be solved using the separation of variables, such that $\phi(r, \theta) = R(r)\Theta(\theta)$. The resolution leads to a general solution of the form

$$\phi_0(r, \theta) = a_0 + b_0 \ln r + \sum_{n=1}^{\infty} \left[A_n r^n + C_n r^{-n}\right] \cos n\theta + \sum_{n=1}^{\infty} \left[B_n r^n + D_n r^{-n}\right] \sin n\theta, \tag{3.46}$$

where the various coefficients a_0, b_0, A_n, B_n, C_n and D_n are obtained using the boundary conditions given by Eqs. (3.32) and (3.43). In our case, we remind that the asymptotic boundary condition is $\phi_0(r \gg \sigma, \theta) = v_\infty r \cos\theta$, which imposes that $a_0 = b_0 = 0$, each $B_n = 0$, $A_n = 0$ for $n > 1$, and $A_1 = v_\infty$. The condition at the interface of the obstacle, i.e. $\partial_r \phi_0(\sigma, \theta) = 0$, imposes that each $D_n = 0$, and that $C_1 = A_1\sigma^2$. In the end, the velocity potential in the incompressible approximation reads

$$\phi_0(\boldsymbol{r}) = v_\infty r \left[1 + \frac{\sigma^2}{r^2}\right] \cos\theta, \tag{3.47}$$

from which one infers $v_{\mathrm{max},0} = |\nabla\phi_0(\sigma, \pm\pi/2)| = 2v_\infty$. The velocity field in the incompressible approximation ($\chi = 0$) is represented in Fig. 3.4, where one can clearly see the stagnation points at the boundaries of the obstacle for $\theta \in \{0, \pi\}$, as well as the points of maximum velocity for $\theta = \pm\pi/2$.

The role of $\varepsilon(n)$ now comes into play as one has to apply the superfluid condition, and so to solve Eqs. (3.25) or (3.26) – which are functions of ν or β – with $v_{\mathrm{max},0} = 2v_\infty$.

Powerlaw nonlinearity $\varepsilon(n) = n^\nu/\nu$: From $v_{\mathrm{max},0} = 2v_\infty$, one can use the condition for superfluid motion given by Eq. (3.25) applied to our problem, which transforms to

$$1 + v_\infty^2 \left[\frac{\nu}{2} - 4\left(1 + \frac{\nu}{2}\right)\right] > 0. \tag{3.48}$$

The resolution of this polynomial leads to

$$v_\infty < v_{c,0} = \sqrt{\frac{2}{8+3\nu}}. \tag{3.49}$$

When $\nu = 1$, one recovers the expression of the critical velocity $v_{c,0} = \sqrt{2/11} = 0.426401$, first established in Ref. [58].

Saturable nonlinearity $\varepsilon(n) = (1+\beta)^2 \frac{n}{1+\beta n}$ with $\beta = 1/n_{\rm sat}$: Similarly to the previous case, one uses the expression of the maximum velocity $v_{\max,0} = 2v_\infty$ in the condition for superfluid motion for a saturable system given by Eq. (3.26). This polynomial reads

$$4(1+\beta)^2 - 2v_\infty^2\left[4\left(3+4\beta+\beta^2\right) - 1 + \beta^2\right] - \beta v_\infty^4 (4-1)^2 > 0, \tag{3.50}$$

and its resolution leads to

$$v_\infty < v_{c,0} = \frac{1}{3}\sqrt{\frac{\sqrt{(1+\beta)^3(121+25\beta)}}{\beta} - \left(5\beta + 16 + \frac{11}{\beta}\right)}. \tag{3.51}$$

One also recovers $v_{c,0} = \sqrt{2/11} = 0.426401$ obtained by Frisch *et al.* in Ref. [58] by taking the limit $\beta \to 0$, i.e. $n_{\rm sat} \gg 1$, in which case $\varepsilon(n) = n$.

3.3.3 A fast convergence in $v_{c,k}$ for $k \geqslant 1$

Things are more complicated when including the compressibility in the problem, because the density will explicitly depend on the position, so the continuity equation does not reduce to $\nabla^2\phi_k(\boldsymbol{r}) = 0$. We invite the reader to refer to Appendix B.1 and B.2 for the full calculations up to order $k = 4$ for powerlaw or saturable nonlinearities. Given the form of the Poisson equation we have to solve for $\phi_k(\boldsymbol{r})$ (i.e. polynomials multiplied by cosines), it is convenient to use the Ansatz [210]

$$\phi_k(\boldsymbol{r}) = \frac{r^{p+2}}{(p+2)^2 - n^2}\cos n\theta, \tag{3.52}$$

which is a particular solution of $\nabla^2\phi_k = r^p \cos n\theta$ provided that $(p+2)^2 - n^2 \neq 0$, and which is used for each term composing the equation. However, there is always a term not satisfying this condition and for which the Ansatz is not usable. We thus include this recalcitrant term with a different Ansatz which reads $A_n r^n \cos n\theta$, where the constants A_n's are defined using

	$\varepsilon(n)$: Powerlaw $\nu = 1$	$\varepsilon(n)$: Powerlaw $\nu = 2/3$	$\varepsilon(n)$: Saturable $\beta = 1$
$v_{c,0}$	0.426401	0.447661	0.491711
$v_{c,1}$	0.390253	0.407540	0.442709
$v_{c,2}$	0.380105	0.396282	0.429186
$v_{c,3}$	0.375853	0.391606	0.423677
$v_{c,4}$	0.373684	0.389243	0.420935
$v_{c,5}$	0.372438	0.387897	–
$v_{c,6}$	0.371663	0.387066	–

Table 3.1: Explicit values for the critical velocity for superfluidity $v_{c,k}$ when including the compressibility χ with the Janzen-Rayleigh expansion up to order k. These results are obtained in the impenetrable regime $U_0 > \varepsilon(1)$, and for different nonlinearities. The convergence is quite fast, and yields a 0.2% difference between orders $k = 5$ and $k = 6$ for the powerlaw nonlinearity, and a 0.6% difference between orders $k = 3$ and $k = 4$ for the saturable nonlinearity.

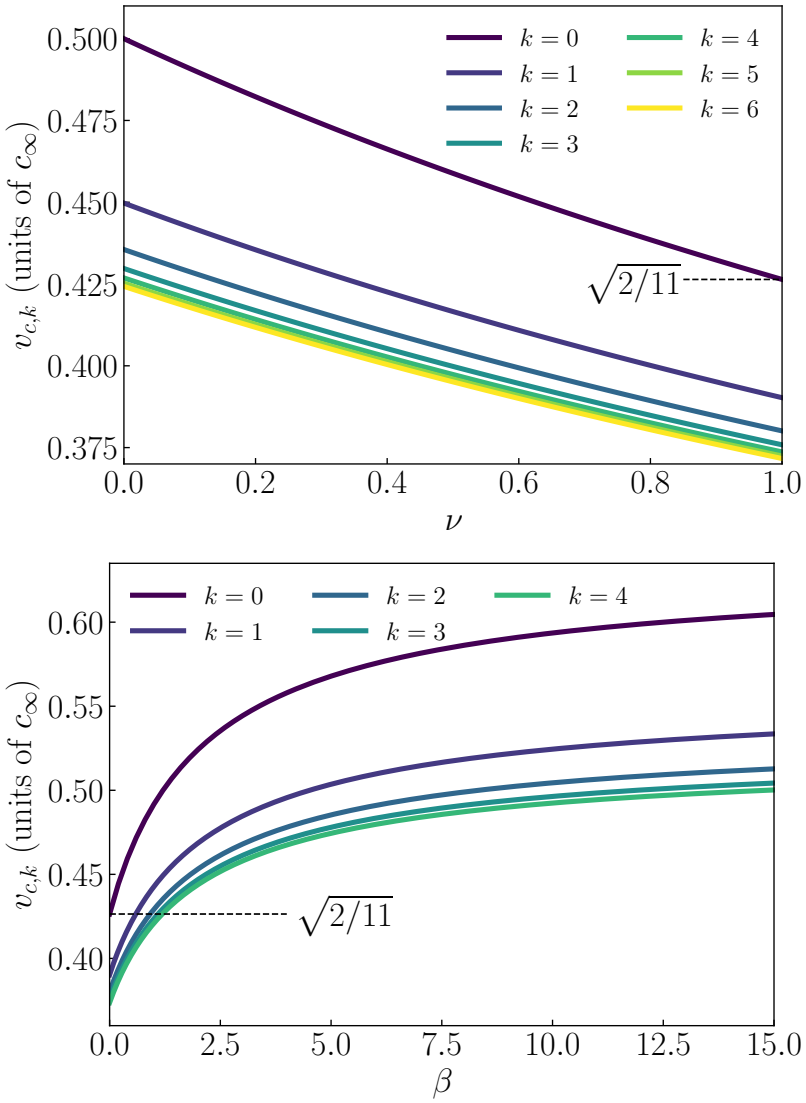

Figure 3.5: Both subfigures represent the critical velocity for superfluidity for an impenetrable disk of typical radius $\sigma \gg \xi_\infty$. The curves for the various k's stand for different orders in the Janzen-Rayleigh expansion. Top: $v_{c,k}$ up to $k = 6$ for a powerlaw nonlinearity as a function of the exponent ν. For $\nu = 1$, one recovers the results of Refs. [58, 59] for each value of k. Bottom: $v_{c,k}$ up $k = 4$ for a saturable nonlinearity, as a function of $\beta = 1/n_{\rm sat}$. One also recovers the results of Ref. [58] for $\beta \to 0$ and $k = 0$. One can clearly see that the higher k, the better the convergence towards the refined value of v_c.

the boundary conditions. In the end, the total velocity potential will be a superposition of all the solutions for each term composing the Poisson equation. It is possible to derive an exact expression for the velocity potential no matter the index $k \geqslant 1$ of the Janzen-Rayleigh expansion:

$$\phi_k(\boldsymbol{r}) = v_\infty r \left[\cos[(2k+1)\theta] \sum_{i=1}^{k+1} A_{i,k} \frac{\sigma^{2i}}{r^{2i}} + \sum_{i=0}^{k-1} \left(\cos[(2i+1)\theta] \sum_{j=1}^{2k+1} B_{i,j,k} \frac{\sigma^{2j}}{r^{2j}} \right) \right], \tag{3.53}$$

where the coefficients $A_{i,j}$ and $B_{i,j,k}$ are computed thanks to the boundary conditions.

The various expressions obtained for $v_{c,k}$'s for the different nonlinearities were then computed numerically from the expressions of $\phi_k(\boldsymbol{r})$, and are respectively represented in the top and bottom part of Fig. 3.5 for a powerlaw nonlinearity as a function of ν, and for a saturable nonlinearity as a function of β. The various $v_{c,k}$'s are represented up to $k = 6$ and

$k = 4$, and show that the higher the order in the Janzen-Rayleigh expansion, the better the convergence towards the refined value of the critical velocity for superfluidity. These results are also explicitly provided in Table 3.1 for $\nu = 1$, $\nu = 2/3$ and $\beta = 1$. We explicitly chose these parameters for ν and β because they correspond to two-dimensional dilute BECs with $na_s^2 \ll a_s/l$, $na_s^2 \gg a_s/l$ for $\nu = 1$ and $\nu = 2/3$ respectively (refer to the TOOLBOX for more details). Note that these results show a one-to-one correspondence with the results of Ref. [59] for $\nu = 1$. The choice of $\beta = 1$ is typically representative of an intermediate value of $n_{\rm sat}$, which is achievable in quantum fluids of light experiments.

3.3.4 How is superfluidity broken?

Relying on the local Landau criterion, it is legitimate to infer that superfluidity will be broken where the local speed of sound is minimum, i.e. where the velocity is maximum, and the density is the most depleted. Intuitively, this should happen at the boundary of the obstacle, as validated by Fig. 3.4, which shows that the velocity is maximum at the poles of the obstacle. We thus performed a numerical simulation of the problem, obtaining results for the density profile reminiscent of the first simulations performed by Frisch *et al.* in Ref. [58].

This simulation consists in the propagation of a disk of radius σ, initially at rest in the fluid at $x = 20$, using a finite-difference method in real space [211, 212]. It is two-fold: First a propagation in imaginary time $t = -i\tau$ to compute the ground state of the system, and then, starting from the ground state, we let it evolve in real time to obtain the exact dynamics of the system. The impenetrability of the disk is encompassed in the boundary condition (3.43). The velocity of the obstacle is then slowly switched on up to a given value of v_∞, helping to maintain the system close to an equilibrium state: This adiabatic ramping prevents quenching effects that would break superfluidity. We have typically used a rectangular grid of size $L_x = 200$ and $L_y = 150$, with $N_x = N_y = 1200$ points. Note that this imbalance between the space increment in x and y is of no consequence, even more so that we are mostly interested in the dynamics along the $x-$axis. The results obtained in Fig. 3.6 are obtained for $\varepsilon(n) = n$, and after an evolution time $T = 125$ (25000 iterations with $dt = 0.005$), for $\sigma = 5$, $U_0 = 1$ and $v_\infty = 0.52$. Referring to the top part of Fig. 3.5, these parameters lead to a dynamics in which superfluidity is well and truly broken.

It is possible to draw an analogy between the system we study and the motion of an almost inviscid classical fluid: Both have a boundary layer of small extension, in which the dynamics takes place. For a classical fluid, boundary layer separation will occur no matter the velocity of the obstacle, destroying the symmetry and resulting in a nonzero drag force. This is however not always the case for our system due to its quantum nature: When $v_\infty < v_c$, nothing of interest will happen and the density will only show a depletion moving at velocity v_∞ where the obstacle is located. The density profile is symmetric, and the obstacle experiences no drag. As soon as $v_\infty > v_c$ (which is the case here), nonlinear structures of typical radius the healing length will be emitted from the north and south poles of the obstacle. This can be seen for example in the top part of Fig. 3.6, where the density profile is close to zero inside the obstacle[1], and clearly exhibits the presence of zero-density points, more or less periodically ejected from the poles of the disk [62, 200, 213]: Vortex-antivortex pairs are created. The disk sheds vortices that have a velocity slower than v_∞, and that form a vortex street that trails behind it. This creates periodic fluctuations in the drag force [161], that decreases as the vortices move downstream, but increases whenever a new pair of vortices is created.

[1]Even though the density at the center of the obstacle is supposed to be strictly null, in practice the fluid can always cross the barrier by tunneling (see Sec. 1.3.2, though for a treatment in 1D), leading to an exponentially small density inside. Although in practice $U_0 = 1$ does not represent a purely impenetrable obstacle ($U_0 \to +\infty$), it is sufficient to observe the emission of vortices typically associated with the breakdown of superfluidity in such cases. Therefore, this mechanism is not restricted to purely impenetrable obstacles, but also occurs for obstacles of lower amplitudes.

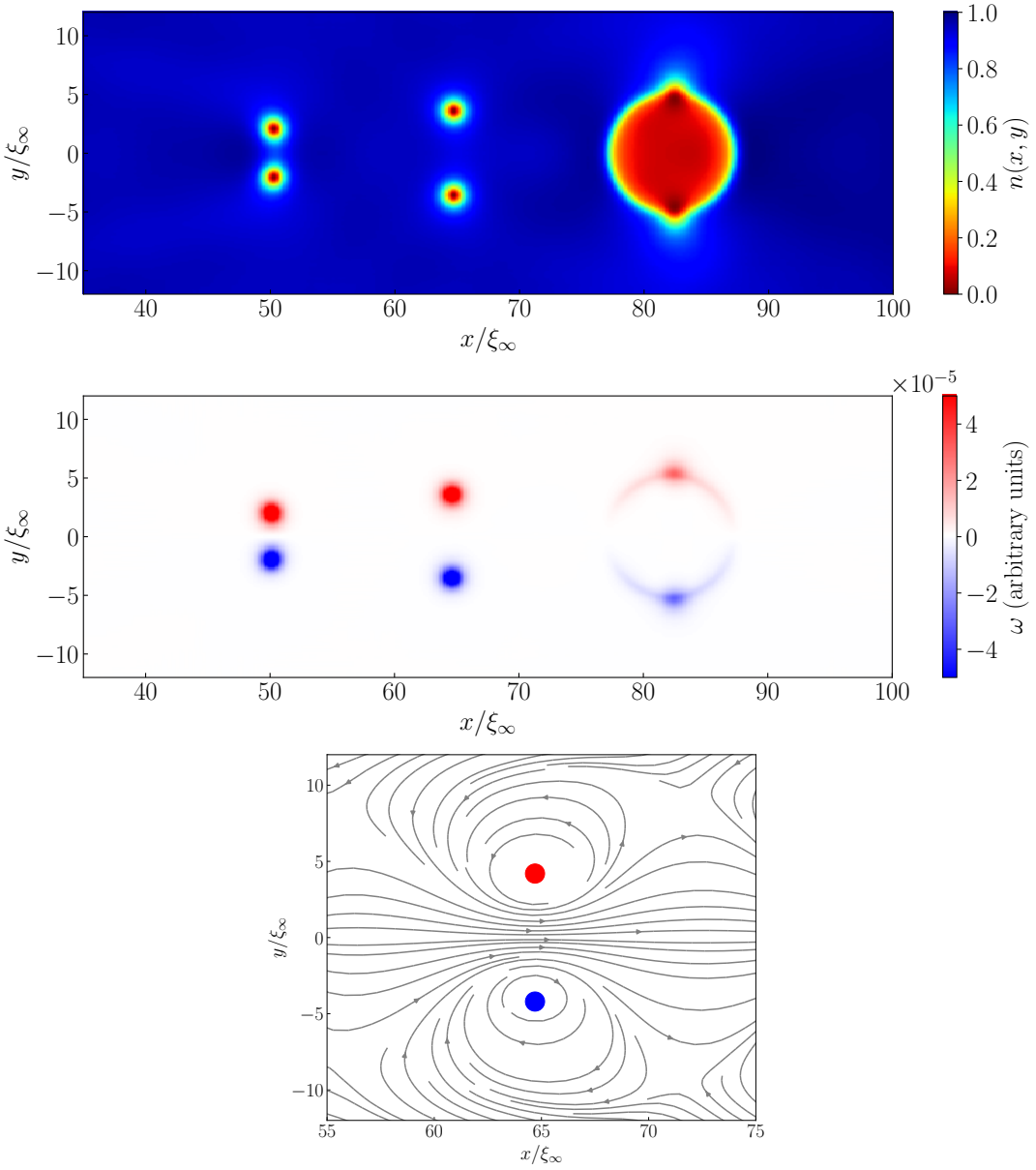

Figure 3.6: Top: Density profile of the equivalent system consisting of a supposedly impenetrable disk ($U_0 = 1$) moving at velocity $\boldsymbol{v}_\infty = 0.52\,\hat{x}$ in a quantum fluid, characterized by $\varepsilon(n) = n$. Since $v_\infty > v_c$, the system is not superfluid, as attested by the formation of vortices at the poles of the obstacle that are then more or less periodically emitted. Middle: Representation of the vorticity $\boldsymbol{\omega}$ of the system. The vortices that are emitted are of opposite circulation. Bottom: Velocity field around the second pair of vortices. Those in red rotate anticlockwise whereas those in blue rotate clockwise: The global vorticity is null.

We also represented the vorticity in the middle part of Fig. 3.6, i.e. the rotational $\boldsymbol{\omega} = \nabla \times \boldsymbol{v}$ of the velocity field. The breakdown of superfluidity follows this scheme: As the obstacle moves within the fluid, a nonzero curl starts to accumulate at the boundary of the obstacle (positive in the top half-plane, and negative in the lower half-plane, as can be seen in the bottom part of Fig. 3.6 where the velocity field is represented around the second pair of vortices), slowly focusing at its poles $(\sigma, \pm\pi/2)$ where the velocity is maximum. At some point, the vorticity exceeds a maximum value, resulting in the ejection of vortices from the obstacle, that are then convected downstream. This process is then repeated as long as the obstacle moves within the fluid.

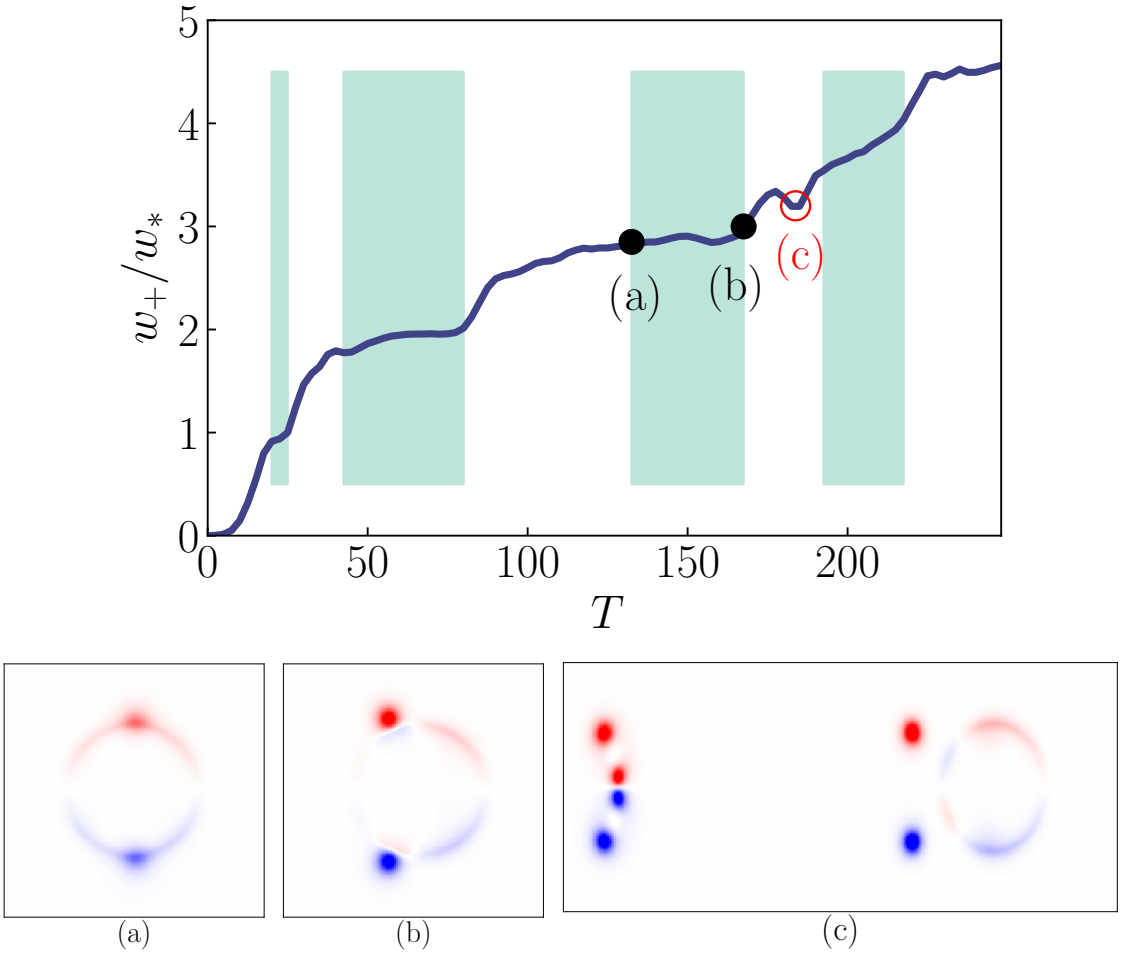

Figure 3.7: Top: Norm of the vorticity ω_+ in the upper half-plane (rescaled by the vorticity ω_* of the first vortex) as a function of the integration time T. The green zones correspond to the period between the time the vortex starts to be distinguishable, and the time of ejection from the obstacle: A vortex is emitted at the end of the plateau. In between these green zones, the vorticity slowly increases all around the obstacle, until it focuses on the upper pole and the process repeats. Bottom: The tags (a–c) represent the vorticity of the system, associated with the different points in the upper figure. Tag (a) shows that the vorticity is distributed everywhere on the obstacle at the beginning of the green zone; Tag (b) represent the moment of maximum focus of the vorticity, corresponding to the emission of vortices; Tag (c) shows an anomaly in the vorticity (which is not supposed to decrease) due to interactions between vortices.

This phenomenon is also illustrated in Fig. 3.7, where we have represented the norm of the vorticity ω_+ of the upper half-plane (rescaled by ω_* the vorticity of the first vortex) as a function of the integration time T. Note that we did not represent the vorticity of the lower half-plane as it is the exact same but with a negative sign, given that the total vorticity is null. The green zones characterize the period of formation of the vortices: The beginning of the zones corresponds to the moment the considered vortex starts to focus on a single point close to the upper pole (see Subfig. (a)), and the end of the green zone is the time of emission of said vortex (see Subfig. (b)). No vorticity is created during that period, thus explaining the various plateaux. Just after a vortex is emitted, the vorticity increases and is distributed everywhere on the upper part of the obstacle, until it focuses again and the process starts anew. Interestingly, the vorticity decreases around $T = 180$: This comes from the fact that the vortices start to interact with each other (see Subfig. (c)), modifying the value of the vorticity and making it harder to define a proper period of formation of vortex (explaining why we do not have a plateau for the last vortex). After this time, it is thus

impossible to properly define the time of emission of the vortex as it is blurred out by the interactions between the previous pairs. Lastly, the green zones are all of different extension, highlighting the fact that the process of formation of vortices is not regular as the dynamics is not stationary: It is thus impossible to define a frequency of emission of the vortices in our case.

In conclusion, we found that as soon as $v_\infty = v_c$, the breakdown of superfluidity in the impenetrable regime typically manifests by the formation of a pair of quantized vortices of opposite circulation at the poles of the obstacle where $\boldsymbol{r} = (\sigma, \pm\pi/2)$ [58, 60, 61]. This is due to an excess of vorticity that builds up in the vicinity of the obstacle as it moves within the fluid, and as long as at least one pair of vortices is emitted, superfluidity is destroyed. Once vortices are ejected, the process begins anew, and pairs of vortices are regularly formed.

3.4 Penetrable obstacles $U_0 < \varepsilon(1)$

If the study of superfluidity in 2D was first applied to impenetrable obstacles (as performed in Refs. [58, 59, 214]) with then an emphasis on their widths [49, 55, 60, 199], more recent works have led us to wonder about the dependence of v_s in the amplitude of the obstacle [60, 61, 195], some even showing a nontrivial dependence in U_0 that has yet to be fully characterized. This is all the more relevant for experimentalists since, in most setups, U_0 is one of the tunable parameters. To our knowledge, the case of penetrable obstacles is much less documented from a theoretical point of view, even if Ref. [60] briefly tackles that problem numerically, though for narrow obstacles.

The calculations are much more complex than for impenetrable obstacles since the fluid can now pass across the obstacle, and the full treatment of the problem involves separating the space into two domains $r < \sigma$ and $r > \sigma$. There is a clear mathematical distinction between these two domains: For $r > \sigma$, the obstacle $U(\boldsymbol{r}) = 0$, and one must then consider $U_0 = 0$ in the equations. For $r < \sigma$ however, the obstacle is not null anymore and the problem is treated with $U_0 \neq 0$. It is thus really important to make the distinction between the case of an impenetrable ($U_0 > \varepsilon(1)$) and a penetrable obstacle ($U_0 < \varepsilon(1)$), as the latter leads to more complicated boundary conditions. One now has to match two solutions for the velocity potential ϕ and its derivative: Inside where $U_0 \neq 0$, and outside where $U_0 = 0$.

This section provides new results going beyond the previous studies that stood only for impenetrable obstacles. We first provide the boundary conditions for the velocity potential and its derivative, matching the solutions between $r = \sigma^-$ and $r = \sigma^+$. Contrary to the results obtained in the impenetrable regime in Sec. 3.3, the boundary condition is now much more complicated and acquires a dependence on U_0. We go beyond these previous results that stood for the impenetrable regime by deriving exact analytical expressions for $v_{c,k}$ for penetrable obstacles, and for a powerlaw or a saturable nonlinearity. However, due to the complexity of the problem, we only pushed the expansion up to the order $k = 2$ in the compressibility, which is already enough to have a relatively well-converged result. This is more than sufficient in practice, considering the inherent errors in potential experiments and the substantial physics of the critical velocity in its incompressible limit, as shown in the previous section.

3.4.1 Boundary conditions at $r = \sigma$

First of all, we provide the boundary conditions at different points in the system. The asymptotic boundary condition defined by Eq. (3.32) is still valid for $r \gg \sigma$. Also, the velocity potential is finite everywhere, especially at $r = 0$, which imposes a strong constraint on the expression of ϕ_k inside the obstacle.

Since the fluid can cross the obstacle, the density inside is now properly defined and needs to be matched with the density outside, adding a second boundary condition. These matching conditions for the velocity potential and its derivative now become

$$\phi|_{r=\sigma^-} = \phi|_{r=\sigma^+}, \tag{3.54a}$$

$$[n\partial_r\phi]_{r=\sigma^-} = [n\partial_r\phi]_{r=\sigma^+}\,. \tag{3.54b}$$

The first condition imposes that the phase of the fluid must be continuous at the interface $r = \sigma$ of the obstacle, i.e. no phase jump. The second expresses the continuity of the radial current in the limit of large σ. It stems from Eq. (3.3b), i.e. the continuity equation $\nabla \cdot (n\boldsymbol{v}) = \partial_r(nv_r) + \partial_\theta(nv_\theta)/r = 0$ integrated along an arbitrary radial cut of a thin annulus of median radius $\sigma \to \infty$. In this case, the orthoradial contribution, $\propto 1/\sigma$, vanishes, leaving one with the continuity of the radial current nv_r at $r = \sigma$, i.e. Eq. (3.54b).

This second condition defined by Eq. (3.54b) is much more complicated than Eq. (3.43) for the impenetrable obstacle because its dependence on $n(\boldsymbol{r})$ induces a nontrivial mixing of the ϕ_k's and their radial derivatives. Yet, it is still possible to derive a recurrence relation between each order in the compressibility.

For example for a powerlaw nonlinearity, one has

$$\sum_{h,i,j=0}^{\infty} \left(-\frac{\nu}{2}\right)^h \binom{\frac{1}{\nu}}{h}\binom{h}{i}\frac{i!}{\prod_{l=1}^{\infty} i_l!}\left\{(1-\nu U_0)^{\frac{1}{\nu}-h}\left[\left(\left(v^2\right)_0-1\right)^h\prod_{l=1}^{\infty}\left(\frac{\left(v^2\right)_l}{\left(v^2\right)_0-1}\right)^{i_l}\partial_r\phi_j\right]_{r=\sigma^-}\right.$$
$$\left. -\left[\left(\left(v^2\right)_0-1\right)^h\prod_{l=1}^{\infty}\left(\frac{\left(v^2\right)_l}{\left(v^2\right)_0-1}\right)^{i_l}\partial_r\phi_j\right]_{r=\sigma^+}\right\} = 0. \tag{3.55}$$

It is also possible to obtain analytical results for a saturable nonlinearity, but we did not derive a recurrence relation and rather solved it with Mathematica. Given the complexity of the boundary conditions, which renders the analytical treatment of the problem unreasonable (cf. Eq. (3.55) for example), we derived analytical results up to $k = 2$ (the results for $k = 1$ are provided in Appendix C) and treated the problem numerically for higher orders.

3.4.2 A dual treatment of the problem

Considering a penetrable obstacle significantly complicates the problem, as it requires solving it in two distinct regions. There is a clear distinction between the dynamics outside the obstacle for $r > \sigma$, where the obstacle is null and the problem must be mathematically treated with $U_0 = 0$ (reminiscent of the impenetrable case), and the dynamics inside the obstacle for $r < \sigma$, where there is no further constraints on the amplitude of the obstacle than $U_0 < \varepsilon(1)$. These two cases are ruled out by different Poisson equations, resulting in different expressions for the velocity potentials $\phi(\boldsymbol{r})$ inside and outside the obstacle.

In theory, two different critical velocities could be derived depending on whether one uses the velocity potential ϕ_k inside or outside the obstacle in the superfluid condition. However, in practice, only one of these critical velocities is physically meaningful; The other is merely a mathematical artifact stemming from our model. In the impenetrable regime, there is only one critical velocity because we only treat the problem for $r > \sigma$ where $U_0 = 0$. However, for a penetrable obstacle, even though we separate the problem into two distinct regions (inside and outside the obstacle), the Landau criterion remains unaffected by this distinction and is unique. Superfluidity is broken where the local speed of sound is maximum, i.e. where the

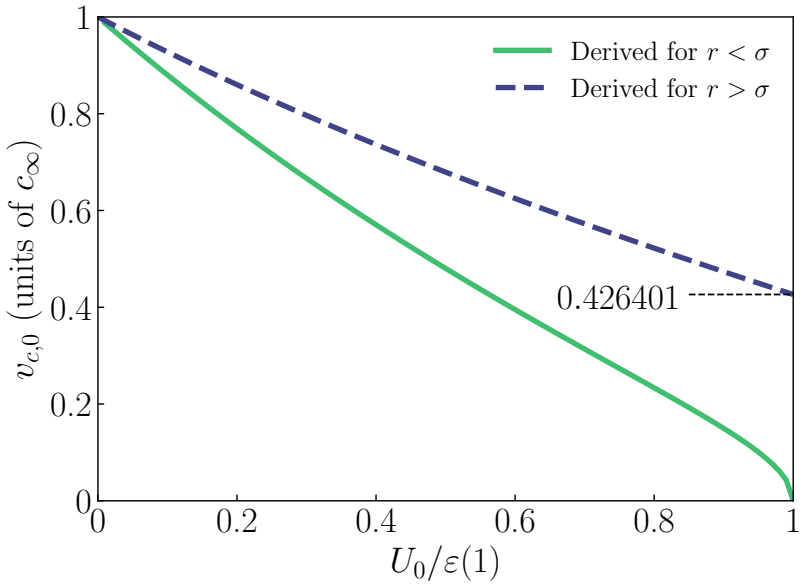

Figure 3.8: Critical velocity for $k = 0$ as a function of the amplitude of the penetrable obstacle. Two velocities are possible, and are derived either from the velocity potential inside (green curve) or outside the obstacle (blue dashed curve). When $U_0 = \varepsilon(1)$, the blue curve reaches the exact same value as $v_{c,0}$ obtained for the impenetrable obstacle. In the end, the "real" critical velocity is the lowest, i.e. the one stemming from inside the obstacle.

density is minimum and $U(\boldsymbol{r})$ is maximum: This occurs inside the obstacle. Deriving a second critical velocity from the velocity potential outside the obstacle makes no sense because it does not exist.

Yet, it remains relevant to mathematically derive this "ghost branch". In Fig. 3.8, we have plotted both critical velocities as a function of the amplitude of the obstacle (which must be lower than $\varepsilon(1)$ since the obstacle is penetrable). These results were derived for $k = 0$ in the Janzen-Rayleigh expansion, and for $\varepsilon(n) = n$. As seen in Fig. 3.8, the "real" critical velocity will indeed be the smallest one, originating from within the obstacle. Although this "ghost branch" has no physical meaning, it is interesting because its value at $U_0 = \varepsilon(1)$ perfectly matches up the value of the one obtained in Sec. 3.3 in the impenetrable regime for $U_0 > \varepsilon(1)$. At this point, $v_{c,0} = 0.426401$, which is the same value as obtained in Refs. [58, 59]. This perfect match actually makes sense because in both cases, we are deriving the critical velocity from the velocity potential outside the obstacle.

3.4.3 The incompressible solution

Even though we have just explained why we derived the critical velocity inside the obstacle, it is still necessary to compute the velocity potential outside the obstacle, to match it with the velocity potential inside at $r = \sigma$. In this paragraph, we then derive the critical velocity for superfluidity using the expression of the velocity potential inside the obstacle, as well as the superfluid conditions with $U_0 \neq 0$.

We provide here analytical results for the incompressible solution ($\chi = 0$), and we do so for a powerlaw and a saturable nonlinearity. The 0^{th} order in k is indeed quite easy since one has to solve the same 2D Laplace equation inside and outside the obstacle, and then match the solutions at $r = \sigma$.

Powerlaw nonlinearity: We first derive the density profile $n(\boldsymbol{r})$, needed in the boundary condition for the derivative of the velocity potential. Its expression is given by Eq. (3.29),

i.e.

$$n(\boldsymbol{r}) = \begin{cases} n_0 = [1-\nu U_0]^{\frac{1}{\nu}} & \text{if } r < \sigma, \\ 1 & \text{otherwise.} \end{cases} \tag{3.56}$$

Using the very same method as in the impenetrable case, implemented with the previously defined boundary conditions (3.54), as well as the asymptotic conditions at $r \gg \sigma$ (also adding the fact that the velocity potential must be finite at $r = 0$), one obtains for the velocity potential

$$\phi_0(\boldsymbol{r}) = v_\infty r\cos\theta \begin{cases} \frac{2}{1+n_0} & \text{if } r < \sigma, \\ 1 + \frac{\sigma^2}{r^2}\frac{1-n_0}{1+n_0} & \text{otherwise.} \end{cases} \tag{3.57}$$

From there, one finds that the maximum velocity is reached inside the obstacle, and is the same everywhere. It reads

$$v_{\max,0} = \frac{2v_\infty}{1+[1-\nu U_0]^{\frac{1}{\nu}}}. \tag{3.58}$$

After solving the superfluid condition (3.25) which now reads

$$1 - \nu U_0 + v_\infty^2 \left[\frac{\nu}{2} - \frac{4}{\left(1+[1-\nu U_0]^{1/\nu}\right)^2}\left(1+\frac{\nu}{2}\right)\right] > 0, \tag{3.59}$$

one obtains the critical velocity for $k = 0$

$$v_\infty < v_{c,0} = \sqrt{\frac{1-\nu U_0}{4\left(1+\frac{\nu}{2}\right)\left[1+(1-\nu U_0)^{\frac{1}{\nu}}\right]^{-2} - \frac{\nu}{2}}}. \tag{3.60}$$

Saturable nonlinearity: Following the exact same scheme, we first derive the density profile using Eq. (3.30)

$$n(\boldsymbol{r}) = \begin{cases} n_0 = \frac{1+\beta-U_0}{1+\beta+\beta U_0} & \text{if } r < \sigma, \\ 1 & \text{otherwise.} \end{cases} \tag{3.61}$$

With the aid of the boundary conditions (3.54), one obtains the velocity potential to the 0^{th} order in k, which also reads

$$\phi_0(\boldsymbol{r}) = v_\infty r\cos\theta \begin{cases} \frac{2}{1+n_0} & \text{if } r < \sigma, \\ 1 + \frac{\sigma^2}{r^2}\frac{1-n_0}{1+n_0} & \text{otherwise,} \end{cases} \tag{3.62}$$

albeit with a different expression for n_0. The maximum velocity potential is then given by

$$v_{\max,0} = 2v_\infty \frac{1+\beta+\beta U_0}{2+2\beta+\beta U_0 - U_0}, \tag{3.63}$$

and is also reached everywhere inside the obstacle.

Things become more complicated when computing the critical velocity for superfluidity since the superfluid condition (3.26) is a fourth-order polynomial in v_∞

$$\begin{aligned} 4\left[(1+\beta)^2 - (1-\beta)^2 U_0 - \beta U_0^2\right] - 2v_\infty^2 \Bigg[4\left(\frac{1+\beta+\beta U_0}{2+2\beta+\beta U_0 - U_0}\right)^2 (3+2\beta(U_0+2)+\beta^2) \\ - 1 - 2\beta U_0 + \beta^2\Bigg] - \beta v_\infty^4 \left[4\left(\frac{1+\beta+\beta U_0}{2+2\beta+\beta U_0 - U_0}\right)^2 - 1\right]^2 > 0. \end{aligned} \tag{3.64}$$

Its resolution leads to

$$v_\infty < v_{c,0} = \sqrt{\frac{-b-\sqrt{b^2-4ac}}{2a}}, \tag{3.65}$$

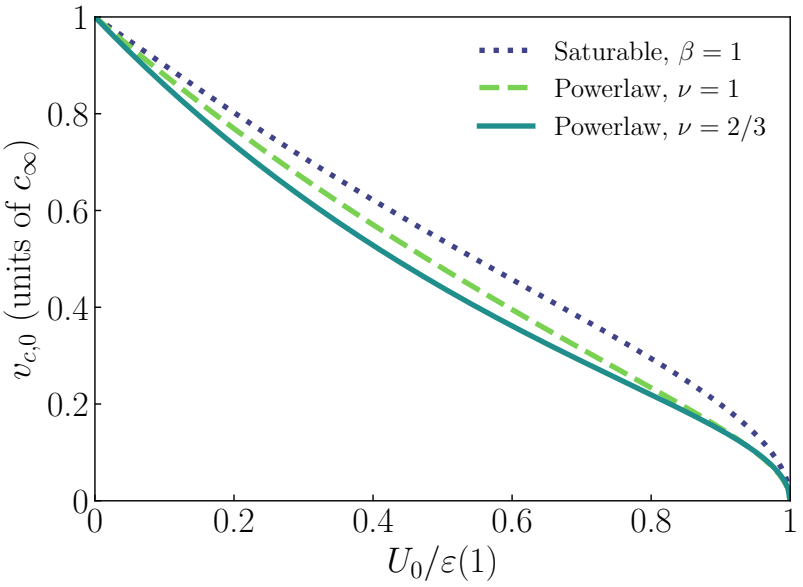

Figure 3.9: Critical velocity for superfluidity $v_{c,0}$ in the incompressible approximation as a function of the amplitude U_0 of a penetrable obstacle ($U_0 < \varepsilon(1)$). The velocity is computed for a powerlaw nonlinearity for $\nu = 1$ (green dashed line) and $\nu = 2/3$ (plain blue line), and for a saturable nonlinearity with $\beta = 1/n_{\rm sat} = 1$ (purple dotted line).

with

$$a = -\beta \left(\frac{v_{\max,0}^2}{v_\infty^2} - 1 \right)^2 , \tag{3.66a}$$

$$b = -2 \left(\beta^2 - 2U_0\beta - 1 + \frac{v_{\max,0}^2}{v_\infty^2}(3 + \beta^2 + 2\beta(2 + U_0)) \right) , \tag{3.66b}$$

$$c = 4 \left[(1+\beta)^2 - \beta U_0^2 - U_0(1-\beta^2) \right] . \tag{3.66c}$$

The expressions of $v_{c,0}$ provided by Eqs. (3.60) and (3.65) (respectively for the powerlaw and the saturable nonlinearity) are represented in Fig. 3.9 as functions of $U_0/\varepsilon(1)$, for $\nu = 1$, $\nu = 2/3$ and $\beta = 1$. According to the Landau criterion, all the curves converge to $v_{c,0} = 1$ for $U_0/\varepsilon(1) \to 0$. Also, the curves vanish when $U_0/\varepsilon(1) \to 1$: This comes from the fact that in the penetrable regime, superfluidity is broken where the density is minimum (i.e. inside the obstacle), and as $U_0/\varepsilon(1) \to 1$, the density inside tends to zero. This results in a zero local sound velocity, and since it is an upper bound for the critical velocity for superfluidity, then $v_c = 0$ as well.

This is reminiscent of what happens in the 1D case in the hydraulic approximation (see Sec. 1.3.2), where the critical velocity strictly drops to zero as soon as the obstacle becomes impenetrable, cutting the fluid into two disconnected parts. Actually, this strict cancellation of v_c is not physical, and arises from the fact that we neglected the quantum pressure in our analytical model. Indeed, v_c must be a continuous function that smoothly matches with its value obtained in the impenetrable regime, as we will later see in the numerical section – in agreement with the experiments of Ref. [195] and corroborated with the numerics of Ref. [61].

3.4.4 Analytical results for $k \geqslant 1$ and comparison with numerics

Aside from the incompressible solution, we analytically derived expressions for $v_{c,k}$ up to order $k = 2$ for both a powerlaw and a saturable nonlinearity. The complexity of the problem

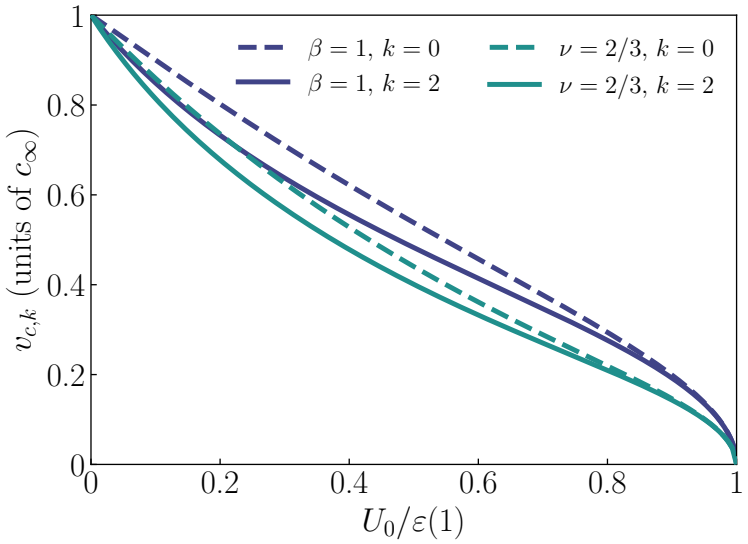

Figure 3.10: Critical velocity for superfluidity $v_{c,k}$ as a function of the amplitude U_0 of a penetrable obstacle ($U_0 < \varepsilon(1)$). The velocity is represented for different orders k in the Janzen-Rayleigh expansion ($k = 0$ and $k = 2$) for a powerlaw nonlinearity for $\nu = 2/3$ (blue lines), and for a saturable nonlinearity with $\beta = 1/n_{\text{sat}} = 1$ (darker blue lines). For the sake of readability, neither curves are represented for $k = 1$.

increases a lot due to the matching condition at the boundary of the obstacle, which is why we only provide analytical expressions for $k = 1$ (for powerlaw and saturable nonlinearities) in Appendix C.1 and C.2 respectively. In terms of the velocity potential, our approach varies depending on whether one is inside or outside the obstacle.

- For $r > \sigma$ (outside the obstacle): We use an Ansatz similar to that employed for the impenetrable obstacle, which is given by Eq. (3.53). This Ansatz is suitable because the boundary conditions at $r = \sigma$ and far from the obstacle are similar to those in the impenetrable case.

- For $r < \sigma$ (inside the obstacle): The velocity potential must be finite at $r = 0$. We use the same Ansatz as for the impenetrable case, provided by Eq. (3.52), and treat the divergent terms accordingly. Here, the velocity potential is thus expressed as a series of polynomials in r (with positive powers this time) multiplied by cosines, ensuring that the potential remains finite at the origin. This time however, we do not provide an exact expression for the velocity potential given the complexity of the problem.

The various expressions we obtained for $v_{c,k}$ are illustrated in Fig. 3.10, plotted as a function of $U_0/\varepsilon(1)$. These results, which apply to both a powerlaw nonlinearity with $\nu = 2/3$ and a saturable nonlinearity with $\beta = 1/n_{\text{sat}} = 1$, exhibit the same limits as those found in the incompressible approximation. Given that the difference in the curves between $k = 1$ and $k = 2$ is relatively small, we only have included results for $k = 0$ and $k = 2$ in the figure. Detailed results for $\nu = 1$, $\nu = 2/3$ and $\beta = 1$ are explicitly provided in Table. 3.2 for $U_0 = \varepsilon(1)/2$ up to the order $k = 2$. The convergence is quite fast, with only a $\sim 1\%$ difference between the orders $k = 1$ and $k = 2$, regardless of the expression of the nonlinearity. This convergence is notably faster than that observed for an impenetrable obstacle, where the difference between the orders $k = 1$ and $k = 2$ was $\sim 3\%$.

A numerical simulation of a system similar to ours is performed in Ref. [61], albeit for a Gaussian obstacle of varying amplitude and $\varepsilon(n) = n$ only. They notably study the critical velocity for superfluidity in this two-dimensional configuration, and observe that for wide σ, v_c exhibits a peculiar behavior: It decreases for $U_0 < \varepsilon(1)$, reaches a minimum around

	$\varepsilon(n)$: Powerlaw $\nu = 1$	$\varepsilon(n)$: Powerlaw $\nu = 2/3$	$\varepsilon(n)$: Saturable $\beta = 1$
$v_{c,0}$ for $U_0 = \varepsilon(1)/2$	0.480375	0.440415	0.538037
$v_{c,1}$ for $U_0 = \varepsilon(1)/2$	0.442265	0.404897	0.488021
$v_{c,2}$ for $U_0 = \varepsilon(1)/2$	0.437787	0.400805	0.482573

Table 3.2: Explicit values for the critical velocity for superfluidity $v_{c,k}$ when including the compressibility χ with the Janzen-Rayleigh expansion up to order $k = 2$. These results are obtained in the penetrable regime for $U_0 = \varepsilon(1)/2$, and for different nonlinearities. The convergence is also quite fast, and yields a $\sim 1\%$ difference between orders $k = 1$ and $k = 2$ no matter the nonlinearity.

$U_0 = \varepsilon(1)$, and increases again to a constant value for $U_0 > \varepsilon(1)$. This dip marks the transition between the two regimes of interest: Penetrable and impenetrable. These results are in accordance with the experimental results of Ref. [195], which also report a dip in the critical velocity near $U_0/\varepsilon(1) = 1$ for the same Gaussian obstacle. This behavior is more or less consistent with our analytical findings, except that we did not find a minimum around $U_0 = \varepsilon(1)$ but rather a discontinuity: v_c vanishes for $U_0 \to 1$, and is constant for $U_0 > 1$.

In order to better understand the discrepancy between our analytical results and the numerics of Ref. [61], we performed a similar numerical simulation, but with a disk-shaped obstacle to remain consistent with our model, and for different expressions of the nonlinear interaction potential. This allows us to obtain a comprehensive view of v_c across different obstacle amplitudes, and to better understand the nature of this minimum. This simulation involves solving the full problem in imaginary-time, thereby accounting for the quantum pressure. We modeled a smoothed-out circular barrier of radius $\sigma/\xi_\infty = 10$ and a shoulder of width $w = 1$ to avoid numerical errors due to sharp gradients. The simulation was conducted on a grid with typical dimensions $L_x = 400$ and $L_y = 100$, with a spatial step $\delta_x = 0.25$ and an imaginary-time step $\delta_\tau = 0.01$. We start the integration from an initial condition, and let it evolve in imaginary time using an explicit finite-difference scheme [211, 212, 215] with periodic boundary conditions, going up to $\tau_{\max} \sim 10^4$.

We compute the ground state in imaginary time, starting from a zero velocity. From there, we slowly increase the velocity v_∞ between each simulation with an increment of $\delta_v = 0.016 * 2\pi/L_x$, until reaching the critical velocity for superfluidity. For further details on the method, refer to Refs. [61, 216]. Note that while the method used for computing v_c is similar to that used for obtaining the density profiles (see Figs. 3.6 and later 3.12), the entire simulation is performed in imaginary time rather than just the ground state, as we did in Sec. 3.3.4 to obtain the real-time dynamics of the system and see the nucleation of vortices.

We determine v_c as the velocity for which the system no longer converges to a stationary solution at long time. Specifically, v_c is identified by observing the system's behavior: At velocities higher than v_c, the system exhibits the emission of hydrodynamic perturbations that move perpendicularly to the flow around the obstacle [61], indicating a nonsuperfluid state. When $v_\infty < v_c$, these perturbations disappear, and the imaginary-time evolution converges to a stationary state. At the transition, the shedding frequency of nonlinear structures from the obstacle is expected to diverge due to a critical slowing-down, which makes it challenging to observe the transition within our finite-time window. Consequently, we have changed our criterion, and defined the nonsuperfluid regime as the one where we observe the emission of at least two perturbations. This adjustment accounts for the fact that the first pair of vortices often results from the transient response of the obstacle, which velocity was not adiabatically ramped to prevent quenching effects. The error bars in Fig. 3.11 arise from the discretization of the velocity in our numerical approach. They account for the fact that we choose v_c to be comprised between the last velocity for which one excitation is emitted and the first velocity for which two excitations are emitted, thus explaining why they are the same size as δ_v.

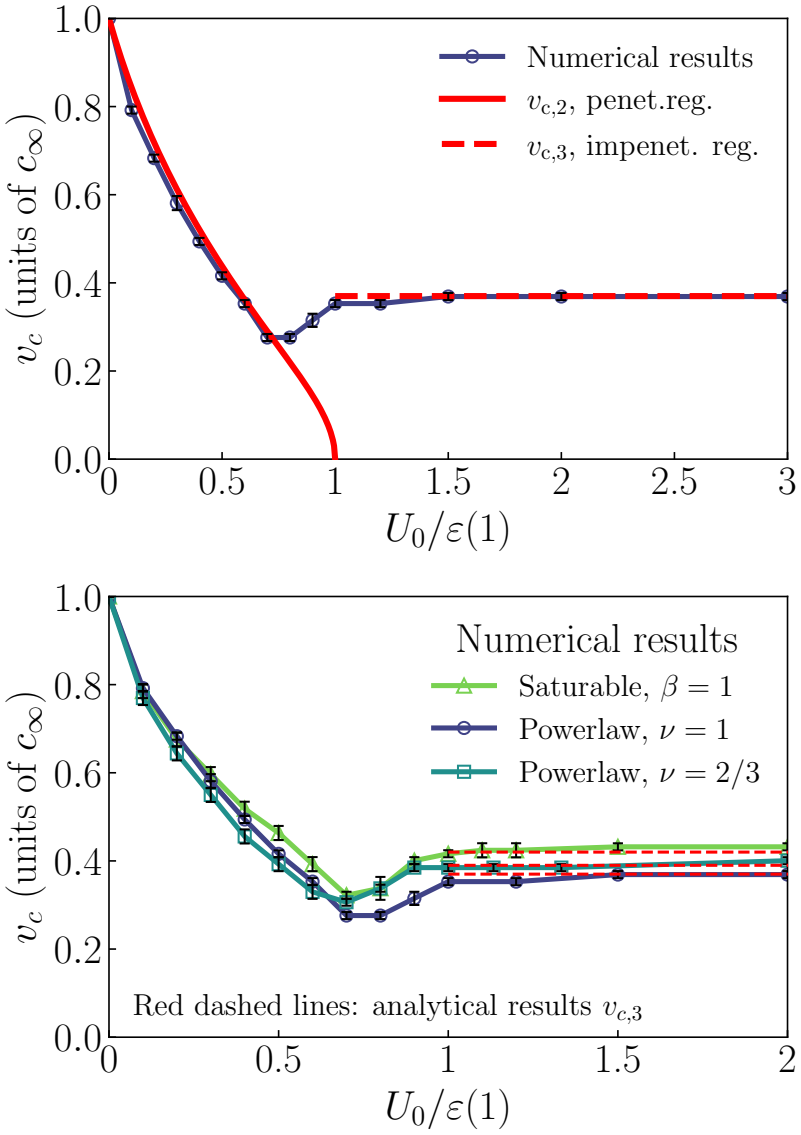

Figure 3.11: Top: Critical velocity for superfluidity as a function of $U_0/\varepsilon(1)$ for $\varepsilon(n) = n$. The purple dots correspond to the numerical simulation, whereas the red lines are the analytical limits we found using the Janzen-Rayleigh expansion. These results were obtained for $k = 2$ in the penetrable regime (plain line), and $k = 3$ in the impenetrable regime (dashed line). The numerical and analytical results are in agreement, except close to the transition around $U_0/\varepsilon(1) = 1$. Bottom: Same critical velocity, but for three different interaction potentials this time, i.e. a saturable nonlinearity with $\beta = 1/n_{\rm sat} = 1$ (green triangles) and a powerlaw nonlinearity with $\nu = 1$ (purple circles) and $\nu = 2/3$ (blue squares). All three curves follow the same behavior and exhibit their minimum around the same value of $U_0/\varepsilon(1) \sim 1$, although for slightly different values of v_c. The red dashed lines represent the analytical limits we found for v_c in the impenetrable regime, and for $k = 3$ in the Janzen-Rayleigh expansion of the velocity potential, and show a really good agreement with the numerics.

These results for the critical velocity are represented in the top part of Fig. 3.11 as a function of $U_0/\varepsilon(1)$, and for $\varepsilon(n) = n$. The purple curve corresponds to the numerical simulation, whereas the green curves are the analytical limits we previously defined for $k = 2$ for penetrable obstacles, and for $k = 3$ for impenetrable obstacles. The agreement between the numerical simulation and our analytical prediction is good in both limits $U_0/\varepsilon(1) \ll 1$ and $U_0/\varepsilon(1) \gg 1$, validating the existence of two different solutions in these regimes. The existence of these two branches comes from the fact that superfluidity is either broken inside the obstacle (penetrable obstacle), or outside of it (impenetrable obstacle). Two different mechanisms for

the breakdown of superfluidity then exist: The emission of vortices outside of the obstacle when $U_0/\varepsilon(1) > 1$, and something happening inside the obstacle when $U_0/\varepsilon(1) < 1$, which will later be explained in Sec. 3.4.5.

Contrary to our analytical prediction however, the critical velocity is actually a continuous function that smoothly connects the penetrable and impenetrable regime. Notably, v_c exhibits a nonzero minimum value close to the transition threshold $U_0/\varepsilon(1) = 1$ ($v_c \simeq 0.28$ for $U_0/\varepsilon \simeq 0.8$). This minimum can be explained as follows: In the penetrable regime, as U_0 increases, the density inside the obstacle becomes more and more depleted. This depletion leads to a decrease in the local Landau velocity and, consequently, v_c. As $U_0/\varepsilon(1)$ approaches 1, the density inside the obstacle is so low that excitations cannot form within it anymore. At this transition, the points of emission of the excitations responsible for the breakdown of superfluidity are thus shifted from the interior of the obstacle towards the exterior (the boundary layer), where the density is more important. This increased density at the boundary layer results in a higher v_c, thus explaining the presence of a minimum in v_c just before the transition. Additionally, the fact that the minimum observed in the numerical simulation is not null can be attributed to the quantum pressure term, which was neglected in the analytical treatment. This term tends to smooth out density gradients in the penetrable-barrier regime, resulting in a higher density within the obstacle, and thus a higher local speed of sound and a nonzero critical velocity. The omission of this term in our analytical model explains why we predicts $v_c = 0$ at the transition. Contrary to the 1D case, this term is now nonnegligible because the fluid is never cut into two independent parts.

The bottom part of Fig. 3.11 shows v_c as a function of $U_0/\varepsilon(1)$ for three different interaction potentials, as indicated in the legend. Despite the different interaction potentials, the qualitative behavior of v_c remains consistent across all cases. Specifically, the curves and their minimum value are just shifted, even if their position remains approximately the same around $U_0/\varepsilon(1) \sim 0.7 - 0.8$. We found a really good agreement with our analytical results no matter the expression of the nonlinearity (as can be seen in the top part of Fig. 3.11, although for $\varepsilon(n) = n$ only), but only represented it for $U_0 > \varepsilon(1)$ (red dashed lines) for the sake of clarity.

3.4.5 How is superfluidity broken?

The formation of a rarefaction wave

When the velocity of the obstacle is below the critical velocity v_c, the fluid remains in a superfluid state. In this regime, the density profile is disturbed only around the obstacle, and superfluidity is maintained. However, when the obstacle's velocity reaches or exceeds v_c, superfluidity is disrupted. To illustrate this, we conducted a numerical simulation of the system for parameters leading to a penetrable obstacle in the nonsuperfluid regime, i.e. $U_0 = 0.7$, $\sigma = 5$ and $v_\infty = 0.5$ (in which case $v_c = 0.276$). The top part of Fig. 3.12 shows the density profile of the fluid. Unlike the case of the impenetrable obstacle, the density does not drop to zero inside a penetrable obstacle. Instead, superfluidity is broken within the obstacle, at the point where the density is the lowest.

As the obstacle moves, a rarefaction wave forms within it [60], which is very probably a Jones-Roberts soliton [217]. This soliton is a finite-amplitude density wave that typically manifests as a pair of vortex-antivortex pair. As shown in Sec. 1.3.1, the depth of a dark soliton is linked to its velocity v_∞, which in our case determines its energy, and then its shape and depth [218]. At high velocity (low energy), the separation between the vortex and the antivortex is very small, causing the vortex cores to almost overlap. This behavior is evident inside the obstacle, as shown in the bottom part of Fig. 3.12, where we have represented the vorticity. On the contrary at lower velocity (which happens when the soliton reaches the boundary of the obstacle), the distance between the two cores increases. At this stage,

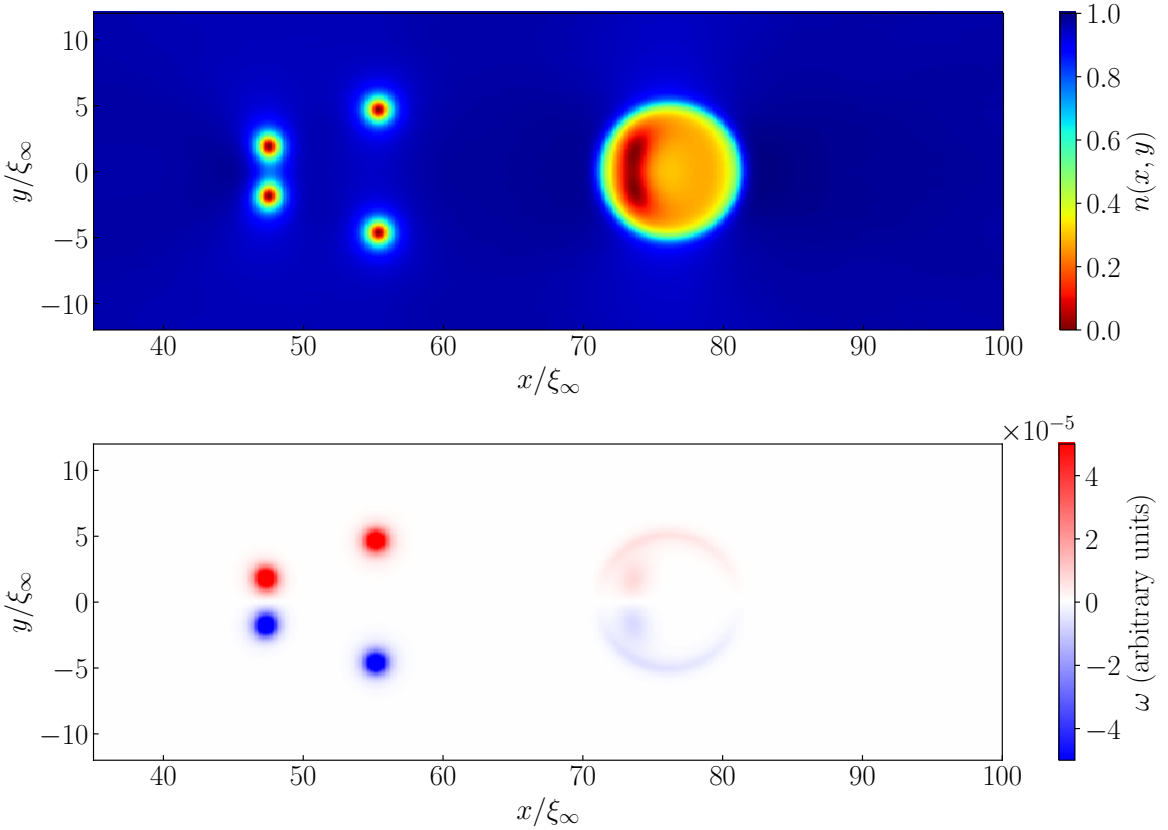

Figure 3.12: Top: Density profile of the equivalent system consisting of a near impenetrable disk moving at velocity $\boldsymbol{v}_\infty = 0.5\,\hat{x}$ in a quantum fluid, characterized by $\varepsilon(n) = n$. Since $v_\infty > v_c$, the system is not superfluid, as attested by the formation of vortices at the boundary of the obstacle that are then more or less periodically emitted. Bottom: Representation of the vorticity $\boldsymbol{\omega}$ of the system. A rarefaction wave appears: Inside the obstacle, the velocity of the perturbation is important and the distance between the two cores is too small. As the wave reaches the boundary of the obstacle, its velocity decreases and the two cores become distinguishable: Vortices of opposite circulation are emitted from the boundary. Those in red rotate anticlockwise whereas those in blue rotate clockwise.

the two vortices of opposite circulation become clearly distinguishable, each exhibiting a zero density at their centers.

Similarly to Sec. 3.3 for an impenetrable obstacle, we also represented in Fig. 3.13 the vorticity ω_+ in the upper half-plane (rescaled by the vorticity ω_* of the first vortex) as a function of the integration time T. Again, we represented in green the time between which the vortices are distinguishable for the first time, and then emitted (see Subfig. (a)), in which case the vorticity is focused on two singular points corresponding to the vortices. In between these zones, the vorticity slowly increases because of the formation of the rarefaction wave within the obstacle, and the creation of vorticity at the boundary of the obstacle. The extension of these green zones is reduced compared to the impenetrable case, because the vortices are not slowly built up, but rather originate from the breaking of the rarefaction wave inside the obstacle when it reaches its boundaries. Interestingly, the frequency of emission of the vortices seems more regular than for the impenetrable case, but the number of vortices is too low to define a proper frequency.

In the impenetrable regime, the vorticity is null everywhere inside the obstacle, as illustrated in Fig. 3.6. This is no longer the case when $U_0 < \varepsilon(1)$: The rarefaction wave inside the obstacle has a nonzero vorticity (see the bottom part of Fig. 3.12), and corresponds to "ghost-like" vortices that are initially too close to be clearly distinguishable. As the velocity of the wave decreases slightly, these "ghost-like" vortices evolve into a pair of well-defined

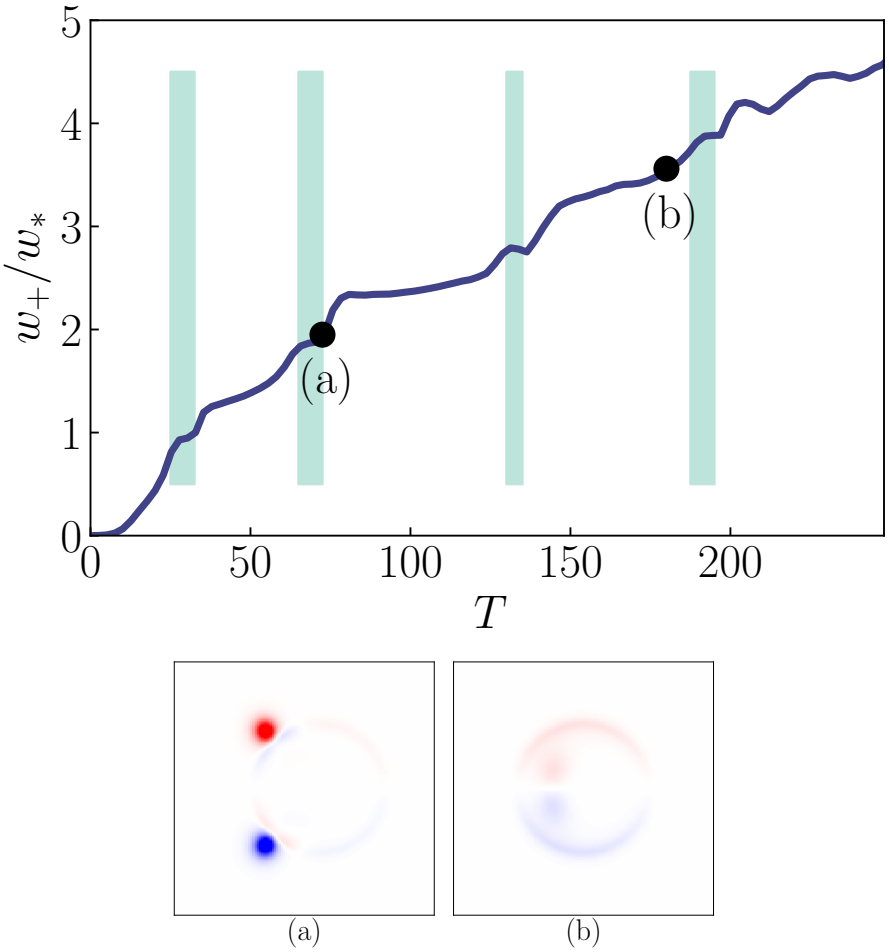

Figure 3.13: Top: Norm of the vorticity ω_+ in the upper half-plane (rescaled by the vorticity ω_* of the first vortex) as a function of the integration time T. The green zones correspond to the period between the time the vortex starts to be distinguishable, and the time of ejection from the obstacle: During that time, the vorticity is more or less constant. In between these green zones, the vorticity increases because of the formation of a rarefaction wave within it, as well as the built-up of vorticity all around the obstacle. Bottom: The associated tags (a–b) represent the vorticity of the system, associated with the different points in the upper figure. Tag (a) shows the moment of emission of the vortices, for which the vorticity is focused on two singular points; Tag (b) shows the built-up of vorticity associated to the rarefaction wave.

vortices of opposite circulation. These vortices are then repeatedly emitted, more or less close to the poles of the obstacle.

Properties of the shedding of vortices

Close to the superfluid transition, the frequency of emission of said vortices tends to zero (corresponding to the divergence of the nucleation time [219]), making it hard to define the exact critical velocity since the simulation runs during a finite time. The vortex shedding frequency then increases, supposedly linearly with $v_\infty - {c_\infty}^2$ [220].

Another important feature is that as the velocity of the obstacle increases and exceeds v_c, the shedding increases and becomes more and more irregular, creating a turbulent wake, and the point of emission of vortices slowly migrates towards the rear side of the obstacle [214]. When the velocity is even larger, different pairs of vortices will be too close and will start

[2]The data extracted from our simulation is not precise enough to corroborate that fact since we collect data each 500 iteration, which is too large to see the linear dependence of the shedding frequency.

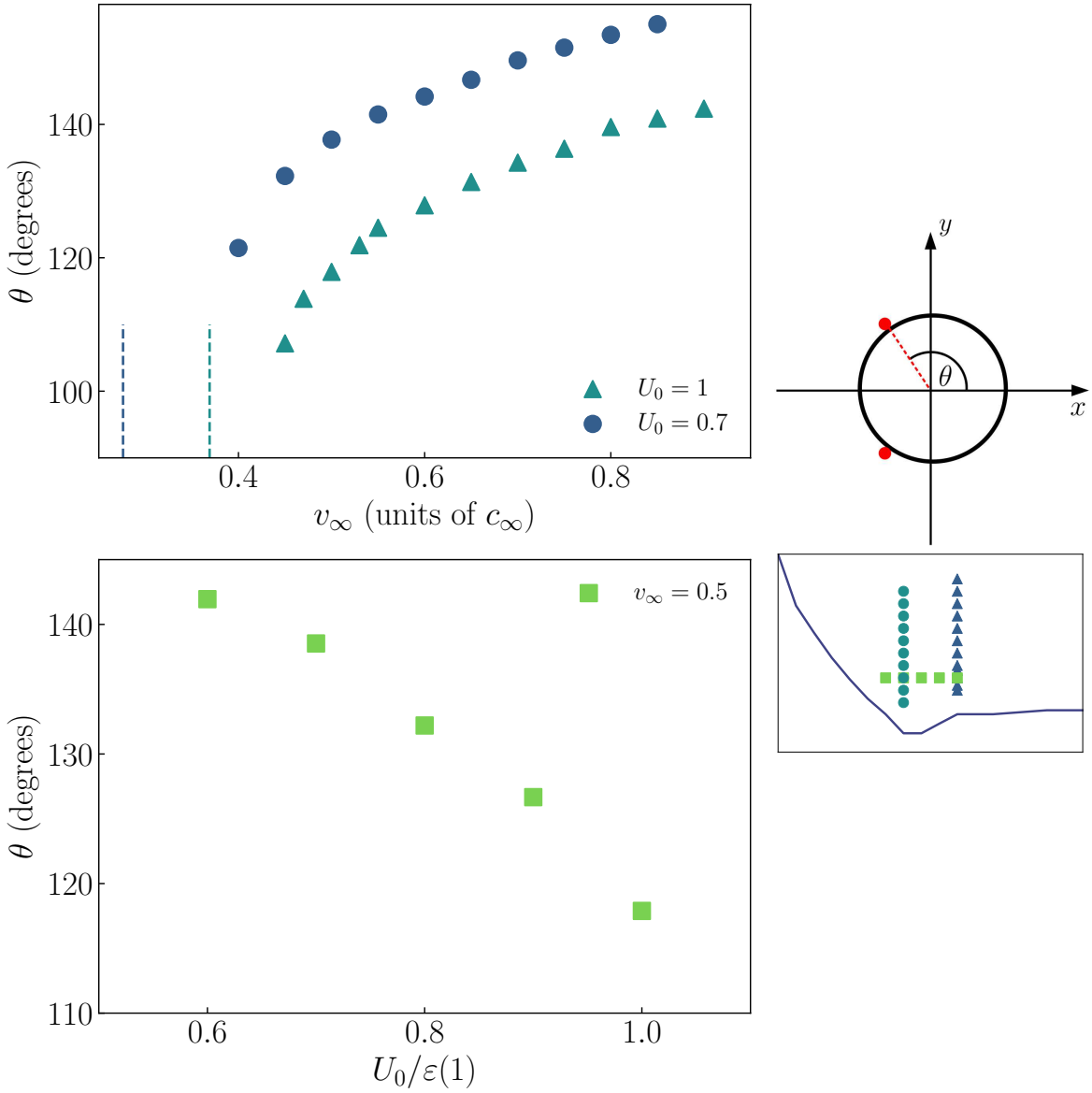

Figure 3.14: Top: Angle of emission θ of the first pair of vortices as a function of the velocity of the obstacle, for $U_0 = 0.7$ (dark blue dots) and $U_0 = 1$ (lighter blue triangles). The colored dashed lines represent the corresponding theoretical critical velocity v_c, which are supposed to be the first values for which we can get data. This was however not the case since the integration time was too short to observe the emission of vortices for such values of v_∞. The figure shows that θ is an increasing function of v_∞, which growth slows down at some point because several pairs of vortices are formed at the same time. Bottom: Same angle of emission θ as a function of U_0 this time, and for $v_\infty = 0.5$. This figure, along with the top part, shows that the smaller U_0 and the larger v_∞, the larger the deviation from the theoretical prediction $\theta = 90°$. The top panel on the right represents a schematics of the angle θ, and the bottom one is a reminder of v_c as a function of U_0, and is here to show for which parameters (U_0, v_∞) we computed θ.

to interact with each other, potentially leading to the formation of turbulent structures for restricted set of parameters [101, 103].

The numerical simulation we performed allowed us to study the angle of emission of the first pair of vortices as a function of the velocity, in both cases of the penetrable and the impenetrable obstacle. This is represented in the top part of Fig. 3.14, for $U_0/\varepsilon(1) \in \{0.7, 1\}$, and $\sigma = 5$. Note that we did not obtain data for $v_\infty < 0.45$ for $U_0 = 1$ and $v_\infty < 0.4$ for $U_0 = 0.7$, since the simulation time we used was too short to see vortices appear below

that. In any case, it was not possible to obtain data for velocities lower than $v_\infty = 0.369$ and $v_\infty = 0.276$ (respectively for $U_0 = 1$ and $U_0 = 0.7$), which correspond to the value of the critical velocity for superfluidity extracted from Fig. 3.12 for $\varepsilon(n) = n$ (one then has $\varepsilon(1) = 1$), and which are represented in dashed lines.

In accordance with Ref. [214], we found that the angle of emission θ of the first pair of vortices (i.e. the angle between the $x-$axis and the upper vortex, see Fig. 3.14) is an increasing function of the velocity of the obstacle. Also, θ seems to converge to the theoretical value of $\theta = 90°$, at least for $U_0 = 1$ (because of the divergence of the nucleation time close to the transition, we do not have enough data for $U_0 = 0.7$ to draw the same conclusion). At some point around $v_\infty = 0.5$, the growth rate of θ is slowing down. This seems to coincide with the fact that the shedding frequency is so large that two pairs of vortices are almost ejected at the same time, which influences the angle of emission of the first pair. It is also interesting to note that even though it is not represented here, the different curves for $U_0/ \in \{0.7, 1\}$ do not collapse into a single curve when representing θ as a function of $v_\infty/v_c(U_0)$ (where one has $v_c \in \{0.276, 0.369\}$ respectively). This could stem from the fact that the mechanisms to break superfluidity down differ: For $U_0 = 0.7$ it is a rarefaction wave whereas for $U_0 = 1$ it is vortices at the boundary of the obstacle.

The top part of Fig. 3.14 also shows that the smaller U_0, the larger θ, which is validated by the bottom part of Fig. 3.14, representing θ as a function of $U_0/\varepsilon(1)$, and for $v_\infty = 0.5$. The small panel in the right part of the figure is here to help the reader in the comprehension of the different simulations we ran: It is a reminder of v_c as a function of U_0, and the various colored markers represent the values of (U_0, v_∞) for which we obtained θ.

3.5 Conclusion

This chapter focused on determining the critical velocity for superfluidity in 2D. To achieve this, we employed the method used in Refs. [58, 59] – leading to analytical results much more complex than those of Chap. 1 – and extended it to obstacles of possibly large amplitude, as well as various expressions of the nonlinear potential $\varepsilon(n)$. To summarize this method: In 2D, the continuity equation is no longer integrable. To address this, we re-express it in the hodograph plane, leading to a new condition for superfluid motion based on the ellipticity of the continuity equation – a condition strictly equivalent to the local Landau criterion in the hydraulic approximation we consider throughout this chapter. This condition relies on knowing the maximum velocity as a function of v_∞, and requires solving the hydrodynamic equations within the hydraulic approximation. We do it for a disk-shaped obstacle using Janzen-Rayleigh expansions of the velocity potential around the incompressible flow limit. Finally, after solving the condition for superfluid motion with said value of $v_{\max}$, one can derive an exact analytical expression for the critical velocity for superfluidity v_c in two dimensions.

Our analytical results for v_c as a function of U_0 and for a large σ indicate that two distinct behaviors are expected, depending on whether the obstacle is penetrable ($U_0/\varepsilon(1) < 1$) or impenetrable ($U_0/\varepsilon(1) > 1$). On the one hand, v_c decreases as a function of U_0 and goes to zero when the obstacle is penetrable. On the other hand, v_c is expected to remain constant once the obstacle becomes impenetrable.

We explain these different behaviors by the existence of two distinct mechanisms for breaking superfluidity in 2D, which are as follows.

- If the obstacle is impenetrable – as previously studied in Refs. [58, 59], although only for $\varepsilon(n) = n$ – superfluidity is broken at the obstacle's boundary by the nucleation of vortices of opposite circulation within the boundary layer. As the obstacle moves through the fluid, these vortices are periodically emitted, supposedly at an angle $\theta = 90°$. However, in agreement with Ref. [214], we demonstrate in Sec. 3.4.5 that this angle of emission is actually greater (at least for the first pair of vortices), and is highly dependent on both U_0 and v_∞.
- For a penetrable obstacle, the mechanism leading to the breakdown of superfluidity is different, as a dynamics within the obstacle is now possible. Superfluidity is disrupted where the density is the lowest – inside the obstacle – by the formation of a rarefaction wave. As this soliton evolves within the obstacle and reaches the boundary of the disk, it then triggers the nucleation of a pair of vortices. Similarly to classical fluid mechanics for high Reynolds number flows, the emission of these vortices is due to boundary layer separation [214], occurring near the rear side at $\theta > \pi/2$ (again, refer to Sec. 3.4.5), despite the maximum velocity being reached at $(\sigma, \pm\pi/2)$.

We also performed a numerical simulation of the system to capture the actual behavior at the transition between penetrable and impenetrable regimes. Following the method used in Ref. [61], we found that v_c exhibits a minimum, likely around $U_0/\varepsilon(1) = 0.7 - 0.8$, which is consistent with the experimental and numerical results reported in Refs. [61, 195] for Gaussian obstacles. Our analytical results are also in good agreement with these numerical simulations. Ultimately, this demonstrates that our simplified model with a large disk is qualitatively adequate for describing real experimental systems.

Despite this good agreement, some discrepancies are observed between our analytical and numerical results, particularly near the transition. Instead of dropping to zero, v_c smoothly links the penetrable and impenetrable regimes instead. This difference arises because our analytical model neglects the quantum pressure, while the numerical simulation accounts for it. This term is indeed significant, as it reduces the density gradients when the obstacle is penetrable, leading to a higher density inside. According to the local Landau criterion, this increases the local speed of sound and, consequently, the critical velocity for superfluidity. Thus, near the transition, v_c does not exactly drop to zero but increases to connect with the value obtained in the impenetrable regime. Additionally, another potential source of discrepancy could be that in our simulation, we modeled the dynamics of a smoother obstacle rather than one with sharp boundaries, which could have a marginal effect on v_c.

Although this consideration goes beyond the scope of the present chapter (as our results are derived only for $\sigma \gg 1$), further studies indicate that the dependence of v_c in σ is also nontrivial, as shown in Refs. [49, 60, 101, 199], albeit for impenetrable obstacles. It is indeed shown that v_c gradually decreases as σ increases, and reaches a plateau for $\sigma \gg 1$ at the theoretical value $v_c = 0.369773$ obtained in the hydraulic approach, as derived by Rica in Ref. [59]. Note that the value of this plateau for $\sigma \gg 1$ is slightly lower than the one we derived for $\varepsilon(n) = n$, as we did not push the Janzen-Rayleigh expansion up to the same order as Rica. The results of Ref. [49] – i.e. not a plateau for $\sigma \gg 1$ but rather $v_c \propto 1/\sigma$ in 2D and 3D – are thus inconsistent with several theoretical (Refs. [58, 59, 61], including our work)

and experimental studies [195] as they predict a zero critical velocity for large obstacles. This likely stems from the Ansatz they use for the density profile, which presents a cusp in 2D at $r = 0$ for a cylindrical obstacle, and which has no $\theta-$dependence even in the presence of a nonzero flow at infinity.

Interestingly, the existence of a minimum in the critical velocity for superfluidity at the transition between the penetrable and impenetrable regimes appears to depend on the width of the obstacle. Specifically, Refs. [61, 195] show that the minimum around $U_0 = \varepsilon(1)$ gradually disappears as σ decreases. This likely results from the quantum pressure playing a more significant role for thin obstacles than for wider ones. Since it tends to increase the value of v_c (as discussed Chap. 1), its minimum value will increase as σ decreases. We even anticipate that for $\sigma \ll 1$, the obstacle might be too thin for a perturbation to form within it, leading instead to the formation of a pair vortices at its poles.

Conclusion

In this thesis manuscript, we have provided a thorough theoretical study of the stationary flow of a quantum fluid past a localized obstacle in both one and two dimensions. In particular, we have characterized the critical velocities separating the stationary-transport phases of the quantum flow, in the parameter space of both the obstacle and interaction potentials. We have investigated the subsonic velocity below which the quantum fluid flows in a superfluid way, in both 1D and 2D, as well as the supersonic velocity marking entry into the stationary dissipative regime of cnoidal waves, in 1D. The analysis has been performed both analytically and numerically within the framework of the nonlinear Schrödinger equation and its associated Madelung hydrodynamic equations, for localized obstacle potentials of arbitrary penetrability and for local interaction potentials of various dependencies on the fluid density. This has made it possible to push the theoretical state of the art towards a more comprehensive and realistic modeling of quantum-transport experiments using, for instance, Bose-condensed ultracold atomic vapors or paraxial beams of superfluid light in low-dimensional geometries. The main results of each chapter are summarized below.

In Chap. 1, we derived exact analytical results for the critical velocity for superfluidity v_c in one-dimensional systems, as a function of the amplitude and the width of the obstacle, and of the parameters of the nonlinear interaction potential $\varepsilon(n)$. This analysis was conducted for repulsive obstacles in both the narrow and wide widths limits – discussed respectively in Sec. 1.3.1 and 1.3.2. Our initial hydraulic approximation for wide obstacles suggested that v_c should exactly drop to zero when the obstacle's amplitude exceeds a certain threshold value. However, we refined our model in Sec. 1.3.2 to account for the possibility of tunneling across the barrier, which remains possible regardless of the obstacle's amplitude. This refinement led to exponentially small corrections to the critical velocity in such cases.

To complement these analytical results, we developed a relaxation algorithm in imaginary time for the stationary superfluid problem, and performed numerical simulations in Sec. 1.3.3 to capture the behavior of the critical speed at intermediate obstacles widths, going beyond the limits previously considered. The numerical results closely matched our analytical predictions, providing a comprehensive understanding of the transition between the very distinct regimes of superfluid and nonstationary flows.

Finally, in Sec. 1.3.4, we extended our model to include linear and homogeneous losses, making it applicable to systems such as quantum fluids of light – an area relevant to ongoing experiment conducted by teams we work in collaboration with. By applying a relevant adiabatic evolution approximation, we found that while these losses reduce the value of v_c, they do not fundamentally alter its behavior. The critical velocity remains a decreasing function of σ and U_0 which agrees with the Landau criterion in the limit $U_0 \ll 1$, in which case v_c is given by the speed of sound in the system.

While Chap. 1 focused on determining v_c, a critical velocity central to understanding superfluidity, Chap. 2 explores another important velocity: The supersonic separatrix v_s – still for one-dimensional systems. This velocity marks the boundary between the nonstationary

regime and a distinct stationary regime characterized by nonsuperfluid transport. Using a Hamiltonian approach, we respectively derived exact analytical expressions for v_s in the narrow and wide obstacle limits in Secs. 2.2 and 2.3, employing a methodology similar to that used in the previous chapter. Additionally, we performed numerical simulations in Sec. 2.4 to investigate v_s for intermediate values of σ, notably revealing that v_s exhibits resonances for values of σ lying between the narrow and wide limits.

In Sec. 2.5, we further analyzed these resonances using a toy model of a square well, showing that they are closely linked to lines of perfect transmission across the obstacle at velocities exceeding v_c. These transmission lines connect the superfluid and stationary supersonic regimes, suggesting that the fluid exhibits a superfluid-like dynamics under these specific conditions.

Overall, both Chap. 1 and Chap. 2 contribute to the broader study of the various regimes of transport possible in a 1D quantum fluid. The results from these chapters, when combined in a single figure, offer a comprehensive characterization of the different regimes defined by v_c and v_s. While we derived exact expressions for v_c in specific limits of σ, it is particularly intriguing to investigate its behavior when σ lies between these limits – which was done using numerical simulations. This is illustrated in Fig. 4.1 (identical to the one in the introductory part of Chap. 2) – a phase diagram that maps the various regimes possible as a function of both U_0 and v_∞, and specifically for a square well with typical width $\sigma = 1$. In this case, all curves are derived numerically.

In this figure, the grey and black lines represent v_c and v_s, respectively. These lines demarcate the superfluid regime (light purple) – where the density profile is symmetric and disturbed only in the vicinity of the obstacle (as seen in Subfig. (a)) – from the nonstationary regime (in grey). The latter is characterized by the repeated emission of nonlinear structures that will interfere with each other, potentially leading to a turbulent profile, as shown in Subfig. (b). The supersonic nonsuperfluid regime is depicted in darker purple, and displays two distinct behaviors depending on the obstacle's parameters. In most cases, a part of the fluid is transmitted across the barrier while another is reflected, resulting in the asymmetric density profile shown in Subfig. (c), featuring a cnoidal wave ahead of the obstacle and no perturbation downstream[3]. Finally, the pink dots indicate a line of perfect transmission along which a different dynamics occurs, achieved under very specific conditions. Here, the fluid exhibits a superfluid-like behavior due to a resonance between the width of the obstacle and the wavelength of the cnoidal wave, as depicted in Subfig. (d), where the density profile resembles that of Subfig. (a).

Chapter 3 focused on the critical velocity for superfluidity in two-dimensional systems, highlighting the complexities introduced by a higher dimensionality. We began by demonstrating in Sec. 3.1.2 that the linear-response theory fails when dealing with a $\delta-$peak obstacle, revealing the need for a more sophisticated approach to determine v_c in 2D systems. Yet, it yields results consistent with the Landau criterion when examining the density profiles far from the origin, where the Green's function indeed exhibits a logarithmic divergence.

In this context, the critical velocity cannot be obtained from the conservation of the current as in one dimension, because the continuity equation in two dimensions is not integrable anymore. We thus developed a multi-step method, detailed in Sec. 3.2, in which we perturbatively treated the continuity equation around an incompressible limit by expanding the

[3] An exact calculation of the density profile – as well as the expression of the drag force – is provided in Sec. 2.2.2 for a $\delta-$peak obstacle.

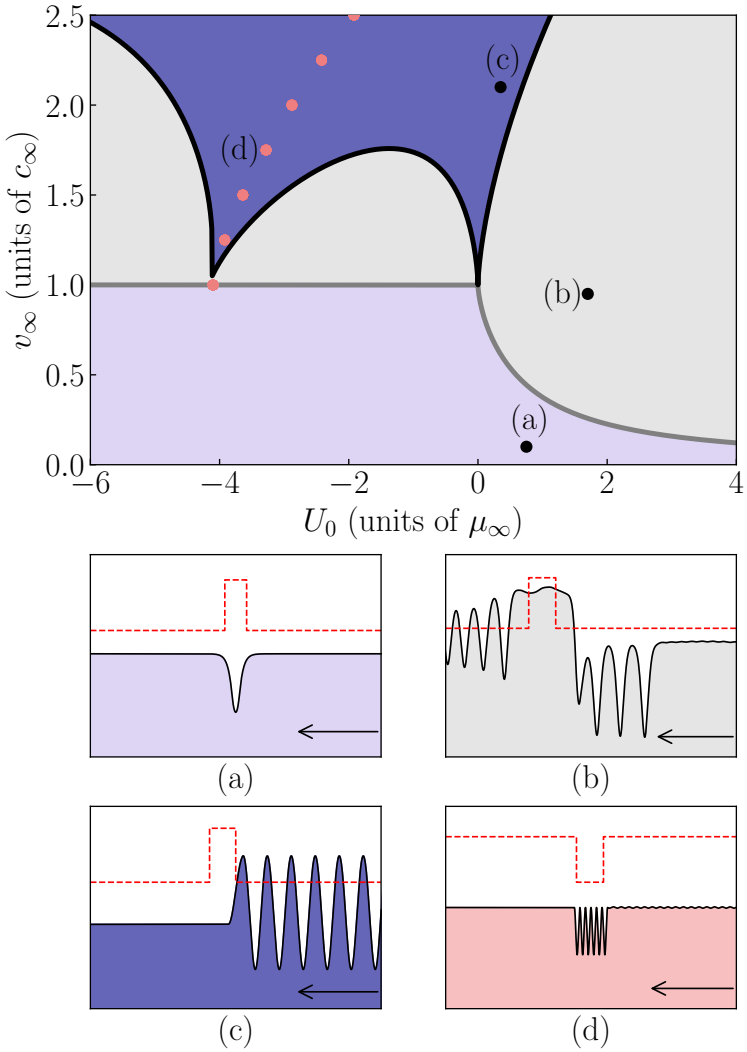

Figure 4.1: Phase diagram illustrating the possible regimes of transport for a 1D quantum fluid characterized by $\varepsilon(n) = n$ flowing from right to left with velocity v_∞, in the presence of a square well obstacle of amplitude U_0 and width $\sigma = 1$ (depicted in red in Subfigs. (a–d)). Depending on the value of (U_0, v_∞), three distinct dynamics can occur: A superfluid regime (light purple), a potentially turbulent nonstationary regime (grey), and a stationary nonsuperfluid regime (darker purple). In the latter, a superfluid-like dynamics can still occur under specific conditions that lead to a perfect transmission across the obstacle. Subfigs. (a–d) show the typical density profiles of the fluid, corresponding to the tags in the main figure.

velocity potential using a Janzen-Rayleigh expansion, and by considering the hydraulic limit (i.e. neglecting the quantum pressure). In this limit, the density obeys an algebraic equation rather than a differential one, making it possible to derive a new condition for superfluid motion.

Our analysis revealed that the critical velocity v_c is highly dependent on the obstacle's amplitude and is – contrary to the results obtained in Chap. 1 – a nonmonotic function of U_0. It is characterized by two branches (obtained respectively for penetrable and impenetrable obstacles), which correspond to two different mechanisms for the breakdown of superfluidity. In Secs. 3.3 and 3.4, we respectively analytically derived v_c to the highest possible order in the Janzen-Rayleigh expansion for different nonlinear interaction potential $\varepsilon(n)$, showing that the critical velocity is a nonmonotonic function of the amplitude U_0 of the obstacle (contrarily to the 1D case). We then performed a imaginary-time numerical simulation of the system in Sec. 3.4.4 in order to characterize the real behavior of v_c at the transition between

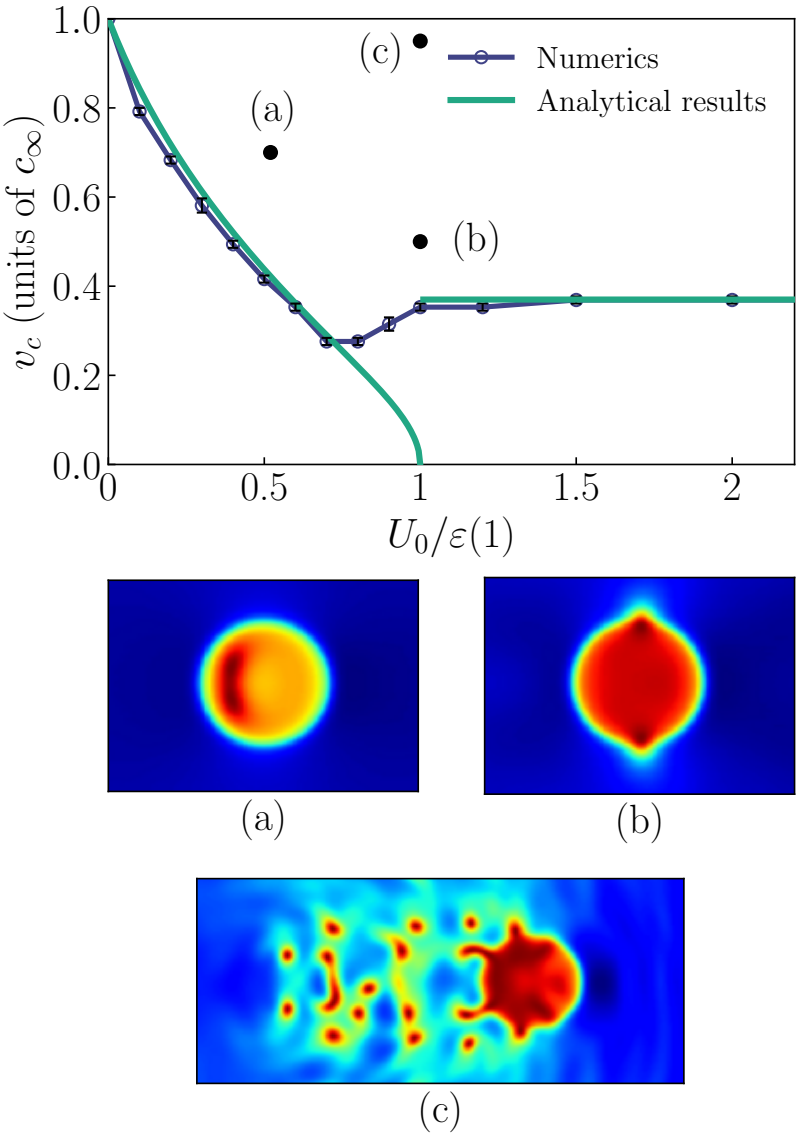

Figure 4.2: Top: Critical velocity v_c as a function of the amplitude $U_0/\varepsilon(1)$ of the obstacle, for $\sigma \gg 1$ and $\varepsilon(n) = n$. The green lines are the analytical limits found in the penetrable and impenetrable regime, whereas the purple line comes from a numerical simulation of the problem, and reveals the true behavior at the transition. Bottom: Subfigs. (a–c) represent the density profile of the quantum fluid for the parameters associated with tags in the main figure. Tag (a) illustrates the formation of a rarefaction wave, tag (b) shows the nucleation of vortices at the poles of the obstacle, and tag (c) illustrates the transition towards a turbulent regime for an important velocity.

penetrable and impenetrable obstacles, and found that it exhibits a minimum. All these results are encompassed in the top part of Fig. 4.2, representing v_c as a function of $U_0/\varepsilon(1)$. The analytical limits we found are represented in green, and are in really good agreement with our numerics (purple), except in the transition zone (in grey), where v_c is smoothed out in order to link the two different regimes.

Finally, we explored the mechanisms underlying the breakdown of superfluidity in Sec. 3.3.4 and 3.4.5. Depending on the flow parameters, this breakdown is driven either by the nucleation of vortices at the poles of the obstacle (impenetrable obstacle, tag (b) in Fig. 4.2), or by the formation of a rarefaction wave within it (penetrable obstacle, tag (a) in Fig. 4.2). We also briefly studied the properties of vortex emission under various flow parameters, and found that under extreme parameters, the system exhibits quantum turbulence (see tag (c)).

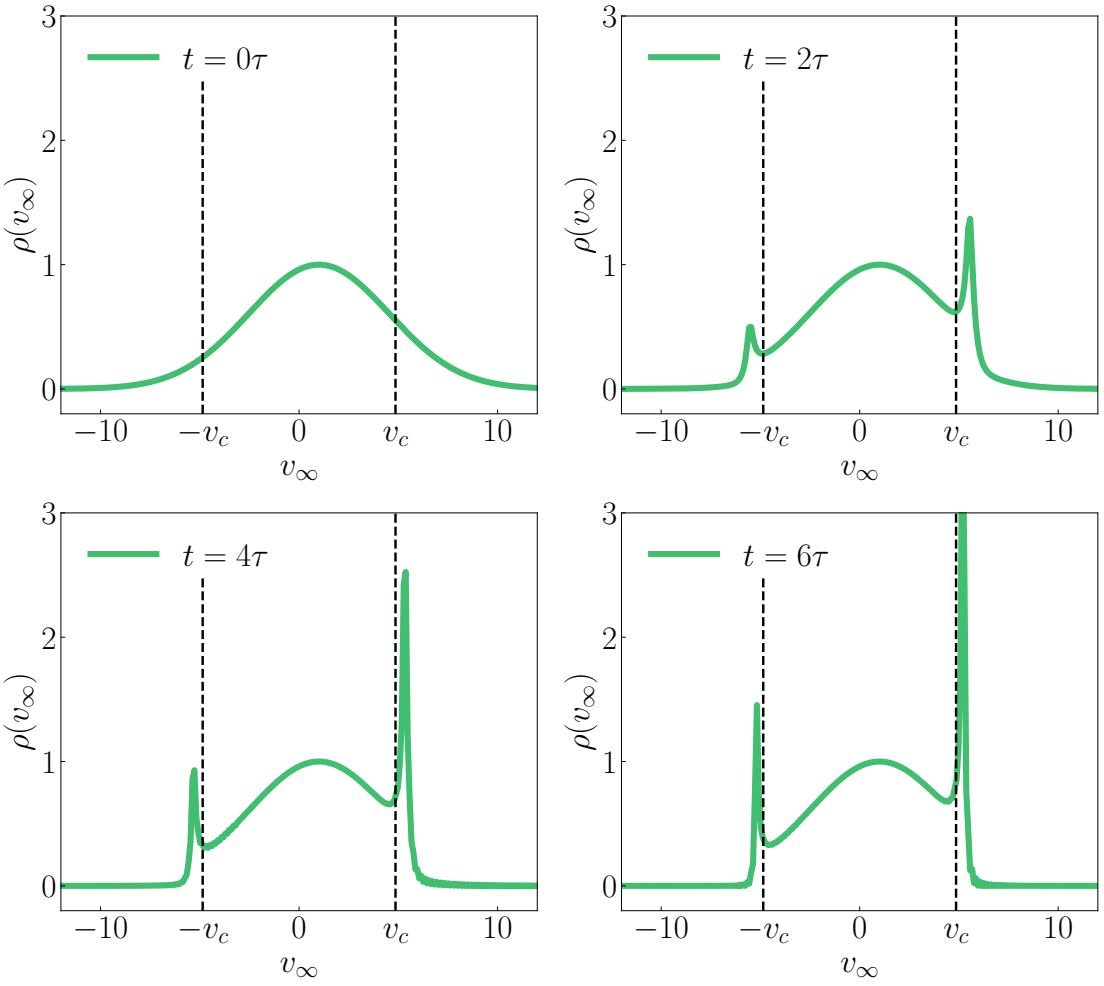

Figure 4.3: Evolution of the velocity probability distribution over time for $t/\tau \in \{0, 2, 4, 6\}$, with characteristic time $\tau = mv_c/F_{\mathrm{d,pert}}$, and $F_{\mathrm{d,pert}}$ the amplitude of the force obtained in the linear-response theory. As time increases, the probability to have $|v_\infty| > v_c$ slowly migrates towards lower velocities – depopulating these states – and stacks on $|v_\infty| = v_c$.

The research conducted during this thesis has been the subject of the publication of three peer-reviewed articles, each introduced at the beginning of the respective chapters. However, our work over the past three years has extended beyond these publications, exploring several additional avenues that hold promising potential for future research.

Building on our work in the 1D regime, we have initiated the exploration of the dynamics of a gas of impurities of mass m moving at supersonic velocities, subjected to the same drag force as modeled in Chap. 2 for a $\delta-$peak obstacle, and obtained preliminary results. We began by developing a simple model for the equation of evolution of the velocity probability distribution. This was then followed by a numerical approach, where we considered an initial off-centered Gaussian distribution. Our results show that, over time, the states with $|v_\infty| > v_c$ are gradually depleted, while a peak emerges in the distribution at $|v_\infty| = v_c$, as illustrated in Fig. 4.3. As the integration progresses, the distribution appears to converge toward an equilibrium state in which the probabilities to have $|v_\infty| > v_c$ become null, and are stacked on $|v_\infty| = v_c$ instead. We also conducted a study of the convergence time, examining how it varies with the parameters of the problem. This work presents intriguing perspectives by demonstrating thermalization towards a highly unconventional state, which could be of significant interest for experimentalists.

Another important perspective to the present one-dimensional study would be to understand and include the effects of quantum fluctuations on the superfluid-nonsuperfluid transition, thus going beyond the mean-field approach we used all along this manuscript. Such fluctuations can indeed play a crucial role in the behavior of a quantum fluid, especially in 1D where correlations are enhanced. For example in the mean-field approach we employed, the drag force linked to energy dissipation (causing a loss of inertia and a deceleration of the system) is strictly null in the superfluid regime. This is what we relied on to determine the critical superfluid velocity (modulo the losses, which smooth the transition around the critical value). However, once quantum fluctuations are taken into account, the system is submitted to a force that is much more complex, as shown in Refs. [57, 156, 184, 185, 221, 222] for example for interacting Bose gases beyond the Gross-Pitaevskii regime. This nonnegligible change in our criterion for superfluid motion then calls for the development of new analytical models to study superfluidity when accounting for the quantum fluctuations.

A significant collaboration has been established with C. Michel and M. Bellec from the experimental team "Waves in Complex Systems" in Nice, focusing on quantum fluids of light in photorefractive crystals. The primary objective is to better qualify the key experimental results presented in Ref. [55], specifically the phase diagram shown in Fig. 3.2. Our goal is to predict the critical velocity in their 2D system using our model, and to confront it to their experimental results. This is an ongoing project, as we are currently developing a numerical model to accurately simulate the obstacle used in their experiments, before computing v_c. This is illustrated in the top part of Fig. 4.4, where the green line represents a radial cut of the obstacle present in their experiment (obtained from a measurement of the intensity profile with the quantum fluid at rest with zero velocity), whereas the dashed line corresponds to the fit we use in out numerical simulation. The obstacle we generate then corresponds to this radial cut revolved around the origin, so that there is a revolution symmetry. The bottom part of Fig. 4.4 represents the intensity profile of the quantum fluid of light moving at $v_\infty = 0.707$ in the presence of the previously-defined obstacle with an amplitude $U_0 = 0.207$. The winglet structure is also present, but there is no revolution symmetry around the origin anymore because of the nonzero current. Such parameters for (U_0, v_∞) correspond to the superfluid regime, as we found that stationary solutions start to disappear for $v_c \in [0.785, 0.801]$. We then compared it to a calculation of v_c for a Gaussian obstacle of the same amplitude, and the same integral as the positive part of the experimental obstacle, and obtained the exact same interval for v_c. The peculiarity of the experimental obstacle, i.e. the presence of winglets on either side, does not impact the value of the critical velocity. This stands as long as the obstacle is far in the penetrable regime and superfluidity is broken inside of it, which is the case that is experimentally relevant. When it is impenetrable however, the winglet structure becomes important because superfluidity is broken at the boundary of the obstacle; This regime is not achievable at the moment in the experiment we are referring to.

Additional discussions are also underway with Q. Glorieux's team at LKB, who possess experimental resources to determine v_c in a different setup (hot atomic vapors). This would provide an opportunity to further test our model with another system. Experiments with quantum fluids of light are particularly promising because, like cold atom experiments, they can probe the penetrable regime.

Along similar lines, a deep interest is also shed to the dynamics of vortices in 2D systems after their emission. Specifically, we have begun investigating the separation distance between vortices in the same pair as a function of the velocity of the obstacle. In the spirit of Ref. [101], a key objective could be to identify the specific parameters that lead to a fully turbulent regime, as shown in tag (c) of Fig. 4.2. Additionally, we aim to potentially observe von Kármán vortex street by breaking a symmetry in the system, either by altering the shape or properties of the obstacle, or introducing noise into the initial ground state in the simulation. This could provide a deeper insight into the transition from orderly vortex dynamics to more

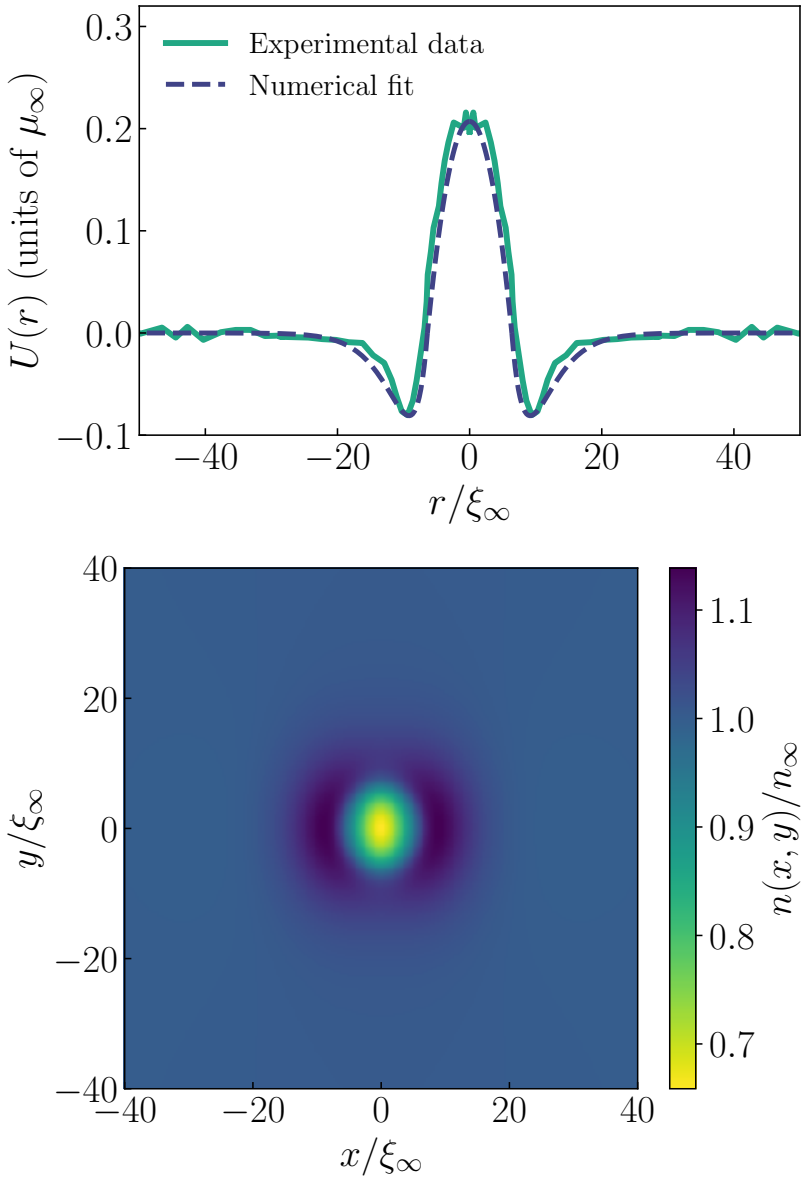

Figure 4.4: Top: The green curves represents a radial cut of the experimental obstacle. To deduce v_c from data as close as possible to the experiments but avoid errors in our simulation, we model it with a fit of the obstacle, represented in dashed line. The obstacle presents a winglet structure on each side, which is not present in the case of a Gaussian obstacle, but which does not impact the value of v_c in a significant way. Bottom: Intensity profile obtained from a quantum fluid of light propagating from left to right at velocity $v_\infty = 0.707$, in the presence of an obstacle modeled by our numerical fit. This corresponds to a superfluid state, as shown by the absence of nonlinear structures.

complex, chaotic behaviors in quantum fluids.

Lastly, a promising direction for future research could involve investigating the transition to superfluidity for systems in the presence of asymmetric obstacles, several of them, or even with disordered potentials as performed in Refs. [48, 50] for example, and see how the critical velocity for superfluidity connects to the properties of the potential, if it fluctuates, if we recover the same limits as derived in this manuscript, etc. This would allow us to test the robustness of the approach we present under more complex conditions, and potentially observe new nontrivial aspects of the critical velocity.

Appendix A

How to determine the condition for superfluidity in 2D?

As it is, the continuity equation $\nabla\cdot(n\boldsymbol{v}) = 0$ is hardly solvable in the $xy-$plane using Cartesian coordinates. It then becomes necessary to perform a change of variables, and derive a "new" continuity equation, easier to solve.

It seems natural to work with polar coordinates given the symmetry of the problem. The velocity of the quantum fluid is easily obtained: $\boldsymbol{v}(\boldsymbol{r}) = (v_x = v\cos\theta, v_y = v\sin\theta)$. We thus want to transform the continuity equation $\nabla\cdot(n\boldsymbol{v}) = 0$, acting on the Cartesian coordinates (x, y), into an equation on the polar coordinates (v, θ).

A.1 Passage in the hodograph plane

A.1.1 Change of variables $(x, y) \to (v, \theta)$

Following the method provided in Sec. 116 of Ref. [207], it is possible to obtain the continuity equation for the velocity components (v_x, v_y), and then by extension for the polar coordinates (v, θ). This involves working in the hodograph plane (v_xv_y-plane) instead of the physical plane ($xy-$plane).

Let us define the Legendre transform $\Phi(v, \theta) = \boldsymbol{v}\cdot\boldsymbol{r} - \phi$: We then have $\mathrm{d}\Phi = x\,\mathrm{d}(v\cos\theta) + y\,\mathrm{d}(v\sin\theta)$. From there, one can easily infer the expressions of x and y

$$x = \partial_v\Phi\,\cos\theta - \partial_\theta\Phi\,\frac{\sin\theta}{v}, \tag{A.1a}$$

$$y = \partial_v\Phi\,\sin\theta + \partial_\theta\Phi\,\frac{\cos\theta}{v}, \tag{A.1b}$$

and the derivatives

$$\partial_v x = \cos\theta\,\partial_v^2\Phi + \frac{\sin\theta}{v^2}\,\partial_\theta\Phi - \frac{\sin\theta}{v}\partial_{v\theta}^2\Phi, \tag{A.2a}$$

$$\partial_\theta x = -\sin\theta\,\partial_v\Phi - \frac{\sin\theta}{v}\,\partial_v^2\Phi - \frac{\cos\theta}{v}\,\partial_\theta\Phi + \cos\theta\partial_{v\theta}^2\Phi, \tag{A.2b}$$

$$\partial_v y = \sin\theta\,\partial_v^2\Phi - \frac{\cos\theta}{v^2}\,\partial_\theta\Phi + \frac{\cos\theta}{v}\partial_{v\theta}^2\Phi, \tag{A.2c}$$

$$\partial_\theta y = \cos\theta\,\partial_v\Phi + \frac{\cos\theta}{v}\,\partial_v^2\Phi - \frac{\sin\theta}{v}\,\partial_\theta\Phi + \sin\theta\partial_{v\theta}^2\Phi. \tag{A.2d}$$

A.1.2 The continuity equation using a Jacobian notation

Let $J\left[(A,B)_{(x,y)}\right]$ be the Jacobian matrix of the application $(x,y)\mapsto(A,B)$; Its determinant is such that

$$\mathrm{Det}\left(J\left[(A,B)_{(x,y)}\right]\right)=\begin{vmatrix}\partial_x A & \partial_y A\\ \partial_x B & \partial_y B\end{vmatrix}. \tag{A.3}$$

When applying this method to our problem, the continuity equation $\nabla\cdot(n\boldsymbol{v})=0$ in Cartesian coordinates (x,y) can be re-expressed in terms of a Jacobian notation. One has $\partial_x(nv_x)+\partial_y(nv_y)=0$, which is equivalent to

$$\mathrm{Det}\left(J\left[(nv_x,y)_{(x,y)}\right]\right)-\mathrm{Det}\left(J\left[(nv_y,x)_{(x,y)}\right]\right)=0. \tag{A.4}$$

The change of variables for the continuity equation involves the determinant of the Jacobian matrix of the application $(x,y)\mapsto(v,\theta)$, defined as $\mathrm{Det}\left(J\left[(x,y)_{(v,\theta)}\right]\right)$. One then has

$$\nabla\cdot(n\boldsymbol{v})=\left\{\mathrm{Det}\left(J\left[(nv_x,y)_{(x,y)}\right]\right)-\mathrm{Det}\left(J\left[(nv_y,x)_{(x,y)}\right]\right)\right\}\mathrm{Det}\left(J\left[(x,y)_{(v,\theta)}\right]\right)=0. \tag{A.5}$$

This equation obeys the chain rule, making it possible to simplify it further, and work exclusively with the polar coordinates (v,θ):

$$\nabla\cdot(n\boldsymbol{v})=\mathrm{Det}\left(J\left[(nv_x,y)_{(v,\theta)}\right]\right)-\mathrm{Det}\left(J\left[(nv_y,x)_{(v,\theta)}\right]\right)=0. \tag{A.6}$$

Using the expressions of the derivatives provided in Eqs. (A.2), one obtains Eq. (3.13), i.e. the "new" continuity equation in the variables (v,θ)

$$\partial_v^2\Phi+\frac{1}{nv}\partial_v(nv)\partial_v\Phi+\frac{1}{nv^2}\partial_v(nv)\partial_\theta^2\Phi=0. \tag{A.7}$$

A.2 A condition for superfluid motion with the method of characteristics

A.2.1 General method of characteristics to solve second-order scalar PDE

The method of characteristic is often used in physics to solve PDEs, by transforming the equation into a system of characteristics [223], i.e. curves along which the PDE becomes an ODE. Let us treat the most general case defined by

$$a\partial_x^2u+2b\partial_x\partial_yu+c\partial_y^2u+d\partial_xu+e\partial_yu=g, \tag{A.8}$$

where u,a,b,c,d,e,g are functions of x and y. We first convert this equation to a coupled first-order system. The second-order PDE can then be written as

$$A\partial_x\nabla u+B\partial_y\nabla u=C, \tag{A.9}$$

with

$$A=\begin{pmatrix}a & 0\\ 0 & 1\end{pmatrix}, \tag{A.10a}$$

$$B=\begin{pmatrix}2b & c\\ -1 & 0\end{pmatrix}, \tag{A.10b}$$

$$C=\begin{pmatrix}g-d\partial_xu-e\partial_yu\\ 0\end{pmatrix}. \tag{A.10c}$$

Characteristics are determined by $\frac{\mathrm{d}y}{\mathrm{d}x} = \lambda$, with λ the eigenvalue of $B - \lambda A$, and are thus given by

$$\begin{vmatrix} 2b - \lambda a & c \\ -1 & -\lambda \end{vmatrix} = 0, \tag{A.11}$$

which leads to $\lambda = (b \pm \sqrt{b^2 - ac})/a$.

The characteristics of a PDE are a convenient quantity for gaining insight into a PDE, as they provide information on the nature of its solutions. They are lines along which disturbances can possibly propagate. 3 families of characteristics can exist depending on the value of λ, and will determine the type of solution one has

- Two distinct real eigenvalues if $b^2 > ac$: The PDE is hyperbolic.
- Two distinct complex eigenvalues if $b^2 < ac$: The PDE is elliptic.
- One real eigenvalue if $b^2 = ac$: The PDE is parabolic.

Any small disturbance will propagate with a finite velocity along the characteristics of the equation if λ is real. The case we are interested in corresponds to elliptic PDEs, since nothing can propagate along an imaginary characteristic. Thus, if λ is complex, there is no curve in the $\{x, y\}$ plane along which a perturbation of the field u may propagate. In other words, the motion is superfluid.

A.2.2 The condition for superfluidity applied to our problem

To solve Eq. (A.7) with the method of characteristic, we consider $a = 1$, $b = 0$, $c = \frac{1}{nv^2}\partial_v(nv)$, $d = \frac{1}{nv}\partial_v(nv)$, $e = 0$ and $g = 0$, with $x \to v$ and $y \to \theta$. This leads to

$$\lambda = \frac{\mathrm{d}\theta}{\mathrm{d}v} = \pm\sqrt{-\frac{1}{nv^2}\partial_v(nv)}. \tag{A.12}$$

For λ to be imaginary, one necessarily needs $\partial_v(nv) > 0$ since n and v are always positive. This is the condition for superfluid motion provided in Eq. (3.15).

Appendix B

Exact resolution of $v_{c,k}$ for an impenetrable obstacle

We provide in this section the detailed calculations leading to the exact analytical expression for the critical velocity for superfluidity in the impenetrable regime, for a powerlaw nonlinearity and a saturable nonlinearity. These results are really complicated as each order k in the Janzen-Rayleigh expansion depends on the previous orders. We provide the various ϕ_k's up to the order $k = 4$ for each nonlinearity (even though we went up to order 6 for a saturable nonlinearity) and then compute the $v_{c,k}$'s from these expressions.

B.1 Results for a powerlaw nonlinearity: $\varepsilon(n) = n^\nu/\nu$

B.1.1 The incompressible solution: $k = 0$

One has to solve Laplace's equation for the velocity potential ϕ_0

$$\nabla^2 \phi_0(\boldsymbol{r}) = 0. \tag{B.1}$$

The resolution with the proper boundary conditions $\phi(r \gg \sigma) = v_\infty r \cos\theta$ and $\partial_r \phi_k(\sigma) = 0$ leads to the exact expression of the velocity potential

$$\phi_0(\boldsymbol{r}) = v_\infty r \left[1 + \frac{\sigma^2}{r^2}\right] \cos\theta, \tag{B.2}$$

and thus $v_{\max} = v_{\max,0} = 2v_\infty$.

To obtain the critical velocity for superfluidity to the zeroth order in the compressibility (i.e. in the incompressible approximation), one has to use the following condition for superfluidity

$$1 + v_\infty^2 \left[\frac{\nu}{2} - \frac{v_{\max}^2}{v_\infty^2}\left(1 + \frac{\nu}{2}\right)\right] > 0. \tag{B.3}$$

This condition is a second-order polynomial in v_∞, which solution is easily obtained. In the end, the resolution leads to

$$v_\infty < v_{c,0} = \sqrt{\frac{2}{8 + 3\nu}}. \tag{B.4}$$

One recovers the celebrated result obtained in Ref. [58] for $\nu = 1$, i.e. $v_{c,0} = \sqrt{2/11}$.

B.1.2 Solution for $k = 1$

One can obtain the equation to determine $\phi_1(\boldsymbol{r})$ using the recurrence relation (3.39). Since $\nabla^2\phi_0 = 0$, this simplifies to

$$\nabla^2\phi_1(\boldsymbol{r}) = \frac{1}{2v_\infty^2}\nabla\phi_0\nabla(v^2)_0, \tag{B.5}$$

with $(v^2)_0 = |\nabla\phi_0|^2$. The resolution with our Ansatz defined by Eq. (3.53), as well as the boundary condition $\partial_r\phi_k(\sigma) = 0$[1] leads to

$$\phi_1(\boldsymbol{r}) = v_\infty r\left[\left(\frac{13\sigma^2}{12r^2} - \frac{\sigma^4}{2r^4} + \frac{\sigma^6}{12r^6}\right)\cos\theta + \left(-\frac{\sigma^2}{4r^2} + \frac{\sigma^4}{12r^4}\right)\cos 3\theta\right]. \tag{B.6}$$

One can then easily determine $v_{\max,1} = |\nabla\phi_1(\sigma, \pm\pi/2)|$, thus leading to $v_{\max} = v_{\max,0} + \chi v_{\max,1} = v_\infty\left(2 + \frac{7v_\infty^2}{6}\right)$.

The condition for superfluidity is still the same as Eq. (B.3), which is a fourth-order polynomial in v_∞. In the end, its resolution leads to

$$v_\infty < v_{c,1} = \frac{1}{2\sqrt{7}}\sqrt{\frac{-24 - 9\nu + \sqrt{1248 + 768\nu + 81\nu^2}}{2 + \nu}}. \tag{B.7}$$

B.1.3 Solution for $k = 2$

Using the expressions for $\nabla^2\phi_0(\boldsymbol{r})$ and $\nabla^2\phi_1(\boldsymbol{r})$ we previously found, the recurrence relation given by Eq. (3.39) simplifies to

$$\nabla^2\phi_2(\boldsymbol{r}) = -\frac{\nu}{2}\nabla^2\phi_1 + \frac{1}{2v_\infty^2}\left[\nabla\phi_0\nabla(v^2)_1 + \nabla\phi_1\nabla(v^2)_0 + \nu\nabla^2\phi_1(v^2)_0\right], \tag{B.8}$$

with $(v^2)_1 = 2\nabla\phi_0\nabla\phi_1$. The resolution for $\phi_2(\boldsymbol{r})$ with our Ansatz leads to

$$\begin{aligned}\phi_2(\boldsymbol{r}) = v_\infty r\Bigg[\Bigg(&\frac{(411+68\nu)\sigma^2}{240r^2} - \frac{(32+3\nu)\sigma^4}{24r^4} + \frac{(39+4\nu)\sigma^6}{48r^6} - \frac{(5+\nu)\sigma^8}{16r^8} \\ &+ \frac{(11+3\nu)\sigma^{10}}{240r^{10}}\Bigg)\cos\theta + \Bigg(-\frac{19\sigma^2}{48r^2} - \frac{(25+61\nu)\sigma^4}{240r^4} + \frac{3(1+\nu)\sigma^6}{16r^6} - \frac{(5+3\nu)\sigma^8}{120r^8} \\ &+ \frac{\sigma^{10}}{144r^{10}}\Bigg)\cos 3\theta + \left(\frac{\sigma^2}{16r^2} + \frac{(1+\nu)\sigma^4}{16r^4} - \frac{(4+3\nu)\sigma^6}{80r^6}\right)\cos 5\theta\Bigg],\end{aligned} \tag{B.9}$$

and thus with $v_{\max} = v_{\max,0} + \chi v_{\max,1} + \chi^2 v_{\max,2} = v_\infty\left(2 + \frac{7v_\infty^2}{6} + \frac{(281+71\nu)v_\infty^4}{120}\right)$. The condition for superfluidity is still given by Eq. (B.3), but now leads to a sixth-order polynomial in v_∞, for which we did not obtain an analytical expression.

B.1.4 Solution for $k = 3$

The velocity potential $\phi_3(\boldsymbol{r})$ is obtained from the recurrence relation (3.39), which simplifies to

$$\begin{aligned}\nabla^2\phi_3(\boldsymbol{r}) = -\frac{\nu}{2}\nabla^2\phi_2 + \frac{1}{2v_\infty^2}\Big[&\nabla\phi_2\nabla(v^2)_0 + \nabla\phi_1\nabla(v^2)_1 + \nabla\phi_0\nabla(v^2)_2 \\ &+ \nu\nabla^2\phi_2(v^2)_0 + \nu\nabla^2\phi_1(v^2)_1\Big],\end{aligned} \tag{B.10}$$

[1] Since $\phi(\boldsymbol{r}) = \phi_0(\boldsymbol{r}) + \chi\phi_1(\boldsymbol{r}) + \chi^2\phi_2(\boldsymbol{r}) + ...$, the boundary condition at infinity defined by $\phi(r \gg \sigma) = v_\infty r\cos\theta$ is already satisfied by $\phi_0(\boldsymbol{r})$. It then does not apply to $\phi_k(\boldsymbol{r})$ with $k \geq 1$.

with $(v^2)_2 = 2\nabla\phi_0\nabla\phi_2 + |\nabla\phi_1|^2$. After resolution with the proper boundary conditions, the velocity potential $\phi_3(\boldsymbol{r})$ becomes

$$\begin{aligned}
\phi_3(\boldsymbol{r}) = v_\infty r\Bigg[\Bigg(&\frac{\left(60\nu^2+459\nu+853\right)\sigma^{14}}{20160r^{14}} - \frac{\left(24\nu^2+252\nu+533\right)\sigma^{12}}{1440r^{12}} \\
&+ \frac{\left(108\nu^2+1557\nu+3898\right)\sigma^{10}}{2880r^{10}} - \frac{\left(180\nu^2+2607\nu+7870\right)\sigma^{8}}{2880r^{8}} + \frac{\left(60\nu^2+2235\nu+9613\right)\sigma^{6}}{2880r^{6}} \\
&+ \frac{\left(472\nu^2+4224\nu+10571\right)\sigma^{2}}{3360r^{2}} - \frac{(489\nu+2248)\sigma^{4}}{720r^{4}}\Bigg)\cos\theta + \Bigg(-\frac{\left(60\nu^2+369\nu+659\right)\sigma^{12}}{6720r^{12}} \\
&+ \frac{\left(180\nu^2+1203\nu+1595\right)\sigma^{10}}{4320r^{10}} - \frac{\left(180\nu^2+4839\nu+6055\right)\sigma^{8}}{7200r^{8}} + \frac{\left(60\nu^2+1281\nu+1430\right)\sigma^{6}}{960r^{6}} \\
&- \frac{\left(13920\nu^2+129456\nu+111455\right)\sigma^{4}}{100800r^{4}} + \frac{(6\nu+17)\sigma^{14}}{1440r^{14}} - \frac{(17\nu+154)R^2\sigma^2}{240r^2}\Bigg)\cos 3\theta \\
&+ \Bigg(\frac{\left(60\nu^2+159\nu-5\right)\sigma^{10}}{6720r^{10}} - \frac{\left(8\nu^2+10\nu-5\right)\sigma^{8}}{96r^{8}} + \frac{\left(30420\nu^2-39339\nu-130670\right)\sigma^{6}}{302400r^{6}} \\
&- \frac{(6\nu+5)\sigma^{12}}{1440r^{12}} + \frac{(388\nu+545)\sigma^{4}}{960r^{4}} + \frac{\sigma^{14}}{1728r^{14}} + \frac{25\sigma^2}{192r^2}\Bigg)\cos 5\theta \\
&+ \Bigg(\frac{\left(20\nu^2+41\nu+17\right)\sigma^{8}}{1344r^{8}} - \frac{\left(4\nu^2+\nu-8\right)\sigma^{6}}{192r^{6}} - \frac{(2\nu+3)\sigma^{4}}{32r^{4}} - \frac{\sigma^2}{64r^2}\Bigg)\cos 7\theta\Bigg]. \quad \text{(B.11)}
\end{aligned}$$

The maximum velocity is now given by $v_{\max} = v_{\max,0} + \chi v_{\max,1} + \chi^2 v_{\max,2} + \chi^3 v_{\max,3} = v_\infty\left(2 + \frac{7v_\infty^2}{6} + \frac{(281+71\nu)v_\infty^4}{120} + \frac{(916100+520119\nu+75420\nu^2)v_\infty^6}{151200}\right)$. The condition for superfluidity is an eighth-order polynomial in v_∞, which is numerically solved.

B.1.5 Solution for $k = 4$

Similarly to the previous sections, we obtain the velocity potential $\phi_4(\boldsymbol{r})$ after resolution of the Poisson equation, now given by

$$\begin{aligned}
\nabla^2\phi_4(\boldsymbol{r}) = -\frac{\nu}{2}\nabla^2\phi_3 + \frac{1}{2v_\infty^2}\Big[&\nabla\phi_3\nabla(v^2)_0 + \nabla\phi_2\nabla(v^2)_1 + \nabla\phi_1\nabla(v^2)_2 + \nabla\phi_0\nabla(v^2)_0 \\
&+ \nu\nabla^3\phi_2(v^2)_0 + \nu\nabla^2\phi_2(v^2)_1 + \nu\nabla^2\phi_1(v^2)_2\Big], \quad \text{(B.12)}
\end{aligned}$$

with $(v^2)_3 = 2\left(\nabla\phi_0\nabla\phi_3 + \nabla\phi_1\nabla\phi_2\right)$. We again use our Ansatz for $\phi_4(\boldsymbol{r})$, leading to

$$\phi_4(\boldsymbol{r}) = v_\infty r\Bigg[\Bigg(\frac{\left(420\nu^3+5027\nu^2+19552\nu+24316\right)\sigma^{18}}{483840r^{18}} - \frac{\left(2130\nu^2+27057\nu+71137\right)\sigma^4}{10080r^4}$$
$$- \frac{\left(300\nu^3+4901\nu^2+21728\nu+29010\right)\sigma^{16}}{53760r^{16}} + \frac{\left(4320\nu^3+82356\nu^2+417060\nu+608605\right)\sigma^{14}}{241920r^{14}}$$
$$- \frac{\left(11340\nu^3+216477\nu^2+1250934\nu+2035135\right)\sigma^{12}}{302400r^{12}} + \frac{\left(4860\nu^3+155241\nu^2+1072320\nu+1990930\right)\sigma^{10}}{172800r^{10}}$$
$$- \frac{\left(18900\nu^3+961875\nu^2+7511022\nu+16090280\right)\sigma^8}{1209600r^8} + \frac{\left(1175580\nu^2+14262588\nu+38212105\right)\sigma^6}{3628800r^6}$$
$$+ \frac{\left(76608\nu^3+823638\nu^2+3254982\nu+4721945\right)\sigma^2}{725760r^2}\Bigg)\cos\theta$$
$$+ \Bigg(\frac{\left(852\nu^2+5073\nu+7613\right)\sigma^{18}}{403200r^{18}} - \frac{\left(1260\nu^3+13401\nu^2+54327\nu+71465\right)\sigma^{16}}{362880r^{16}}$$
$$+ \frac{\left(3780\nu^3+50247\nu^2+189318\nu+222896\right)\sigma^{14}}{241920r^{14}} - \frac{\left(8100\nu^3+221415\nu^2+935166\nu+1030970\right)\sigma^{12}}{403200r^{12}}$$
$$+ \frac{\left(12600\nu^3+255660\nu^2+1295193\nu+1400360\right)\sigma^{10}}{302400r^{10}}$$
$$+ \frac{\left(35040\nu^2+279749\nu+301605\right)\sigma^6}{44800r^6} - \frac{\left(1580400\nu^3+22266000\nu^2+93707574\nu+82126265\right)\sigma^4}{18144000r^4}$$
$$- \frac{\left(944\nu^2+9400\nu+30641\right)\sigma^2}{26880r^2} - \frac{\left(18900\nu^3+1704015\nu^2+15791469\nu+18073850\right)\sigma^8}{3024000r^8}\Bigg)\cos 3\theta$$
$$+ \Bigg(-\frac{\left(3780\nu^3+140187\nu^2+252771\nu+54970\right)\sigma^8}{120960r^8} + \frac{\left(3780\nu^3+31383\nu^2+88227\nu+61820\right)\sigma^{14}}{725760r^{14}}$$
$$- \frac{\left(10500\nu^3+82035\nu^2+179444\nu+82510\right)\sigma^{12}}{403200r^{12}} + \frac{\left(37800\nu^3+2169360\nu^2+4779801\nu+1705895\right)\sigma^{10}}{4233600r^{10}}$$
$$+ \frac{(9\nu+23)\sigma^{18}}{10368r^{18}} - \frac{\left(2556\nu^2+11007\nu+12595\right)\sigma^{16}}{604800r^{16}} + \frac{\left(28020\nu^2+341009\nu+459205\right)\sigma^4}{201600r^4}$$
$$+ \frac{\left(1008000\nu^3+13613240\nu^2+8320429\nu-17187945\right)\sigma^6}{14112000r^6} + \frac{(68\nu+881)\sigma^2}{3840r^2}\Bigg)\cos 5\theta$$
$$+ \Bigg(\frac{\sigma^{18}}{20736r^{18}} - \frac{(9\nu+5)\sigma^{16}}{17280r^{16}} + \frac{\left(852\nu^2+1065\nu-575\right)\sigma^{14}}{403200r^{14}} - \frac{\left(80568\nu^2+152307\nu+30610\right)\sigma^6}{241920r^6}$$
$$- \frac{\left(420\nu^3+1247\nu^2-1467\nu-2915\right)\sigma^{12}}{120960r^{12}} + \frac{\left(100\nu^3+75\nu^2-436\nu-440\right)\sigma^{10}}{2560r^{10}}$$
$$+ \frac{\left(-2274300\nu^3+10795227\nu^2+40214880\nu+26537750\right)\sigma^8}{50803200r^8} - \frac{(653\nu+1075)\sigma^4}{1920r^4} - \frac{31\sigma^2}{768r^2}\Bigg)\cos 7\theta$$
$$+ \Bigg(\frac{\left(-28\nu^3-57\nu^2+6\nu+44\right)\sigma^{10}}{4608r^{10}} + \frac{\left(4\nu^3-9\nu^2-48\nu-38\right)\sigma^8}{512r^8} + \frac{3\left(4\nu^2+9\nu+4\right)\sigma^6}{256r^6}$$
$$+ \frac{5(3\nu+5)\sigma^4}{384r^4} + \frac{\sigma^2}{256r^2}\Bigg)\cos 9\theta\Bigg]. \quad \text{(B.13)}$$

The maximum velocity is now given by $v_{\max} = v_{\max,0}+\chi v_{\max,1}+\chi^2 v_{\max,2}+\chi^3 v_{\max,3}+\chi^4 v_{\max,4}$, which reduces to

$$v_{\max} = v_\infty\left(2+\frac{7v_\infty^2}{6}+\frac{(281+71\nu)v_\infty^4}{120}+\frac{(916100+520119\nu+75420\nu^2)v_\infty^6}{151200}\right.$$
$$\left.+\left[\frac{1991\nu^3}{4032}+\frac{1669625\nu^2}{338688}+\frac{86755847\nu}{5292000}+\frac{115656949}{6350400}\right]v_\infty^8\right). \quad \text{(B.14)}$$

This leads to a tenth-order polynomial in v_∞ to solve in order to obtain the condition for superfluidity. Again, we perform this step numerically.

Even though we still have exact analytical expressions for $\phi_k(\boldsymbol{r})$ up to order 6, writing them would be quite cumbersome as it would take too much space. Concerning the obtention of $v_{c,k}$ from these velocity potentials, we numerically solved the condition for superfluidity for $k \geq 2$ since it is a $2(k+1)-$order polynomial in v_∞.

B.2 Results for a saturable nonlinearity: $\varepsilon(n) = (1+\beta)^2\frac{n}{1+\beta n}$ with $\beta = 1/n_{\text{sat}}$

B.2.1 The incompressible solution: $k = 0$

The resolution for $\phi_0(\boldsymbol{r})$ is quite similar to that for the powerlaw nonlinearity: One has to solve the same Laplace's equation for the velocity potential ϕ_0

$$\nabla^2\phi_0(\boldsymbol{r}) = 0, \quad \text{(B.15)}$$

with the same boundary conditions $\phi(r \gg \sigma) = v_\infty r\cos\theta$ and $\partial_r\phi_k(\sigma) = 0$, thus leading to the same expression for $\phi_0(\boldsymbol{r})$

$$\phi_0(\boldsymbol{r}) = v_\infty r\left[1+\frac{\sigma^2}{r^2}\right]\cos\theta. \quad \text{(B.16)}$$

The maximum velocity is then also given by $v_{\max} = v_{\max,0} = 2v_\infty$.

The only difference occurs on the condition for superfluidity, which highly depends on the expression of the nonlinear interaction potential $\varepsilon(n)$. For a saturable nonlinearity, one thus has to solve

$$4(1+\beta)^2 - 2v_\infty^2\left[\frac{v_{\max}^2}{v_\infty^2}\left(3+4\beta+\beta^2\right)-1+\beta^2\right] - \beta v_\infty^4\left(\frac{v_{\max}^2}{v_\infty^2}-1\right)^2 > 0. \quad \text{(B.17)}$$

This condition is now a fourth-order polynomial in v_∞, which solution is

$$v_\infty < v_{c,0} = \frac{1}{3}\sqrt{\frac{\sqrt{(1+\beta)^3(121+25\beta)}}{\beta} - \left(5\beta+16+\frac{11}{\beta}\right)}. \quad \text{(B.18)}$$

One also recovers the celebrated result obtained in Ref. [58] in the limit $\beta \to 0$, i.e. $v_{c,0} = \sqrt{2/11}$.

B.2.2 Solution for $k = 1$

One can obtain the equation to determine $\phi_1(\boldsymbol{r})$ using the recurrence relation (3.42) this time. Since $\nabla^2\phi_0 = 0$, this simplifies to the same equation as for the powerlaw nonlinearity

$$\nabla^2\phi_1(\boldsymbol{r}) = \frac{1}{2v_\infty^2}\nabla\phi_0\nabla(v^2)_0, \quad \text{(B.19)}$$

with $(v^2)_0 = |\nabla\phi_0|^2$. The resolution with our Ansatz defined by Eq. (3.53), as well as the boundary condition $\partial_r\phi_k(\sigma) = 0$ also leads to

$$\phi_1(\boldsymbol{r}) = v_\infty r\left[\left(\frac{13\sigma^2}{12r^2} - \frac{\sigma^4}{2r^4} + \frac{\sigma^6}{12r^6}\right)\cos\theta + \left(-\frac{\sigma^2}{4r^2} + \frac{\sigma^4}{12r^4}\right)\cos 3\theta\right], \tag{B.20}$$

with the same $v_{\max,1} = |\nabla\phi_1(\sigma, \pm\pi/2)|$, thus leading to $v_{\max} = v_{\max,0} + \chi v_{\max,1} = v_\infty\left(2 + \frac{7v_\infty^2}{6}\right)$.

Contrary to the resolution for the powerlaw nonlinearity, the condition for superfluidity is provided by (B.17), which leads to an eighth-order polynomial in v_∞, which needs to be solved numerically.

B.2.3 Solution for $k = 2$

Using the expressions for $\nabla^2\phi_0(\boldsymbol{r})$ and $\nabla^2\phi_1(\boldsymbol{r})$ we previously found, the recurrence relation given by Eq. (3.42) simplifies to

$$\nabla^2\phi_2(\boldsymbol{r}) = -\frac{1}{2}\frac{1-\beta}{1+\beta}\nabla^2\phi_1 + \frac{1}{2v_\infty^2}\left[\nabla\phi_0\nabla(v^2)_1 + \nabla\phi_1\nabla(v^2)_0 + \frac{1-\beta}{1+\beta}\nabla^2\phi_1(v^2)_0\right], \tag{B.21}$$

with $(v^2)_1 = 2\nabla\phi_0\nabla\phi_1$. This is now a different equation than for the powerlaw nonlinearity. The resolution for $\phi_2(\boldsymbol{r})$ with our Ansatz leads to

$$\begin{aligned}\phi_2(\boldsymbol{r}) = \frac{v_\infty r}{8(1+\beta)}\Bigg[\Bigg(&\frac{(479+343\beta)\sigma^2}{30r^2} - \frac{(35+29\beta)\sigma^4}{3r^4} + \frac{(43+35\beta)\sigma^6}{6r^6} - \frac{(3+2\beta)\sigma^6}{r^8} \\ &+ \frac{(7+4\beta)\sigma^{10}}{15r^{10}}\Bigg)\cos\theta + \Bigg(-\frac{19(1+\beta)\sigma^2}{6r^2} + \frac{(-43+18\beta)\sigma^4}{15r^4} + \frac{3\sigma^6}{r^6} - \frac{15(4+\beta)\sigma^8}{2r^8} \\ &+ \frac{(1+\beta)\sigma^{10}}{18r^{10}}\Bigg)\cos 3\theta + \left(\frac{(1+\beta)\sigma^2}{2r^2} + \frac{\sigma^4}{r^4} - \frac{(7+\beta)\sigma^6}{10r^6}\right)\cos 5\theta\Bigg],\end{aligned} \tag{B.22}$$

and thus $v_{\max} = v_{\max,0} + \chi v_{\max,1} + \chi^2 v_{\max,2} = v_\infty\left(2 + \frac{7v_\infty^2}{6} + \frac{v_\infty^4}{60}\frac{176+105\beta}{1+\beta}\right)$. The condition for superfluidity is still given by Eq. (B.17), but now leads to a twelfth-order polynomial in v_∞, for which we did not obtain an analytical expression.

B.2.4 Solution for $k = 3$

Using the recurrence relation (3.42), the Poisson equation to solve to obtain the velocity potential $\phi_3(\boldsymbol{r})$ reads

$$\begin{aligned}\nabla^2\phi_3(\boldsymbol{r}) = &-\frac{1}{2}\frac{1-\beta}{1+\beta}\nabla^2\phi_2 + \frac{\beta}{4(1+\beta)^2}\nabla^2\phi_1 + \frac{1}{2v_\infty^2}\Big[\nabla\phi_0\nabla(v^2)_2 + \nabla\phi_1\nabla(v^2)_1 + \nabla\phi_2\nabla(v^2)_0 \\ &+ \frac{1-\beta}{1+\beta}\left(\nabla^2\phi_2(v^2)_0 + \nabla^2\phi_1(v^2)_1\right) - \frac{\beta}{(1+\beta)^2}\nabla^2\phi_1(v^2)_0\Big] + \frac{1}{4v_\infty^4}\frac{\beta}{(1+\beta)^2}\nabla^2\phi_1(v^2)_0(v^2)_0,\end{aligned} \tag{B.23}$$

with $(v^2)_2 = 2\nabla\phi_0\nabla\phi_2 + |\nabla\phi_1|^2$.

Its resolution leads to the analytical expression of the velocity potential

$$\begin{aligned}\phi_3(\boldsymbol{r}) = v_\infty r\Bigg[&\left(\frac{\left(227\beta^2+823\beta+686\right)\sigma^{14}}{10080(\beta+1)^2r^{14}} - \frac{\left(305\beta^2+1042\beta+809\right)\sigma^{12}}{1440(\beta+1)^2r^{12}}\right.\\
&+\frac{\left(2449\beta^2+7688\beta+5563\right)\sigma^{10}}{2880(\beta+1)^2r^{10}}-\frac{\left(5443\beta^2+15560\beta+10657\right)\sigma^{8}}{2880(\beta+1)^2r^{8}}+\frac{\left(3719\beta^2+9583\beta+5954\right)\sigma^{6}}{1440(\beta+1)^2r^{6}}\\
&\left.-\frac{\left(1759\beta^2+4496\beta+2737\right)\sigma^{4}}{720(\beta+1)^2r^{4}}+\frac{\left(2273\beta^2+6890\beta+5089\right)\sigma^{2}}{1120(\beta+1)^2r^{2}}\right)\cos\theta\\
&+\left(\frac{\left(11\beta^2+34\beta+23\right)\sigma^{14}}{1440(\beta+1)^2r^{14}} - \frac{\left(175\beta^2+629\beta+544\right)\sigma^{12}}{3360(\beta+1)^2r^{12}} + \frac{\left(286\beta^2+1505\beta+1489\right)\sigma^{10}}{2160(\beta+1)^2r^{10}}\right.\\
&-\frac{\left(698\beta^2+5965\beta+5537\right)\sigma^{8}}{3600(\beta+1)^2r^{8}}+\frac{\left(209\beta^2+2800\beta+2771\right)\sigma^{6}}{960(\beta+1)^2r^{6}}+\frac{\left(4081\beta^2-208990\beta-254831\right)\sigma^{4}}{100800(\beta+1)^2r^{4}}\\
&\left.-\frac{\left(137\beta^2+308\beta+171\right)\sigma^{2}}{240(\beta+1)^2r^{2}}\right)\cos 3\theta\\
&+\left(\frac{\left(\beta^2-10\beta-11\right)\sigma^{12}}{1440(\beta+1)^2r^{12}} - \frac{\left(52\beta^2+35\beta-107\right)\sigma^{10}}{3360(\beta+1)^2r^{10}} + \frac{\left(7\beta^2+18\beta-13\right)\sigma^{8}}{96(\beta+1)^2r^{8}}\right.\\
&-\frac{\left(60911\beta^2+291760\beta+139589\right)\sigma^{6}}{302400(\beta+1)^2r^{6}}+\frac{\left(157\beta^2+1090\beta+933\right)\sigma^{4}}{960(\beta+1)^2r^{4}}+\frac{\sigma^{14}}{1728r^{14}}+\frac{25\sigma^2}{192r^2}\Bigg)\cos 5\theta\\
&+\left(\frac{\left(-2\beta^2+7\beta+39\right)\sigma^{8}}{672(\beta+1)^2r^{8}}+\frac{\left(5\beta^2+20\beta+3\right)\sigma^{6}}{192(\beta+1)^2r^{6}}-\frac{\left(\beta^2+6\beta+5\right)\sigma^{4}}{32(\beta+1)^2r^{4}}-\frac{\sigma^2}{64r^2}\right)\cos 7\theta\Bigg],\end{aligned} \tag{B.24}$$

and thus to $v_{\max} = v_{\max,0} + \chi v_{\max,1} + \chi^2 v_{\max,2} + \chi^3 v_{\max,3}$, with

$$v_{\max,3} = \frac{v_\infty^6}{151200}\frac{471401\beta^2+1756780\beta+1511639}{(1+\beta)^2}. \tag{B.25}$$

The condition for superfluid motion is now given by a $16^{\text{th}}-$order polynomial in v_∞, which is obviously solved numerically to obtain v_c.

B.2.5 Solution for $k = 4$

The Poisson equation we derive to obtain the velocity potential $\phi_4(\boldsymbol{r})$ is now given by

$$\begin{aligned}\nabla^2\phi_4(\boldsymbol{r}) = -\frac{1}{2}\frac{1-\beta}{1+\beta}\nabla^2\phi_3 + \frac{\beta}{4(1+\beta)^2}\nabla^2\phi_2 + \frac{1}{2v_\infty^2}\Big[&\nabla\phi_0\nabla(v^2)_3 + \nabla\phi_1\nabla(v^2)_2\\
&+\nabla\phi_2\nabla(v^2)_1 + \nabla\phi_3\nabla(v^2)_0 + \frac{1-\beta}{1+\beta}\left(\nabla^2\phi_3(v^2)_0 + \nabla^2\phi_2(v^2)_1 + \nabla^2\phi_1(v^2)_2\right)\\
-\frac{\beta}{(1+\beta)^2}\left(\nabla^2\phi_2(v^2)_0 + \nabla^2\phi_1(v^2)_1\right)\Big] + &\frac{1}{4v_\infty^4}\frac{\beta}{(1+\beta)^2}\left(\nabla^2\phi_2(v^2)_0(v^2)_0 + 2\nabla^2\phi_1(v^2)_1(v^2)_0\right),\end{aligned} \tag{B.26}$$

with $(v^2)_3 = 2\left(\nabla\phi_0\nabla\phi_3 + \nabla\phi_1\nabla\phi_2\right)$. We again use our Ansatz for $\phi_4(\boldsymbol{r})$, leading to

$$\begin{aligned}
\phi_4(\boldsymbol{r}) = v_\infty r\Bigg[\Bigg(&\frac{\left(9371\beta^3+52409\beta^2+90673\beta+49315\right)\sigma^{18}}{483840(\beta+1)^3r^{18}} - \frac{\left(11883\beta^3+64225\beta^2+107081\beta+55939\right)\sigma^{16}}{53760(\beta+1)^3r^{16}}\\
&+\frac{\left(269581\beta^3+1388775\beta^2+2214255\beta+1112341\right)\sigma^{14}}{241920(\beta+1)^3r^{14}} - \frac{\left(494669\beta^3+2397657\beta^2+3637251\beta+1756943\right)\sigma^{12}}{151200(\beta+1)^3r^{12}}\\
&+\frac{\left(1068991\beta^3+4846749\beta^2+6981669\beta+3223351\right)\sigma^{10}}{172800(\beta+1)^3r^{10}} - \frac{\left(9522233\beta^3+40391583\beta^2+55375827\beta+24582077\right)\sigma^{8}}{1209600(\beta+1)^3r^{8}}\\
&+\frac{\left(25125097\beta^3+99840747\beta^2+128365923\beta+53650273\right)\sigma^{6}}{3628800(\beta+1)^3r^{6}} - \frac{\left(23105\beta^3+92820\beta^2+119877\beta+50162\right)\sigma^{4}}{5040(\beta+1)^3r^{4}}\\
&+\frac{E\sigma^2}{r^2}\Bigg)\cos\theta + \Bigg(\frac{\left(1696\beta^3+8757\beta^2+13830\beta+6769\right)\sigma^{18}}{201600(\beta+1)^3r^{18}} - \frac{\left(29279\beta^3+157107\beta^2+263241\beta+140453\right)\sigma^{16}}{362880(\beta+1)^3r^{16}}\\
&+\frac{\left(80045\beta^3+467211\beta^2+838287\beta+466241\right)\sigma^{14}}{241920(\beta+1)^3r^{14}} - \frac{\left(309119\beta^3+2095329\beta^2+3949461\beta+2195651\right)\sigma^{12}}{403200(\beta+1)^3r^{12}}\\
&+\frac{\left(348227\beta^3+2837637\beta^2+5402823\beta+2963813\right)\sigma^{10}}{302400(\beta+1)^3r^{10}} - \frac{\left(1983748\beta^3+18876573\beta^2+34649142\beta+17794117\right)\sigma^{8}}{1512000(\beta+1)^3r^{8}}\\
&+\frac{\left(28448\beta^3+305953\beta^2+585702\beta+308197\right)\sigma^{6}}{22400(\beta+1)^3r^{6}} - \frac{\left(22185\beta^3+82523\beta^2+101323\beta+40985\right)\sigma^{2}}{26880(\beta+1)^3r^{2}} + \frac{D\sigma^4}{r^4}\Bigg)\cos 3\theta\\
&+\Bigg(-\frac{\left(2072\beta^3+13011\beta^2+24018\beta+13079\right)\sigma^{16}}{302400(\beta+1)^3r^{16}} + \frac{\left(598\beta^3+46065\beta^2+130512\beta+92605\right)\sigma^{14}}{362880(\beta+1)^3r^{14}}\\
&+\frac{\left(25399\beta^3-54331\beta^2-392219\beta-354489\right)\sigma^{12}}{403200(\beta+1)^3r^{12}} - \frac{\left(471173\beta^3+176928\beta^2-4565073\beta-4346428\right)\sigma^{10}}{2116800(\beta+1)^3r^{10}}\\
&+\frac{\left(30697\beta^3+63744\beta^2-185247\beta-225854\right)\sigma^{8}}{60480(\beta+1)^3r^{8}} + \frac{\left(73108\beta^3+514733\beta^2+855742\beta+414117\right)\sigma^{4}}{100800(\beta+1)^3r^{4}}\\
&+\frac{(7\beta+16)\sigma^{18}}{5184(\beta+1)r^{18}} + \frac{(813\beta+949)\sigma^2}{3840(\beta+1)r^2} + \frac{\sigma^6 C}{r^6}\Bigg)\cos 5\theta + \Bigg(-\frac{\left(394\beta^2+1127\beta-671\right)\sigma^{14}}{201600(\beta+1)^2r^{14}}\\
&+\frac{\left(207\beta^3+2335\beta^2+3593\beta+905\right)\sigma^{12}}{40320(\beta+1)^3r^{12}} - \frac{\left(29\beta^3+759\beta^2+1831\beta+701\right)\sigma^{10}}{2560(\beta+1)^3r^{10}} + \frac{\sigma^{18}}{20736r^{18}} - \frac{31\sigma^2}{768r^2}\\
&+\frac{\left(41129\beta^2+45556\beta-263485\right)\sigma^{6}}{241920(\beta+1)^2r^{6}} + \frac{(2\beta-7)\sigma^{16}}{8640(\beta+1)r^{16}} - \frac{(211\beta+864)\sigma^4}{960(\beta+1)r^4} + \frac{B\sigma^8}{r^8}\Bigg)\cos 7\theta\\
&+\Bigg(\frac{A\sigma^{10}}{r^{10}} - \frac{\left(3\beta^3+57\beta^2+161\beta+91\right)\sigma^{8}}{512(\beta+1)^3r^{8}} - \frac{\left(3\beta^2-8\beta-51\right)\sigma^{6}}{256(\beta+1)^2r^{6}} + \frac{5(\beta+4)\sigma^4}{192(\beta+1)r^4} + \frac{\sigma^2}{256r^2}\Bigg)\cos 9\theta\Bigg], \qquad \text{(B.27)}
\end{aligned}$$

with

$$A = \frac{1}{9}\left(\frac{5\left(3\beta^2-8\beta-51\right)}{256(\beta+1)^2} + \frac{7\left(3\beta^3+57\beta^2+161\beta+91\right)}{512(\beta+1)^3} - \frac{5(\beta+4)}{64(\beta+1)} - \frac{1}{256}\right), \qquad \text{(B.28a)}$$

$$B = \frac{-607603\beta^3+32516943\beta^2+117495303\beta+75273557}{50803200(\beta+1)^3}, \qquad \text{(B.28b)}$$

$$C = -\frac{6451567\beta^3+31380212\beta^2+24067783\beta-2876862}{7056000(\beta+1)^3}, \qquad \text{(B.28c)}$$

$$D = -\frac{9104291\beta^3+148003101\beta^2+332257449\beta+199680239}{18144000(\beta+1)^3}, \qquad \text{(B.28d)}$$

$$E = \frac{2213993\beta^3+10798227\beta^2+17154975\beta+8877173}{725760(\beta+1)^3}. \qquad \text{(B.28e)}$$

The maximum velocity is given by $v_{\max} = v_{\max,0} + \chi v_{\max,1} + \chi^2 v_{\max,2} + \chi^3 v_{\max,3} + \chi^4 v_{\max,4}$, with

$$v_{\max,4} = \frac{v_\infty^8}{127008000}\frac{794391527\beta^3+4765768797\beta^2+8804616453\beta+5084105183}{(\beta+1)^3}. \qquad \text{(B.29)}$$

The superfluid condition is now a $20^{\text{th}}-$order polynomial in v_∞, which is also solved numerically. In a similar fashion to what we did for the powerlaw nonlinearity, we have thus derived exact analytical expressions for $\phi_k(\boldsymbol{r})$ up to order 4, and used them to numerically solve the condition for superfluidity, which is now a $4(k+1)-$order polynomial in v_∞.

Appendix C

Exact resolution of $v_{c,k}$ for a penetrable obstacle for $k = 1$

In this section, we provide the exact results for $v_{c,k}$ for penetrable obstacles. Although our analysis extends up to $k = 2$, the complete results would require several pages to display. Therefore, we have limited the presentation here to $k = 1$ here.

Building upon the results obtained in the incompressible approximation (provided in Sec. 3.4.3), one can derive the results for $k \geqslant 1$. One has to solve the problem twice: Inside and outside the obstacle, and then treat the boundary accordingly to match perfectly the two solutions and find the relevant ϕ_k, which is the one inside the obstacle.

The Poisson equation to solve to obtain $\phi_1^{\text{int}}(\boldsymbol{r})$ and $\phi_1^{\text{ext}}(\boldsymbol{r})$ is provided by Eq. (3.39) and reads

$$(1 - \nu U_0)\nabla^2\phi_1(\boldsymbol{r}) = \frac{1}{2v_\infty^2}\nabla\phi_0\nabla(v^2)_0. \tag{C.1}$$

C.1 Results for a powerlaw nonlinearity: $\varepsilon(n) = n^\nu/\nu$

Inside the obstacle ($r < \sigma$)

Equation (C.1) actually reduces to the Laplace equation since $(v^{2,\text{int}})_0$ is a constant. Using our Ansatz to solve this equation, as well as the fact that the velocity potential must be finite at $r = 0$, one obtains

$$\phi_1^{\text{int}}(\boldsymbol{r}) = v_\infty r\left[a\cos\theta + \frac{br^2}{\sigma^2}\cos 3\theta\right]. \tag{C.2}$$

Outside the obstacle ($r > \sigma$)

The Poisson equation does not reduce to the Laplace equation this time, complexifying the expression of the velocity potential outside the obstacle

$$\begin{aligned}\phi_1^{\text{ext}}(\boldsymbol{r}) = v_\infty r\Bigg[&\left(\frac{A\sigma^2}{r^2} + \frac{\sigma^6\left(\left(\frac{1}{1-\nu U_0}\right)^{1/\nu} - 1\right)^3}{12r^6\left(\left(\frac{1}{1-\nu U_0}\right)^{1/\nu} + 1\right)^3} - \frac{\sigma^4\left(\left(\frac{1}{1-\nu U_0}\right)^{1/\nu} - 1\right)^2}{2r^4\left(\left(\frac{1}{1-\nu U_0}\right)^{1/\nu} + 1\right)^2}\right)\cos\theta \\ &+ \left(\frac{B\sigma^4}{r^4} - \frac{\sigma^2\left(\left(\frac{1}{1-\nu U_0}\right)^{1/\nu} - 1\right)}{4r^2\left(\left(\frac{1}{1-\nu U_0}\right)^{1/\nu} + 1\right)}\right)\Bigg]\cos 3\theta.\end{aligned} \tag{C.3}$$

After using the proper boundary condition at the interface

$$\phi_1^{\text{int}}(\sigma) = \phi_1^{\text{ext}}(\sigma) \tag{C.4a}$$

$$(1-\nu U_0)^{\frac{1}{\nu}}\partial_r\phi_1^{\text{int}}(\sigma) - \frac{1}{2}(1-\nu U_0)^{\frac{1}{\nu}-1}[(v^{2,\text{int}}(\sigma))_0 - 1]\partial_r\phi_0^{\text{int}}(\sigma) = \partial_r\phi_1^{\text{ext}} - \frac{1}{2}[(v^{2,\text{ext}}(\sigma))_0 - 1]\partial_r\phi_0^{\text{ext}}(\sigma), \tag{C.4b}$$

one obtains

$$\begin{aligned} a = &\frac{\left(\frac{1}{1-\nu U_0}\right)^{1/\nu}(1-\nu U_0)^{1/\nu}}{(\nu U_0-1)\left(\left(\frac{1}{1-\nu U_0}\right)^{1/\nu}+1\right)^3((1-\nu U_0)^{1/\nu}+1)} + \frac{2\left(\frac{1}{1-\nu U_0}\right)^{2/\nu}(1-\nu U_0)^{1/\nu}}{(\nu U_0-1)\left(\left(\frac{1}{1-\nu U_0}\right)^{1/\nu}+1\right)^3((1-\nu U_0)^{1/\nu}+1)} \\ &- \frac{3\left(\frac{1}{1-\nu U_0}\right)^{3/\nu}(1-\nu U_0)^{1/\nu}}{(\nu U_0-1)\left(\left(\frac{1}{1-\nu U_0}\right)^{1/\nu}+1\right)^3((1-\nu U_0)^{1/\nu}+1)} + \frac{2\nu U_0\left(\frac{1}{1-\nu U_0}\right)^{3/\nu}}{3(\nu U_0-1)\left(\left(\frac{1}{1-\nu U_0}\right)^{1/\nu}+1\right)^3((1-\nu U_0)^{1/\nu}+1)} \\ &- \frac{2\left(\frac{1}{1-\nu U_0}\right)^{3/\nu}}{3(\nu U_0-1)\left(\left(\frac{1}{1-\nu U_0}\right)^{1/\nu}+1\right)^3((1-\nu U_0)^{1/\nu}+1)} - \frac{2\nu U_0}{3(\nu U_0-1)\left(\left(\frac{1}{1-\nu U_0}\right)^{1/\nu}+1\right)^3((1-\nu U_0)^{1/\nu}+1)} \\ &+ \frac{2}{3(\nu U_0-1)\left(\left(\frac{1}{1-\nu U_0}\right)^{1/\nu}+1\right)^3((1-\nu U_0)^{1/\nu}+1)}, \end{aligned} \tag{C.5a}$$

$$b = -\frac{\left(\left(\frac{1}{1-\nu U_0}\right)^{1/\nu}-1\right)^2}{6\left(\left(\frac{1}{1-\nu U_0}\right)^{1/\nu}+1\right)^2((1-\nu U_0)^{1/\nu}+1)}, \tag{C.5b}$$

$$A = a + \frac{\left(5\left(\frac{1}{1-\nu U_0}\right)^{1/\nu}+7\right)\left(\left(\frac{1}{1-\nu U_0}\right)^{1/\nu}-1\right)^2}{12\left(\left(\frac{1}{1-\nu U_0}\right)^{1/\nu}+1\right)^3}, \tag{C.5c}$$

$$B = \frac{4b\left(\left(\frac{1}{1-\nu U_0}\right)^{1/\nu}+1\right)+\left(\frac{1}{1-\nu U_0}\right)^{1/\nu}-1}{4\left(\left(\frac{1}{1-\nu U_0}\right)^{1/\nu}+1\right)}. \tag{C.5d}$$

From there, one can deduce the expression of the maximum velocity using the expression of ϕ_1^{int}

$$\begin{aligned} v_{\max} &= v_{\max,0} + \chi v_{\max,1} \\ &= v_\infty\Bigg(\frac{2}{1+(1-\nu U_0)^{1/\nu}} + \frac{v_\infty^2}{6(\nu U_0-1)\left(\left(\frac{1}{1-\nu U_0}\right)^{1/\nu}+1\right)^3\left((1-\nu U_0)^{1/\nu}+1\right)}\times \\ &\Bigg[\left(6(1-\nu U_0)^{1/\nu}+4\right)\left(\frac{1}{1-\nu U_0}\right)^{1/\nu} + \left(18(1-\nu U_0)^{1/\nu}+7\right)\left(\frac{1}{1-\nu U_0}\right)^{2/\nu} \\ &- \nu U_0\left(4\left(\frac{1}{1-\nu U_0}\right)^{1/\nu} + 7\left(\frac{1}{1-\nu U_0}\right)^{2/\nu}+1\right)+1\Bigg]\times\left[\left(\frac{1}{1-\nu U_0}\right)^{1/\nu}-1\right]\Bigg). \end{aligned} \tag{C.6}$$

The last step is to solve the condition for superfluid motion given by Eq. (3.25)

$$1 - \nu U_0 + v_\infty^2\left[\frac{\nu}{2} - \frac{v_{\max}^2}{v_\infty^2}\left(1+\frac{\nu}{2}\right)\right] > 0. \tag{C.7}$$

with the previously defined $v_{\max}$, leading to a fourth-order polynomial in v_∞. This step is performed numerically given the complexity of the maximum velocity.

C.2 Results for a saturable nonlinearity: $\varepsilon(n) = (1+\beta)^2 \frac{n}{1+\beta n}$ with $\beta = 1/n_{\text{sat}}$

Inside the obstacle ($r < \sigma$)

Interestingly, Eq. (C.1) also simplifies into the Laplace equation since $(v^{2,\text{ext}})_0$ is a constant. Using our Ansatz to solve this equation, as well as the fact that the velocity potential must be finite at $r = 0$, one obtains the exact same solution as for the powerlaw nonlinearity (except for the value of the constants a and b)

$$\phi_1^{\text{int}}(\boldsymbol{r}) = v_\infty r \left[a\cos\theta + \frac{br^2}{\sigma^2}\cos 3\theta \right]. \tag{C.8}$$

Outside the obstacle ($r > \sigma$)

Similarly to the previous section, the Poisson equation does not reduce to the Laplace equation outside the obstacle. The velocity potential outside the obstacle is given by

$$\phi_1^{\text{ext}}(\boldsymbol{r}) = v_\infty r \Bigg[\left(\frac{A\sigma^2}{r^2} + \frac{(\beta+1)^3\sigma^6 U_0^3}{12r^6(2(\beta+1)+(\beta-1)U_0)^3} - \frac{(\beta+1)^2\sigma^4 U_0^2}{2r^4(2(\beta+1)+(\beta-1)U_0)^2} \right)\cos\theta + \left(\frac{B\sigma^4}{r^4} - \frac{(\beta+1)\sigma^2 U_0}{4r^2(2(\beta+1)+(\beta-1)U_0)} \right)\cos 3\theta \Bigg]. \tag{C.9}$$

The boundary conditions at the interface now read

$$\phi_1^{\text{int}}(\sigma) = \phi_1^{\text{ext}}(\sigma) \tag{C.10a}$$

$$\frac{1+\beta-U_0}{1+\beta+\beta U_0}\partial_r\phi_1^{\text{int}}(\sigma) - \frac{1}{2}\left(\frac{1+\beta}{1+\beta+\beta U_0}\right)^2 [(v^{2,\text{int}}(\sigma))_0 - 1]\partial_r\phi_0^{\text{int}}(\sigma) = \partial_r\phi_1^{\text{ext}} - \frac{1}{2}[(v^{2,\text{ext}}(\sigma))_0 - 1]\partial_r\phi_0^{\text{ext}}(\sigma). \tag{C.10b}$$

Using these matching condition, one can derive the expression of the various constant in the velocity potentials

$$a = \frac{-6(\beta+1)^3 + 2\beta^2 U_0^3 + 2\beta\left(-\beta^2+\beta+2\right)U_0^2 - (\beta+1)^2(7\beta-3)U_0}{(2(\beta+1)+(\beta-1)U_0)^3}, \tag{C.11a}$$

$$b = -\frac{(\beta+\beta U_0+1)^2}{(2(\beta+1)+(\beta-1)U_0)^2}, \tag{C.11b}$$

$$A = \frac{1}{12}\left(12a - \frac{(\beta+1)^3 U_0^3}{(2(\beta+1)+(\beta-1)U_0)^3} + \frac{6(\beta+1)^2 U_0^2}{(2(\beta+1)+(\beta-1)U_0)^2}\right), \tag{C.11c}$$

$$B = \frac{8b(\beta+1)+4b(\beta-1)U_0+(\beta+1)U_0}{8(\beta+1)+4(\beta-1)U_0}. \tag{C.11d}$$

Again, the expression of the maximum velocity using the expression is deduced from the velocity potential ϕ_1^{int} inside the obstacle, leading to

$$v_{\max} = v_{\max,0} + \chi v_{\max,1} = v_\infty\left(\frac{2(\beta+\beta U_0+1)}{2\beta+\beta U_0-U_0+2} + v_\infty^2\frac{\beta U_0\left(8(\beta+1)^2+\beta(3\beta-1)U_0^2+2\left(5\beta^2+4\beta-1\right)U_0\right)}{(2(\beta+1)+(\beta-1)U_0)^3}\right). \tag{C.12}$$

Finally, we must solve the condition for superfluid motion given by Eq. (3.26) with this expression for the maximum velocity, i.e.

$$4\Big[(1+\beta)^2 - \left(1-\beta^2\right)U_0 - \beta U_0^2\Big] - 2v_\infty^2\left[\frac{v_{\max}^2}{v_\infty^2}\left(3+2\beta(U_0+2)+\beta^2\right) - 1 - 2\beta U_0 + \beta^2\right] - \beta v_\infty^4\left(\frac{v_{\max}^2}{v_\infty^2} - 1\right)^2 > 0. \quad \text{(C.13)}$$

The numerical resolution of this polynomial leads to the expression of $v_{c,1}$ for a penetrable obstacle.

Bibliography

Bibliography

[1] R. J. Donnelly, "The Discovery of Superfluidity," *Physics Today*, vol. **48**, pp. 30–36, 07 1995. 1

[2] L. P. Pitaevskii, "50 years of Landau's theory on superfluidity," *Journal of Low Temperature Physics*, vol. **87**, no. 3, pp. 127–135, 1992.

[3] S. Balibar, "The Discovery of Superfluidity," *Journal of Low Temperature Physics*, vol. **146**, pp. 441–470, 01 2007. 2

[4] A. J. Leggett, "Superfluidity," *Rev. Mod. Phys.*, vol. **71**, pp. S318–S323, 03 1999.

[5] S. Balibar, "Laszlo Tisza and the two-fluid model of superfluidity," *Comptes Rendus Physique*, vol. **18**, pp. 586–591, 11 2017. 1, 5

[6] D. Van Delft and P. Kes, "The discovery of superconductivity," *Physics Today*, vol. **63**, pp. 38–43, 09 2010. 1

[7] D. Van Delft, "Little cup of helium, big science," *Physics Today*, vol. **61**, pp. 36–42, 03 2008. 1

[8] M. H. Anderson, J. R. Ensher, M. R. Matthews, C. E. Wieman, and E. A. Cornell, "Observation of Bose-Einstein Condensation in a Dilute Atomic Vapor," *Science*, vol. **269**, pp. 198–201, 07 1995. 1, 8, 12, 19, 91

[9] K. B. Davis, M.-O. Mewes, M. R. Andrews, N. J. van Druten, D. S. Durfee, D. M. Kurn, and W. Ketterle, "Bose-Einstein Condensation in a Gas of Sodium Atoms," *Phys. Rev. Lett.*, vol. **75**, pp. 3969–3973, 11 1995. 1, 8, 11, 12, 19, 91

[10] W. S. Book, *Nobel Lectures, Physics 1901-1921.* Elsevier Publishing Company, Amsterdam, 01 1967. 1

[11] W. H. Keesom and A. P. Keesom, "New measurements on the specific heat of liquid helium," *Physica*, vol. **2**, pp. 557–572, 03 1935. 2

[12] M. J. Buckingham and W. M. Fairbank, "The Nature of the Lambda Transition," *Progress in Low Temperature Physics III*, 1961. 2

[13] P. Kapitza, "Viscosity of Liquid Helium below the λ-Point," *Nature*, vol. **141**, p. 74, 01 1938. 2, 10

[14] J. F. Allen and A. D. Misener, "Flow of Liquid Helium II," *Nature*, vol. **141**, p. 75, 01 1938. 2, 10

[15] O. Penrose and L. Onsager, "Bose-Einstein Condensation and Liquid Helium," *Phys. Rev.*, vol. **104**, pp. 576–584, 11 1956. 3, 12, 25

[16] O. Penrose, "CXXXVI. On the quantum mechanics of helium II," *The London, Edinburgh, and Dublin Philosophical Magazine and Journal of Science*, vol. **42**, pp. 1373–1377, 06 1951. 12

[17] C. N. Yang, "Concept of Off-Diagonal Long-Range Order and the Quantum Phases of Liquid He and of Superconductors," *Rev. Mod. Phys.*, vol. **34**, pp. 694–704, 10 1962. 3

[18] D. S. Petrov, *Bose-Einstein Condensation in Low-Dimensional Trapped Gases*. PhD thesis, Universiteit van Amsterdam, 2003. 3, 25, 26

[19] L. P. Pitaevskii and S. Stringari, *Bose-Einstein Condensation and Superfluidity*. Oxford University Press, Oxford, 01 2016. 4, 6, 7, 11, 26, 29, 38, 100

[20] N. D. Mermin and H. Wagner, "Absence of Ferromagnetism or Antiferromagnetism in One- or Two-Dimensional Isotropic Heisenberg Models," *Phys. Rev. Lett.*, vol. **17**, pp. 1133–1136, 11 1966. 4

[21] P. C. Hohenberg, "Existence of Long-Range Order in One and Two Dimensions," *Phys. Rev.*, vol. **158**, pp. 383–386, 06 1967. 4

[22] Y. Kagan, B. V. Svistunov, and G. V. Shlyapnikov, "Influence on inelastic processes of the phase transition in a weakly collisional two-dimensional Bose gas," *Soviet Journal of Experimental and Theoretical Physics*, vol. **66**, pp. 314, 08 1987. 4

[23] M. Schwartz, "Off-diagonal long-range behavior of interacting Bose systems," *Phys. Rev. B*, vol. **15**, pp. 1399–1403, 02 1977. 4

[24] J. Bardeen, L. N. Cooper, and J. R. Schrieffer, "Microscopic Theory of Superconductivity," *Phys. Rev.*, vol. **106**, pp. 162–164, 04 1957. 5

[25] L. Tisza, "Transport Phenomena in Helium II," *Nature*, vol. **141**, p. 913, 05 1938. 5

[26] L. Tisza, "Sur la supraconductibilité thermique de l'hélium II liquide et la statistique de Bose-Einstein," *C. r. hebd. séances Acad. sci. Paris*, vol. **207**, p. 1035, 06 1938.

[27] L. Tisza, "La viscosité de l'hélium liquide et la statistique de Bose-Einstein," *C. r. hebd. séances Acad. sci. Paris*, vol. **207**, p. 1186, 06 1938. 5

[28] L. D. Landau, "Theory of the Superfluidity of Helium II," *Phys. Rev.*, vol. **60**, pp. 356–358, 08 1941. 5

[29] R. Donnelly, "The two-fluid theory and second sound in liquid helium," *Physics Today*, vol. **62**, pp. 34–39, 10 2009. 5

[30] L. D. Landau, "The theory of superfluidity of Helium II," *J. Phys. USSR*, vol. **5**, p. 71, 08 1941. 5, 10

[31] C. Cohen-Tannoudji, *Leçons du Collège de France*. 1996-2000. 6, 7

[32] C. Chin, R. Grimm, P. Julienne, and E. Tiesinga, "Feshbach resonances in ultracold gases," *Rev. Mod. Phys.*, vol. **82**, pp. 1225–1286, 04 2010. 6

[33] L. P. Pitaevskii, "Vortex Lines in an Imperfect Bose Gas," *Soviet Physics JETP-USSR*, vol. **13**, pp. 451, 08 1961. 7

[34] E. P. Gross, "Structure of a Quantised Vortex in Boson Systems," *Il Nuovo Cimento*, vol. **20**, pp. 454–477, 03 1961. 7

[35] N. N. Bogoliubov, "On the theory of superfluidity," *J. Phys. (USSR)*, vol. **11**, pp. 23–32, 1947. 8

[36] R. Lopes, C. Eigen, N. Navon, D. Clément, R. P. Smith, and Z. Hadzibabic, "Quantum Depletion of a Homogeneous Bose-Einstein Condensate," *Phys. Rev. Lett.*, vol. **119**, p. 190404, 11 2017. 8

[37] D. S. Jin, J. R. Ensher, M. R. Matthews, C. E. Wieman, and E. A. Cornell, "Collective Excitations of a Bose-Einstein Condensate in a Dilute Gas," *Phys. Rev. Lett.*, vol. **77**, pp. 420–423, 07 1996. 9

[38] M.-O. Mewes, M. R. Andrews, N. J. van Druten, D. M. Kurn, D. S. Durfee, C. G. Townsend, and W. Ketterle, "Collective Excitations of a Bose-Einstein Condensate in a Magnetic Trap," *Phys. Rev. Lett.*, vol. **77**, pp. 988–991, 08 1996.

[39] R. Onofrio, C. Raman, J. M. Vogels, J. R. Abo-Shaeer, A. P. Chikkatur, and W. Ketterle, "Observation of Superfluid Flow in a Bose-Einstein Condensed Gas," *Phys. Rev. Lett.*, vol. **85**, pp. 2228–2231, 09 2000. 91

[40] J. Steinhauer, R. Ozeri, N. Katz, and N. Davidson, "Excitation Spectrum of a Bose-Einstein Condensate," *Phys. Rev. Lett.*, vol. **88**, p. 120407, 03 2002. 9

[41] S. Utsunomiya, L. Tian, G. Roumpos, C. W. Lai, N. Kumada, T. Fujisawa, M. Kuwata-Gonokami, A. Löffler, S. Höfling, A. Forchel, and Y. Yamamoto, "Observation of Bogoliubov excitations in exciton-polariton condensates," *Nature Physics*, vol. **4**, pp. 700–705, 08 2008. 9, 92

[42] Q. Fontaine, T. Bienaimé, S. Pigeon, E. Giacobino, A. Bramati, and Q. Glorieux, "Observation of the Bogoliubov Dispersion in a Fluid of Light," *Phys. Rev. Lett.*, vol. **121**, p. 183604, 10 2018. 9, 15, 17, 20

[43] Q. Fontaine, P.-E. Larré, G. Lerario, T. Bienaimé, S. Pigeon, D. Faccio, I. Carusotto, E. Giacobino, A. Bramati, and Q. Glorieux, "Interferences between Bogoliubov excitations in superfluids of light," *Phys. Rev. Research*, vol. **2**, p. 043297, 12 2020. 9, 15, 17, 52

[44] D. Vocke, T. Roger, F. Marino, E. M. Wright, I. Carusotto, M. Clerici, and D. Faccio, "Experimental characterization of nonlocal photon fluids," *Optica*, vol. **2**, pp. 484–490, 05 2015. 9, 15

[45] V. Hakim, "Nonlinear Schrödinger flow past an obstacle in one dimension," *Phys. Rev. E*, vol. **55**, pp. 2835–2845, 03 1997. 11, 12, 35, 37, 39, 41, 43, 44, 45, 62, 74

[46] I. Danshita and S. Tsuchiya, "Stability of Bose-Einstein condensates in a Kronig-Penney potential," *Phys. Rev. A*, vol. **75**, p. 033612, 03 2007.

[47] N. Pavloff, "Breakdown of superfluidity of an atom laser past an obstacle," *Phys. Rev. A*, vol. **66**, p. 013610, 07 2002. 11, 13, 14, 33, 35, 62, 67, 71

[48] M. Albert, T. Paul, N. Pavloff, and P. Leboeuf, "Breakdown of the superfluidity of a matter wave in a random environment," *Phys. Rev. A*, vol. **82**, p. 011602, 07 2010. 11, 43, 133

[49] J. S. Stießberger and W. Zwerger, "Critcal velocity of superfluid flow past large obstacles in Bose-Einstein condensates," *Phys. Rev. A*, vol. **62**, p. 061601, 11 2000. 11, 92, 111, 124

[50] M. Albert, T. Paul, N. Pavloff, and P. Leboeuf, "Dipole Oscillations of a Bose-Einstein Condensate in the Presence of Defects and Disorder," *Phys. Rev. Lett.*, vol. **100**, p. 250405, 06 2008. 11, 133

[51] T. Paul, P. Leboeuf, N. Pavloff, K. Richter, and P. Schlagheck, "Nonlinear transport of Bose-Einstein condensates through waveguides with disorder," *Phys. Rev. A*, vol. **72**, p. 063621, 12 2005. 11, 12

[52] P. Leboeuf and N. Pavloff, "Bose-Einstein beams: Coherent propagation through a guide," *Phys. Rev. A*, vol. **64**, p. 033602, 08 2001. 11, 13, 31, 34, 36, 37, 58, 59, 60, 62, 63, 78, 80, 81

[53] R. Feynman, *Chapter II Application of Quantum Mechanics to Liquid Helium*, vol. **1** of *Progress in Low Temperature Physics*. Elsevier, 1955. 11, 12

[54] C. Michel, O. Boughdad, M. Albert, P.-E. Larré, and M. Bellec, "Superfluid motion and drag-force cancellation in a fluid of light," *Nature Communications*, vol. **9**, pp. 2108, 05 2018. 11, 15, 16, 17, 19, 20, 32, 52, 92

[55] A. Eloy, O. Boughdad, M. Albert, P.-E. Larré, F. Mortessagne, M. Bellec, and C. Michel, "Experimental observation of turbulent coherent structures in a superfluid of light," *EPL*, vol. **134**, pp. 26001, 07 2021. 13, 15, 16, 17, 19, 20, 38, 52, 58, 92, 93, 111, 132

[56] A. C. Berceanu, E. Cancellieri, and F. M. Marchetti, "Drag in a resonantly driven polariton fluid," *Journal of Physics: Condensed Matter*, vol. **24**, pp. 235802, 05 2012. 32, 52, 53

[57] A. Y. Cherny, J.-S. Caux, and J. Brand, "Theory of superfluidity and drag force in the one-dimensional Bose gas," *Frontiers of Physics*, vol. **7**, pp. 54–71, 10 2012. 11, 67, 132

[58] T. Frisch, Y. Pomeau, and S. Rica, "Transition to dissipation in a model of superflow," *Phys. Rev. Lett.*, vol. **69**, pp. 1644–1647, 09 1992. 11, 91, 92, 94, 99, 103, 106, 107, 108, 111, 113, 123, 124, V, IX

[59] S. Rica, "A remark on the critical speed for vortex nucleation in the nonlinear Schrödinger equation," *Physica D: Nonlinear Phenomena*, vol. **148**, pp. 221–226, 01 2001. 91, 92, 94, 101, 103, 104, 107, 108, 111, 113, 123, 124

[60] F. Pinsker and N. G. Berloff, "Transitions and excitations in a superfluid stream passing small impurities," *Phys. Rev. A*, vol. **89**, p. 053605, 05 2014. 92, 111, 119, 124

[61] H. Kwak, J. H. Jung, and Y. Shin, "Minimum critical velocity of a Gaussian obstacle in a Bose-Einstein condensate," *Phys. Rev. A*, vol. **107**, p. 023310, 02 2023. 11, 13, 92, 111, 115, 116, 117, 124, 125

[62] W. J. Kwon, S. W. Seo, and Y.-i. Shin, "Periodic shedding of vortex dipoles from a moving penetrable obstacle in a Bose-Einstein condensate," *Physical Review A*, vol. **92**, p. 033613, 09 2015. 11, 13, 108

[63] C. Josserand, Y. Pomeau, and S. Rica, "Vortex shedding in a model of superflow," *Physica D: Nonlinear Phenomena*, vol. **134**, pp. 111–125, 10 1999. 92

[64] T. W. Neely, E. C. Samson, A. S. Bradley, M. J. Davis, and B. P. Anderson, "Observation of Vortex Dipoles in an Oblate Bose-Einstein Condensate," *Phys. Rev. Lett.*, vol. **104**, p. 160401, 04 2010. 11

[65] A. Einstein, "Quantentheorie des einatomigen idealen Gases," *Sitzungsberichte der Preussischen Akademie der Wissenschaften*, pp. 261–267, 1924. 11

[66] E. L. Raab, M. Prentiss, A. Cable, S. Chu, and D. E. Pritchard, "Trapping of Neutral Sodium Atoms with Radiation Pressure," *Phys. Rev. Lett.*, vol. **59**, pp. 2631–2634, 12 1987. 11

[67] W. Ketterle and N. J. Van Druten, "Evaporative Cooling of Trapped Atoms," *Advances in Atomic, Molecular, and Optical Physics*, vol. **37**, pp. 181–236, 01 1996. 11

[68] C. Raman, M. Köhl, R. Onofrio, D. S. Durfee, C. E. Kuklewicz, Z. Hadzibabic, and W. Ketterle, "Evidence for a Critical Velocity in a Bose-Einstein Condensed Gas," *Phys. Rev. Lett.*, vol. **83**, pp. 2502–2505, 09 1999. 12, 35, 91

[69] P. Engels and C. Atherton, "Stationary and Nonstationary Fluid Flow of a Bose-Einstein Condensate Through a Penetrable Barrier," *Phys. Rev. Lett.*, vol. **99**, p. 160405, 10 2007. 19, 58, 91

[70] K. W. Madison, F. Chevy, W. Wohlleben, and J. Dalibard, "Vortex Formation in a Stirred Bose-Einstein Condensate," *Phys. Rev. Lett.*, vol. **84**, pp. 806–809, 01 2000. 12, 13

[71] A. P. Chikkatur, A. Görlitz, D. M. Stamper-Kurn, S. Inouye, S. Gupta, and W. Ketterle, "Suppression and Enhancement of Impurity Scattering in a Bose-Einstein Condensate," *Phys. Rev. Lett.*, vol. **85**, pp. 483–486, 07 2000. 12, 35

[72] J. R. Abo-Shaeer, C. Raman, J. M. Vogels, and W. Ketterle, "Observation of Vortex Lattices in Bose-Einstein Condensates," *Science*, vol. **292**, pp. 476–479, 03 2001. 12

[73] V. L. Ginzburg and L. P. Pitaevskii, "On the Theory of Superfluidity," *Soviet Physics JETP*, vol. **34**, pp. 858–861, 11 1958. 12

[74] W. F. Vinen, "The detection of single quanta of circulation in liquid helium II," *Proc. R. Soc. Lond. A*, vol. **260**, pp. 218–236, 02 1961. 12

[75] E. J. Yarmchuk, M. J. V. Gordon, and R. E. Packard, "Observation of Stationary Vortex Arrays in Rotating Superfluid Helium," *Phys. Rev. Lett.*, vol. **43**, pp. 214–217, 07 1979. 12

[76] P. Engels, I. Coddington, P. C. Haljan, V. Schweikhard, and E. A. Cornell, "Observation of Long-Lived Vortex Aggregates in Rapidly Rotating Bose-Einstein Condensates," *Phys. Rev. Lett.*, vol. **90**, p. 170405, 05 2003. 12

[77] R. J. Donnelly, "Quantized Vortices in Helium II," *Journal of Fluid Mechanics*, vol. **233**, p. 691–692, 1991. 12

[78] S. Stringari, "Phase Diagram of Quantized Vortices in a Trapped Bose-Einstein Condensed Gas," *Phys. Rev. Lett.*, vol. **82**, pp. 4371–4375, 05 1999. 12

[79] A. L. Fetter, "Rotating trapped Bose-Einstein condensates," *Rev. Mod. Phys.*, vol. **81**, pp. 647–691, 05 2009. 13

[80] A. A. Abrikosov, "On the Magnetic Properties of Superconductors of the Second Group," *Sov. Phys. JETP*, vol. **5**, pp. 1174–1182, 12 1957. 13

[81] U. Essmann and H. Träuble, "The direct observation of individual flux lines in type II superconductors," *Physics Letters A*, vol. **24**, pp. 526–527, 05 1967.

[82] H. F. Hess, R. B. Robinson, R. C. Dynes, J. M. Valles, and J. V. Waszczak, "Scanning-Tunneling-Microscope Observation of the Abrikosov Flux Lattice and the Density of States near and inside a Fluxoid," *Phys. Rev. Lett.*, vol. **62**, pp. 214–216, 01 1989. 13

[83] B. Jackson, J. F. McCann, and C. S. Adams, "Vortex Formation in Dilute Inhomogeneous Bose-Einstein Condensates," *Phys. Rev. Lett.*, vol. **80**, pp. 3903–3906, 05 1998. 13

[84] K. Staliunas, "Vortices and dark solitons in the two-dimensional nonlinear Schrödinger equation," *Chaos, Solitons & Fractals*, vol. **4**, no. 8, pp. 1783–1796, 1994. 13

[85] P. Nozières and D. Pines, *The Theory of Quantum Liquids, Vol. II.* Addison-Wesley, Redwood City, 1990. 13

[86] Y. Lim, Y. Lee, J. Goo, D. Bae, and Y. Shin, "Vortex shedding frequency of a moving obstacle in a Bose–Einstein condensate," *New Journal of Physics*, vol. **24**, pp. 083020, 08 2022. 13

[87] C. Becker, S. Stellmer, P. Soltan-Panahi, S. Dörscher, M. Baumert, E.-M. Richter, J. Kronjäger, K. Bongs, and K. Sengstock, "Oscillations and interactions of dark and dark–bright solitons in Bose–Einstein condensates," *Nature Physics*, vol. **4**, p. 496–501, 05 2008. 13

[88] T. Busch and J. R. Anglin, "Motion of Dark Solitons in Trapped Bose-Einstein Condensates," *Phys. Rev. Lett.*, vol. **84**, pp. 2298–2301, 03 2000. 13

[89] G. A. Swartzlander and C. T. Law, "Optical vortex solitons observed in Kerr nonlinear media," *Phys. Rev. Lett.*, vol. **69**, pp. 2503–2506, 10 1992. 13

[90] C. Lobo, A. Sinatra, and Y. Castin, "Vortex Lattice Formation in Bose-Einstein Condensates," *Phys. Rev. Lett.*, vol. **92**, p. 020403, 01 2004.

[91] G. Lerario, A. Maître, R. Boddeda, Q. Glorieux, E. Giacobino, S. Pigeon, and A. Bramati, "Vortex-stream generation and enhanced propagation in a polariton superfluid," *Phys. Rev. Research*, vol. **2**, p. 023049, 04 2020.

[92] P. Azam, A. Griffin, S. Nazarenko, and R. Kaiser, "Vortex creation, annihilation, and nonlinear dynamics in atomic vapors," *Phys. Rev. A*, vol. **105**, p. 043510, 04 2022. 13

[93] A. De Rossi, S. Trillo, A. V. Buryak, and Y. S. Kivshar, "Snake instability of one-dimensional parametric spatial solitons," *Opt. Letters*, vol. **22**, pp. 868–870, 01 1997.

[94] F. Claude, S. V. Koniakhin, A. Maître, S. Pigeon, G. Lerario, D. D. Stupin, Q. Glorieux, E. Giacobino, D. Solnyshkov, G. Malpuech, and A. Bramati, "Taming the snake instabilities in a polariton superfluid," *Optica*, vol. **7**, pp. 1660–1665, 12 2020. 13

[95] M. Kobayashi and M. Tsubota, "Quantum turbulence in a trapped Bose-Einstein condensate," *Phys. Rev. A*, vol. **76**, p. 045603, 10 2007. 13, 58

[96] E. A. L. Henn, J. A. Seman, G. Roati, K. M. F. Magalhães, and V. S. Bagnato, "Emergence of Turbulence in an Oscillating Bose-Einstein Condensate," *Phys. Rev. Lett.*, vol. **103**, p. 045301, 07 2009. 13

[97] A. Armaroli, S. Trillo, and A. Fratalocchi, "Suppression of transverse instabilities of dark solitons and their dispersive shock waves," *Phys. Rev. A*, vol. **80**, p. 053803, 11 2009. 13

[98] S. K. Ivanov, J.-E. Suchorski, A. M. Kamchatnov, M. Isoard, and N. Pavloff, "Formation of dispersive shock waves in a saturable nonlinear medium," *Phys. Rev. E*, vol. **102**, p. 032215, 09 2020. 16

[99] S. Jia, W. Wan, and J. W. Fleischer, "Dispersive Shock Waves in Nonlinear Arrays," *Phys. Rev. Lett.*, vol. **99**, p. 223901, 11 2007. 15, 16

[100] W. Wan, S. Jia, and J. W. Fleischer, "Dispersive superfluid-like shock waves in nonlinear optics," *Nature Physics*, vol. **3**, p. 46–51, 12 2006. 13, 15

[101] K. Sasaki, N. Suzuki, and H. Saito, "Bénard–von Kármán Vortex Street in a Bose-Einstein Condensate," *Phys. Rev. Lett.*, vol. **104**, p. 150404, 04 2010. 13, 92, 122, 124, 132

[102] M. T. Reeves, T. P. Billam, B. P. Anderson, and A. S. Bradley, "Identifying a Superfluid Reynolds Number via Dynamical Similarity," *Phys. Rev. Lett.*, vol. **114**, p. 155302, 04 2015.

[103] W. J. Kwon, J. H. Kim, S. W. Seo, and Y. Shin, "Observation of von Kármán Vortex Street in an Atomic Superfluid Gas," *Phys. Rev. Lett.*, vol. **117**, p. 245301, 12 2016. 13, 122

[104] C. F. Barenghi, L. Skrbek, and K. R. Sreenivasan, "Introduction to quantum turbulence," *Proceedings of the National Academy of Sciences*, vol. **111**, p. 4647–4652, 03 2014. 13, 58

[105] S. Nazarenko and M. Onorato, "Wave turbulence and vortices in Bose–Einstein condensation," *Physica D: Nonlinear Phenomena*, vol. **219**, pp. 1–12, 07 2006.

[106] M. Tsubota, "Quantum turbulence—from superfluid helium to atomic Bose–Einstein condensates," *Journal of Physics: Condensed Matter*, vol. **21**, pp. 164207, 03 2009.

[107] M. Baker-Rasooli, W. Liu, T. Aladjidi, A. Bramati, and Q. Glorieux, "Turbulent dynamics in a two-dimensional paraxial fluid of light," *Phys. Rev. A*, vol. **108**, p. 063512, 12 2023. 13, 58

[108] A. M. Leszczyszyn, G. A. El, Y. G. Gladush, and A. M. Kamchatnov, "Transcritical flow of a Bose-Einstein condensate through a penetrable barrier," *Phys. Rev. A*, vol. **79**, p. 063608, 06 2009. 13, 43, 58

[109] A. M. Kamchatnov and N. Pavloff, "Generation of dispersive shock waves by the flow of a Bose-Einstein condensate past a narrow obstacle," *Phys. Rev. A*, vol. **85**, p. 033603, 03 2012. 13, 58

[110] T. Paul, K. Richter, and P. Schlagheck, "Nonlinear Resonant Transport of Bose-Einstein Condensates," *Phys. Rev. Lett.*, vol. **94**, p. 020404, 01 2005. 13, 58, 82

[111] K. Rapedius, D. Witthaut, and H. J. Korsch, "Analytical study of resonant transport of Bose-Einstein condensates," *Phys. Rev. A*, vol. **73**, p. 033608, 03 2006. 82

[112] K. Rapedius and H. J. Korsch, "Barrier transmission for the one-dimensional nonlinear Schrödinger equation: Resonances and transmission profiles," *Phys. Rev. A*, vol. **77**, p. 063610, 06 2008. 58

[113] A. Paris-Mandoki, J. Shearring, F. Mancarella, T. M. Fromhold, A. Trombettoni, and P. Krüger, "Superfluid flow above the critical velocity," *Sci. Rep.*, vol. **7**, 08 2017. 13, 59, 86

[114] M. Vaupel, K. Staliunas, and C. O. Weiss, "Hydrodynamic phenomena in laser physics: Modes with flow and vortices behind an obstacle in an optical channel," *Phys. Rev. A*, vol. **54**, pp. 880–892, 07 1996. 14

[115] P. Coullet, L. Gil, and F. Rocca, "Optical vortices," *Optics Communications*, vol. **73**, pp. 403–408, 11 1989. 14, 16

[116] V. L. Ginzburg and D. A. Kirzhnits, "On the superfluidity of neutron stars," *Zh. Eksperim. i Teor. Fiz.*, vol. **47**, 11 1964. 14

[117] A. Sedrakian and J. W. Clark, "Superfluidity in nuclear systems and neutron stars," *The European Physical Journal A*, vol. **55**, 09 2019. 14

[118] A. Amo, J. Lefrere, S. Pigeon, C. Adrados, C. Ciuti, I. Carusotto, R. Houdré, E. Giacobino, and A. Bramati, "Superfluidity of polaritons in semiconductor microcavities," *Nature Physics*, vol. **5**, pp. 805–810, 09 2009. 14, 92

[119] A. Amo, S. Pigeon, D. Sanvitto, V. G. Sala, R. Hivet, I. Carusotto, F. Pisanello, G. Leménager, R. Houdré, E. Giacobino, C. Ciuti, and A. Bramati, "Polariton Superfluids Reveal Quantum Hydrodynamic Solitons," *Science*, vol. **332**, pp. 1167–1170, 06 2011. 15

[120] G. Lerario, A. Fieramosca, F. Barachati, D. Ballarini, K. S. Daskalakis, L. Dominici, M. De Giorgi, S. A. Maier, G. Gigli, S. Kéna-Cohen, and D. Sanvitto, "Room-temperature superfluidity in a polariton condensate," *Nature Physics*, vol. **13**, p. 837–841, 06 2017. 14

[121] I. Carusotto and C. Ciuti, "Quantum fluids of light," *Rev. Mod. Phys.*, vol. **85**, pp. 299–366, 02 2013. 14, 16, 38, 92

[122] J. Kasprzak, M. Richard, S. Kundermann, A. Baas, P. Jeambrun, J. M. J. Keeling, F. M. Marchetti, M. H. Szymańska, R. André, J. L. Staehli, V. Savona, P. B. Littlewood, B. Deveaud, and Le Si Dang, "Bose-Einstein condensation of exciton polaritons," *Nature*, vol. **443**, pp. 409–414, 09 2006. 14

[123] G. Nardin, G. Grosso, Y. Léger, B. Pięt̨ka, F. Morier-Genoud, and B. Deveaud-Plédran, "Hydrodynamic nucleation of quantized vortex pairs in a polariton quantum fluid," *Nature Physics*, vol. **7**, pp. 635–641, 04 2011. 15

[124] P. Azam, A. Fusaro, Q. Fontaine, J. Garnier, A. Bramati, A. Picozzi, R. Kaiser, Q. Glorieux, and T. Bienaimé, "Dissipation-enhanced collapse singularity of a nonlocal fluid of light in a hot atomic vapor," *Physical Review A*, vol. **104**, p. 013515, 07 2021. 15, 17, 20

[125] N. Šantić, A. Fusaro, S. Salem, J. Garnier, A. Picozzi, and R. Kaiser, "Nonequilibrium Precondensation of Classical Waves in Two Dimensions Propagating through Atomic Vapors," *Phys. Rev. Lett.*, vol. **120**, p. 055301, 02 2018. 15, 17

[126] O. Boughdad, A. Eloy, F. Mortessagne, M. Bellec, and C. Michel, "Anisotropic nonlinear refractive index measurement of a photorefractive crystal via spatial self-phase modulation," *Opt. Express*, vol. **27**, pp. 30360–30370, 10 2019. 15

[127] C. Denz, M. Schwab, and C. Weilnau, *Transverse-Pattern Formation in Photorefractive Optics*. Springer Berlin, 2003. 15

[128] D. Vocke, K. Wilson, F. Marino, I. Carusotto, E. M. Wright, T. Roger, B. P. Anderson, P. Öhberg, and D. Faccio, "Role of geometry in the superfluid flow of nonlocal photon fluids," *Phys. Rev. A*, vol. **94**, p. 013849, 07 2016. 15

[129] T. D. Ferreira, N. A. Silva, and A. Guerreiro, "Superfluidity of light in nematic liquid crystals," *Phys. Rev. A*, vol. **98**, p. 023825, 08 2018.

[130] M. Elazar, S. Bar-Ad, V. Fleurov, and R. Schilling, "An All-Optical Event Horizon in an Optical Analogue of a Laval Nozzle," *Lecture Notes in Physics*, vol. **870**, pp. 275–296, 08 2013. 15

[131] P. Leboeuf and S. Moulieras, "Superfluid Motion of Light," *Phys. Rev. Lett.*, vol. **105**, p. 163904, 10 2010. 15

[132] I. Carusotto, "Superfluid light in bulk nonlinear media," *Proc. R. Soc. A*, vol. **470**, p. 20140320, 07 2014. 16

[133] P.-E. Larré and I. Carusotto, "Propagation of a quantum fluid of light in a cavityless nonlinear optical medium: General theory and response to quantum quenches," *Phys. Rev. A*, vol. **92**, p. 043802, 10 2015. 15

[134] T. Aladjidi, *Full optical control of quantum fluids of light in hot atomic vapors*. PhD thesis, Sorbonne université, 2023. 15, 32

[135] S. N. Bose, "Plancks Gesetz und Lichtquantenhypothese," *Zeitschrift für Physik*, vol. **26**, pp. 178–181, 07 1924. 16

[136] Y. Pomeau and S. Rica, "Diffraction non linéaire," *C. R. Acad. Sci. Paris*, vol. **317**, p. 1287, 1993. 16

[137] R. W. Boyd, *Nonlinear Optics*. Academic Press, 2008. 16

[138] G. P. Agrawal, *Nonlinear Fiber Optics*. Academic Press, 2013. 16, 38

[139] I. Bloch, J. Dalibard, and S. Nascimbène, "Quantum simulations with ultracold quantum gases," *Nature Physics*, vol. **8**, pp. 267–276, 04 2012. 17

[140] R. Blatt and C. F. Roos, "Quantum simulations with trapped ions," *Nature Physics*, vol. **8**, pp. 277–284, 04 2012.

[141] C. Gross and I. Bloch, "Quantum simulations with ultracold atoms in optical lattices," *Science*, vol. **357**, pp. 995–1001, 09 2017. 17

[142] C. Noh and D. G. Angelakis, "Quantum simulations and many-body physics with light," *Reports on Progress in Physics*, vol. **80**, pp. 016401, 11 2016. 17

[143] I. Bloch, J. Dalibard, and W. Zwerger, "Many-body physics with ultracold gases," *Rev. Mod. Phys.*, vol. **80**, pp. 885–964, 07 2008. 17

[144] I. Carusotto, *Analog black holes in quantum fluids of light*, pp. 1673–1678. World Scientific Publishing Company, 01 2018. 17

[145] P.-E. Larré, *Fluctuations quantiques et effets non-linéaires dans les condensats de Bose-Einstein : des ondes de choc dispersives au rayonnement de Hawking acoustique*. PhD thesis, Université Paris-Sud, 2013.

[146] M. Jacquet, M. Joly, F. Claude, L. Giacomelli, Q. Glorieux, A. Bramati, I. Carusotto, and E. Giacobino, "Analogue quantum simulation of the Hawking effect in a polariton superfluid," *The European Physical Journal D*, vol. **76**, 08 2022.

[147] C. R. Almeida and M. Jacquet, "Analogue gravity and the Hawking effect: historical perspective and literature review," *The European Physical Journal H*, vol. **48**, 12 2023.

[148] F. Belgiorno, S. L. Cacciatori, M. Clerici, V. Gorini, G. Ortenzi, L. Rizzi, E. Rubino, V. G. Sala, and D. Faccio, "Hawking Radiation from Ultrashort Laser Pulse Filaments," *Phys. Rev. Lett.*, vol. **105**, p. 203901, 11 2010.

[149] M. Ornigotti, S. Bar-Ad, A. Szameit, and V. Fleurov, "Analog gravity by an optical vortex: Resonance enhancement of Hawking radiation," *Phys. Rev. A*, vol. **97**, p. 013823, 01 2018. 17

[150] C. C. Bradley, C. A. Sackett, J. J. Tollett, and R. G. Hulet, "Evidence of Bose-Einstein Condensation in an Atomic Gas with Attractive Interactions," *Phys. Rev. Lett.*, vol. **75**, pp. 1687–1690, 08 1995. 19

[151] C. Menotti and S. Stringari, "Collective oscillations of a one-dimensional trapped Bose-Einstein gas," *Phys. Rev. A*, vol. **66**, p. 043610, 10 2002. 19

[152] F. Gerbier, "Quasi-1D Bose-Einstein condensates in the dimensional crossover regime," *Europhysics Letters*, vol. **66**, pp. 771, 06 2004. 19

[153] A. Muñoz Mateo and V. Delgado, "Effective mean-field equations for cigar-shaped and disk-shaped Bose-Einstein condensates," *Phys. Rev. A*, vol. **77**, p. 013617, 01 2008. 20

[154] E. Estrecho, T. Gao, N. Bobrovska, D. Comber-Todd, M. D. Fraser, M. Steger, K. West, L. N. Pfeiffer, J. Levinsen, M. M. Parish, T. C. H. Liew, M. Matuszewski, D. W. Snoke, A. G. Truscott, and E. A. Ostrovskaya, "Direct measurement of polariton-polariton interaction strength in the Thomas-Fermi regime of exciton-polariton condensation," *Phys. Rev. B*, vol. **100**, p. 035306, 07 2019. 20

[155] F. Dalfovo, L. Pitaevskii, and S. Stringari, "Order parameter at the boundary of a trapped Bose gas," *Physical Review A*, vol. **54**, p. 4213–4217, 11 1996. 28, 46

[156] G. E. Astrakharchik and L. P. Pitaevskii, "Motion of a heavy impurity through a Bose-Einstein condensate," *Phys. Rev. A*, vol. **70**, p. 013608, 07 2004. 29, 32, 67, 132

[157] H. Lamb, *Hydrodynamics*. Cambridge University Press, Cambridge, 1997. 31, 59, 62

[158] W. Thomson, "On Ship Waves," *Proceedings of the Institution of Mechanical Engineers*, vol. **38**, no. 1, pp. 409–434, 1887. 32

[159] I. Carusotto, S. X. Hu, L. A. Collins, and A. Smerzi, "Bogoliubov-Čerenkov Radiation in a Bose-Einstein Condensate Flowing against an Obstacle," *Phys. Rev. Lett.*, vol. **97**, p. 260403, 12 2006. 32

[160] L. D. Landau and E. M. Lifshitz, *Electrodynamics of Continuous Media*. New York: Pergamon, 1984. 32

[161] T. Winiecki, J. F. McCann, and C. S. Adams, "Pressure Drag in Linear and Nonlinear Quantum Fluids," *Phys. Rev. Lett.*, vol. **82**, pp. 5186–5189, 06 1999. 32, 108

[162] M. Wouters and I. Carusotto, "Superfluidity and Critical Velocities in Nonequilibrium Bose-Einstein Condensates," *Phys. Rev. Lett.*, vol. **105**, p. 020602, 07 2010. 32, 52, 53, 92

[163] P.-E. Larré, N. Pavloff, and A. M. Kamchatnov, "Wave pattern induced by a localized obstacle in the flow of a one-dimensional polariton condensate," *Phys. Rev. B*, vol. **86**, p. 165304, 10 2012. 32, 33, 34, 52, 53, 67

[164] R. Desbuquois, L. Chomaz, T. Yefsah, J. Léonard, J. Beugnon, C. Weitenberg, and J. Dalibard, "Superfluid behaviour of a two-dimensional Bose gas," *Nature Physics*, vol. **8**, p. 645–648, 07 2012. 32, 91

[165] L. D. Landau, "On the Theory of Superfluidity of Helium II," *J. Phys. URSS*, vol. **11**, p. 91, 1947. 35

[166] M. Remoissenet, *Hydrodynamic Solitons*, pp. 88–122. Springer Berlin Heidelberg, 1994. 38

[167] A. Chabchoub, O. Kimmoun, H. Branger, N. Hoffmann, D. Proment, M. Onorato, and N. Akhmediev, "Experimental Observation of Dark Solitons on the Surface of Water," *Phys. Rev. Lett.*, vol. **110**, p. 124101, 03 2013. 38

[168] J. S. Russell, *Report on Waves*. Technical report, Report of the fourteenth meeting of the British Association for the Advancement of Science, York, 1844. 38

[169] A. M. Weiner, J. P. Heritage, R. J. Hawkins, R. N. Thurston, E. M. Kirschner, D. E. Leaird, and W. J. Tomlinson, "Experimental Observation of the Fundamental Dark Soliton in Optical Fibers," *Phys. Rev. Lett.*, vol. **61**, pp. 2445–2448, 11 1988. 38

[170] D. J. Frantzeskakis, "Dark solitons in atomic Bose–Einstein condensates: from theory to experiments," *Journal of Physics A: Mathematical and Theoretical*, vol. **43**, pp. 213001, 05 2010. 38

[171] J. Denschlag, J. E. Simsarian, D. L. Feder, C. W. Clark, L. A. Collins, J. Cubizolles, L. Deng, E. W. Hagley, K. Helmerson, W. P. Reinhardt, S. L. Rolston, B. I. Schneider, and W. D. Phillips, "Generating Solitons by Phase Engineering of a Bose-Einstein Condensate," *Science*, vol. **287**, pp. 97–101, 01 2000.

[172] S. Burger, K. Bongs, S. Dettmer, W. Ertmer, K. Sengstock, A. Sanpera, G. V. Shlyapnikov, and M. Lewenstein, "Dark Solitons in Bose-Einstein Condensates," *Phys. Rev. Lett.*, vol. **83**, pp. 5198–5201, 12 1999.

[173] S. Stellmer, C. Becker, P. Soltan-Panahi, E.-M. Richter, S. Dörscher, M. Baumert, J. Kronjäger, K. Bongs, and K. Sengstock, "Collisions of Dark Solitons in Elongated Bose-Einstein Condensates," *Phys. Rev. Lett.*, vol. **101**, p. 120406, 09 2008. 38

[174] A. Maître, G. Lerario, A. Medeiros, F. Claude, Q. Glorieux, E. Giacobino, S. Pigeon, and A. Bramati, "Dark-Soliton Molecules in an Exciton-Polariton Superfluid," *Phys. Rev. X*, vol. **10**, p. 041028, 11 2020. 38

[175] V. E. Zakharov and A. B. Shabat, "Exact Theory of Two-dimensional Self-focusing and One-dimensional Self-modulation of Waves in Nonlinear Media," *Soviet Physics JETP*, vol. **34**, pp. 62–69, 12 1970. 38

[176] N. Bilas, *Transport dans les condensats de Bose-Einstein unidimensionnels désordonnés*. PhD thesis, Université de Paris-Sud, 2023. 38

[177] G. Watanabe, F. Dalfovo, F. Piazza, L. P. Pitaevskii, and S. Stringari, "Critical velocity of superfluid flow through single-barrier and periodic potentials," *Phys. Rev. A*, vol. **80**, p. 053602, 11 2009. 43

[178] D. J. Griffiths and D. F. Schroeter, *Introduction to Quantum Mechanics*. Cambridge University Press, 3 ed., 2018. 47, 78, 86

[179] P.-E. Larré, S. Biasi, F. Ramiro-Manzano, L. Pavesi, and I. Carusotto, "Pump-and-probe optical transmission phase shift as a quantitative probe of the Bogoliubov dispersion relation in a nonlinear channel waveguide," *Eur. Phys. J. D*, vol. **71**, 06 2017. 52

[180] D. Dries, S. E. Pollack, J. M. Hitchcock, and R. G. Hulet, "Dissipative transport of a Bose-Einstein condensate," *Phys. Rev. A*, vol. **82**, p. 033603, 09 2010. 58

[181] T. Paul, M. Hartung, K. Richter, and P. Schlagheck, "Nonlinear transport of Bose-Einstein condensates through mesoscopic waveguides," *Phys. Rev. A*, vol. **76**, p. 063605, 12 2007. 60, 78

[182] J. J. Sylvester, "LX. On a remarkable discovery in the theory of canonical forms and of hyperdeterminants," *The London, Edinburgh, and Dublin Philosophical Magazine and Journal of Science*, vol. **2**, no. 12, pp. 391–410, 1851. 65

[183] P.-E. Larré and I. Carusotto, "Optomechanical signature of a frictionless flow of superfluid light," *Phys. Rev. A*, vol. **91**, p. 053809, 05 2015. 65, 71

[184] A. G. Sykes, M. J. Davis, and D. C. Roberts, "Drag Force on an Impurity below the Superfluid Critical Velocity in a Quasi-One-Dimensional Bose-Einstein Condensate," *Phys. Rev. Lett.*, vol. **103**, p. 085302, 08 2009. 67, 132

[185] G. Lang, F. Hekking, and A. Minguzzi, "Dynamic structure factor and drag force in a one-dimensional strongly interacting Bose gas at finite temperature," *Phys. Rev. A*, vol. **91**, p. 063619, 06 2015. 67, 132

[186] T. Tsuzuki, "Nonlinear waves in the Pitaevskii-Gross equation," *Journal of Low Temperature Physics*, vol. **4**, pp. 441–457, 04 1971. 68

[187] D. J. Korteweg and G. de Vries, "XLI. On the change of form of long waves advancing in a rectangular canal, and on a new type of long stationary waves," *The London, Edinburgh, and Dublin Philosophical Magazine and Journal of Science*, vol. **39**, no. 240, pp. 422–443, 1895. 68

[188] G. I. Martone, A. Recati, and N. Pavloff, "Supersolidity of cnoidal waves in an ultracold Bose gas," *Phys. Rev. Research*, vol. **3**, p. 013143, 02 2021. 68

[189] M. Abramowitz and I. A. Stegun, *Handbook of Mathematical Functions with Formulas, Graphs, and Mathematical Tables*. Dover, New York, 1965. 68

[190] L. D. Carr, C. W. Clark, and W. P. Reinhardt, "Stationary solutions of the one-dimensional nonlinear Schrödinger equation. I. Case of repulsive nonlinearity," *Phys. Rev. A*, vol. **62**, p. 063610, 11 2000. 68

[191] J. Huynh, M. Albert, and P.-E. Larré, "Critical velocity for superfluidity in the one-dimensional mean-field regime: From matter to light quantum fluids," *Phys. Rev. A*, vol. **105**, p. 023305, 02 2022. 74

[192] T. Paul, M. Albert, P. Schlagheck, P. Leboeuf, and N. Pavloff, "Anderson localization of a weakly interacting one-dimensional Bose gas," *Phys. Rev. A*, vol. **80**, p. 033615, 09 2009. 78

[193] C. Cohen-Tannoudji, B. Diu, and F. Laloë, *Quantum Mechanics Vol. I.* Blackwell Verlag GmbH, 2019. 83

[194] V. P. Singh, C. Weitenberg, J. Dalibard, and L. Mathey, "Superfluidity and relaxation dynamics of a laser-stirred two-dimensional Bose gas," *Phys. Rev. A*, vol. **95**, p. 043631, 04 2017. 91

[195] W. J. Kwon, G. Moon, S. W. Seo, and Y. Shin, "Critical velocity for vortex shedding in a Bose-Einstein condensate," *Phys. Rev. A*, vol. 91, p. 053615, 05 2015. 91, 92, 111, 115, 117, 124, 125

[196] J. Rønning and L. Angheluta, "Precursory patterns to vortex nucleation in stirred Bose-Einstein condensates," *Phys. Rev. Research*, vol. **5**, p. 023108, 05 2023. 92

[197] N. P. Müller and G. Krstulovic, "Critical velocity for vortex nucleation and roton emission in a generalized model for superfluids," *Phys. Rev. B*, vol. **105**, p. 014515, 01 2022.

[198] O. R. Stockdale, M. T. Reeves, and M. J. Davis, "Dynamical Mechanisms of Vortex Pinning in Superfluid Thin Films," *Phys. Rev. Lett.*, vol. **127**, p. 255302, 12 2021. 92

[199] T. Aioi, T. Kadokura, T. Kishimoto, and H. Saito, "Controlled Generation and Manipulation of Vortex Dipoles in a Bose-Einstein Condensate," *Phys. Rev. X*, vol. **1**, p. 021003, 10 2011. 92, 111, 124

[200] C. Huepe and M.-E. Brachet, "Scaling laws for vortical nucleation solutions in a model of superflow," *Physica D: Nonlinear Phenomena*, vol. **140**, pp. 126–140, 06 2000. 92, 108

[201] K. G. Lagoudakis, M. Wouters, M. Richard, A. Baas, I. Carusotto, R. André, Le Si Dang, and B. Deveaud-Plédran, "Quantized vortices in an exciton–polariton condensate," *Nature Physics*, vol. **4**, pp. 706–710, 08 2008. 92

[202] A. Amo, D. Sanvitto, F. P. Laussy, D. Ballarini, E. del Valle, M. D. Martin, A. Lemaître, J. Bloch, D. N. Krizhanovskii, M. S. Skolnick, C. Tejedor, and L. Viña, "Collective fluid dynamics of a polariton condensate in a semiconductor microcavity," *Nature*, vol. **457**, pp. 291–295, 01 2009.

[203] I. Carusotto and C. Ciuti, "Probing Microcavity Polariton Superfluidity through Resonant Rayleigh Scattering," *Phys. Rev. Lett.*, vol. **93**, p. 166401, 10 2004. 92

[204] S. Pigeon and A. Aftalion, "Critical velocity in resonantly driven polariton superfluids," *Physica D: Nonlinear Phenomena*, vol. **415**, p. 132747, 01 2021. 92

[205] L. A. Peña Ardila, G. E. Astrakharchik, and S. Giorgini, "Strong coupling Bose polarons in a two-dimensional gas," *Phys. Rev. Research*, vol. **2**, p. 023405, 06 2020. 95

[206] Y. G. Gladush, L. A. Smirnov, and A. M. Kamchatnov, "Generation of Cherenkov waves in the flow of a Bose–Einstein condensate past an obstacle," *Journal of Physics B: Atomic, Molecular and Optical Physics*, vol. **41**, pp. 165301, 08 2008. 96

[207] L. D. Landau and Lifshitz, *Fluid Mechanics*. Pergamon Press Oxford, England, 1959. 97, 104, I

[208] O. Janzen, "Beitrag zu einer Theorie der stationären Strömung kompressibler Flüssigkeiten," *Phys. Zeits*, vol. **14**, p. 639, 1913. 101

[209] L. Rayleigh, "I. On the flow of compressible fluid past an obstacle," *The London, Edinburgh, and Dublin Philosophical Magazine and Journal of Science*, vol. **32**, p. 1, 07 1916. 101

[210] I. Imai, "On the Flow of a Compressible Fluid past a Circular Cylinder," *Nippon Sugaku-Buturigakkwai Kizi Dai 3 Ki*, vol. **20**, pp. 636–645, 1938. 106

[211] M. M. Cerimele, M. L. Chiofalo, F. Pistella, S. Succi, and M. P. Tosi, "Numerical solution of the Gross-Pitaevskii equation using an explicit finite-difference scheme: An application to trapped Bose-Einstein condensates," *Phys. Rev. E*, vol. **62**, pp. 1382–1389, 07 2000. 108, 117

[212] A. Minguzzi, S. Succi, F. Toschi, M. Tosi, and P. Vignolo, "Numerical methods for atomic quantum gases with applications to Bose–Einstein condensates and to ultracold fermions," *Physics Reports*, vol. **395**, no. 4, pp. 223–355, 2004. 108, 117

[213] T. Winiecki, B. Jackson, J. F. McCann, and C. S. Adams, "Vortex shedding and drag in dilute Bose-Einstein condensates," *Journal of Physics B: Atomic, Molecular and Optical Physics*, vol. **33**, pp. 4069, 10 2000. 108

[214] N. G. Berloff and P. H. Roberts, "Motions in a Bose condensate: VII. Boundary-layer separation," *Journal of Physics A: Mathematical and General*, vol. **33**, pp. 4025, 06 2000. 111, 121, 123, 124

[215] M. L. Chiofalo, S. Succi, and M. P. Tosi, "Ground state of trapped interacting Bose-Einstein condensates by an explicit imaginary-time algorithm," *Phys. Rev. E*, vol. **62**, pp. 7438–7444, 11 2000. 117

[216] J. Huynh, F. Hébert, M. Albert, and P.-E. Larré, "Critical velocity of a two-dimensional superflow past a potential barrier of arbitrary penetrability," *Phys. Rev. A*, vol. **109**, p. 013317, 01 2024. 117

[217] C. A. Jones and P. H. Roberts, "Motions in a Bose condensate. IV. Axisymmetric solitary waves," *Journal of Physics A: Mathematical and General*, vol. **15**, pp. 2599, 08 1982. 119

[218] H. Proud, *Soliton structures in Bose-Einstein condensates*. PhD thesis, University of Birmingham, 2018. 119

[219] K. Fujimoto and M. Tsubota, "Nonlinear dynamics in a trapped atomic Bose-Einstein condensate induced by an oscillating Gaussian potential," *Phys. Rev. A*, vol. **83**, p. 053609, 05 2011. 121

[220] B. Jackson, J. F. McCann, and C. S. Adams, "Dissipation and vortex creation in Bose-Einstein condensed gases," *Phys. Rev. A*, vol. **61**, p. 051603, 04 2000. 121

[221] D. C. Roberts, "Force on a moving point impurity due to quantum fluctuations in a Bose-Einstein condensate," *Phys. Rev. A*, vol. **74**, p. 013613, 07 2006. 132

[222] B. Reichert, Z. Ristivojevic, and A. Petković, "The Casimir-like effect in a one-dimensional Bose gas," *New Journal of Physics*, vol. **21**, pp. 053024, 05 2019. 132

[223] A. Hogg, *Mathematical Methods Lectures*. University of Bristol, 2017. II